Magnetic structures, phase diagram and spin waves of magneto-electric LiNiPO4

Jensen, Thomas Bagger Stibius

Publication date:
2007

Document Version
Publisher's PDF, also known as Version of record

Risø DTU
National Laboratory
for Sustainable Energy

Risø-PhD-thesis

Magnetic structures, phase diagram and spin waves of magneto-electric $LiNiPO_4$

Thomas Bagger Stibius Jensen

Risø-PhD-40(EN)

Risø National Laboratory for Sustainable Energy
Technical University of Denmark
Roskilde, Denmark
June 2007

Author: Thomas Bagger Stibius Jensen
Title: Magnetic structures, phase diagram and spin waves of magneto-electric $LiNiPO_4$
Department: Materials Research Department

This thesis is submitted in partial fulfilment of the requirements for the Ph.D. degree at University of Copenhagen

Risø-PhD-40(EN)
June 2007

Abstract (max. 2000 char.):

This is a summary of my work on the compound $LiNiPO_4$, performed as a phD student at the MaterialsResearch Department at Risoe National Laboratory, Denmark. Officially the project was also affiliated with the University of Copenhagen. Besides the work on $LiNiPO_4$ presented here, I have also been involved in studies of the borocarbide rare earth materials as part of my project. I shall not be discussing the borocarbides in this thesis, and instead refer to the published articles [1, 2] on $TmNi_2B_2C$ and coming article [3] on $TbNi_2B_2C$.
$LiNiPO_4$ is a magneto-electric material, having co-existing antiferromagnetic and ferroelectric phases when suitable magnetic fields are applied at low temperatures. Such systems have received growing interest in recent years, but the nature of the magnetic-electric couplings is yet to be fully understand. Hopefully, studying $LiNiPO_4$ will shed further light on the subject, especially since the crystal structure of $LiNiPO_4$ is rather simple compared to most relevant multiferroic materials.
Although the study of the magnetic-electric couplings is of main interest to the many scientists guiding me through the last three years, it is not the primary subject of this thesis. The objective of the phD project has been to provide groundwork that may be beneficiary to future studies of $LiNiPO_4$. More specifically, we have mapped out the magnetic HT phase diagram with magnetic fields below 14.7 T applied along the crystallographic c-axis, determined the magnetic structures for the phases in the phase diagram, and have set up a spin model Hamiltonian describing the spin wave dynamics and estimating the relevant magnetic interactions.

ISBN 978-87-550-3692-5

Contract no.:

Group's own reg. no.:

Sponsorship:

Cover :

Pages: 131
Tables:
References:

Information Service Department
Risø National Laboratory for Sustainable Energy
Technical University of Denmark
P.O.Box 49
DK-4000 Roskilde
Denmark
Telephone +45 46774004
bibl@risoe.dk
Fax +45 46774013
www.risoe.dtu.dk

Contents

Preface

In this second addition a few typo's found in the original thesis have been corrected - and probably many still awaits finding. Apart from correcting typographical errors, including this Preface and a change in the page numbering, the present version is identical to the thesis submitted in June 2007. The following major points must be addressed.

Firstly, the spin wave modeling of this work is valid in the low temperature zero field region (section 7.2.2), but not at higher temperatures (section 7.2.3) or in applied magnetic field (section 7.2.4). Concerning the zero field spin wave modeling at low temperatures, professor Jens Jensen has pointed out that the anisotropy terms $D_x S$ and $D_y S$ in equation (6.86) and (6.92) should be replaced with $D_x(S - 1/2)$ and $D_y(S - 1/2)$. Effectively this will make the calculated anisotropies for the best fit twice as large as the values given in the thesis, i.e. the correct anisotropies are $D_x = 0.339$ meV and $D_y = 1.82$ meV.

Secondly, the discussion in section 5.7 concerning the magneto-electric (ME) effect in $LiNiPO_4$ is very sparse at best. A better understanding of the ME effect, largely based on a microscopic model, was attained shortly after completing the thesis. A summary can be found in T. B. S. Jensen *et al., Phys. Rev. Lett. ??* (2008).

July 2008,
Thomas B. S. Jensen

Chapter 1

Introduction

This is a summary of my work on the compound $LiNiPO_4$, performed as a phD student at the Materials Research Department at Risoe National Laboratory, Denmark. Officially the project was also affiliated with the University of Copenhagen. Besides the work on $LiNiPO_4$ presented here, I have also been involved in studies of the borocarbide rare earth materials as part of my project. I shall not be discussing the borocarbides in this thesis, and instead refer to the published articles [1, 2] on $TmNi_2B_2C$ and coming article [3] on $TbNi_2B_2C$.

$LiNiPO_4$ is a magneto-electric material, having co-existing antiferromagnetic and ferroelectric phases when suitable magnetic fields are applied at low temperatures. Such systems have received growing interest in resent years, but the nature of the magnetic-electric couplings is yet to be fully understand. Hopefully, studying $LiNiPO_4$ will shed further light on the subject, especially since the crystal structure of $LiNiPO_4$ is rather simple compared to most relevant multiferroic materials.

Although the study of the magnetic-electric couplings is of main interest to the many scientists guiding me through the last three years, it is not the primary subject of this thesis. The objective of the phD project has been to provide groundwork that may be beneficiary to future studies of $LiNiPO_4$. More specifically, we have mapped out the magnetic HT phase diagram with magnetic fields below 14.7 T applied along the crystallographic c-axis, determined the magnetic structures for the phases in the phase diagram, and have set up a spin model Hamiltonian describing the spin wave dynamics and estimating the relevant magnetic interactions.

As a student I have often found it hard to read and understand scientific publications; the major problem being the lack of details making it hard, often impossible, for me to retrace the path from "A" to "B" - and sometimes even to understand "A" and "B". The drawback of including details is that they may seriously compromise the readability, and I fear that especially my chapters 3 and 6 might suffer from this. The philosophy is, however, that while the chapters may be hard to read, they should make it easier to ultimately *understand* what is done. Hopefully the interested readers will be able to use the methods for themselves after working though the thesis.

I have tried to write a thesis that I would have liked to have read at the beginning of my project. Maybe this criteria of success has not been completely fulfilled, but at least I hope the end result is readable and not too seriously flawed.

The text is organized as follows. In chapter 2 we review some of the basic properties of $LiNiPO_4$, and go through some standard textbook theory on magnetism. We also briefly discuss neutron scattering, which is the experimental method used for all our main experiments on $LiNiPO_4$, but only very superficially. Chapter 3 describes a few group theoretical concepts, and their relation to magnetic structures and the neutron scattering cross-section. The magnetic phase diagram and related experiments are given in chapter 4, while the magnetic structures are determined in chapter 5. In chapter 6 I develop the relevant theory for analyzing the inelastic spin wave experiments described and examined in chapter 7. Finally I end with concluding remarks in chapter 8.

Chapter 2

Background information

2.1 Introduction

In this chapter we review some "well-known" properties of $LiNiPO_4$. Furthermore, we shall briefly discuss a few elements of magnetism and neutron scattering. All the theory described in this chapter is kept on an introductional level, and can be found described in standard text books on the respective subjects.

2.2 Known properties of $LiNiPO_4$

$LiNiPO_4$ is part of a family of compounds, called the lithium (ortho)phosphates, with members $LiMPO_4$, where M = Co, Ni, Mn, Fe, Cu are transition metals. The lithium phosphates have been studied with some interest, hoping to help providing cathode materials for a new generation of rechargeable lithium batteries. One of the drawbacks for this specific purpose is that the materials are all insulators. For instance, the prime candidate, $LiFePO_4$, has an electronic resistivity of $\sim 10^8$ Ωm at room temperature [4], or about the same as wood.

The lithium phosphates have also received attention because of their magnetic properties. Investigating the magnetic properties of lithium nickel phosphate is the main motivation for this phD project. As background information, we begin by reviewing some of the "need to know" properties of $LiNiPO_4$.

2.2.1 Crystal structure

The crystal structure of $LiNiPO_4$ has been determined by Abrahams and Easson [5], analyzing powder diffraction data from an x-ray scattering experiment. Their analysis showed that $LiNiPO_4$ is orthorhombic, with crystallographic space group *Pnma* (space group number 62 in [6]). The crystal symmetries of $LiNiPO_4$ is described in more detail in chapter 3.

	site	x	y	z
Li	4(a)	0.0	0.0	0.0
Ni	4(c)	0.2756	0.25	0.9825
P	4(c)	0.0943	0.25	0.4167
O(1)	4(c)	0.1008	0.25	0.7427
O(2)	4(c)	0.4492	0.25	0.1978
O(3)	8(d)	0.1668	0.0439	0.2783

Table 2.1: Atomic positions of non-equivalent ions in $LiNiPO_4$, taken from [5]

.

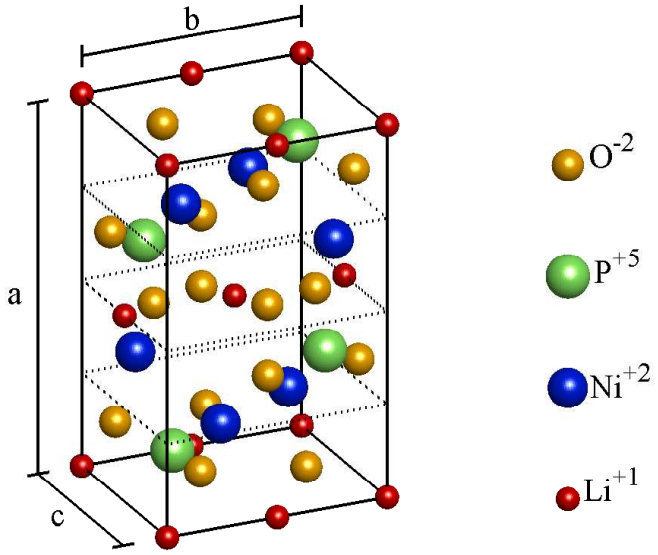

Figure 2.1: The conventionally defined chemical unit cell of $LiNiPO_4$.

The standard choice of the chemical unit cell for $LiNiPO_4$ is depicted in figure 2.1. At room temperature, Abrahams [5] found the lattice parameters to be $a = 10.032$ Å, $b = 5.854$ Å, $c = 4.677$ Å, and the atomic positions of non-equivalent ions within the unit cell as given in table 2.2.1 (using normalized lattice units). At low temperatures the lattice parameters are slightly smaller than the room-temperature values. In our low-temperature experiments we find that the lattice parameters were approximately

$$a = 10.02\,\text{Å}, \quad b = 5.83\,\text{Å}, \quad c = 4.66\,\text{Å}. \tag{2.1}$$

2.2.2 Magnetic ordering in $LiNiPO_4$

Magnetization studies [7], performed as early as 1966, on a polycrystalline powder of $LiNiPO_4$, followed a Curie-Weiss law in the paramagnetic phase, with coefficients $p_{eff} = 3.35\mu_B$ and $\theta = 23.2$ K. Here the effective number of Bohr magnetons, p_{eff}, is connected to the total angular momentum J by $p_{eff} = g[J(J+1)]^{1/2}$ (see for instance [8]). The susceptibility measurements of this experiment, shown in figure 2.4, indicated a paramagnetic-antiferromagnetic phase transition around 23 ± 2 K. As we shall discuss in some detail later (section 2.3), the magnetism in $LiNiPO_4$ is due to S = 1 spins, localized around the Ni^{2+} ions. The other ions in the system, Li^+, P^{5+} and O^{2-}, are all nonmagnetic. The value $p_{eff} = 3.35\mu_B$ indicates a non-zero contribution from the orbital angular momentum L of the nickel ions at higher temperatures. Santoro *et al.* [7] showed, analyzing neutron powder diffraction patterns, that the Ni spin at low temperatures order antiferromagnetically as shown in figure 2.2. Here, the spins point parallel or anti-parallel to the crystallographic c axis, and are antiferromagnetic ordered in ferromagnetic ac planes.

Scattering experiments performed on single crystals provide better data, and therefore often more precise information, than powder experiments. In 2004 David Vaknin and co-workers [9] published elastic neutron data from a $LiNiPO_4$ single crystal, demonstrating a commensurate-incommensurate (C-IC) magnetic phase transition around 20.8 K in zero field. The phase transition was detected by a splitting of the antiferromagnetic (0,1,0) peak into peaks at $(0, 1\pm q, 0)$, as shown in figure 2.3. The (0,1,0) peak signifies the commensurate phase, while the $(0, 1 \pm q, 0)$ peaks signifies the incommensurate phase. The wave vector q is called the modulation vector, or the incommensurate wave vector. In Vaknins experiment, the incommensurate wave vector was temperature dependent, but the direction was always along K. The size of domains (in this case magnetically ordered domains) is, as a rule of thumb, estimated as the reciprocal peak width; of course after taking

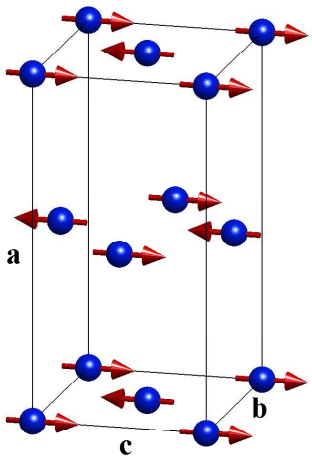

Figure 2.2: The anti-ferromagnetic magnetic structure for $LiNiPO_4$ for temperatures below $\sim$ 21 K, determined by powder diffraction [7]. The depicted magnetic unit cell, showing the Ni ions and the localized spins, has been displaced (0.25,0.25,0) rlu compared to the chemical unit cell shown in figure 2.1.

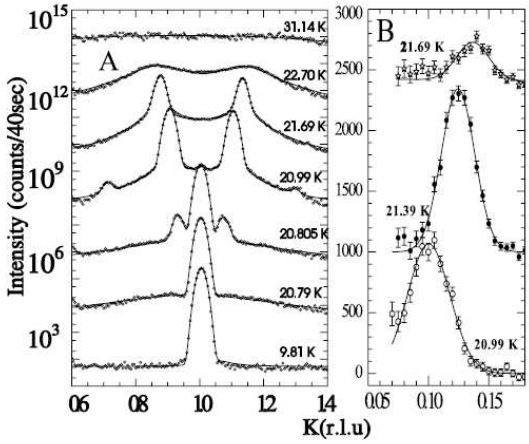

Figure 2.3: Elastic $(0, K, 0)$ neutron measurements in zero field, from [9]. A resolution limited (0,1,0) peak signals the commensurate antiferromagnetic phase for T below 20.8 K. At T$\simeq$ 20.8 K, both the commensurate (0,1,0) and the incommensurate $(0, 1\pm q, 0)$ peaks are present, indicating a first order C-IC phase transition. Above 21.8 K the peaks broaden and there is no long range magnetic order.

the instrumental resolution[1] into account. From figure 2.3 it is observed that the commensurate phase is very well ordered, since here the (0,1,0) peaks are resolution limited. The incommensurate phase is equally well ordered in a narrow temperature region ranging from approximately 20.8-21.8 K, while at temperatures above 21.8 K the scattering becomes increasingly diffuse, signaling the disappearance of long range IC order.

Bulk magnetization measurements [10] on a $LiNiPO_4$ single crystal, with a strong magnetic field applied along the crystallographic c-axis, indicates the appearance of several magnetic phase transitions as function of field. Figure 2.5 shows the observed transition fields, detectable as kinks and jumps in the magnetization curves as function of temperature. In this thesis we shall study the lowest lying of these transitions.

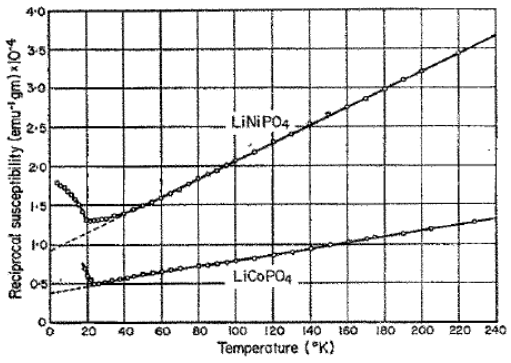

Figure 2.4: Reciprocal magnetic susceptibility of polycrystalline $LiNiPO_4$ and $LiCoPO_4$ in zero field. Figure taken from [7].

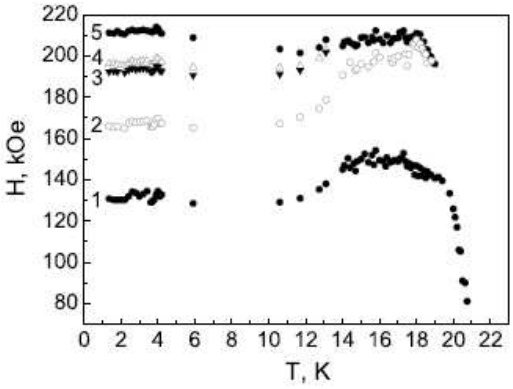

Figure 2.5: Temperature dependence of threshold fields, $H \parallel c$, determined by magnetization measurements on a $LiNiPO_4$ single crystal (Khrustalyov *et al.* [10]). The numbering 1-5 refer to the 5 observed kinks in the magnetization.

[1]The instrumental resolution is the unavoidable broadening of peaks which in theory are delta-functions, due to the geometry of the instrument.

2.2.3 Magneto-electric properties

Materials that have both magnetic and ferroelectric phases are called multiferroics. Such compounds have received growing attention in recent years [11, 12] driven by a desire to understand the underlying physics, but also because they have potentially interesting applications [13, 14]. For most of these systems the ferroelectric and magnetic phases have very different ordering temperatures, showing that the coupling between the magnetism and electric polarization is negligible, but for some the magnetic and electric orderings are closely related. This is, for instance, the case of $TbMnO_3$ and $Ni_3V_2O_8$, which both exhibit magnetic phase transitions that coincide with the ferroelectric ones [15, 16, 17].

Another group of multiferroics where the magnetic and electric properties are strongly coupled, are the so-called magneto-electric compounds. These systems have ferro- or antiferromagnetic (FM or AFM) phases where the application of a magnetic field will induce electric polarization. The reverse is also true; applying an electric field will induce a macroscopic magnetization. The size of the magneto-electric effect is frequently given by magneto-electric coefficients, $\alpha_{\mu\nu}$, defined as

$$\alpha_{\mu\nu} = \frac{P_\mu}{\mu_0 H_\nu}, \quad \mu, \nu = x, y, z. \tag{2.2}$$

Here P_μ is the electric polarization induced in the μ-direction, when applying a magnetic field $\mu_0 H_\nu$ along ν.

The lithium-phosphates all posses a strong magneto-electric effect. In figure 2.6, taken from [9], the magneto-electric coefficients of $LiNiPO_4$ are shown in applied fields of 0.5 Tesla and as function of temperatures. We note that α_{xz} and α_{zx} are both non-zero in the commensurate phase, but drop to zero above the C-IC phase transition temperature of 20.8 K. Therefore, for temperatures below 20.8 K, applying a magnetic field along the crystallographic a-direction will induce a polarization along c, and applying a field along c will induce a polarization along a. Applying a field along b does not induce an electric polarization in $LiNiPO_4$. In figure 2.7, from [18], the electric polarization P_z of $LiNiPO_4$ as function of an magnetic field H_x, applied along the a-axis, is shown for various temperatures.

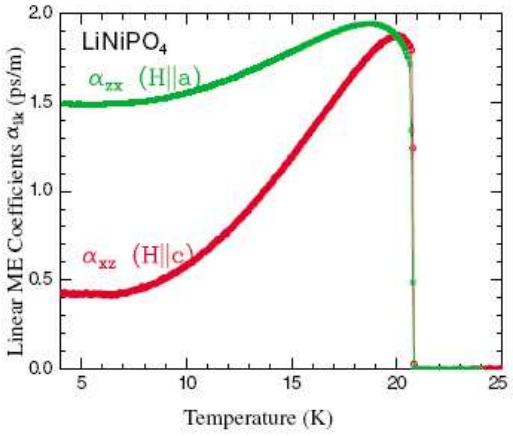

Figure 2.6: Magneto-electric coefficients of $LiNiPO_4$ as function of temperatures, measured in applied fields of 0.5 T. Figure taken from [9].

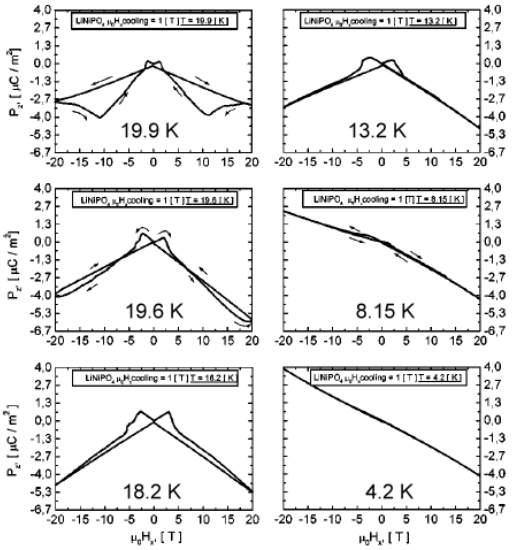

Figure 2.7: Electric polarization P_z along the crystallographic c-axis as function of field, H_x, applied along a. Figure taken from [18].

2.3 Magnetism

In this section, the energy levels and quantum states of the Ni^{2+} ions in $LiNiPO_4$ is described, and the nature of the various magnetic interactions we shall encounter later in the thesis will be discussed.

2.3.1 Isolated many-electron atom

We begin by briefly reviewing the treatment of an isolated atom, or ion[2], consisting of a nucleus with charge $+Ze$ surrounded by N electrons. A good introductional understanding [19] of the energy levels and eigenstates of an isolated atom can be provided by a Hamiltonian including

1) The kinetic energy of the electrons,
2) The electrostatic Coulomb energy between the electrons and the nucleus (considered to be point-like and of infinite mass),
3) The electrostatic Coulomb energy between the electrons,
4) The magnetic interactions between the spin of the electrons and their orbital movements (spin-orbit interactions).

These four terms are described by the following Hamiltonian

$$\mathcal{H} = \sum_{i=1}^{N}\left(-\frac{\hbar^2}{2m}\nabla_{r_i}^2 - \frac{Ze^2}{4\pi\varepsilon_0 r_i}\right) + \sum_{i<j=1}^{N}\frac{e^2}{4\pi\varepsilon_0 r_{ij}} + \sum_{i=1}^{N}\xi(r_i)\mathbf{l}_i\cdot\mathbf{s}_i. \tag{2.3}$$

Here $\mathbf{r}_i$ is the position operator of the i'th electron, $\mathbf{r}_{ij} = \mathbf{r}_i - \mathbf{r}_j$, and $\mathbf{l}_i$ and $\mathbf{s}_i$ are the orbital angular momentum and spin operators of the i'th electron. The spin-orbit coupling parameter $\xi(r_i)$ can be calculated as

$$\xi(r_i) = \frac{1}{2m^2c^2}\frac{1}{r_i}\frac{\mathrm{d}V_c(r_i)}{\mathrm{d}r_i}, \tag{2.4}$$

by use of the central field potential $V_c(r)$, introduced below. The eigenvalue problem

$$\mathcal{H}\Psi(q_1,\ldots,q_N) = E\Psi(q_1,\ldots,q_N), \tag{2.5}$$

where $q_i \equiv (\mathbf{r}_i, s_i)$ are the space and spin coordinates, is impossible to solve exact, but approximate solutions can be provided by the use of perturbation theory. This is generally done in the following three steps.

Step 1: The central field approximation

Considering the electrons as independent particles moving in an effective Coulomb potential $V_{eff}(r)$ from the nucleus and the other electrons has proved to be a successful approximation. The average electron cloud of the "first" $N-1$ electrons gives a large spherical symmetric contribution, $S(r)$, to the potential of the N'th electron, and we write

$$\begin{aligned}\mathcal{H} &= \sum_{i=1}^{N}\left(-\frac{\hbar^2}{2m}\nabla_{r_i}^2 + V_c(r_i)\right) + \left[\sum_{i<j=1}^{N}\frac{e^2}{4\pi\varepsilon_0 r_{ij}} - \sum_{i=1}^{N}S(r_i)\right] + \sum_{i=1}^{N}\xi(r_i)\mathbf{l}_i\cdot\mathbf{s}_i \\ &= \mathcal{H}_c + \mathcal{H}_1 + \mathcal{H}_{so},\end{aligned} \tag{2.6}$$

where

$$V_c(r) = -\frac{Ze^2}{4\pi\varepsilon_0 r} + S(r), \tag{2.7}$$

[2]Everything said about atoms in this section also applies to ions.

is the spherical symmetric part of $V_{eff}(r)$. The Hamiltonian

$$\mathcal{H}_1 = \sum_{i<j=1}^{N} \frac{e^2}{4\pi\varepsilon_0 r_{ij}} - \sum_{i=1}^{N} S(r_i), \tag{2.8}$$

describes the non-spherical part of the electron-electron Coulomb interactions, while

$$\mathcal{H}_{so} = \sum_{i=1}^{N} \xi(r_i)\mathbf{l}_i \cdot \mathbf{s}_i, \tag{2.9}$$

is the energy of the spin-orbit interactions. Both $\mathcal{H}_1$ and $\mathcal{H}_{so}$ are much smaller than the central field Hamiltonian

$$\mathcal{H}_c = \sum_{i=1}^{N} \left(-\frac{\hbar^2}{2m}\nabla_{r_i}^2 + V_c(r_i) \right), \tag{2.10}$$

and are treated by perturbation theory. Regarding $\mathcal{H}_1$ and $\mathcal{H}_{so}$ as perturbations of $\mathcal{H}_c$, the first step is to solve the unperturbed eigenvalue problem

$$\mathcal{H}_c \Psi(q_1, \ldots, q_N) = E\Psi(q_1, \ldots, q_N). \tag{2.11}$$

Assuming the central field potential $V_c(r)$ is known, (2.11) can be solved by separation of the variables. This means finding single electron eigenfunctions $u_\alpha(q) \equiv u_{nlm_lm_s}(q)$ to the spherical symmetrical eigenvalue problem

$$\left(-\frac{\hbar^2}{2m}\nabla_{r_i}^2 + V_c(r_i) \right) u_{nlm_lm_s}(q) = E_{nl} u_{nlm_lm_s}(q), \tag{2.12}$$

where

$$\mathbf{s}^2 u_{nlm_lm_s}(q) = \frac{3}{4}\hbar^2 u_{nlm_lm_s}(q), \tag{2.13}$$

and

$$s_z u_{nlm_lm_s}(q) = m_s \hbar u_{nlm_lm_s}(q). \tag{2.14}$$

These equations are solved in every standard textbook on Quantum Mechanics, and have eigenfunctions

$$u_{nlm_lm_s}(q) = u_{nlm_l}(\mathbf{r})\chi_{1/2,m_s} = R_{nl}(r)Y_{lml}(\theta,\phi)\chi_{1/2,m_s}. \tag{2.15}$$

Here $\chi_{1/2,m_s}$ are spin 1/2 eigenfunctions, $Y_{lml}(\theta,\phi)$ are spherical harmonics and R_{nl} is a radial function satisfying the radial equation (given in atomic units)

$$-\frac{1}{2}\left(\frac{d^2}{dr^2} + \frac{2}{r}\frac{d}{dr} - \frac{l(l+1)}{r^2} + V_c(r) \right) R_{nl}(r) = E_{nl} R_{nl}(r). \tag{2.16}$$

The four quantum numbers fulfil the conditions

$$n = 1, 2, \ldots, \quad l = 0, 1, 2, \ldots, n-1, \quad m_l = -l, -l+1, \ldots, l, \quad m_s = \pm\frac{1}{2}, \tag{2.17}$$

and the eigenenergies E_{nl} generally depend on n and l, but not on m_l and m_s. The problem of finding the central potential V_c is usually solved by an iterative process, known as the Hartree-Fock method, which shall not be discussed here.

Having solved the eigenvalue equations (2.12), the single electron eigenstates, $u_{nlm_lm_s}(q)$, are used as entries in so-called Slater determinants

$$\Psi(q_1, q_2, \ldots, q_N) = \frac{1}{\sqrt{N!}} \begin{vmatrix} u_\alpha(q_1) & u_\beta(q_1) & \ldots & u_\nu(q_1) \\ u_\alpha(q_2) & u_\beta(q_2) & \ldots & u_\nu(q_2) \\ \vdots & & & \\ u_\alpha(q_N) & u_\beta(q_N) & \ldots & u_\nu(q_N) \end{vmatrix}. \tag{2.18}$$

The Slater determinants are eigenstates to the many particle problem (2.11) and are antisymmetric under permutation of electron numbering and fulfil the Pauli principle. The energy[3] of a specific Slater determinant is given as

$$E_c = E_{n_1 l_1} + E_{n_2 l_2} + \ldots + E_{n_N l_N}. \tag{2.19}$$

The N pairs of n and l quantum numbers entering the determinant, $\{n_1 l_1, n_2 l_2, \ldots, n_N l_N\}$, is called the electronic configuration. It follows from (2.19) that many-electron states having the same electronic configuration will have the same same energy in the unperturbed system.

In the central field approximation, the ground state configuration for a given atom is constructed by filling electrons into the single electron levels with the lowest energies, while still respecting the Pauli principle. Although the sequence of the single electron energy levels E_{nl} is fairly universal, there are inconsistencies going from one element to the next. It is therefore necessary to apply the whole Hartree-Fock procedure in order to evaluate the correct ground state configuration for any given atom.

Step 2: L-S coupling

In the central field approximation, the energy of a many-electron eigenstate will depend on the quantum numbers $\{n_1 l_1, n_2 l_2, \ldots, n_N l_N\}$, but not on $\{m_{l1} m_{s1}, m_{l2} m_{s2}, \ldots, m_{lN} m_{sN}\}$. Therefore the energy levels are highly degenerate. Taking the perturbations, $\mathcal{H}_1$ and $\mathcal{H}_{so}$, into account will lift some of these degeneracies. In the following we will assume that $\mathcal{H}_1 \gg \mathcal{H}_{so}$, since this is the case for the elements we shall be dealing with in this thesis (and for most other as well).

Regarding $\mathcal{H}_1$ as a perturbation, but neglecting $\mathcal{H}_{so}$, the Hamiltonian reads

$$\mathcal{H}' = \mathcal{H}_c + \mathcal{H}_1. \tag{2.20}$$

This Hamiltonian does not commute with the individual single electron operators, $\mathbf{l}_i$ and $\mathbf{s}_i$, but does still commute with the operators $\mathbf{L} = \sum_i \mathbf{l}_i$ and $\mathbf{S} = \sum_i \mathbf{s}_i$. This is because the forces described by $\mathcal{H}_c$ and $\mathcal{H}_1$ are all internal when considering the atom as a whole, and do not couple orbital and spin operators. Hence, there are eigenfunctions of $\mathcal{H}'$ that are simultaneously eigenfunctions for $\mathbf{L}^2$, $\mathbf{S}^2$, L_z and S_z. These eigenfunctions, $|\alpha L S M_L M_S\rangle$, where α is a quantum number representing additional information, are constructed as linear combinations of Slater determinants having the same electronic configuration. In an isolated atom there are no preferred direction of $\mathbf{L}$ or $\mathbf{S}$, so the energy depends exclusively on the size of L and S. Each energy level, known as a LS multiplet, is therefore $(2L+1)(2S+1)$ times degenerated. The spectroscopic terminology for an energy level with quantum numbers L and S is ${}^{2S+1}L$, with capital letters $S, P, D, F, \ldots$ for values $L = 0, 1, 2, 3, \ldots$.

Step 3: Spin-orbit interactions

So far we have seen that $\mathcal{H}_c$ specifies the energy levels according to the electronic configuration $\{n_1 l_1, \ldots, n_N l_N\}$. When $\mathcal{H}_1$ comes into play, these energy levels are split into LS multiplets characterized by $\mathbf{L}^2$ and $\mathbf{S}^2$. The last step of the perturbation treatment of the isolated atom is to consider the effect of the spin-orbit interactions, $\mathcal{H}_{so}$.

Since the effect of $\mathcal{H}_{so}$ is assumed to be much smaller than $\mathcal{H}_c$ and $\mathcal{H}_1$, the spin-orbit interactions do not mix states belonging to different LS multiplets. Consequently, $\mathcal{H}_{so}$ will be working within the Hilbert space of a specific LS multiplet, and the perturbation will be described by matrix elements of the form

$$\begin{aligned} \langle \alpha L S M_L M_S | \mathcal{H}_2 | \alpha' L S M'_L M'_S \rangle &= \sum_{i=1}^{N} \langle \alpha L S M_L M_S | \xi(r_i) \mathbf{l}_i \cdot \mathbf{s}_i | \alpha' L S M'_L M'_S \rangle \\ &= \langle \alpha L S M_L M_S | N \xi(r) \mathbf{l} \cdot \mathbf{s} | \alpha' L S M'_L M'_S \rangle. \end{aligned} \tag{2.21}$$

[3]Without going into details we mention that the energy, E_c, is *not* the actual ground state energy, found by solving the full set of Hartree-Fock equations. Rather, E_c is the so-called Hartree energy which is calculated by neglecting exchange terms.

Here we have used that the electrons are indistinguishable and the matrix elements therefore are the same for all i. In order to rewrite the spin-orbit coupling term, $\mathcal{H}_{so}$, we use the following theorem, which is proved in appendix A.

Theorem 1 *Within a LS multiplet, the spin-orbit coupling term, $\mathcal{H}_{so}$, can be written as*

$$\mathcal{H}_{so} = \sum_{i=1}^{N} \xi(r_i)\mathbf{l}_i \cdot \mathbf{s}_i = \lambda(\mathbf{L} \cdot \mathbf{S}). \tag{2.22}$$

When the spin-orbit interactions are taken into account, L_z and S_z are no longer good quantum numbers because $\mathcal{H}_{so}$ does not commute with $\mathbf{L}$ and $\mathbf{S}$, and the LS multiplets are split into so-called fine structure multiplets. However, the total angular momentum, $\mathbf{J} = \mathbf{L} + \mathbf{S}$, still commutes with the full Hamiltonian $\mathcal{H} = \mathcal{H}_c + \mathcal{H}_1 + \mathcal{H}_{so}$, since all the forces in $\mathcal{H}$ are internal. Using Theorem 1, and $\mathbf{J}^2 = \mathbf{L}^2 + \mathbf{S}^2 + 2\mathbf{L} \cdot \mathbf{S}$, we have that

$$\mathcal{H}_{so} = \lambda(\mathbf{L} \cdot \mathbf{S}) = \frac{\lambda}{2}(\mathbf{J}^2 - \mathbf{L}^2 - \mathbf{S}^2), \tag{2.23}$$

showing that also $\mathbf{L}^2$ and $\mathbf{S}^2$ commutes with $\mathcal{H}$. The eigenstates to the full Hamiltonian can therefore be labelled $|\alpha LSJM_J\rangle$. Since the total angular momentum has no preferred direction, the eigenenergies do not depend on J_z, and the fine structure energy levels, written as $^{2S+1}L_J$, will be $(2J+1)$ times degenerated.

Hund's rules

There are three empirically established rules, known as Hund's rules, which are often used to find the ground state, and the level scheme of equivalent electronic configurations. The Hund's rules are:

1. For a given configuration, the term with the largest possible value of S has the lowest energy. The energy of the other terms increase with decreasing S.
2. For a given configuration and a given value of S, the term with the largest possible value of L has the lowest energy.
3. *Landé's interval rule.* For given value of S and L, the multiplet having the lowest energy fulfils:

   $J = |L - S|$, if the outer shell is less than half-filled.

   $J = L + S$, if the outer shell that is more than half-filled.

As an example we show the lowest lying energy levels for a free Ni^{2+} ion[4] in figure 2.8. The lowest lying electronic configuration is [Ar]$3d^8$, which is split due to $\mathcal{H}_1$ and $\mathcal{H}_{so}$. Although the sequence of the LS multiplets do not rigourously follow Hund's rules, the ground state, $^3F_4$, is as expected from the rules.

[4]The data given in figure 2.8 is taken from the NIST Atomic Spectra Database.

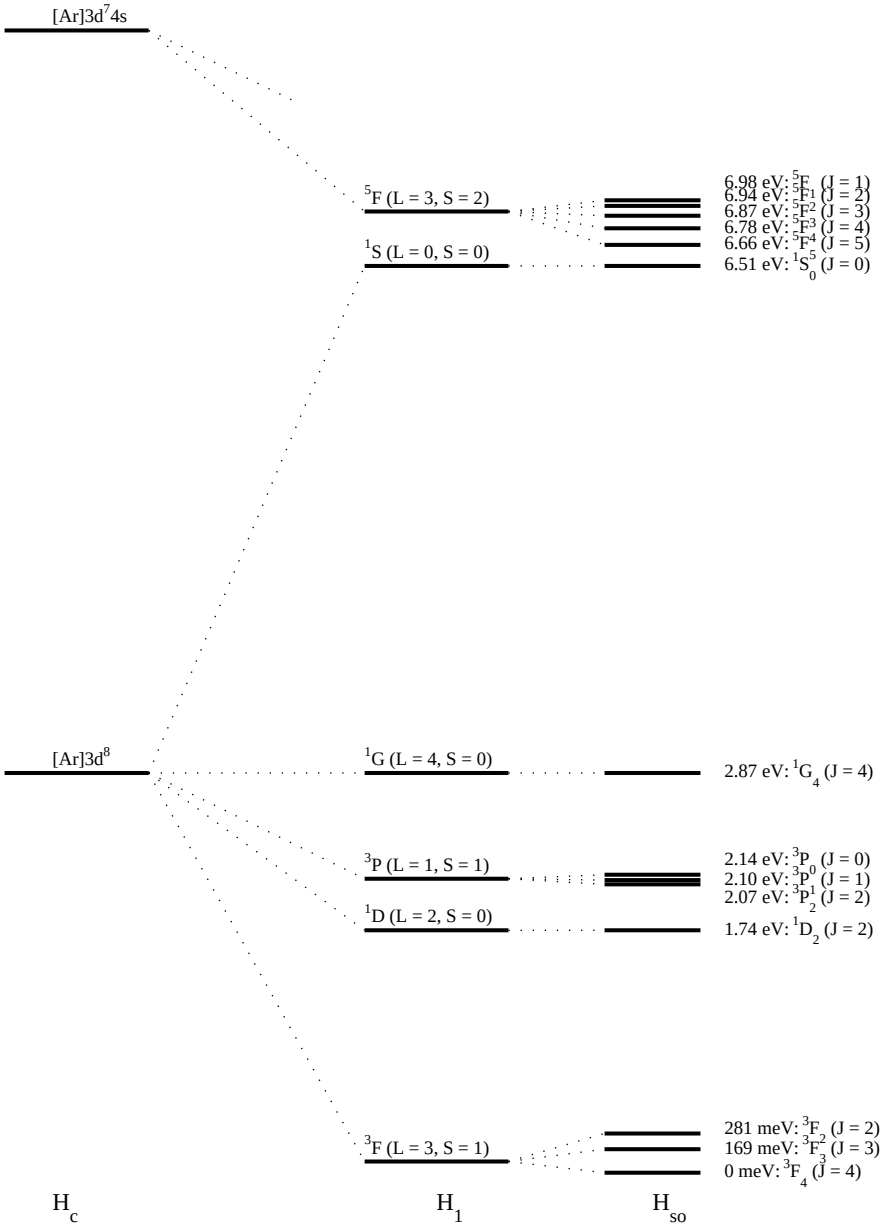

Figure 2.8: The lowest lying energy levels for a free Ni^{2+} ion. The energy levels are succeedingly split up when applying the perturbations $\mathcal{H}_1$ and $\mathcal{H}_{so}$, as shown in the figure and described in the text. The depicted data was taken from the NIST Atomic Spectra Database.

2.3.2 Band structure of $LiNiPO_4$

There are many methods developed to calculate the electron states and energy levels in crystals, and we shall briefly discuss one of these; namely the tight binding model [20]. The starting point of the tight binding method is to assume that in the vicinity of every lattice point the full crystal Hamiltonian, $\mathcal{H}$, can be approximated by the Hamiltonian, $\mathcal{H}_{ion}$, of an isolated ion situated at the lattice point. Furthermore, it is assumed that the single electron eigenfunctions, $\psi_n(\mathbf{r})$, of $\mathcal{H}_{ion}$, found by the methods sketched in section 2.3.1, are well localized, i.e. that $\psi_n(\mathbf{r})$ is very small when $\mathbf{r}$ becomes the size of the lattice constants. Under these assumptions, the full crystal Hamiltonian $\mathcal{H}$ can be solved with Bloch type solutions

$$\Psi_{\mathbf{k}}(\mathbf{r}) = \sum_{\mathbf{R}} e^{i\mathbf{k}\cdot\mathbf{R}}\phi(\mathbf{r}-\mathbf{R}), \tag{2.24}$$

where $\mathbf{R}$ are crystal lattice points, and $\mathbf{k}$ is a Block wave vector. The functions $\phi(\mathbf{r})$ are called Wannier functions and are localized around the lattice points. For a Bravais crystal the Wannier functions are written as

$$\phi(\mathbf{r}) = \sum_{n} b_n\psi_n(\mathbf{r}), \tag{2.25}$$

where $\psi_n(\mathbf{r})$ are the single electron orbitals of $\mathcal{H}_{ion}$. When the crystal is not a Bravais lattice the Wannier functions are composed of molecular orbitals, $\psi^{MO}(\mathbf{r})$, so that

$$\phi(\mathbf{r}) = \sum_{n} b_n\psi_n^{MO}(\mathbf{r}). \tag{2.26}$$

In a unit cell with m ions, the molecular orbitals can be written as

$$\psi_n^{MO}(\mathbf{r}) = \lambda_{n,1}\psi_{n,1}(\mathbf{r}-\mathbf{d}_1) + \ldots + \lambda_{n,m}\psi_{n,m}(\mathbf{r}-\mathbf{d}_m), \tag{2.27}$$

where $\psi_{n,j}(\mathbf{r}-\mathbf{d}_j)$ are the single atom orbitals from the j'th ion, situated at position $\mathbf{d}_j$ within the unit cell.

The tight binding calculation results in a series of energy bands, $E(\mathbf{k})$, for the single electron states. When the tight binding assumptions are justified, these energy bands will be rather narrow and lie in the vicinity of the eigenenergies, E_{nl}, of the isolated ions. Furthermore, the individual Wannier functions will be composed only by electron states $\psi_\alpha(\mathbf{r})$ having almost the same eigenenergies $E_\alpha \approx E_{nl}$, and which are not too spatially separated. In other words, the further apart in energy or space two states $\psi_\alpha(\mathbf{r}-\mathbf{d}_i)$ and $\psi_\beta(\mathbf{r}-\mathbf{d}_j)$ are, the less they mix. Although the tight binding model is used to describe well localized electrons, an electron in a tight binding level is found with equal probability in any cell of the crystal. This is because the eigenstates $\Psi_{\mathbf{k}}(\mathbf{r})$, given in (2.24), are Bloch states. How such electrons can be localized, is seen by using that electrons in Bloch states with energy $E(\mathbf{k})$ and wave vector $\mathbf{k}$ have a mean velocity of $\mathbf{v}(\mathbf{k}) = \partial E/\partial\mathbf{k}$. For the inner most electrons, the core electrons, the energy bands are constant and the electrons have velocities $\partial E/\partial\mathbf{k} = 0$. The core electrons do therefore not move around in the crystal, but are tied to individual nuclei. For the electrons further out, the so-called valence electrons, the energy bands, $E(\mathbf{k})$, are not constant. However, if the tight binding assumptions are justified, these valence bands will be very narrow. Since the slope of $E(\mathbf{k})$ is very small for such narrow bands, the ability of the valence electrons to move through the crystal is practically non-existing.

For quantitative band structure calculations of real materials the tight binding model is generally too simple, and more elaborate methods are needed. As in the tight binding model, these methods construct energy bands via Bloch functions of suitable molecular orbitals. It is a general feature of all band theories, that the electrons are localized when the energy bands are flat, and that they loose more of their localization when the bands become more dispersive.

Figure 2.9 show the result of realistic calculations of the electronic structure in $LiFePO_4$ and $LiNiPO_4$. The band structure depicted in figure 2.9(a) is for $LiFePO_4$, but calculations on $LiNiPO_4$ gives a similar level scheme. The arrows $\uparrow$ and $\downarrow$ correspond to the bands of electrons with spin $\uparrow$ or $\downarrow$, respectively. Below the Fermi level, $E_F = 0$, all bands are relatively flat, reflecting that the lithium phosphates are insulators. The energy levels from approximately -3.3 eV to $E_F = 0$ eV are composed primarily of Fe 3d states with

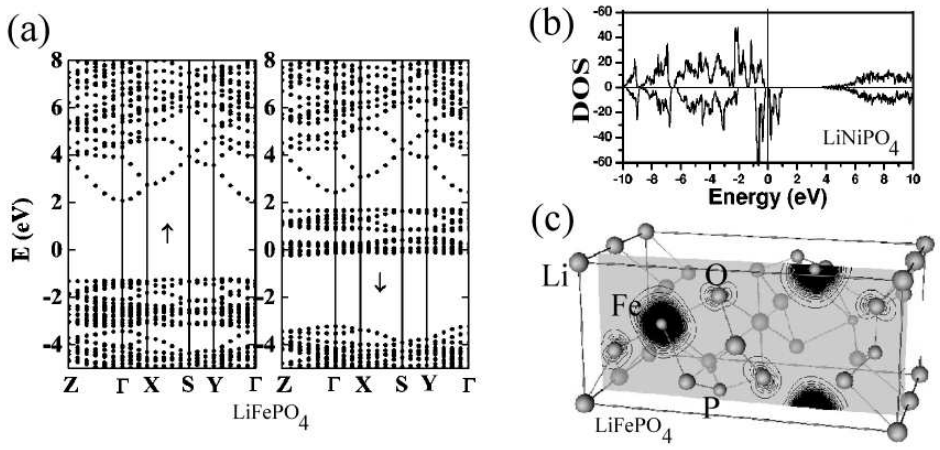

Figure 2.9: (a) Electronic band structure for $LiFePO_4$, taken from [21]. The bands below and just above the Fermi energy, $E_F = 0$ eV, show very little dispersion, and the electrons are in localized states. The dispersive conduction bands are situated high above E_F. The bands around E_F are Fe 3d states forming narrow bands above the O 2p bands with relative little mixing (see (c)). The 3d states are split into five non-degenerate bands by the crystal field, as described in the text. The band structure for $LiNiPO_4$ (not shown) is quite similar to the one depicted here for $LiFePO_4$, but where the Fermi energy is slightly higher due to nickel having two 3d electrons more than iron. (b) Total spin-polarized density of states (DOS) for $LiNiPO_4$, taken from [22]. Here positive DOS values corresponds to majority (↑) spin electrons, while negative values corresponds to minority (↓) electrons. (c) Electron-density contour plot for the majority electrons (marked as ↑ in (a)) in $LiFePO_4$, with energies ranging from -3.3 to -1.1 eV, taken from [21]. In this energy range the electron states are formed mainly from Fe 3d states, with only a small mixing of the O 2p states. Also in $LiNiPO_4$, the Ni 3d states and the O 2p states mix only slightly.

only a slight mixing of O 2p states, as can be seen in figure 2.9(c). From figure 2.9(a) and (b), we see that the single electron orbitals are occupied according to Hund's first rule, filling all 3d spin ↑ states before the ↓ states. The symmetry of the single electron 3d eigenstates is dictated by the crystal field from the surrounding oxygen ions. The 3d spatial orbitals are split into five non-degenerate single electron states, which, in a simplified picture, can be written as[5]

$$\begin{aligned} t_{2g}: &\quad \psi_{xy} = \frac{1}{i\sqrt{2}}(\psi_2 - \psi_{-2}), \quad \psi_{yz} = -\frac{1}{i\sqrt{2}}(\psi_1 + \psi_{-1}), \quad \psi_{zx} = -\frac{1}{\sqrt{2}}(\psi_1 - \psi_{-1}), \\ e_g: &\quad \psi_{x^2-y^2} = \frac{1}{\sqrt{2}}(\psi_2 + \psi_{-2}), \quad \psi_{3z^2-r^2} = \psi_0. \end{aligned} \tag{2.28}$$

The mixing[6] of magnetic 3d orbitals and the surrounding oxygen orbitals in the t_{2g} and e_g states is illustrated in figure 2.10(a) and (b). The t_{2g} states have a smaller overlap with the surrounding O 2p orbitals than the e_g states. As a consequence the t_{2g} states have a lower energy than the e_g states. Figure 2.9(a) and (b) shows that Hund's rule of maximizing spin is stronger than the crystal field splitting for $LiNiPO_4$ and $LiFePO_4$, and the single electron orbitals are filled according to figure 2.10(c).

For the lithium phosphates it is believed that Hund's second rule of maximizing L is also stronger than the crystal field. The spin-orbit interaction is even smaller than the crystal field for transition metals, and will not be considered at this point. The many-electron ground state is therefore determined by applying Hund's first two rules to find the lowest lying LS multiplet, and then considering the crystal field Hamiltonian as a perturbation. The crystal field splitting of the LS multiplet[7] is dictated by the symmetry of the crystal. In

[5]Here ψ_m are single-electron 3d orbitals with $m_l = m$.

[6]Although the mixing of O 2p and Ni 3d orbitals is small, the symmetry of the Ni orbitals is strongly affected by the O ions through electrostatic forces.

[7]The principles on how to calculate the crystal field level splitting is described in [24].

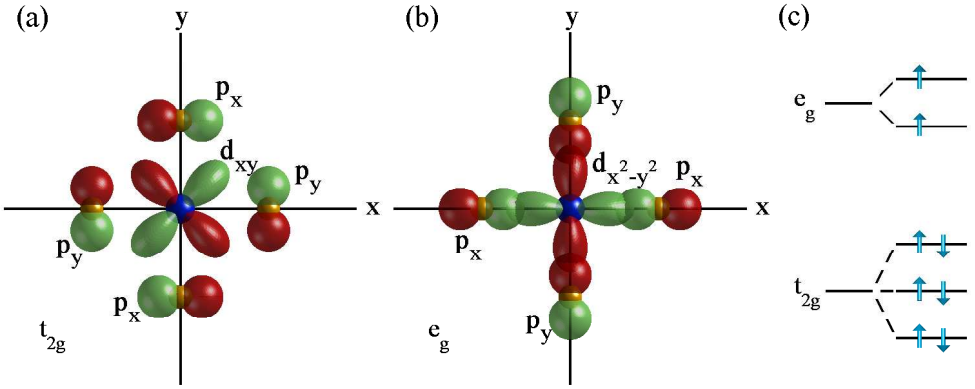

Figure 2.10: (a) Example of a t_{2g} orbital (schematic), slightly mixing a single-electron 3d state from Ni^{2+} with the 2p states from the neighboring O^{2-} ions. There is little overlap of the electron clouds and the electrostatic repulsion is therefore small. (b) Example of an e_g orbital (schematic), mixing a 3d electron from Ni^{2+} with the 2p electrons from neighboring O^{2-} ions. Due to the overlap of the electron clouds, the electrostatic repulsion is larger than for the t_{2g} states, and the energy consequently higher. (c) The crystal field splitting of the five Ni^{2+} single-electron 3d levels in $LiNiPO_4$. The many-electron states are sums of Slater determinants, like the one depicted here, where eight electrons have been placed in the crystal field split levels. Generally, the lowest many-electron states of LiNiPO4 are found using Hund's first two rules, as explained in the text, and are therefore still ^{3}F states. The crystal field splitting of the ^{3}F levels is similar to the splitting of the ^4F levels of Co^{2+}, illustrated in figure 2.11.

$LiNiPO_4$, the ^3F ground state of the Ni^{2+} ions will split up into 7 spatially non-degenerate many-particle eigenstates (similar to the splitting of the ^4F levels of Co^{2+} shown in figure 2.11). Although the crystal field splitting of the energy levels, to our knowledge, has not been calculated for $LiNiPO_4$, this has been done

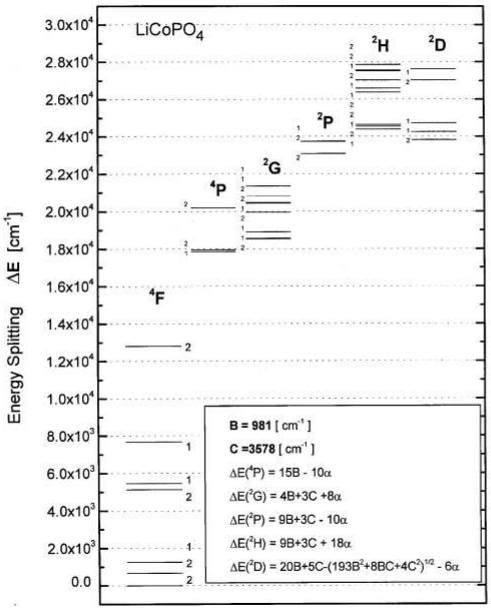

Figure 2.11: Crystal field splitting of the Co^{2+} ground multiplets in $LiCoPO_4$, from [23].

for the iso-structural material $LiCoPO_4$. The calculated level scheme for the Co^{2+} states in $LiCoPO_4$, taken from [23], is shown in figure 2.11.

Quenching of the total angular momentum

It can be shown (see for instance [24]) that the crystal field Hamiltonian, $\mathcal{H}_{CF}$, can be given as a real function. The eigenstates, $|n\rangle$, to $\mathcal{H}_{CF}$ can therefore also be written as real functions. Since the operator, $\mathbf{L}$, for the total angular orbital momentum is purely imaginary, we have that $\langle n|\mathbf{L}|n\rangle$ is also purely imaginary. When $\langle n|\mathbf{L}|n\rangle$ is imaginary

$$\langle n|\mathbf{L}|n\rangle = \langle n|\mathbf{L}|n\rangle^* = -\langle n|\mathbf{L}|n\rangle, \tag{2.29}$$

and it follows that

$$\langle n|\mathbf{L}|n\rangle = 0. \tag{2.30}$$

In $LiNiPO_4$, the crystal field split ground state level, $|0\rangle$, is non-degenerate[8] in the orbital part, and consequently the expectation value of the total angular momentum is

$$\langle 0|\mathbf{L}|0\rangle = 0. \tag{2.31}$$

When (2.31) applies for the ground state level, we say that the angular momentum is quenched.

2.3.3 Magnetic interactions and spin Hamiltonian

We have already discussed that the Ni^{2+} ions in $LiNiPO_4$ have a ^{3}F many-electron ground state with a total spin $S = 1$. These spins are accompanied with a magnetic moment $\boldsymbol{\mu} = -g\mu_B\mathbf{S}$, where g is Lande's g-value. Since $\mathbf{L}$ is quenched, Lande's g-value is $g = 2$. The magnetic moments, localized on the Ni^{2+} ions, experience the surroundings in various ways. Here we shall briefly introduce the various magnetic interactions[9] used in later discussions of our experimental data.

Generally the size of the magnetic interactions are much smaller than the crystal field splitting of the nickel ^3F levels. The ground state determined by the crystal field do therefore not mix with the higher lying states. Consequently, the magnetic interactions are studied in the Hilbert space connected to the ground state, and we may assume in the following that the total angular momentum, $\mathbf{L}$, is quenched.

Direct exchange

In the language of second quantization[10], the potential energy between two Ni^{2+} 3d electrons is given as an operator

$$V_{ee} = \frac{1}{2}\sum_{s_1,s_2}\int d\mathbf{r}_1 d\mathbf{r}_2 \Psi^\dagger_{s_1}(\mathbf{r}_1)\Psi^\dagger_{s_2}(\mathbf{r}_2)\frac{e^2}{4\pi\epsilon_0 r_{12}}\Psi_{s_2}(\mathbf{r}_2)\Psi_{s_1}(\mathbf{r}_1). \tag{2.32}$$

The quantum field operator

$$\Psi^\dagger_s(\mathbf{r}) = \sum_{nm} a^\dagger_{nms}\phi^*_{nm}(\mathbf{r})\chi^*_s, \tag{2.33}$$

creates a spin s electron at position $\mathbf{r}$, while

$$\Psi_s(\mathbf{r}) = \sum_{nm} a_{nms}\phi_{nm}(\mathbf{r})\chi_s, \tag{2.34}$$

destroys a spin s electron at $\mathbf{r}$. Here the functions $\phi_{nm}(\mathbf{r})$ are orthogonal d-orbitals, with quantum numbers m, centered around the n'th lattice point, and χ_s are the spin eigenfunctions for electrons with $m_s = s$. The

[8] If the ground state is degenerate in the orbital part, off-diagonal elements may cause the expectation value of $\mathbf{L}$ to be non-zero.

[9] The dipole-dipole interaction between nearest neighboring Ni spins in $LiNiPO_4$ is around 0.005 meV. This is much smaller than the exchange and anisotropy interactions (see the values in chapter 7) and will therefore not be included in the discussion.

[10] A short introduction to the formalism of second quantization is given in [25], and a more detailed account in [26].

operators $a^\dagger_{nms}$ and a_{nms} are Fermi operators, creating and destructing an electron in an $|nms\rangle$ state, and satisfying the usual Fermi anti-commutator relations

$$\begin{aligned}\{a_\alpha, a^\dagger_{\alpha'}\} &= a_\alpha a^\dagger_{\alpha'} + a^\dagger_{\alpha'} a_\alpha = \delta_{\alpha\alpha'},\\ \{a^\dagger_\alpha, a^\dagger_{\alpha'}\} &= \{a_\alpha, a_{\alpha'}\} = 0.\end{aligned} \tag{2.35}$$

Inserting (2.33) and (2.34) in (2.32), and using that $|\chi_s|^2 = 1$, we find that

$$\begin{aligned}V_{ee} =& \frac{1}{2}\sum_{\substack{n_1m_1\\n_2m_2}}\sum_{\substack{n_3m_3\\n_4m_4}}\sum_{s_1s_2} a^\dagger_{n_1m_1s_1}a^\dagger_{n_2m_2s_2}a_{n_3m_3s_2}a_{n_4m_4s_1}\\ &\times\int d\mathbf{r}_1 d\mathbf{r}_2 \phi^\dagger_{n_1m_1}(\mathbf{r}_1)\phi^\dagger_{n_2m_2}(\mathbf{r}_2)\,\frac{e^2}{4\pi\epsilon_0 r_{12}}\,\phi_{n_3m_3}(\mathbf{r}_2)\phi_{n_4m_4}(\mathbf{r}_1).\end{aligned} \tag{2.36}$$

Due to the Fermi operators, the mean value of V_{ee} is zero unless $(n_1, m_1) = (n_4, m_4)$ and $(n_2, m_2) = (n_3, m_3)$, or $(n_1, m_1) = (n_3, m_3)$ and $(n_2, m_2) = (n_4, m_4)$. Defining

$$K^{m_1m_2}_{n_1n_2} = \int d\mathbf{r}_1 d\mathbf{r}_2 \phi^\dagger_{n_1m_1}(\mathbf{r}_1)\phi^\dagger_{n_2m_2}(\mathbf{r}_2)\,\frac{e^2}{4\pi\epsilon_0 r_{12}}\,\phi_{n_2m_2}(\mathbf{r}_2)\phi_{n_1m_1}(\mathbf{r}_1), \tag{2.37}$$

and

$$J^{m_1m_2}_{n_1n_2} = \int d\mathbf{r}_1 d\mathbf{r}_2 \phi^\dagger_{n_1m_1}(\mathbf{r}_1)\phi^\dagger_{n_2m_2}(\mathbf{r}_2)\,\frac{e^2}{4\pi\epsilon_0 r_{12}}\,\phi_{n_1m_1}(\mathbf{r}_2)\phi_{n_2m_2}(\mathbf{r}_1), \tag{2.38}$$

we can write

$$\begin{aligned}V_{ee} =& \frac{1}{2}\sum_{\substack{n_1m_1\\n_2m_2}}\sum_{s_1s_2} K^{m_1m_2}_{n_1n_2}a^\dagger_{n_1m_1s_1}a_{n_1m_1s_1}a^\dagger_{n_2m_2s_2}a_{n_2m_2s_2}\\ &-\frac{1}{2}\sum_{\substack{n_1m_1\\n_2m_2}}\sum_{s_1s_2} J^{m_1m_2}_{n_1n_2}a^\dagger_{n_1m_1s_1}a_{n_1m_1s_2}a^\dagger_{n_2m_2s_2}a_{n_2m_2s_1} = V_{Coulomb} + V_{DE}.\end{aligned} \tag{2.39}$$

The first term

$$V_{Coulomb} = \frac{1}{2}\sum_{\substack{n_1m_1\\n_2m_2}}\sum_{s_1s_2} K^{m_1m_2}_{n_1n_2}a^\dagger_{n_1m_1s_1}a_{n_1m_1s_1}a^\dagger_{n_2m_2s_2}a_{n_2m_2s_2}, \tag{2.40}$$

is the usual Coulomb energy between pairs of 3d electrons, and does not result in magnetic interactions between the spins. The second term

$$V_{DE} = -\frac{1}{2}\sum_{\substack{n_1m_1\\n_2m_2}}\sum_{s_1s_2} J^{m_1m_2}_{n_1n_2}a^\dagger_{n_1m_1s_1}a_{n_1m_1s_2}a^\dagger_{n_2m_2s_1}a_{n_2m_2s_2}, \tag{2.41}$$

is a correction term due to the properties of the Fermi operators, and will give a ferromagnetic interaction between the Ni spin. We see this by first writing V_{DE} as

$$V_{DE} = -\frac{1}{2}\sum_{\substack{n_1m_1\\n_2m_2}} J^{m_1m_2}_{n_1n_2}\left(\frac{1}{2} + 2\mathbf{s}^{m_1}_{n_1}\cdot\mathbf{s}^{m_2}_{n_2}\right) = K_0 - \sum_{\substack{n_1m_1\\n_2m_2}} J^{m_1m_2}_{n_1n_2}\mathbf{s}^{m_1}_{n_1}\cdot\mathbf{s}^{m_2}_{n_2}. \tag{2.42}$$

The derivation of (2.42) is given in Appendix B. The first term in (2.42) is simply a constant energy, K_0, which does not contribute to any magnetic interactions. The second term can be rewritten, using that the single-electron states of Ni^{2+} in $LiNiPO_4$ are filled according to Hund's rules, as illustrated in figure 2.10(c). In the figure, all the t_{2g} levels are fully occupied. Therefore $\mathbf{s}^{t_{2g}}_n = 0$, and do not contribute in (2.42). However, the two half-filled e_g orbitals are occupied with only a single electron each. These two electrons both have

their spin pointing in the direction of the total spin $\mathbf{S}$, so that $\mathbf{s}_n^{e_g} = \mathbf{S}_n/2$, since $S_n = 1$. Using this, and omitting the constant term K_0, the direct exchange interaction can be written as

$$V_{DE} = -\sum_{n_1 n_2} J_{n_1 n_2}^{DE} \mathbf{S}_{n_1} \cdot \mathbf{S}_{n_2}, \tag{2.43}$$

where

$$J_{n_1 n_2}^{DE} = \frac{1}{4} \sum_{m_1' m_2'} J_{n_1 n_2}^{m_1' m_2'}. \tag{2.44}$$

In (2.44) the sum is only over half-filled orbitals m'. Introducing the Fourier transform

$$\frac{1}{r_{12}} = \frac{1}{V} \sum_{\mathbf{k}} \frac{4\pi}{k^2} e^{i\mathbf{k}\cdot(\mathbf{r}_1 - \mathbf{r}_2)}, \tag{2.45}$$

we find that

$$\begin{aligned} J_{n_1 n_2}^{m_1 m_2} =& \frac{1}{V} \sum_{\mathbf{k}} \frac{e^2}{\epsilon_0 k^2} \int d\mathbf{r}_1 \phi_{n_1 m_1}^*(\mathbf{r}_1) \phi_{n_2 m_2}(\mathbf{r}_1) e^{i\mathbf{k}\cdot\mathbf{r}_1} \int d\mathbf{r}_2 \phi_{n_2 m_2}^*(\mathbf{r}_2) \phi_{n_1 m_1}(\mathbf{r}_2) e^{-i\mathbf{k}\cdot\mathbf{r}_2} \\ =& \frac{1}{V} \sum_{\mathbf{k}} \frac{e^2}{\epsilon_0 k^2} \left| \int d\mathbf{r} \phi_{n_1 m_1}^*(\mathbf{r}) \phi_{n_2 m_2}(\mathbf{r}) e^{i\mathbf{k}\cdot\mathbf{r}} \right|^2 > 0, \end{aligned} \tag{2.46}$$

and consequently $J_{n_1 n_2}^{DE} > 0$. The direct exchange interaction given by (2.43) is therefore always a ferromagnetic interaction.

Super-exchange

Another type of exchange interaction, called super-exchange or kinetic exchange [24, 27], is found from second order perturbation theory using the crystal field potential, V_{CF}, as the perturbation. We consider processes as the one sketched in figure 2.12. Here, an electron from a Ni ion (blue) transfers via the the crystal field from intermediate ions (yellow), to another Ni ion. Then one of the electrons on the second Ni ion jumps back to the first Ni ion. Such processes are described by a Hamiltonian

$$\mathcal{H}_{SE} = \sum_{\substack{n_1 m_1 s_1 \\ n_2 m_2 s_2}} \Delta E_{n_1 m_1, n_2 m_2}^{(2)} a_{n_1 m_1 s_2}^\dagger a_{n_2 m_2 s_2} a_{n_2 m_2 s_1}^\dagger a_{n_1 m_1 s_1}, \tag{2.47}$$

where $\Delta E_{n_1 m_1, n_2 m_2}^{(2)}$ is given by second order perturbation theory as[11]

$$\Delta E_{n_1 m_1, n_2 m_2}^{(2)} = -\frac{\langle n_1 m_1 | V_{CF} | n_2 m_2 \rangle \langle n_2 m_2 | V_{CF} | n_1 m_1 \rangle}{E_{n_1 - 1, n_2 + 1} - E_{n_1, n_2}}. \tag{2.48}$$

Here

$$\langle n_2 m_2 | V_{CF} | n_1 m_1 \rangle = \int d\mathbf{r} \phi_{m_2}^*(\mathbf{r} - \mathbf{R}_{n_2}) V_{CF}(\mathbf{r}) \phi_{m_1}(\mathbf{r} - \mathbf{R}_{n_1}) \equiv b_{n_1 n_2}^{m_1 m_2}. \tag{2.49}$$

We note that all terms in $\Delta E_{n_1 m_1, n_2 m_2}^{(2)}$ are determined by electrostatic forces and therefore independent of spin. To evaluate $E_{n_1 - 1, n_2 + 1} - E_{n_1, n_2}$ we assume that the electrostatic repulsion is U for every pair of electrons situated on a given Ni ion. Then

$$E_{n_1 - 1, n_2 + 1} = \frac{(n_1 - 1)(n_1 - 2)}{2} U + \frac{(n_2 + 1) n_2}{2} U, \tag{2.50}$$

[11] The notation introduced at this point is slightly ambiguous, since n_1 signifies both the lattice point and the number of d-electrons situated at $\mathbf{R}_{n_1}$.

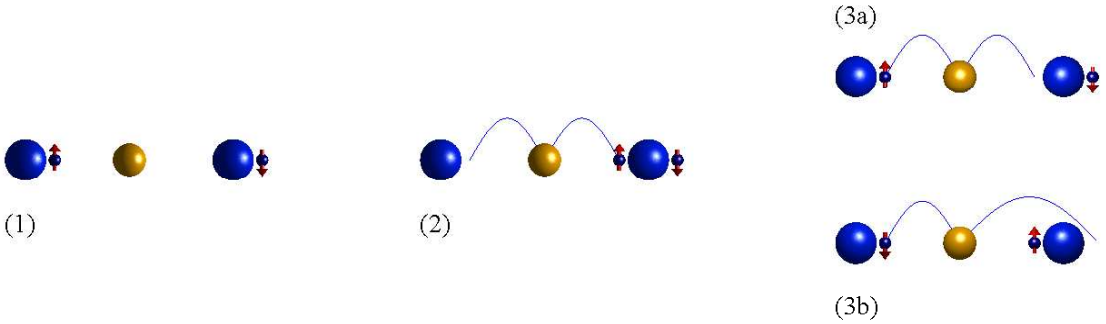

Figure 2.12: Proces responsible for the antiferromagnetic super-exchange interaction. (1) Two Ni^{2+} ions (large blue balls) in their ground state. For simplicity we only show a single 3d electron (small blue balls, with arrows illustrating the direction of the electron spin) around each Ni^{2+}. (2) One of the depicted electrons jump, via an intermediate oxygen (yellow ball), from one Ni ion to the other. This is only possible if the other depicted electron, already in the receiving half-filled orbital, has a spin opposite to the jumping electron. This is equivalent to requiring that the total spin, $\mathbf{S}_1$ and $\mathbf{S}_2$, of the two Ni^{2+} ions are opposite, i.e. $\mathbf{S}_1 = -\mathbf{S}_2$. In other words, the process favors an antiferromagnetic spin-spin interaction. (3) One of the two depicted electrons jump, via the oxygen, back to the first ion, leaving both Ni ions in their ground state.

and

$$E_{n_1,n_2} = \frac{n_1(n_1-1)}{2}U + \frac{n_2(n_2-1)}{2}U, \tag{2.51}$$

giving

$$E_{n_1-1,n_2+1} - E_{n_1,n_2} = U(1+n_2-n_1) = U, \tag{2.52}$$

since $n_1 = n_2$. So, we can write (2.47) as

$$\mathcal{H}_{SE} = \sum_{\substack{n_1 m_1 s_1 \\ n_2 m_2 s_2}} \frac{|b^{m_1 m_2}_{n_1 n_2}|^2}{U} a^\dagger_{n_1 m_1 s_2} a_{n_2 m_2 s_2} a^\dagger_{n_2 m_2 s_1} a_{n_1 m_1 s_1}. \tag{2.53}$$

As with the direct exchange, we rewrite H_{SE}, and find

$$\mathcal{H}_{SE} = -\sum_{\substack{n_1 n_2 \\ m_1 m_2}} \frac{|b^{m_1 m_2}_{n_1 n_2}|^2}{U} \left(\frac{1}{2} - 2\mathbf{s}_1 \cdot \mathbf{s}_2\right). \tag{2.54}$$

Omitting the constant term, and using Hund's rules, we write

$$\mathcal{H}_{SE} = \sum_{n_1 n_2} J^{SE}_{n_1 n_2} \mathbf{S}_1 \cdot \mathbf{S}_2, \tag{2.55}$$

where

$$J^{SE}_{n_1 n_2} = \frac{1}{(2S)^2} \sum_{m1m2} 2\frac{|b^{m_1 m_2}_{n_1 n_2}|^2}{U}. \tag{2.56}$$

Clearly $J^{SE}_{n_1 n_2}$ is always positive, and therefore favors an anti-ferromagnetic configuration of the spins.

Combining (2.43) and (2.55) we get an expression for the so-called Heisenberg exchange interaction, namely

$$\mathcal{H} = \sum_{n_1 n_2} J_{12}\ \mathbf{S}_1 \cdot \mathbf{S}_2, \tag{2.57}$$

where

$$J_{12} = \frac{1}{(2S)^2} \sum_{m_1 m_2} \left[2\frac{|b^{m_1 m_2}_{n_1 n_2}|^2}{U} - J^{m_1 m_2}_{n_1 n_2}\right], \tag{2.58}$$

can be both positive and negative.

Single-ion anisotropy

We now consider the many-electron states of a single Ni^{2+} ion. As previously mentioned, the lowest ^3F multiplet has been split into 7 levels by the crystal field. Let us call these levels $0, 1, \ldots, 6$. They are non-degenerate in the orbital part, but three times degenerate in the spin part. In other words, the many-electron states corresponding to level n can be written as

$$|n\rangle \in \text{span}\{|nM_S\rangle \mid M_S = -1, 0, 1\}. \tag{2.59}$$

Here $n = 0, \ldots, 6$ are also the quantum numbers connected to the orbital part of the states, and M_S is the z component of the total spin.

We are now going to take the spin-orbit coupling term, $\mathcal{H}_{so} = \lambda \mathbf{L} \cdot \mathbf{S}$, into account as a perturbation. Let us assume we are in the lowest energy level, 0, with orbital states $|0\rangle$. First order perturbation theory gives

$$\Delta E^{(1)} = \langle 0M_S|\lambda \mathbf{L} \cdot \mathbf{S}|0M_S\rangle = \lambda \langle 0|\mathbf{L}|0\rangle \cdot \langle M_S|\mathbf{S}|M_S\rangle = 0, \tag{2.60}$$

because the angular momentum $\mathbf{L}$ is quenched[12].

Going to second order in the perturbation, and using the Einstein convention of summation over double indices, we find that

$$\begin{aligned}\Delta E^{(2)} &= -\sum_{n,M_S'} \frac{\langle 0M_S|\lambda L_\mu S_\mu|nM_S'\rangle\langle nM_S'|\lambda L_\nu S_\nu|0M_S\rangle}{E_n - E_0} = -\sum_{n,M_S'} \frac{\lambda^2\langle 0|L_\mu|n\rangle\langle n|L_\nu|0\rangle\langle M_S|S_\mu|M_S'\rangle\langle M_S'|S_\nu|M_S\rangle}{E_n - E_0} \\ &= -\lambda^2\Lambda_{\mu\nu}\sum_{M_S'}\langle M_S|S_\mu|M_S'\rangle\langle M_S'|S_\nu|M_S\rangle = -\lambda^2\Lambda_{\mu\nu}\langle M_S|S_\mu S_\nu|M_S\rangle,\end{aligned} \tag{2.61}$$

where

$$\Lambda_{\mu\nu} = \sum_n \frac{\langle 0|L_\mu|n\rangle\langle n|L_\nu|0\rangle}{E_n - E_0}. \tag{2.62}$$

Writing (2.61) as

$$\Delta E^{(2)} = \langle 0M_S| - \lambda^2\Lambda_{\mu\nu}S_\mu S_\nu|0M_S\rangle, \tag{2.63}$$

we see that the energy shift due to the perturbation H_{so} is described by an operator

$$\mathcal{H}_A = -\lambda^2\Lambda_{\mu\nu}S_\mu S_\nu \equiv D_{\mu\nu}S_\mu S_\nu, \tag{2.64}$$

within the level 0. The operator, $\mathcal{H}_A$, is called the single ion anisotropy operator, and the constants $D_{\mu\nu}$ are called single ion anisotropy constants. One of the major goals of this thesis is to set forward a spin Hamiltonian for $LiNiPO_4$, and to evaluate the relevant Heisenberg and single ion anisotropy constants.

Dzyaloshinsky-Moriya interaction

The last magnetic interaction we shall discuss in this chapter is an anisotropic exchange interaction between pairs of spins, called the Dzyaloshinsky-Moriya (DM) interaction [28]. The discussion presented in this section is taken from [24].

We consider two magnetic Ni^{2+} ions, with spin operators $\mathbf{S}_1$ and $\mathbf{S}_2$, and assume that both are in the lowest of the crystal field split many-electron ^3F levels. Let us call these (ground state) levels g_1 and g_2, respectively. As perturbation we use the spin-orbit coupling on each ion, $\mathbf{L}_1 \cdot \mathbf{S}_1$ and $\mathbf{L}_2 \cdot \mathbf{S}_2$, and the exchange interaction, V_{exch}, between the ions. We wish to evaluate the following equivalent second order processes (in perturbation theory all equivalent processes must be taken into account):

- Ion 1 is exited by $\mathbf{L}_1 \cdot \mathbf{S}_1$ from the ground state g_1 to a higher state n_1. Ion 1 is then transferred, via the exchange interaction with ion 2, from the higher state n_1 back to the ground state g_1.

[12] The angular momentum is quenched in all seven levels, i.e. $\langle n|\mathbf{L}|n\rangle = 0$, where $n = 0, \ldots, 6$. This is because all the levels, being split by the crystal field, are non-degenerate in their orbital part due to the low symmetry of $LiNiPO_4$.

- Ion 1 is exited, via the exchange interaction with ion 2, from the ground state g_1 to a higher state n_1. Ion 1 is then transferred by $\mathbf{L}_1 \cdot \mathbf{S}_1$ from the higher state n_1 back to the ground state g_1.
- Ion 2 is exited by $\mathbf{L}_2 \cdot \mathbf{S}_2$ from the ground state g_2 to a higher state n_2. Ion 2 is then transferred via the exchange interaction with ion 1 from the higher state n_2 back to the ground state g_2.
- Ion 2 is exited via the exchange interaction with ion 1 from the ground state g_2 to a higher state n_2. Ion 2 is then transferred by $\mathbf{L}_2 \cdot \mathbf{S}_2$ from the higher state n_2 back to the ground state g_2.

These processes result in a second order correction to the energy

$$\begin{aligned}\Delta E^{(2)} = -\lambda \Bigg(&\sum_{n_1} \frac{\langle g_1|\mathbf{L}_1 \cdot \mathbf{S}_1|n_1\rangle\langle n_1 g_2|V_{exch}|g_1 g_2\rangle + \langle g_1 g_2|V_{exch}|n_1 g_2\rangle\langle n_1|\mathbf{L}_1 \cdot \mathbf{S}_1|g_1\rangle}{E_{n_1} - E_{g_1}} \\ &+ \sum_{n_2} \frac{\langle g_2|\mathbf{L}_2 \cdot \mathbf{S}_2|n_2\rangle\langle n_2 g_1|V_{exch}|g_2 g_1\rangle + \langle g_2 g_1|V_{exch}|n_2 g_1\rangle\langle n_2|\mathbf{L}_2 \cdot \mathbf{S}_2|g_2\rangle}{E_{n_2} - E_{g_2}} \Bigg).\end{aligned} \tag{2.65}$$

Within the multiplet, we can write (2.65) as an operator, using

$$\langle n_1 g_2|V_{exch}|g_1 g_2\rangle = J(n_1 g_2, g_1 g_2)\mathbf{S}_1 \cdot \mathbf{S}_2, \tag{2.66}$$

where $J(n_1 g_2, g_1 g_2)(= J(g_1 g_2, n_1 g_2))$ is a sum of exchange integrals of the form

$$\int d\mathbf{r} d\mathbf{r}' \psi^*_{t_{2g}}(\mathbf{r} - \mathbf{R}_2)\psi^*_{e_g}(\mathbf{r}' - \mathbf{R}_1)\frac{e^2}{|\mathbf{r} - \mathbf{r}'|}\psi_{t'_{2g}}(\mathbf{r} - \mathbf{R}_1)\psi_{t_{2g}}(\mathbf{r}' - \mathbf{R}_2), \tag{2.67}$$

and

$$\langle n'|\mathbf{L} \cdot \mathbf{S}|n\rangle = \langle n'|\mathbf{L}|n\rangle \cdot \mathbf{S}. \tag{2.68}$$

Since $\langle n'|\mathbf{L}|n\rangle$ is purely imaginary, so that $\langle n'|\mathbf{L}|n\rangle = -\langle n|\mathbf{L}|n'\rangle$, we write

$$\begin{aligned}&\langle g_1|\mathbf{L}_1 \cdot \mathbf{S}_1|n_1\rangle\langle n_1 g_2|V_{exch}|g_1 g_2\rangle + \langle g_1 g_2|V_{exch}|n_1 g_2\rangle\langle n_1|\mathbf{L}_1 \cdot \mathbf{S}_1|g_1\rangle \\ &= \sum_\mu J(n_1 g_2, g_1 g_2)\langle g_1|L_{1\mu}|n_1\rangle\big[S_{1\mu}(\mathbf{S}_1 \cdot \mathbf{S}_2) - (\mathbf{S}_1 \cdot \mathbf{S}_2)S_{1\mu}\big] \\ &= \sum_\mu J(n_1 g_2, g_1 g_2)\langle g_1|L_{1\mu}|n_1\rangle\big[S_{1\mu}, \mathbf{S}_1 \cdot \mathbf{S}_2\big],\end{aligned} \tag{2.69}$$

and similar when interchanging 1 and 2. So (2.65) can be written as an operator

$$\begin{aligned}\mathcal{H}_{DM} = 2\lambda \sum_\mu \Bigg(&\sum_{n_1} \frac{J(n_1 g_2, g_1 g_2)\langle g_1|L_{1\mu}|n_1\rangle[S_{1\mu}, \mathbf{S}_1 \cdot \mathbf{S}_2]}{E_{n_1} - E_{g_1}} \\ &+ \sum_{n_2} \frac{J(g_1 n_2, g_1 g_2)\langle g_2|L_{2\mu}|n_2\rangle[S_{2\mu}, \mathbf{S}_1 \cdot \mathbf{S}_2]}{E_{n_2} - E_{g_2}} \Bigg).\end{aligned} \tag{2.70}$$

By use of the commutator relations

$$\begin{aligned}[\mathbf{S}_1, \mathbf{S}_1 \cdot \mathbf{S}_2] &= -i\mathbf{S}_1 \times \mathbf{S}_2, \\ [\mathbf{S}_2, \mathbf{S}_1 \cdot \mathbf{S}_2] &= -i\mathbf{S}_2 \times \mathbf{S}_1 = i\mathbf{S}_1 \times \mathbf{S}_2,\end{aligned} \tag{2.71}$$

(2.70) can be written as

$$\mathcal{H}_{DM} = \mathbf{D} \cdot (\mathbf{S}_1 \times \mathbf{S}_2). \tag{2.72}$$

Here we have defined the Dzyaloshinsky-Moriya vector, $\mathbf{D}$, as

$$\mathbf{D} = -2i\lambda \left(\sum_{n_1} \frac{\langle g_1|\mathbf{L}_1|n_1\rangle}{E_{n_1} - E_{g_1}} J(n_1 g_2, g_1 g_2) - \sum_{n_2} \frac{\langle g_2|\mathbf{L}_2|n_2\rangle}{E_{n_2} - E_{g_2}} J(g_1 n_2, g_1 g_2) \right). \tag{2.73}$$

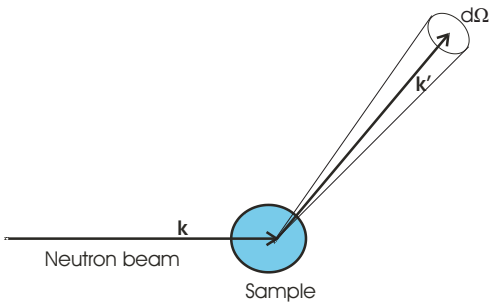

Figure 2.13: Incoming monochromatic beam of neutrons, with energy E and wave vector $\mathbf{k}$, is scattered by the sample. The differential scattering cross-section, defined by (2.74), is the number of neutrons per second and per incoming flux, that are being scattered into the small solid angle $d\Omega$ around the direction defined by $\mathbf{k}'$, and with final energy in $[E', E' + dE']$.

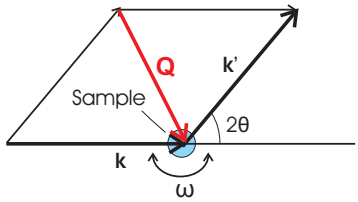

Figure 2.14: The scattering triangle, showing incoming neutrons with wave vector $\mathbf{k}$, scattered neutrons with $\mathbf{k}'$, and the scattering vector $\mathbf{Q} = \mathbf{k} - \mathbf{k}'$. The scattering angle, 2θ, is twice the angle, θ, appearing in the well-known Bragg's law for elastic scattering. The angle ω describes the relative rotation of the sample.

The allowed directions of the DM vector, $\mathbf{D}$, is dictated by the crystal symmetry, and it is possible to formulate some general rules [24, 28] that are often helpful. However, the symmetry of $LiNiPO_4$ is too complicated for those rules to be of much use for us, and we shall not quote them here. Instead we deduce the possible DM interactions for the specific case of $LiNiPO_4$ in chapter 5.

2.4 Neutron scattering

All the results presented in this thesis are from neutron scattering experiments. To interpret the measured data one has to connect the experiment with theoretical calculations. The bridge between experiment and theory is in many cases gapped by a quantity called the neutron scattering cross-section. Here we define the neutron scattering cross-section, and, without deriving the expressions in any way, show some of the mathematical forms it can take, and which will be used in coming chapters. For more detailed discussions of the fundamentals on neutron scattering, we refer to standard text-books on the subject, like for instance [29]. We end this section by giving a very short description of the three instruments we have used for the neutron experiments presented in this thesis.

2.4.1 The scattering cross-section

In a neutron experiment (or other scattering experiments for that matter) we usually measure quantities that are connected to the so-called scattering cross-section. Consider a monochromatic beam of neutrons, with energy E and wave vector $\mathbf{k}$, hitting a sample. Most of the neutrons will just pass through the sample, but some are scattered. If the flux of the incoming beam of neutrons is Φ, we define the *partial differential neutron scattering cross-section* as

$$\frac{d^2\sigma}{d\Omega dE'} = \frac{\text{Number of scattered neutrons per second with energy in } [E', E' + dE'] \text{ and direction in } d\Omega}{\Phi d\Omega dE'}. \tag{2.74}$$

We illustrate the definition of the partial differential neutron scattering cross-section in figure 2.13. The angle $d\Omega$ is a solid angle around a certain direction, here given by the wave vector $\mathbf{k}'$. It is customary to define the scattering vector

$$\mathbf{Q} = \mathbf{k} - \mathbf{k}', \tag{2.75}$$

and the scattering energy

$$\hbar\omega = E - E', \tag{2.76}$$

as the wave vector and energy which is transferred to the crystal in the process. Using Fermi's golden rule, it is possible [29] to write the partial differential cross-section as

$$\left(\frac{d^2\sigma(\mathbf{Q},\omega)}{d\Omega dE'}\right)_{\lambda\to\lambda'} = \frac{k'}{k}\left(\frac{m}{2\pi\hbar^2}\right)^2 |\langle \mathbf{k}'\lambda'|V|\mathbf{k}\lambda\rangle|^2 \delta(E_\lambda - E_{\lambda'} + E - E'). \tag{2.77}$$

Here λ and λ' describe the state of the sample, and E_λ, $E_{\lambda'}$ the energy of the sample, before and after the scattering process. The scattering potential V depends on the nature of the considered scattering processes as discussed below, and the delta function ensures energy conservation.

The differential cross-section is defined as

$$\frac{d\sigma}{d\Omega} = \int dE' \frac{d^2\sigma}{d\Omega dE'}, \tag{2.78}$$

and is the number of neutrons per second scattered into a solid angle $d\Omega$ in the given direction divided by the incomming flux. The scattering of a neutron on an ion is due to one of the following two interactions:

Nuclear forces between the neutron and the nucleus.

Here the scattering potential is

$$V = \sum_j V_j(\mathbf{r} - \mathbf{R}_j), \tag{2.79}$$

where $\mathbf{R}_j$ is the position of the ions in the sample, and the short-ranged nuclear forces are approximated by the so-called Fermi pseudopotential

$$V_j(\mathbf{r}) = \frac{2\pi\hbar^2}{m} b_j \delta(\mathbf{r}). \tag{2.80}$$

The constants b_j are called the scattering length and depend on the type and spin state of the nuclei considered. The nuclear scattering cross-section for coherent elastic scattering on a single crystal can be written [30] as

$$\frac{d\sigma_N}{d\Omega}(\mathbf{Q}) = N\frac{(2\pi)^3}{V_0}\sum_\tau |F_N(\mathbf{Q})|^2 \delta(\mathbf{Q} - \boldsymbol{\tau}), \tag{2.81}$$

where

$$F_N(\mathbf{Q}) = \sum_{\mathbf{d}} \bar{b}_d e^{i\mathbf{Q}\cdot\mathbf{d}} e^{-W_d}, \tag{2.82}$$

is called the nuclear structure factor. Here $\bar{b}_d$ is the coherent scattering length, and W_d is the Debye-Waller factor of the ion positioned at $\mathbf{d}$, reflecting the thermal ionic movements in the crystal. We mention, that coherent nuclear scattering $\bar{b}_d$ is the mean scattering length of a particular type of ions in the system. This is opposed to incoherent scattering, reflecting the random distribution of different nuclear ionic isotopes and nuclear spin states, causing a diffuse background signal.

The reader is reminded about the well known definition of the reciprocal lattice vectors

$$\mathbf{a}^* = 2\pi\frac{\mathbf{b}\times\mathbf{c}}{\mathbf{a}\cdot(\mathbf{b}\times\mathbf{c})}, \quad \mathbf{b}^* = 2\pi\frac{\mathbf{c}\times\mathbf{a}}{\mathbf{a}\cdot(\mathbf{b}\times\mathbf{c})}, \quad \mathbf{c}^* = 2\pi\frac{\mathbf{a}\times\mathbf{b}}{\mathbf{a}\cdot(\mathbf{b}\times\mathbf{c})}, \tag{2.83}$$

where $\mathbf{a}, \mathbf{b}, \mathbf{c}$, are the lattice vectors in direct space. The reciprocal lattice consists of vectors $\boldsymbol{\tau}$, where

$$\boldsymbol{\tau} = H\mathbf{a}^* + K\mathbf{b}^* + L\mathbf{c}^*, \quad H, K, L \in \mathbb{Z}. \tag{2.84}$$

From the scattering triangle (figure 2.14) we find

$$Q = |\mathbf{k} - \mathbf{k}'| = 2k\sin\theta = 2\frac{2\pi}{\lambda}\sin\theta. \tag{2.85}$$

Since the reciprocal lattice vectors $\boldsymbol{\tau}$ are connected to Bragg planes with interspacing d through $\tau = 2\pi/d$, we immediately find

$$\mathbf{Q} = \boldsymbol{\tau} \Rightarrow Q = \frac{2\pi}{d} \Rightarrow 2d\sin\theta = \lambda. \tag{2.86}$$

We can always multiply a reciprocal lattice vector with an integer n and still get a reciprocal lattice vector, so the delta-function in (2.81) is equivalent to

$$n\lambda = 2d\sin\theta, \tag{2.87}$$

which is recognized as the well-known Bragg law of elastic scattering.

Magnetic interactions

The magnetic moment of a neutron will interact with the unpaired electrons in an ion. The potential energy of the neutron in the field from an electron with spin $\mathbf{s}$ and momentum $\mathbf{p}$ can be written as

$$V_{mag} = -\frac{\mu_0}{4\pi}\gamma\mu_N 2\mu_B \boldsymbol{\sigma}\cdot(\mathbf{W}_s + \mathbf{W}_L). \tag{2.88}$$

Here $\gamma = 1.913$ is the neutron gyromagnetic ratio, $\boldsymbol{\sigma}$ the Pauli spin operator for the neutron, and

$$\mu_N = \frac{e\hbar}{2m_p}, \tag{2.89}$$

the nuclear magneton, with m_p being the mass of a proton. The term

$$\mathbf{W}_s = \nabla\times\left(\frac{\mathbf{s}\times\mathbf{R}}{R^3}\right), \tag{2.90}$$

where $\mathbf{R}$ is the position of the neutron relative to the electron, is due to the magnetic dipole interaction between the spin of the neutron and the spin of the electron. The second term

$$\mathbf{W}_L = \frac{1}{\hbar}\frac{\mathbf{p}\times\mathbf{R}}{R^3}, \tag{2.91}$$

is derived from the Biot-Savart law, and describes the potential of the neutron in the magnetic field created from the orbital motion of the electron.

Using the potential (2.88), the elastic magnetic cross-section can be written as

$$\frac{d\sigma_M}{d\Omega}(\mathbf{Q}) = \left(\frac{\gamma r_0}{2\mu_B}\right)^2 |\widehat{\mathbf{Q}}\times[\langle\mathbf{M}(\mathbf{Q})\rangle\times\widehat{\mathbf{Q}}]|^2, \tag{2.92}$$

where $r_0 = \frac{\mu_0 e^2}{4\pi m_e}$ is the classical radius of the electron, $\widehat{\mathbf{Q}} = \mathbf{Q}/Q$ a unit vector in the direction of the scattering vector and $\langle\mathbf{M}(\mathbf{Q})\rangle$ the thermal average of the Fourier component

$$\mathbf{M}(\mathbf{Q}) = \sum_n\sum_d \mathbf{m}_d(\mathbf{R}_n)e^{i\mathbf{Q}\cdot\mathbf{R}_{nd}}, \tag{2.93}$$

of the magnetization operator $\mathbf{M}(\mathbf{r})$. Later in this thesis we shall use the differential magnetic cross-section for inelastic scattering, which is given as equation (6.28) in chapter 6.

2.4.2 Instruments used in the experiments

The triple axis spectrometer, RITA-II at PSI

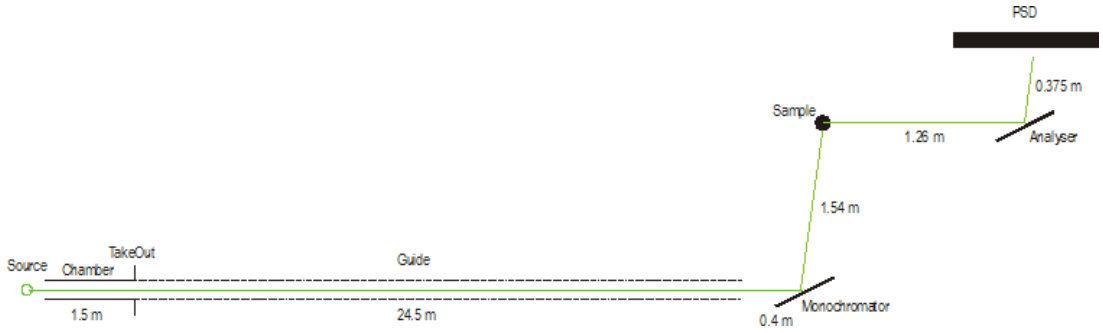

Figure 2.15: A schematic overview of the cold source triple axis spectrometer, RITA-II.

RITA-II at PSI is an example of a so-called triple axis spectrometer (TAS). The three axes are (1) the monochromator axis, (2) the sample axis, and (3) the analyzer axis. The schematic overview of RITA, given in figure 2.15, illustrates the basic setup of a triple axis spectrometer. RITA receives neutrons from the spallation neutron source, SINQ, where neutrons are created from an beam of protons hitting a lead target. For some of the instruments, including RITA, the neutrons are slowed down by a cold moderator of liquid hydrogen with temperature 25 K (cold source) before entering the neutron guide leading to the instrument.

Both the monochromator and analyzer on RITA are composed of pyrolytic graphite (PG) single crystals, making use of the Bragg law

$$n\lambda = 2d\sin\theta, \tag{2.94}$$

to reflect only neutrons with certain energies. In almost all our experiments the analyzer was set to reflect 5 meV neutrons. Without going into instrumental details, we show, in figure 2.16 [31], the non-conventional 7 blade analyzer of RITA. Unlike in an ordinary TAS, the 7 analyzer crystals, or *blades*, of RITA can be worked separately if this is desired, measuring for instance at 7 different scattering vectors at a time.

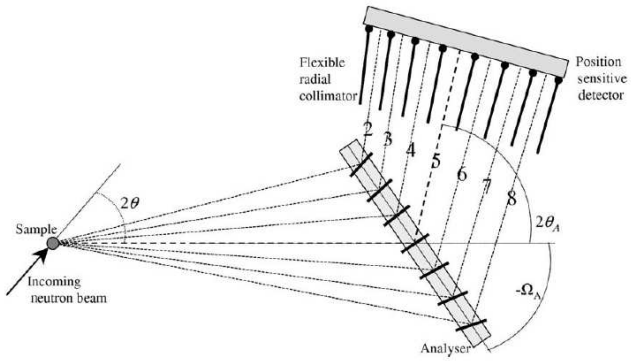

Figure 2.16: A schematic overview of the 7 blade analyzer on RITA. Figure taken from [31].

The triple axis spectrometer, IN8 at ILL with MAD detector box

The beam line IN8 at the nuclear reactor at ILL, is known to have the largest monochromatic flux of all thermal three-axis spectrometers in the world [32]. In figure 2.17, taken from [32], the monochromatic neutron flux at the sample position at IN8 is shown for different choices of the monochromator crystals. In our experiments at IN8 we mostly used the Cu monochromator crystals, set to reflect 30 meV neutrons ($ki = 3.9$ Å^{-1}).

On our IN8 experiment we used a multi-detector analyzer (MAD) with 48 separate Cu analyzer crystals, each about 75 mm high [33]. This was an unusual setup for IN8, since the MAD box primarily had been used at the beam line IN3, but it worked extremely well for our purposes (see section 7.3). Figure 2.18 show a top view of the MAD detector box.

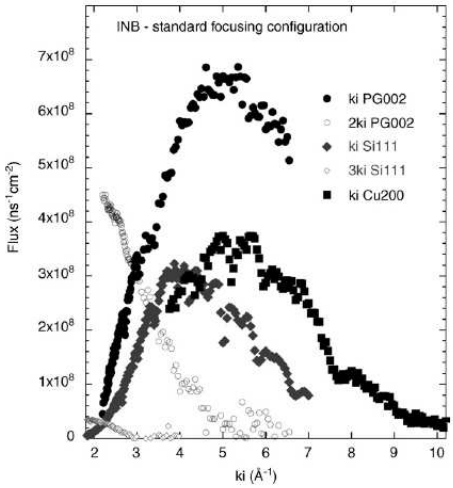

Figure 2.17: Monochromatic neutron flux (closed symbols) at the sample position on IN8 for different choice of monochromator crystals. Open symbols represent higher order contamination. Figure taken from [32].

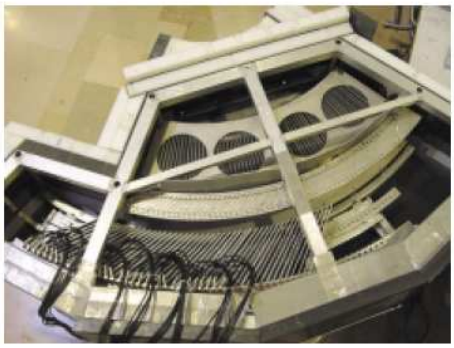

Figure 2.18: Top view of the MAD box. The row of Helium detectors is at the bottom of the picture. Figure taken from [34].

The single crystal diffraction instrument, TriCS, at PSI

In a diffraction experiment it is usually preferred not to include an analyzer (the third axis) in the experimental setup. This is to ensure that all the diffracted intensity, from a given Bragg peak, is collected by a single measurement, typically an omega scan rotating the crystal.

Figure 2.19 gives an overview of the single crystal diffractometer, TriCS, situated at PSI. When no analyzer is present, as in the figure, we say the instrument is in a two-axis mode. TriCS receives neutrons from SINQ, but unlike for RITA, the neutrons guided to TriCS are moderated by water at room temperature. TriCS is therefore called a thermal instrument, and is provided with neutrons having higher energies than at RITA. There are two different choices of the monochromator at TriCS, using either Ge-311 or C-002 crystals, and in our experiments we have used both. The Germanium monochromator reflecting neutrons at wavelength $\lambda = 1.18$ Å and energy 58.7 meV were used for the incommensurate scans (scans around non-integral $\mathbf{Q}$), while the Graphite provided neutrons with $\lambda = 2.3$ Å and energy 15.5 meV for the commensurate scans (scans around integral $\mathbf{Q}$).

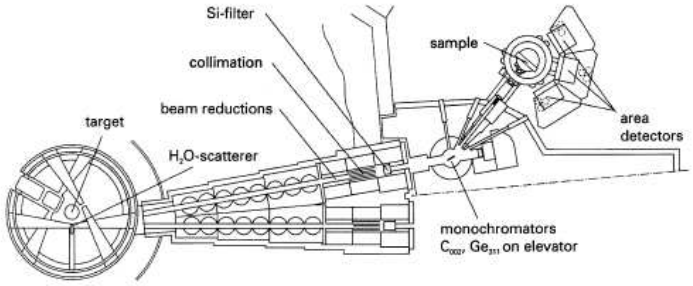

Figure 2.19: Schematic overview of the single crystal diffractometer TriCS. Figure taken from [35].

Lorentz factor

When performing a diffraction experiment, the main idea is to gather information from as many different scattering vectors as possible. Having this information one can hopefully deduce the structure (atomic or magnetic) by comparing the intensities of the collected peaks. The experiments on TriCS were performed without analyzer, and with a large detector opening to make sure that all the scattered intensity for a given scattering vector was collected. We perform measurements by rotating the crystal relative to the instrument in small steps, i.e. by rotating the angle ω shown in figure 2.14. Counting the number of scattered neutrons for every value of ω, and then integrating over ω, the scattered integrated intensity for the given $\mathbf{Q}$ is found. In such omega scans, one has to correct the integrated intensities by a factor, known as the Lorentz factor. This is because the path of the omega scan in reciprocal space depends on the scattering vector around which the scan is performed. The integrated intensity, $I(\mathbf{Q})$, for an omega scan can be written as [29]

$$I(\mathbf{Q}) = N\frac{(2\pi)^3}{V_0}\Phi\frac{|F(\boldsymbol{\tau})|^2}{Q} = \frac{N}{V_0}\phi\frac{\lambda^3}{\sin\theta}|F(\boldsymbol{\tau})|^2, \tag{2.95}$$

where N is the number of unit cells, $V_0 = abc$ is the volume of a unit cell and $F(\boldsymbol{\tau})$ is the appropriate structure factor. Since we usually compare intensities for different scattering vectors $\mathbf{Q}_1$ and $\mathbf{Q}_2$, we have

$$\frac{I(\mathbf{Q}_1)}{I(\mathbf{Q}_2)} = \frac{F(\boldsymbol{\tau}_1)|^2/\sin\theta_1}{F(\boldsymbol{\tau}_2)|^2/\sin\theta_2}. \tag{2.96}$$

Therefore, when comparing integrated intensities collected in a series of omega scans, we have to normalize with the so-called Lorentz factor

$$\frac{1}{\sin\theta}. \tag{2.97}$$

Magnetic form factor

Unlike the point-like nuclear scattering between the neutron and the nucleus, the magnetic neutron scattering is due to the electron cloud surrounding the nucleus and cannot be described by a delta-function. The spatial extension of the electrons is reflected in the scattering cross-section by a factor called the magnetic form factor $f(\mathbf{Q})$ (see for instance formula (3.100)). The magnetic form factor is essentially the Fourier transform of the density of unpaired electrons. Since the electron cloud is not point-like, but has a finite size in real space, the Fourier transform is decreasing as a function of $\mathbf{Q}$ in reciprocal space; i.e. when Q becomes larger, the form factor becomes smaller. The magnetic form factor is for instance tabulated in [36, 37].

Chapter 3

Magnetic structure determination Part A

Introductional theory

This chapter is devoted to theory upon which we base much of the analysis of our elastic diffraction experiments described in chapter 5. We focus mainly on two subjects. The first is the group theoretical concept of irreducible representations, and their connection to magnetic structures. This hardly constitutes standard text-book material, but since irreducible representations are widely used when analyzing magnetic structures it seems well worth trying to understand the basics. The sections concerning irreducible representations and magnetic structures are based on discussions with Mogens Stibius Jensen from DTU (the Technical University of Denmark), and on [38, 39, 40, 30]. The second subject of the chapter is applying the concept of irreducible basis vectors to the magnetic scattering cross-section. The relevance of these subjects are perhaps best understood when going through the examples of chapter 5.

3.1 Describing magnetically ordered structures

In a system with localized spins the magnetic structure is described by the thermal mean value, $\mathbf{m}(\mathbf{r}) = \langle \widehat{\mathbf{m}}(\mathbf{r}) \rangle$, of the magnetic moment for all magnetic ions in the system. Here $\widehat{\mathbf{m}}(\mathbf{r})$ is the quantum mechanical operator measuring the magnetic moment of the ion at position $\mathbf{r}$. In the conventionally defined chemical unit cell of $LiNiPO_4$ there are four magnetic Ni^{2+} ions, situated at positions

$$\begin{aligned} \mathbf{r}_1 &= (0.275, 0.25, 0.98), \quad \mathbf{r}_2 = (0.775, 0.25, 0.52), \\ \mathbf{r}_3 &= (0.725, 0.75, 0.02), \quad \mathbf{r}_4 = (0.225, 0.75, 0.48), \end{aligned} \tag{3.1}$$

relative to the unit cell. The magnetic unit cell (see for instance figure 2.2) is defined as having the same size, but being displaced (0.25,0.25,0) rlu compared to the chemical unit cell.

We can Fourier expand the magnetic moments, $\mathbf{m}_j(\mathbf{R}_n) \equiv \mathbf{m}(\mathbf{R}_n + \mathbf{r}_j)$, connected to each of the positions j = 1-4, and write

$$\mathbf{m}_j(\mathbf{R}_n) = \sum_{\mathbf{k}} \mathbf{m}_j(\mathbf{k}) e^{-i\mathbf{k}\cdot\mathbf{R}_n}, \quad j = 1, 2, 3, 4, \tag{3.2}$$

where the wave vectors $\mathbf{k}$ belong to the first Brillouin zone, j is the number of the ion within the unit cell, and $\mathbf{R}_n$ is the position of the n'th unit cell. The magnetic structure is completely determined once all the Fourier components $\mathbf{m}_j(\mathbf{k})$ have been found.

In figure 3.1 we consider two possible examples of magnetic structures in $LiNiPO_4$. The figure depict the magnetic Ni^{2+} ions and the mean values of their magnetic moments projected on a *bc*-plane. The first example (figure 3.1a) has non-vanishing Fourier components only for $\mathbf{k} = 0$. Therefore

$$\mathbf{m}_j(\mathbf{R}_n) = \mathbf{m}_j(0) = \big(m_{jx}(0), m_{jy}(0), m_{jz}(0)\big), \quad j = 1, 2, 3, 4, \tag{3.3}$$

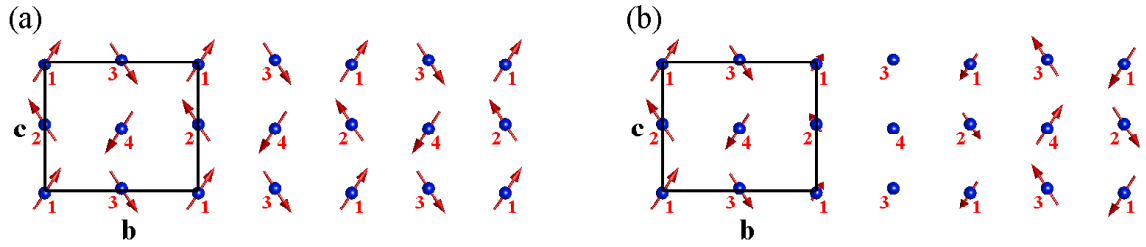

Figure 3.1: (a) Commensurate magnetic structure of localized magnetic moments described by a single wave vector $\mathbf{k} = 0$, as explained in the text. (b) Incommensurate magnetic structure described by a single wave vector $\mathbf{k} = (0, k, 0)$.

and the structure is completely determined by the 12 Fourier components

$$m_{1x}(0), m_{1y}(0), m_{1z}(0), \ldots, m_{4z}(0). \tag{3.4}$$

In the second example (figure 3.1b) the moments are modulated by a wave vector $\mathbf{k} \neq 0$ parallel to the crystallographic b direction. Since $\mathbf{m}_j(\mathbf{R}_n)$ is a real number, the Fourier transforms fulfil that $\mathbf{m}_j(-\mathbf{k}) = \mathbf{m}_j(\mathbf{k})^*$. If all other Fourier components are zero, i.e. if $\mathbf{m}_j(\mathbf{k}') = 0$ for all $\mathbf{k}' \neq \pm\mathbf{k}$, we have that

$$\mathbf{m}_j(\mathbf{R}_n) = \mathbf{m}_j(\mathbf{k})^* e^{i\mathbf{k}\cdot\mathbf{R}_n} + \mathbf{m}_j(\mathbf{k}) e^{-i\mathbf{k}\cdot\mathbf{R}_n}, \tag{3.5}$$

which is also completely described by 12 Fourier components, namely

$$m_{1x}(\mathbf{k}), m_{1y}(\mathbf{k}), m_{1z}(\mathbf{k}), \ldots, m_{4z}(\mathbf{k}). \tag{3.6}$$

In both examples the magnetic structure is said to be a single $\mathbf{k}$ structure ($\mathbf{k} = 0$ for (a) and $\mathbf{k} \neq 0$ for (b)). This is equivalent to saying that only 12 Fourier components are needed for determining the magnetic structure. When $\mathbf{k} = 0$ the structure is said to be commensurate, while it is incommensurate for $\mathbf{k} \neq 0$. Naturally one could imagine more complex structures, described by more than one $\mathbf{k}$, and where more than 12 Fourier components have to be determined. However, we shall limit our discusion to single $\mathbf{k}$ structures.

In the coming sections we will decompose the magnetic structures of $LiNiPO_4$ into components connected to certain operators, called irreducible basis vectors, that reflect the symmetry of the system. Doing this is not restricting or "mysterious" in any way, but is simply a matter of writing the magnetic structures in a form that experience has shown to be very convenient.

The concept of irreducible basis vectors is often introduced when group theory is used to classify the solutions of a physical problem. In our case we use the irreducible basis vectors for the following two reasons. First of all, the associated magnetic components have especially simple structure factors (section 3.5), which greatly simplifies the data analysis. Secondly, it can be shown (section 3.3.4) that the quadratic terms in the spin Hamiltonian consist exclusively of products of irreducible basis vectors (operators) transforming identically under the symmetry elements of the system; we say they belong to the same irreducible representation. As a consequence the magnetic ground state is likely to be described by only a few irreducible basis vectors. All in all, the associated magnetic components are the natural choice for describing the magnetic structures in crystals. To continue we first introduce some basic definitions and concepts.

3.2 Symmetries and transformations

3.2.1 A few basic concepts

Groups and subgroups

It is well known that a set $G = \{g\}$ together with a composition constitutes a group if

(a) $g_1, g_2 \in G \Rightarrow g_1 g_2 \in G$,

(b) $g_1(g_2 g_3) = (g_1 g_2) g_3$,

(c) $\exists e \in G \; \forall g \in G : ge = eg = g$,

(d) $\forall g \in G \; \exists g^{-1} \in G : gg^{-1} = g^{-1}g = e$.

The number of elements in G is called the order of the group and is written $|G|$. Two group elements g_1, g_2 are said to commute if $g_1 g_2 = g_2 g_1$. A group where all elements commute is called Abelian or commutative. A subset $H \subset G$ that is also a group (with the same composition as in G) is called a subgroup of G.

Co-sets and factor groups

Suppose G is a group and H is a subgroup of G. For any element $g \in G$ we can construct a subset of G called the left co-set $gH = \{gh | h \in H\}$. It is easy to show that the co-sets constitute a class division of G. We can also construct the right co-set $Hg = \{hg | h \in H\}$ of H. A subgroup H is called a normal subgroup if $gH = Hg$ for all $g \in G$. From the set of co-sets for a normal subgroup H, a group can be constructed by regarding the co-sets as individual elements with the following composition

$$(g_1 H)(g_2 H) = (g_1 g_2) H. \tag{3.7}$$

This group of co-sets is called the factor group, G/H, and has order

$$|G/H| = \frac{|G|}{|H|}. \tag{3.8}$$

Conjugate elements, classes

Two elements g_1, g_2 are said to be conjugate, if there is an element $g \in G$ so that

$$g_1 = g g_2 g^{-1}. \tag{3.9}$$

The set of elements conjugated to a given element, g, constitutes a class, $[g]$, and the set of classes $\{[g_1], [g_2], \ldots\}$ defines a class division of G. For an Abelian group the classes consist of only one element, $[g] = \{g\}$, and the number of classes equals the order $|G|$ of the group.

Homomorphy, isomorphy

A relation $\Gamma : G \to G'$ between two groups G and G' is called a homomorphy, if

$$\Gamma(g_1 g_2) = \Gamma(g_1)\Gamma(g_2), \tag{3.10}$$

for all elements $g_1, g_2 \in G$. If Γ is also one-to-one, the groups G and G' are said to be isomorphic, and we write $G \cong G'$.

Symmetries

A transformation preserving distances between all points of a given body and bringing the body "on top" of itself, is called a symmetry element, or symmetry, of the body. The set of all symmetry elements constitutes a group, known as the symmetry group of the body. Any symmetry element can be constructed by the following three operations

(1) Rotations, $R(\alpha, l)$, with angle α around an axis l,

(2) Mirror reflections, m_π, in a plane π,

(3) Translations, $T_{\mathbf{t}}$, with translation vector $\mathbf{t}$.

A symmetry group where any element leaves at least one point of the body fixed is called a point group. It can be shown that the symmetry group for finite bodies is always a point group. Dealing with crystals, that are assumed infinite in size, we will come to consider groups other than point groups.

	1	$2'_x$	$2'_y$	$2'_z$	$\bar{1}$	m'_{xy}	m'_{xz}	m'_{yz}
$\mathbf{r}_1$	$\mathbf{r}_1$	$\mathbf{r}_2+00\bar{1}$	$\mathbf{r}_3+\bar{1}0\bar{1}$	$\mathbf{r}_4+0\bar{1}1$	$\mathbf{r}_3+\bar{1}\bar{1}\bar{1}$	$\mathbf{r}_2+00\bar{1}$	$\mathbf{r}_1$	$\mathbf{r}_4+001$
$\mathbf{r}_2$	$\mathbf{r}_2$	$\mathbf{r}_1+10\bar{1}$	$\mathbf{r}_4+\bar{1}0\bar{1}$	$\mathbf{r}_3+\bar{1}1\bar{1}$	$\mathbf{r}_4+\bar{1}\bar{1}\bar{1}$	$\mathbf{r}_1+10\bar{1}$	$\mathbf{r}_2$	$\mathbf{r}_3+\bar{1}01$
$\mathbf{r}_3$	$\mathbf{r}_3$	$\mathbf{r}_4+1\bar{1}0$	$\mathbf{r}_1+\bar{1}1\bar{1}$	$\mathbf{r}_2+\bar{1}\bar{1}0$	$\mathbf{r}_1+\bar{1}\bar{1}\bar{1}$	$\mathbf{r}_4+100$	$\mathbf{r}_3+0\bar{1}0$	$\mathbf{r}_2+\bar{1}10$
$\mathbf{r}_4$	$\mathbf{r}_4$	$\mathbf{r}_3+0\bar{1}0$	$\mathbf{r}_2+\bar{1}1\bar{1}$	$\mathbf{r}_1+0\bar{1}0$	$\mathbf{r}_2+\bar{1}\bar{1}\bar{1}$	$\mathbf{r}_3$	$\mathbf{r}_4+0\bar{1}0$	$\mathbf{r}_1+010$
S_x	S_x	S_x	$-S_x$	$-S_x$	S_x	$-S_x$	$-S_x$	S_x
S_y	S_y	$-S_y$	S_y	$-S_y$	S_y	$-S_y$	S_y	$-S_y$
S_z	S_z	$-S_z$	$-S_z$	S_z	S_z	S_z	$-S_z$	$-S_z$

Table 3.1: The transformed positions of $\mathbf{r}_1$-$\mathbf{r}_4$ and transformed spin components S_x, S_y, S_z under the symmetry elements in G.

3.2.2 Symmetry group of $LiNiPO_4$

The symmetry group of $LiNiPO_4$ is $G \otimes G_T$. Here $G_T = \{T_{\mathbf{T}} \mid \mathbf{T} = n\mathbf{a} + m\mathbf{b} + l\mathbf{c}\}$ is the group of integer lattice translations ($\mathbf{a}, \mathbf{b}, \mathbf{c}$ are the lattice vectors of the unit cell in $LiNiPO_4$), and

$$G = \{1, 2'_x, 2'_y, 2'_z, \bar{1}, m'_{xy}, m'_{xz}, m'_{yz}\}, \tag{3.11}$$

where[1]

$$\begin{aligned}
&1 \text{ is the identity :} && 1(x,y,z) = (x,y,z), && (3.12a)\\
&2'_x \text{ is a } 180^\circ \text{ screw axis around } (x, 0.25, 0.25) : && 2'_x(x,y,z) = (x+0.5, 0.5-y, 0.5-z), && (3.12b)\\
&2'_y \text{ is a } 180^\circ \text{ screw axis around } (0, y, 0) : && 2'_y(x,y,z) = (-x, y+0.5, -z), && (3.12c)\\
&2'_z \text{ is a } 180^\circ \text{ screw axis around } (0.25, 0, z) : && 2'_z(x,y,z) = (0.5-x, -y, z+0.5), && (3.12d)\\
&\bar{1} \text{ is inversion in } (0,0,0) : && \bar{1}(x,y,z) = (-x,-y,-z), && (3.12e)\\
&m'_{xy} \text{ is a glide plane } z = 0.25 \text{ with glide vector } (0.5,0,0) : && m'_{xy}(x,y,z) = (x+0.5, y, 0.5-z), && (3.12f)\\
&m'_{xz} \text{ is a mirror plane } y = 0.25 \text{ without glide vector :} && m'_{xz}(x,y,z) = (x, 0.5-y, z), && (3.12g)\\
&m'_{yz} \text{ is a glide plane } x = 0.25 \text{ with glide vector } (0,0.5,0.5) : && m'_{yz}(x,y,z) = (0.5-x, y+0.5, z+0.5). && (3.12h)
\end{aligned}$$

The screw axis symmetry elements, $2'_\alpha$, are 180° rotation around an axis, followed by half a lattice translation along the direction of α. A glide plane, m'_π, is a mirror reflection in the plane π, followed by a translation $T_{\mathbf{t}}$, where the glide vector $\mathbf{t}$ is parallel to π. Strictly speaking G is not a group without the use of integer lattice translations $T_{\mathbf{T}}$. However, the symmetry elements in G *modulo* integer lattice translations constitute a factor group G/G_T. The factor group G/G_T is isomorph to the point group $D_{2h} = \{1, 2_x, 2_y, 2_z, \bar{1}, m_{xy}, m_{xz}, m_{yz}\}$, where the unprimed operations are just ordinary 180° rotations and mirror planes. The group table for D_{2h} is given in table 3.2. It is readily checked that D_{2h}, and therefore G/G_T, is Abelean. For later use we also list, in table 3.1, the transformed positions of $\mathbf{r}_1$-$\mathbf{r}_4$ (in the defining unit cell), and the transformed components of any pseudo-vector $\mathbf{S}$, under the symmetry operations of G.

3.2.3 Unitary transformations

In quantum mechanics the state of a given physical system is described by a vector $|\psi\rangle$ in a Hilbert space. Measurements are described by Hermitian[2] operators[3], O, giving as result the inner product

$$\langle\psi|O|\psi\rangle, \tag{3.13}$$

[1] The coordinates and vectors are given in units of lattice constants. We shall often be using units normalized to the lattice or the reciprocal lattice without mentioning this specifically.

[2] We remind the reader that Hermitian operators, O, fulfil that $O^\dagger = O$, and unitary operators, U, that $U^\dagger = U^{-1}$.

[3] All operators are considered linear (we shall not discuss the concept of anti-linear operators).

D_{2h}	1	2_x	2_y	2_z	$\bar{1}$	m_{xy}	m_{xz}	m_{yz}
1	1	2_x	2_y	2_z	$\bar{1}$	m_{xy}	m_{xz}	m_{yz}
2_x	2_x	1	2_z	2_y	m_{yz}	m_{xz}	m_{xy}	$\bar{1}$
2_y	2_y	2_z	1	2_x	m_{xz}	m_{yz}	$\bar{1}$	m_{xy}
2_z	2_z	2_y	2_x	1	m_{xy}	$\bar{1}$	m_{yz}	m_{xz}
$\bar{1}$	$\bar{1}$	m_{yz}	m_{xz}	m_{xy}	1	2_x	2_y	2_z
m_{xy}	m_{xy}	m_{xz}	m_{yz}	$\bar{1}$	2_z	1	2_x	2_y
m_{xz}	m_{xz}	m_{xy}	$\bar{1}$	m_{yz}	2_y	2_x	1	2_z
m_{yz}	m_{yz}	$\bar{1}$	m_{xy}	m_{xz}	2_x	2_y	2_z	1

Table 3.2: Group table of D_{2h}.

if the system is in a well defined state, $|\psi\rangle$, before the measurement. Experiments at finite temperatures, T, typically measures the thermal mean value

$$\langle O\rangle = \frac{\sum_n e^{-E_n/k_BT}\langle\psi_n|O|\psi_n\rangle}{\sum_n e^{-E_n/k_BT}}, \tag{3.14}$$

since thermal fluctuations continuously move the system from state to state. Transformations of the system are formally described by unitary operators, U, taking the system from a quantum mechanical state $|\psi\rangle$ to a state $|\psi'\rangle$, where

$$|\psi'\rangle = U|\psi\rangle. \tag{3.15}$$

Let O be any operator, and U any transformation. The transformed operator, O', is defined as the operator giving the same results when measuring on transformed states, $|\psi'\rangle$, as O does on non-transformed states, $|\psi\rangle$. Formally, this is written as

$$\langle\psi'|O'|\psi'\rangle = \langle\psi|O|\psi\rangle. \tag{3.16}$$

Since $|\psi'\rangle = U|\psi\rangle$, we find that

$$\langle\psi|O|\psi\rangle = \langle\psi'|O'|\psi'\rangle = \langle\psi|U^\dagger O'U|\psi\rangle \Rightarrow O = U^\dagger O'U, \tag{3.17}$$

which, using that U is unitary, is equivalent to

$$O' = UOU^\dagger. \tag{3.18}$$

For any operator, O, and any transformation, U, we can define the transformed operator by (3.18).

Taking the mean value of the original operator, O, in a transformed state, $|\psi'\rangle$, gives

$$\langle\psi'|O|\psi'\rangle = \langle\psi|U^\dagger OU|\psi\rangle = \langle\psi|(U^{-1})O(U^{-1})^\dagger|\psi\rangle, \tag{3.19}$$

showing that mean values transform as the inverse transformation of the operators. Since the symmetry properties of the magnetic structures and those of the spin operators[4] are closely related by (3.19), the magnetic structures with particularly nice transformation properties can be found by studying the transformation of spin operators. So we turn our attention towards spin operators.

3.2.4 Transformation of spin operators

Spin operators in real space

We consider $LiNiPO_4$ with four magnetic ions per unit cell. The symmetry elements are lattice translations, 180° screw axis rotations and glide planes. A lattice translation $T_{\mathbf{R}_m}$ moves any lattice point $\mathbf{R}_n$ to the lattice

[4]We shall not make a point of distinguishing between spin operators and the operators measuring the total magnetic momentum of an ion.

point $\mathbf{R}_n+\mathbf{R}_m$, and does not change the orientation of the crystal. The spin operator, $\mathbf{S}_j(\mathbf{R}_n) \equiv \mathbf{S}(\mathbf{R}_n+\mathbf{r}_j)$, measuring the spin of a magnetic ion at position $\mathbf{R}_n + \mathbf{r}_j$, transforms according to

$$T_{\mathbf{R}_m}\mathbf{S}_j(\mathbf{R}_n)T^{\dagger}_{\mathbf{R}_m} = \mathbf{S}_j(\mathbf{R}_n + \mathbf{R}_m). \tag{3.20}$$

This is easily realized since $\mathbf{S}_j(\mathbf{R}_n + \mathbf{R}_m)$ gives the same result on the transformed system, as $\mathbf{S}_j(\mathbf{R}_n)$ gives on the non-transformed system.

Let us introduce the notation

$$U = \{\varphi|\mathbf{t}_\varphi\} \in G, \tag{3.21}$$

especially suited to describe the screw axis and glide plane symmetry elements in G. Here $\varphi \in D_{2h}$ are symmetry elements from the point group D_{2h}, and $\mathbf{t}_\varphi$ are the accompanying non-integer translations. We have that

$$\{\varphi|\mathbf{t}_\varphi\}(\mathbf{R}_n + \mathbf{r}_j) = \varphi(\mathbf{R}_n) + \varphi(\mathbf{r}_j) + \mathbf{t}_\varphi = \varphi(\mathbf{R}_n) + \mathbf{r}_i + \mathbf{R}_0. \tag{3.22}$$

Here $\mathbf{R}_0$ are the lattice vectors given in table 3.1, and reflects that $\mathbf{R}_n$ and $\mathbf{R}_n + \mathbf{r}_j$ are not necessarily transformed into the same unit cell by U. Besides spatial translations, the system may also be rotated or reflected by U. The transformed operators, $U\mathbf{S}_j(\mathbf{R}_n)U^{\dagger}$, must follow the orientation of the transformed system in order to reproduce the action of $\mathbf{S}_j(\mathbf{R}_n)$ on the non-transformed states. Therefore

$$U\mathbf{S}_j(\mathbf{R}_n)U^{\dagger} = U\mathbf{S}(\mathbf{R}_n + \mathbf{r}_j)U^{\dagger} = \mathbf{S}\big(\varphi(\mathbf{R}_n) + \mathbf{r}_i + \mathbf{R}_0\big)\mathbf{D}(\varphi) = \mathbf{S}_i\big(\varphi(\mathbf{R}_n) + \mathbf{R}_0\big)\mathbf{D}(\varphi), \tag{3.23}$$

which in terms of vector components is written as

$$US_{j\nu}(\mathbf{R}_n)U^{\dagger} = S_{i\mu}\big(\varphi(\mathbf{R}_n) + \mathbf{R}_0\big)D_{\mu\nu}(\varphi). \tag{3.24}$$

The 3×3 matrix, $\mathbf{D}(\varphi)$, introduced in (3.23) and (3.24), is the "rotation" matrix of φ, describing how the components of a pseudo vector transform under φ. The matrix elements, $D_{\mu\nu}(\varphi)$, are easily deduced from table 3.1.

Spin operators in k-space

We now introduce the Fourier transforms

$$\mathbf{S}_j(\mathbf{k}) = \frac{1}{N}\sum_n \mathbf{S}_j(\mathbf{R}_n)e^{i\mathbf{k}\cdot\mathbf{R}_n}, \quad j = 1, 2, 3, 4, \tag{3.25}$$

with the inverse relation

$$\mathbf{S}_j(\mathbf{R}_n) = \sum_n \mathbf{S}_j(\mathbf{k})e^{-i\mathbf{k}\cdot\mathbf{R}_n}. \tag{3.26}$$

The spin operators $\mathbf{S}_j(\mathbf{k})$ transform under a lattice translation according to

$$\begin{aligned} T_{\mathbf{R_m}}\mathbf{S}_j(\mathbf{k})T^{\dagger}_{\mathbf{R_m}} &= \frac{1}{N}\sum_n \mathbf{S}_j(\mathbf{R}_n + \mathbf{R_m})e^{i\mathbf{k}\cdot\mathbf{R}_n} = e^{-i\mathbf{k}\cdot\mathbf{R_m}}\frac{1}{N}\sum_n \mathbf{S}_j(\mathbf{R}_n + \mathbf{R_m})e^{i\mathbf{k}\cdot(\mathbf{R}_n+\mathbf{R}_m)} \\ &= e^{-i\mathbf{k}\cdot\mathbf{R_m}}\mathbf{S}_j(\mathbf{k}). \end{aligned} \tag{3.27}$$

For a transformation $U = \{\varphi|\mathbf{t}_\varphi\}$, we use (3.23) and find

$$\begin{aligned} U\mathbf{S}_j(\mathbf{k})U^{\dagger} &= \frac{1}{N}\sum_n \mathbf{S}_i\big(\varphi(\mathbf{R}_n) + \mathbf{R}_0\big)e^{i\mathbf{k}\cdot\mathbf{R}_n}\mathbf{D}(\varphi) = \frac{1}{N}\sum_n \mathbf{S}_i\big(\varphi(\mathbf{R}_n) + \mathbf{R}_0\big)e^{i\varphi(\mathbf{k})\cdot\varphi(\mathbf{R}_n)}\mathbf{D}(\varphi) \\ &= e^{-i\varphi(\mathbf{k})\cdot\mathbf{R_0}}\frac{1}{N}\sum_n \mathbf{S}_i\big(\varphi(\mathbf{R}_n) + \mathbf{R}_0\big)e^{i\varphi(\mathbf{k})\cdot(\varphi(\mathbf{R}_n)+\mathbf{R}_0)}\mathbf{D}(\varphi) = e^{-i\varphi(\mathbf{k})\cdot\mathbf{R_0}}\mathbf{S}_j(\varphi(\mathbf{k}))\mathbf{D}(\varphi), \end{aligned} \tag{3.28}$$

since $\mathbf{k}\cdot\mathbf{R}_n = \varphi(\mathbf{k})\cdot\varphi(\mathbf{R}_n)$ for any rotation or reflection. Writing (3.28) for the individual spin components gives

$$US_{j\nu}(\mathbf{k})U^{\dagger} = e^{-i\varphi(\mathbf{k})\cdot\mathbf{R_0}}S_{j\mu}(\varphi(\mathbf{k}))D_{\mu\nu}(\varphi), \quad \mu, \nu = x, y, z. \tag{3.29}$$

We note from (3.29) that a spin operator $S_{j\nu}(\mathbf{k})$ is transformed by $U = \{\varphi|\mathbf{t}_\varphi\}$ into a linear combination of spin operators with the same $\mathbf{k}$, *if and only if* φ leaves $\mathbf{k}$ invariant, i.e. if $\varphi(\mathbf{k}) = \mathbf{k}$. From the symmetry elements fulfilling this requirement, we can construct a factor group (modulo lattice translations), called the little group $G_\mathbf{k}$.

3.2.5 Representation theory for $LiNiPO_4$

We begin with the following formal definition.

Definition 1 (Representation of a group) *Let G be a group, V a vector space and $L(V)$ a group of linear operators of V. We say that the operator group $L(V)$ is a representation of the group G with the representation space V, if there exists a homomorphy $\Gamma : G \to L(V)$. If the vector space V has dimension n, then the representation is said to have degree (or dimension) n. If Γ is an isomorph mapping of G on $L(V)$, the representation is said to be faithful.*

Since we are considering single $\mathbf{k}$ structures in $LiNiPO_4$, we are interested in the 12 dimensional complex vector space $V_\mathbf{k}$, spanned by the 12 spin operators

$$\begin{aligned} &S_{1x}(\mathbf{k}),\ S_{1y}(\mathbf{k}),\ S_{1z}(\mathbf{k}),\ S_{2x}(\mathbf{k}),\ S_{2y}(\mathbf{k}),\ S_{2z}(\mathbf{k}),\\ &S_{3x}(\mathbf{k}),\ S_{3y}(\mathbf{k}),\ S_{3z}(\mathbf{k}),\ S_{4x}(\mathbf{k}),\ S_{4y}(\mathbf{k}),\ S_{4z}(\mathbf{k}). \end{aligned} \tag{3.30}$$

Once a basis in $V_\mathbf{k}$ has been chosen, all linear operators on $V_\mathbf{k}$ can be written as 12×12 matrices. One would think that the 12 vectors

$$|1\rangle = S_{1x}(\mathbf{k}), \quad |2\rangle = S_{1y}(\mathbf{k}), \quad |3\rangle = S_{1z}(\mathbf{k}), \tag{3.31}$$
$$|4\rangle = S_{2x}(\mathbf{k}), \quad |5\rangle = S_{2y}(\mathbf{k}), \quad |6\rangle = S_{2z}(\mathbf{k}), \tag{3.32}$$
$$|7\rangle = S_{3x}(\mathbf{k}), \quad |8\rangle = S_{3y}(\mathbf{k}), \quad |9\rangle = S_{3z}(\mathbf{k}), \tag{3.33}$$
$$|10\rangle = S_{4x}(\mathbf{k}), \quad |11\rangle = S_{4y}(\mathbf{k}), \quad |12\rangle = S_{4z}(\mathbf{k}), \tag{3.34}$$

is the best choice of basis, but as we shall soon see this is often not the case. Suppose we have a group[5] G and a group representation $\Gamma : G \to \mathcal{L}(V_\mathbf{k})$ with the representation space $V_\mathbf{k}$. Here $\mathcal{L}(V_\mathbf{k})$ is the space of linear operators on $V_\mathbf{k}$. With an arbitrary basis, $\{|1\rangle\text{-}|12\rangle\}$, the matrix representation for the group elements, $g \in G$, are written as

$$\mathbf{\Gamma}(g) = \begin{pmatrix} a_{11} & a_{12} & a_{13} & \dots & a_{1,12} \\ a_{21} & a_{22} & a_{23} & \dots & a_{2,12} \\ a_{31} & a_{32} & a_{33} & \dots & a_{3,12} \\ a_{41} & a_{42} & a_{43} & \dots & a_{4,12} \\ a_{51} & a_{52} & a_{53} & \dots & a_{5,12} \\ a_{61} & a_{62} & a_{63} & \dots & a_{6,12} \\ a_{71} & a_{72} & a_{73} & \dots & a_{7,12} \\ a_{81} & a_{82} & a_{83} & \dots & a_{8,12} \\ a_{91} & a_{92} & a_{93} & \dots & a_{9,12} \\ a_{10,1} & a_{10,2} & a_{10,3} & \dots & a_{10,12} \\ a_{11,1} & a_{11,2} & a_{11,3} & \dots & a_{11,12} \\ a_{12,1} & a_{12,2} & a_{12,3} & \dots & a_{12,12} \end{pmatrix}. \tag{3.35}$$

If we now were to change the basis in $V_\mathbf{k}$, the 12×12 matrices, $\mathbf{\Gamma}(g)$, representing the linear operators, $\Gamma(g)$, would also change. It is sometimes possible to find especially suited basis vectors, $\{|1'\rangle\text{-}|12'\rangle\}$, so the matrices in the "new" basis are written on the same block form for all the group elements $g \in G$. For instance, the

[5] Here G is a non-specified group. Later on we shall use the little group, $G_\mathbf{k}$, as G.

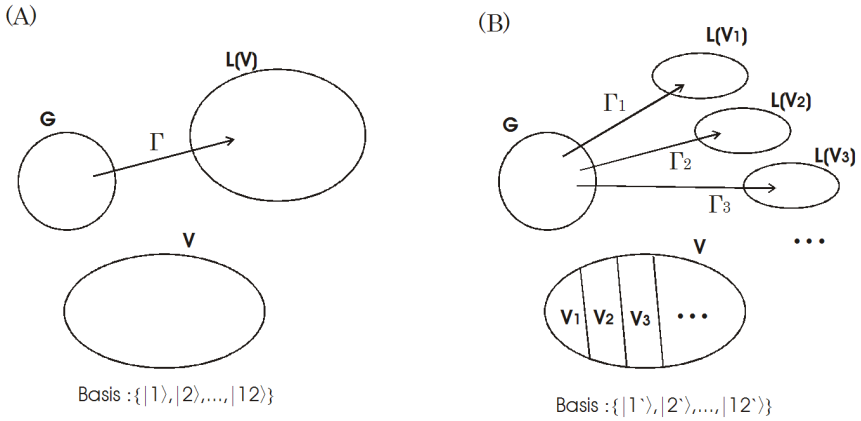

Figure 3.2: (A) Matrix representation Γ of a group G when choosing an arbitrary basis for a vector space. Here a group element $g \in G$ is represented by a 12×12 matrix, $\Gamma(g)$, in the operator space $L(V)$. (B) For a suitable choice of basis in V, the representation is reduced into simpler representations. For instance, in the subspace V_1, the group elements $g \in G$ will be represented by a $n_1 \times n_1$ matrix, $\Gamma_1(g)$, where $n_1 < 12$. The irreducible representations we are considering in $LiNiPO_4$ are one dimensional, so here $n_1 = 1$, and the group elements are represented by complex numbers.

matrix representations could perhaps be written as

$$\mathbf{\Gamma}(g) = \begin{pmatrix} a_{11} & a_{12} & a_{13} & \dots & a_{1,12} \\ a_{21} & a_{22} & a_{23} & \dots & a_{2,12} \\ a_{31} & a_{32} & a_{33} & \dots & a_{3,12} \\ a_{41} & a_{42} & a_{43} & \dots & a_{4,12} \\ a_{51} & a_{52} & a_{53} & \dots & a_{5,12} \\ a_{61} & a_{62} & a_{63} & \dots & a_{6,12} \\ a_{71} & a_{72} & a_{73} & \dots & a_{7,12} \\ a_{81} & a_{82} & a_{83} & \dots & a_{8,12} \\ a_{91} & a_{92} & a_{93} & \dots & a_{9,12} \\ a_{10,1} & a_{10,2} & a_{10,3} & \dots & a_{10,12} \\ a_{11,1} & a_{11,2} & a_{11,3} & \dots & a_{11,12} \\ a_{12,1} & a_{12,2} & a_{12,3} & \dots & a_{12,12} \end{pmatrix} \xrightarrow{\text{basis change}} \begin{pmatrix} b_{11} & b_{12} & 0 & 0 & 0 & 0 & \dots & 0 \\ b_{21} & b_{22} & 0 & 0 & 0 & 0 & \dots & 0 \\ 0 & 0 & b_{33} & b_{34} & b_{35} & 0 & \dots & 0 \\ 0 & 0 & b_{43} & b_{44} & b_{45} & 0 & \dots & 0 \\ 0 & 0 & b_{53} & b_{54} & b_{55} & 0 & \dots & 0 \\ 0 & 0 & 0 & 0 & 0 & b_{66} & \dots & 0 \\ & & & & \ddots & & & \end{pmatrix}, \quad (3.36)$$

for all $g \in G$. If this can be done we say that the representation Γ is reducible, and that it has been reduced by the change of basis. The vector space itself is divided into subspaces, $V_{\mathbf{k}} = V_1 \oplus V_2 \oplus \dots$, where $V_1 \subseteq V_{\mathbf{k}}$ is spanned by the basis vectors $\{|1'\rangle, |2'\rangle\}$ connected with the first "block", $V_2 \subseteq V_{\mathbf{k}}$ is spanned by the basis vectors $\{|3'\rangle, |4'\rangle, |5'\rangle\}$ connected with the second "block", and so on. In this particular example, a symmetry element $g \in G$ is represented by a 2×2 matrix

$$\Gamma_1(g) = \begin{pmatrix} b_{11} & b_{12} \\ b_{21} & b_{22} \end{pmatrix} \in \mathcal{L}(V_1), \quad (3.37)$$

in the two-dimensional subspace V_1, while g is represented by a 3×3 matrix

$$\Gamma_2(g) = \begin{pmatrix} b_{33} & b_{34} & b_{35} \\ b_{43} & b_{44} & b_{45} \\ b_{53} & b_{54} & b_{55} \end{pmatrix} \in \mathcal{L}(V_2), \quad (3.38)$$

in the 3 dimensional subspace V_2. By this procedure, the large representation, Γ, is reduced to a number of smaller representations, Γ_j, and we write

$$\Gamma = \Gamma_1 + \Gamma_2 + \dots \quad (3.39)$$

For at least one basis in $V_{\mathbf{k}}$, the representation, $\mathbf{\Gamma}(g)$, cannot be reduced further, no matter which other basis is used. When this happens, the subspaces $V_1, V_2, \ldots$ are said to be irreducible subspaces of $V_{\mathbf{k}}$, the representations $\Gamma_1, \Gamma_2, \ldots$ to be irreducible representations of the group G, and the basis vectors spanning the irreducible vector spaces V_j are called irreducible basis vectors.

From the formalism it is clear that vectors from a given irreducible subspace V_j are transformed into the same subspace V_j by all $g \in G$. In particular, when V_j is a one-dimensional irreducible subspace, any vector $v \in V_j$ will be transformed into $\beta_g v$ by $g \in G$, where $\beta_g = e^{i\varphi_g}$ is simply a phase factor. In this case $\beta_g = e^{i\varphi_g}$ is obviously a one-dimensional representation of g in V_j.

A few group theoretical theorems

For any given group representation, Γ, of a group G, and for any group element $g \in G$, we define the character, $\chi^{\Gamma}(g)$, as the trace of the matrix representation $\mathbf{\Gamma}(g)$ of $\Gamma(g)$, regardless of the choice of basis. Since the trace of the matrix representations are invariant under change of basis, the definition of the character $\chi^{\Gamma}(g)$ is unambiguous.

We state without proof the following group theoretical theorems for finite groups.

Theorem 2 *The number, $N(G)$, of non-equivalent irreducible representations of a group G equals the number of conjugation classes in G.*

Theorem 3 *Let d_ν be the dimension of the irreducible representation Γ_ν of a group G. Then*

$$\sum_{\nu=1}^{N(G)} d_\nu^2 = |G|. \tag{3.40}$$

Here the sum runs over all $N(G)$ non-equivalent irreducible representations of G.

Theorem 4 *Let Γ be a given representation of a group G. Then Γ can be written as*

$$\Gamma = \sum_{\nu=1}^{N(G)} a_\nu \Gamma_\nu, \tag{3.41}$$

where Γ_ν are the non-equivalent irreducible representations of G. The number of times, a_ν, each irreducible representation appears in the representation (3.41), is given by

$$a_\nu = \frac{1}{|G|} \sum_{g \in G} \chi^{\Gamma}(g) \chi^{\Gamma_\nu}(g)^*. \tag{3.42}$$

Theorem 4 requires the character table of both the representation Γ and all of the irreducible representations Γ_ν. If these are known, we can find the irreducible basis vectors, A^ν, for a given irreducible representation Γ_ν by projecting [38, 41] test functions $\psi \in V_{\mathbf{k}}$ into the irreducible subspace $V_\nu \in V_{\mathbf{k}}$, by

$$A_\nu^i = \sum_g \Gamma^*_{\nu,ii}(g) g(\psi), \quad i = 1, \ldots, d_\nu. \tag{3.43}$$

If there are more than one equivalent irreducible subspace in $V_{\mathbf{k}}$, the projecting procedure has to be done with more than one test function.

3.3 Irreducible representations

3.3.1 Example 1: The group T of integer lattice translations

The transformation rule (3.27) show that the operator $T_{\mathbf{R}_0}$, where $\mathbf{R}_0$ is an integer lattice translation, is represented by

$$\Gamma_{\mathbf{k}}(\mathbf{R}_0) = e^{-i\mathbf{k}\cdot\mathbf{R}_0}, \tag{3.44}$$

within the vector space $V_{\mathbf{k}}$. That $\Gamma_{\mathbf{k}}$ is a homomorphy can easily be seen by

$$\Gamma_{\mathbf{k}}(\mathbf{R}_n + \mathbf{R}_m) = e^{-i\mathbf{k}\cdot(\mathbf{R}_n+\mathbf{R}_m)} = e^{-i\mathbf{k}\cdot\mathbf{R}_n} e^{-i\mathbf{k}\cdot\mathbf{R}_m} = \Gamma_{\mathbf{k}}(\mathbf{R}_n)\Gamma_{\mathbf{k}}(\mathbf{R}_m). \tag{3.45}$$

Since the representation is one-dimensional it cannot be reduced any further, and $\Gamma_{\mathbf{k}}$ is consequently an irreducible representation of the group G_T of lattice translations.

3.3.2 Example 2: Irreducible representation and basis vectors for $\mathbf{k} = (0, k_y, 0)$

It has been establish experimentally [9] that the zero field magnetic structure in the incommensurate phase has a modulation vector $\mathbf{k} = (0, k_y, 0)$ in the first Brillouin zone. This is seen for instance in figure 2.3, chapter 2. As we have already argued, the transformation properties of a single $\mathbf{k}$ structure is mirrored by the transformation properties of the 12 spin operators $S_{j\mu}(\mathbf{k}) \in V_{\mathbf{k}}$. In section 3.3.1 we have explained that all vectors in $V_{\mathbf{k}}$ are irreducible basis vectors of the lattice translation group, but we have yet to examine the other symmetries of the system. From (3.29) we see that only symmetries leaving $\mathbf{k}$ invariant transform the spin operators within $V_{\mathbf{k}}$. For instance, using table 3.1 and (3.29), we see that

$$2'_x S_{3z}(\mathbf{k}) 2'^{\dagger}_x = -e^{i\mathbf{k}\cdot\mathbf{R}_0} S_{4z}(-\mathbf{k}) \in V_{-\mathbf{k}}, \quad \mathbf{R}_0 = (1, -1, 0), \tag{3.46}$$

because $2'_x(\mathbf{k}) = -\mathbf{k}$ when $\mathbf{k} = (0, k_y, 0)$. Wanting to stay within the vector space $V_{\mathbf{k}}$, we therefore restrict ourselves to symmetries that leave $\mathbf{k}$ invariant. These elements constitute a group, $G_{\mathbf{k}} \otimes T$, where $G_{\mathbf{k}} = \{\, g \in G/T \mid g(\mathbf{k}) = \mathbf{k}\}$ is a factor group known as the little group of $\mathbf{k}$. For $\mathbf{k} = (0, k_y, 0)$, the little group is

$$G_{\mathbf{k}} = \{1, 2'_y, m'_{xy}, m'_{yz}\}. \tag{3.47}$$

We now look for the irreducible basis vectors in $V_{\mathbf{k}}$ for the little group $G_{\mathbf{k}}$. Since $G_{\mathbf{k}}$ is Abelian, the number of conjugation classes equals the group order, $|G_{\mathbf{k}}| = 4$. Using this in theorem 2, we find that the number of non-equivalent irreducible representations is 4. Furthermore, from theorem 3, the dimension of the irreducible representations must fulfil

$$d_1^2 + d_2^2 + d_3^2 + d_4^2 = |G_{\mathbf{k}}| = 4. \tag{3.48}$$

This is only possible if $d_1 = d_2 = d_3 = d_4 = 1$. Therefore the irreducible representations of $G_{\mathbf{k}}$ are all one-dimensional, and the irreducible basis vectors are vectors $v \in V_{\mathbf{k}}$, where

$$1v1^{\dagger} = v, \quad 2'_y v 2'^{\dagger}_y = \beta_1 v, \quad m'_{xy} v m'^{\dagger}_{xy} = \beta_2 v, \quad m'_{yz} v m'^{\dagger}_{yz} = \beta_3 v. \tag{3.49}$$

Here β_1, β_2 and β_3 are complex phase factors representing $2'_y$, m'_{xy} and m'_{yz} in the irreducible subspace spanned by v.

From table 3.1 we see that x, y and z spin components are not mixed by the group elements. Naturally this is also reflected in the irreducible basis vectors. So we search for linear combinations

$$\begin{aligned} v_x &= x_1 S_{1x}(\mathbf{k}) + x_2 S_{2x}(\mathbf{k}) + x_3 S_{3x}(\mathbf{k}) + x_4 S_{4x}(\mathbf{k}), \\ v_y &= y_1 S_{1y}(\mathbf{k}) + y_2 S_{2y}(\mathbf{k}) + y_3 S_{3y}(\mathbf{k}) + y_4 S_{4y}(\mathbf{k}), \\ v_z &= z_1 S_{1z}(\mathbf{k}) + z_2 S_{2z}(\mathbf{k}) + z_3 S_{3z}(\mathbf{k}) + z_4 S_{4z}(\mathbf{k}), \end{aligned} \tag{3.50}$$

transforming according to (3.49). Let us first examine the case of v_x.

- For the symmetry $2'_y$, we have from (3.49), that

$$2'_y v_x 2'^{\dagger}_y = \beta_1 v_x = \beta_1 x_1 S_{1x}(\mathbf{k}) + \beta_1 x_2 S_{2x}(\mathbf{k}) + \beta_1 x_3 S_{3x}(\mathbf{k}) + \beta_1 x_4 S_{4x}(\mathbf{k}). \tag{3.51}$$

  Furthermore, from table 3.1 and (3.29)

$$2'_y v_x 2'^{\dagger}_y = -x_1 S_{3x}(\mathbf{k}) - x_2 S_{4x}(\mathbf{k}) - x_3 e^{-i2\pi k_y} S_{1x}(\mathbf{k}) - x_4 e^{-i2\pi k_y} S_{2x}(\mathbf{k}). \tag{3.52}$$

Comparing (3.51) and (3.52) we find that

$$\beta_1 x_1 = -x_3 e^{-i2\pi k_y}, \quad \beta_1 x_2 = -x_4 e^{-i2\pi k_y}, \quad \beta_1 x_3 = -x_1, \quad \beta_1 x_4 = -x_2, \tag{3.53}$$

giving[6]

$$\beta_1 x_1 = -\beta_1^2 x_3 = -x_3 e^{-i2\pi k_y} \Rightarrow \beta_1^2 = e^{-i2\pi k_y} \Rightarrow \beta_1 = \pm e^{-i\pi k_y}. \tag{3.54}$$

- For the symmetry m'_{xy}, we have

$$m'_{xy} v_x m'^{\dagger}_{xy} = \beta_2 v_x = \beta_2 x_1 S_{1x}(\mathbf{k}) + \beta_2 x_2 S_{2x}(\mathbf{k}) + \beta_2 x_3 S_{3x}(\mathbf{k}) + \beta_2 x_4 S_{4x}(\mathbf{k}). \tag{3.55}$$

and

$$m'_{xy} v_x m'^{\dagger}_{xy} = -x_1 S_{2x}(\mathbf{k}) - x_2 S_{1x}(\mathbf{k}) - x_3 S_{4x}(\mathbf{k}) - x_4 S_{3x}(\mathbf{k}). \tag{3.56}$$

Therefore

$$\beta_2 x_1 = -x_2, \quad \beta_2 x_2 = -x_1, \quad \beta_2 x_3 = -x_4, \quad \beta_2 x_4 = -x_3, \tag{3.57}$$

and

$$\beta_2 x_1 = -\beta_2^2 x_2 = -x_2 \Rightarrow \beta_2^2 = 1 \Rightarrow \beta_2 = \pm 1. \tag{3.58}$$

- For m'_{yz}

$$m'_{yz} v_x m'^{\dagger}_{yz} = \beta_3 v_x = \beta_3 x_1 S_{1x}(\mathbf{k}) + \beta_3 x_2 S_{2x}(\mathbf{k}) + \beta_3 x_3 S_{3x}(\mathbf{k}) + \beta_3 x_4 S_{4x}(\mathbf{k}). \tag{3.59}$$

and

$$m'_{yz} v_x m'^{\dagger}_{yz} = x_1 S_{4x}(\mathbf{k}) + x_2 S_{3x}(\mathbf{k}) + x_3 e^{-i2\pi k_y} S_{2x}(\mathbf{k}) + x_4 e^{-i2\pi k_y} S_{1x}(\mathbf{k}). \tag{3.60}$$

We find that

$$\beta_3 x_1 = x_4 e^{-i2\pi k_y}, \quad \beta_3 x_2 = x_3 e^{-i2\pi k_y}, \quad \beta_3 x_3 = x_2, \quad \beta_3 x_4 = x_1, \tag{3.61}$$

giving

$$\beta_3 x_1 = \beta_3^2 x_4 = x_4 e^{-i2\pi k_y} \Rightarrow \beta_3^2 = e^{-i2\pi k_y} \Rightarrow \beta_3 = \pm e^{-i\pi k_y}. \tag{3.62}$$

All in all, we have found that

$$\beta_1 = \sigma_1 \beta, \quad \beta_2 = \sigma_2, \quad \beta_3 = \sigma_3 \beta, \tag{3.63}$$

where

$$\sigma_\nu = \pm 1, \quad \beta = e^{-i\pi k_y}. \tag{3.64}$$

From (3.53), (3.57) and (3.61) we have the further requirement

$$x_1 = \beta_3 x_4 = -\beta_2 \beta_3 x_3 = \beta_1^{-1} \beta_2 \beta_3 x_1 \Rightarrow \beta_1^{-1} \beta_2 \beta_3 = 1, \tag{3.65}$$

which is equivalent to the following condition

$$\sigma_1 \sigma_2 \sigma_3 = 1 \Rightarrow (\sigma_1, \sigma_2, \sigma_3) = \begin{cases} (1,1,1) \\ (-1,1,-1) \\ (1,-1,-1) \\ (-1,-1,1) \end{cases}. \tag{3.66}$$

We have now determined all four irreducible representations Γ_1-Γ_4 of $G_{\mathbf{k}}$, with $\mathbf{k} = (0, k_y, 0)$. Their character table is given in table 3.3. We have also included the character table of the 12 dimensional representation, Γ, found using the basis

$$\begin{aligned} |1\rangle &= S_{1x}(\mathbf{k}), & |2\rangle &= S_{1y}(\mathbf{k}), & |3\rangle &= S_{1z}(\mathbf{k}), \\ |4\rangle &= S_{2x}(\mathbf{k}), & |5\rangle &= S_{2y}(\mathbf{k}), & |6\rangle &= S_{2z}(\mathbf{k}), \\ |7\rangle &= S_{3x}(\mathbf{k}), & |8\rangle &= S_{3y}(\mathbf{k}), & |9\rangle &= S_{3z}(\mathbf{k}), \\ |10\rangle &= S_{4x}(\mathbf{k}), & |11\rangle &= S_{4y}(\mathbf{k}), & |12\rangle &= S_{4z}(\mathbf{k}). \end{aligned}$$

[6] One may think that the result (3.54) is immediately given from the transformation rule (3.27). However, (3.27) is valid for integer lattice translations only and cannot be applied here.

$G_{\mathbf{k}}$	1	$2'_y$	m'_{xy}	m'_{yz}	a_ν	basis vectors
Γ_1	1	β	1	β	3	A_x, G_y, C_z
Γ_2	1	-β	1	-β	3	G_x, A_y, F_z
Γ_3	1	β	-1	-β	3	C_x, F_y, A_z
Γ_4	1	-β	-1	β	3	F_x, C_y, G_z
Γ	12	0	0	0		

Table 3.3: Character table and basis functions for the irreducible representations of $G_{\mathbf{k}}$, with $\mathbf{k} = (0, k_y, 0)$. Here, the constant $\beta = e^{-i\pi k_y}$. The character table for the reducible representation Γ is discussed in the text. The number of times a_ν the irreducible representations appear in $V_{\mathbf{k}}$ is calculated by use of (3.42).

The characters, $\chi^{\Gamma}(g)$, of Γ are easily deduced from table 3.1, by noting how many of the spin operators, $S_{j\mu}(\mathbf{k})$, are left invariant under the symmetry operations $g \in G_{\mathbf{k}}$. Furthermore, in table 3.3, we give the irreducible basis vectors to the irreducible representations[7]. These can be calculated in the following two ways.

Method 1. Constructing the irreducible basis vectors

From (3.53), (3.57) and (3.61) we have that

$$x_2 = -\beta_2 x_1, \quad x_3 = -\beta_1^{-1} x_1, \quad x_4 = \beta_3^{-1} x_1. \tag{3.67}$$

For the irreducible representation Γ_1 we have, from table 3.3, that

$$\beta_1 = \beta, \quad \beta_2 = 1, \quad \beta_3 = \beta, \tag{3.68}$$

with $\beta = e^{-i\pi k_y}$. Combining (3.67) and (3.68) gives

$$x_1 = 1, \quad x_2 = -1, \quad x_3 = -\beta^{-1}, \quad x_4 = \beta^{-1}. \tag{3.69}$$

An irreducible basis vector for Γ_1 can now be constructed by inserting (3.69) into the expression for v_x, giving

$$\Gamma_1: \quad A_x(\mathbf{k}) \equiv S_{1x}(\mathbf{k}) - S_{2x}(\mathbf{k}) - \beta^{-1} S_{3x}(\mathbf{k}) + \beta^{-1} S_{4x}(\mathbf{k}), \tag{3.70}$$

where $\beta^{-1} = e^{i\pi k_y}$. Similarly, for the other irreducible representations

$$\begin{aligned} \Gamma_2: \quad & G_x(\mathbf{k}) \equiv S_{1x}(\mathbf{k}) - S_{2x}(\mathbf{k}) + \beta^{-1} S_{3x}(\mathbf{k}) - \beta^{-1} S_{4x}(\mathbf{k}), \\ \Gamma_3: \quad & C_x(\mathbf{k}) \equiv S_{1x}(\mathbf{k}) + S_{2x}(\mathbf{k}) - \beta^{-1} S_{3x}(\mathbf{k}) - \beta^{-1} S_{4x}(\mathbf{k}), \\ \Gamma_4: \quad & F_x(\mathbf{k}) \equiv S_{1x}(\mathbf{k}) + S_{2x}(\mathbf{k}) + \beta^{-1} S_{3x}(\mathbf{k}) + \beta^{-1} S_{4x}(\mathbf{k}). \end{aligned} \tag{3.71}$$

Method 2. Using group theoretical theorems

Since the character table for the irreducible representations has been determined, we do not need to go through the same calculations for v_y and v_z. Using table 3.1 and (3.41) with

$$\psi = S_{1y}(\mathbf{k}), \tag{3.72}$$

[7] We shall return to the physical meaning of these basis vectors, or operators, in section 3.4.

as trial function, we find the following basis vectors for the irreducible representations.

$$\Gamma_1: \quad \sum_{g\in G_{\mathbf{k}}} \Gamma_1^*(g) g S_{1y}(\mathbf{k}) g^\dagger = S_{1y}(\mathbf{k}) - S_{2y}(\mathbf{k}) + \beta^{-1} S_{3y}(\mathbf{k}) - \beta^{-1} S_{4y}(\mathbf{k}) \equiv G_y, \tag{3.73}$$

$$\Gamma_2: \quad \sum_{g\in G_{\mathbf{k}}} \Gamma_2^*(g) g S_{1y}(\mathbf{k}) g^\dagger = S_{1y}(\mathbf{k}) - S_{2y}(\mathbf{k}) - \beta^{-1} S_{3y}(\mathbf{k}) + \beta^{-1} S_{4y}(\mathbf{k}) \equiv A_y, \tag{3.74}$$

$$\Gamma_3: \quad \sum_{g\in G_{\mathbf{k}}} \Gamma_3^*(g) g S_{1y}(\mathbf{k}) g^\dagger = S_{1y}(\mathbf{k}) + S_{2y}(\mathbf{k}) + \beta^{-1} S_{3y}(\mathbf{k}) + \beta^{-1} S_{4y}(\mathbf{k}) \equiv F_y, \tag{3.75}$$

$$\Gamma_4: \quad \sum_{g\in G_{\mathbf{k}}} \Gamma_4^*(g) g S_{1y}(\mathbf{k}) g^\dagger = S_{1y}(\mathbf{k}) + S_{2y}(\mathbf{k}) - \beta^{-1} S_{3y}(\mathbf{k}) - \beta^{-1} S_{4y}(\mathbf{k}) \equiv C_y. \tag{3.76}$$

Similarly, for the trial function $\psi = S_{1z}(\mathbf{k})$, we get

$$\Gamma_1: \quad \sum_{g\in G_{\mathbf{k}}} \Gamma_1^*(g) g S_{1z}(\mathbf{k}) g^\dagger = S_{1z}(\mathbf{k}) + S_{2z}(\mathbf{k}) - \beta^{-1} S_{3z}(\mathbf{k}) - \beta^{-1} S_{4z}(\mathbf{k}) \equiv C_z, \tag{3.77}$$

$$\Gamma_2: \quad \sum_{g\in G_{\mathbf{k}}} \Gamma_2^*(g) g S_{1z}(\mathbf{k}) g^\dagger = S_{1z}(\mathbf{k}) + S_{2z}(\mathbf{k}) + \beta^{-1} S_{3z}(\mathbf{k}) + \beta^{-1} S_{4z}(\mathbf{k}) \equiv F_z, \tag{3.78}$$

$$\Gamma_3: \quad \sum_{g\in G_{\mathbf{k}}} \Gamma_3^*(g) g S_{1z}(\mathbf{k}) g^\dagger = S_{1z}(\mathbf{k}) - S_{2z}(\mathbf{k}) - \beta^{-1} S_{3z}(\mathbf{k}) + \beta^{-1} S_{4z}(\mathbf{k}) \equiv A_z, \tag{3.79}$$

$$\Gamma_4: \quad \sum_{g\in G_{\mathbf{k}}} \Gamma_4^*(g) g S_{1z}(\mathbf{k}) g^\dagger = S_{1z}(\mathbf{k}) - S_{2z}(\mathbf{k}) + \beta^{-1} S_{3z}(\mathbf{k}) - \beta^{-1} S_{4z}(\mathbf{k}) \equiv G_z. \tag{3.80}$$

3.3.3 Example 3: Irreducible representation and basis vectors in the commensurate phase, $\mathbf{k} = 0$

G_0	1	$2'_x$	$2'_y$	$2'_z$	$\bar{1}$	m'_{xy}	m'_{xz}	m'_{yz}	a_ν	basis vectors
Γ_1	1	1	1	1	1	1	1	1	1	G_y
Γ_2	1	1	-1	-1	1	-1	-1	1	2	F_x, G_z
Γ_3	1	-1	1	-1	1	-1	1	-1	1	F_y
Γ_4	1	-1	-1	1	1	1	-1	-1	2	G_x, F_z
Γ_5	1	1	1	1	-1	-1	-1	-1	2	C_x, A_z
Γ_6	1	1	-1	-1	-1	1	1	-1	1	A_y
Γ_7	1	-1	1	-1	-1	1	-1	1	2	A_x, C_z
Γ_8	1	-1	-1	1	-1	-1	1	1	1	C_y
Γ	12	0	0	0	0	0	-4	0		

Table 3.4: Irreducible representations of the point group G_0, relevant for the zero-field commensurate phase.

For $\mathbf{k} = 0$, the appropriate spin operators, $S_{j\mu}(0) \cong S_{j\mu}$, span a 12 dimensional vector space V_0, and the little group G_0 equals the full factor group $G/T \simeq D_{2h}$. Applying the same methods as in section 3.3.2, it is straightforward to find the irreducible representations and irreducible basis vectors. Here we will just give the final result. We find that there are 8 one-dimensional irreducible representations of G_0, with character table given in table 3.4, and where the irreducible basis vectors are

$$\begin{aligned} A_\mu &= S_{1\mu} - S_{2\mu} - S_{3\mu} + S_{4\mu}, \quad \mu = x, y, z, \\ C_\mu &= S_{1\mu} + S_{2\mu} - S_{3\mu} - S_{4\mu}, \quad \mu = x, y, z, \\ F_\mu &= S_{1\mu} + S_{2\mu} + S_{3\mu} + S_{4\mu}, \quad \mu = x, y, z, \\ G_\mu &= S_{1\mu} - S_{2\mu} + S_{3\mu} - S_{4\mu}, \quad \mu = x, y, z. \end{aligned} \tag{3.81}$$

In the table, we also give the characters for the representation, Γ, found using $\{S_{\jmath\mu} | j = 1, 2, 3, 4, \ \mu = x, y, z\}$ as basis. The characters of Γ are deduced as before, noting that a spin operator changing sign under a transformation gives a contribution to the trace (and therefore to the character) of -1.

3.3.4 Symmetry constraints on the spin Hamiltonian

As we have discussed in chapter 2, the system is situated in a ground state determined by the crystal field. Magnetic interactions work within the vector space of this ground state. The operator describing the relevant magnetic interactions within this Hilbert space is called the spin Hamiltonian. We have already, in section 2.3, presented some of the potential operators in the spin Hamiltonian. The discussed operators were connected to exchange-, single ion anisotropy and DM interactions, and were all quadratic in the spins.

Now, let us instead write the quadratic terms of the spin Hamiltonian using the irreducible basis vectors A_μ, G_μ, C_μ and F_μ. This is not a problem, since any given single ion spin operator can be expressed as a sum of irreducible basis vectors. So, we consider a spin Hamiltonian of the form

$$\mathcal{H}_s = \sum_{\mathbf{q}} \sum_{\gamma_1, \gamma_2} \xi_{12}(\mathbf{q}) \gamma_1(\mathbf{q}) \gamma_2(\mathbf{q})^\dagger, \tag{3.82}$$

where $\gamma_1 = A_\mu, G_\mu, C_\mu, F_\mu$, $\gamma_2 = A_\nu, G_\nu, C_\nu, F_\nu$ and $\xi_{12}(\mathbf{q})$ is a coupling parameter. Now, we require that the entries in the Hamiltonian are invariant under all the symmetry operations of $LiNiPO_4$. Assume that $\gamma_1(\mathbf{q})$ belongs to the irreducible representation Γ_i and that $\gamma_2(\mathbf{q})$ belong to Γ_j. Looking at the character table of the irreducible representations, we see that if $\Gamma_i \neq \Gamma_j$, there will exist a group element g where

$$g\gamma_i(\mathbf{q})g^\dagger g\gamma_j(\mathbf{q})^\dagger g^\dagger \neq \gamma_i(\mathbf{q})\gamma_j(\mathbf{q})^\dagger. \tag{3.83}$$

In fact, it is obvious that the product $\gamma_1(\mathbf{q})\gamma_2(\mathbf{q})^\dagger$ is invariant under all symmetry elements *if and only if* $\Gamma_i = \Gamma_j$.

Let us illustrate this by an example. Consider for instance the two terms, $A_x G_y^\dagger$ for $\mathbf{q} = 0$, and, $A_x(\mathbf{q})G_y(\mathbf{q})^\dagger$ for $\mathbf{q} = (0, q, 0)$. From table 3.81 we see that $2'_x A_x 2_x^\dagger = -A_x$ while[8] $2'_x G_y^\dagger 2_x'^\dagger = G_y^\dagger$. Therefore

$$2'_x A_x G_y^\dagger 2_x'^\dagger = 2'_x A_x 2_x^\dagger 2'_x G_y^\dagger 2_x'^\dagger = -A_x G_y^\dagger, \tag{3.84}$$

is not invariant under $2'_x$ and the term is not allowed in the Hamiltonian for $\mathbf{q} = 0$. On the other hand, from table 3.3 we see that $A_x(\mathbf{q})$ and $G_y(\mathbf{q})$ both belong to the same irreducible representation. Therefore, for all little group elements (the little group being the appropriate symmetries for the magnetic system), we have that

$$gA_x(\mathbf{q})G_y(\mathbf{q})^\dagger g^\dagger = gA_x(\mathbf{q})g^\dagger gG_y(\mathbf{q})^\dagger g^\dagger = \beta'\beta'^* A_x(\mathbf{q})G_y(\mathbf{q})^\dagger = A_x(\mathbf{q})G_y(\mathbf{q})^\dagger, \quad \beta' = 1, \beta, \tag{3.85}$$

showing that $A_x(\mathbf{q})G_y(\mathbf{q})^\dagger$ is invariant and allowed in the Hamiltonian for $\mathbf{q} = (0, q, 0)$.

All in all, we have argued that a product of two irreducible basis vectors is allowed in the spin Hamiltonian if and only if they belong to the same irreducible representation.

3.4 Irreducible basis vectors and magnetic structures

In the previous section we found the linear combinations of spin operators transforming as simple as possible under the symmetries of $LiNiPO_4$. In group theoretical language we found the irreducible basis vectors for the little group in the vector space of spin operators. At least one of these basis vectors has a non-zero mean value when the system is magnetically ordered, and for each non-zero mean value there is a corresponding magnetic structure. In this section we shall briefly discuss which magnetic structures correspond to non-zero mean values of the various irreducible basis vectors.

3.4.1 Magnetic basis structures in the commensurate phase, $\mathbf{k} = 0$

Taking the (thermal) mean value of the irreducible basis vectors, we have that

$$\begin{aligned}
\langle A_\mu\rangle &= \langle S_{1\mu}\rangle - \langle S_{2\mu}\rangle - \langle S_{3\mu}\rangle + \langle S_{4\mu}\rangle, \quad \mu = x, y, z,\\
\langle C_\mu\rangle &= \langle S_{1\mu}\rangle + \langle S_{2\mu}\rangle - \langle S_{3\mu}\rangle - \langle S_{4\mu}\rangle, \quad \mu = x, y, z,\\
\langle F_\mu\rangle &= \langle S_{1\mu}\rangle + \langle S_{2\mu}\rangle + \langle S_{3\mu}\rangle + \langle S_{4\mu}\rangle, \quad \mu = x, y, z,\\
\langle G_\mu\rangle &= \langle S_{1\mu}\rangle - \langle S_{2\mu}\rangle + \langle S_{3\mu}\rangle - \langle S_{4\mu}\rangle, \quad \mu = x, y, z,
\end{aligned} \tag{3.86}$$

and therefore

$$\begin{aligned}
\langle S_{1\mu}\rangle &= \frac{1}{4}\Big(\langle A_\mu\rangle + \langle C_\mu\rangle + \langle F_\mu\rangle + \langle G_\mu\rangle\Big), \quad \mu = x, y, z,\\
\langle S_{2\mu}\rangle &= \frac{1}{4}\Big(-\langle A_\mu\rangle + \langle C_\mu\rangle + \langle F_\mu\rangle - \langle G_\mu\rangle\Big), \quad \mu = x, y, z,\\
\langle S_{3\mu}\rangle &= \frac{1}{4}\Big(-\langle A_\mu\rangle - \langle C_\mu\rangle + \langle F_\mu\rangle + \langle G_\mu\rangle\Big), \quad \mu = x, y, z,\\
\langle S_{4\mu}\rangle &= \frac{1}{4}\Big(\langle A_\mu\rangle - \langle C_\mu\rangle + \langle F_\mu\rangle - \langle G_\mu\rangle\Big), \quad \mu = x, y, z.
\end{aligned} \tag{3.87}$$

Suppose the system is in a state where $\langle A_x\rangle \neq 0$, and $\langle A_y\rangle = \langle A_z\rangle = \langle C_x\rangle = \ldots = \langle G_z\rangle = 0$. Then, from (3.87), we have that

$$\langle S_{1x}\rangle = \frac{1}{4}\langle A_x\rangle, \quad \langle S_{2x}\rangle = -\frac{1}{4}\langle A_x\rangle, \quad \langle S_{3x}\rangle = -\frac{1}{4}\langle A_x\rangle, \quad \langle S_{4x}\rangle = \frac{1}{4}\langle A_x\rangle. \tag{3.88}$$

[8] We use that $g\gamma^\dagger g^\dagger = (g\gamma g^\dagger)^\dagger = (\beta\gamma)^\dagger = \beta^*\gamma^\dagger$.

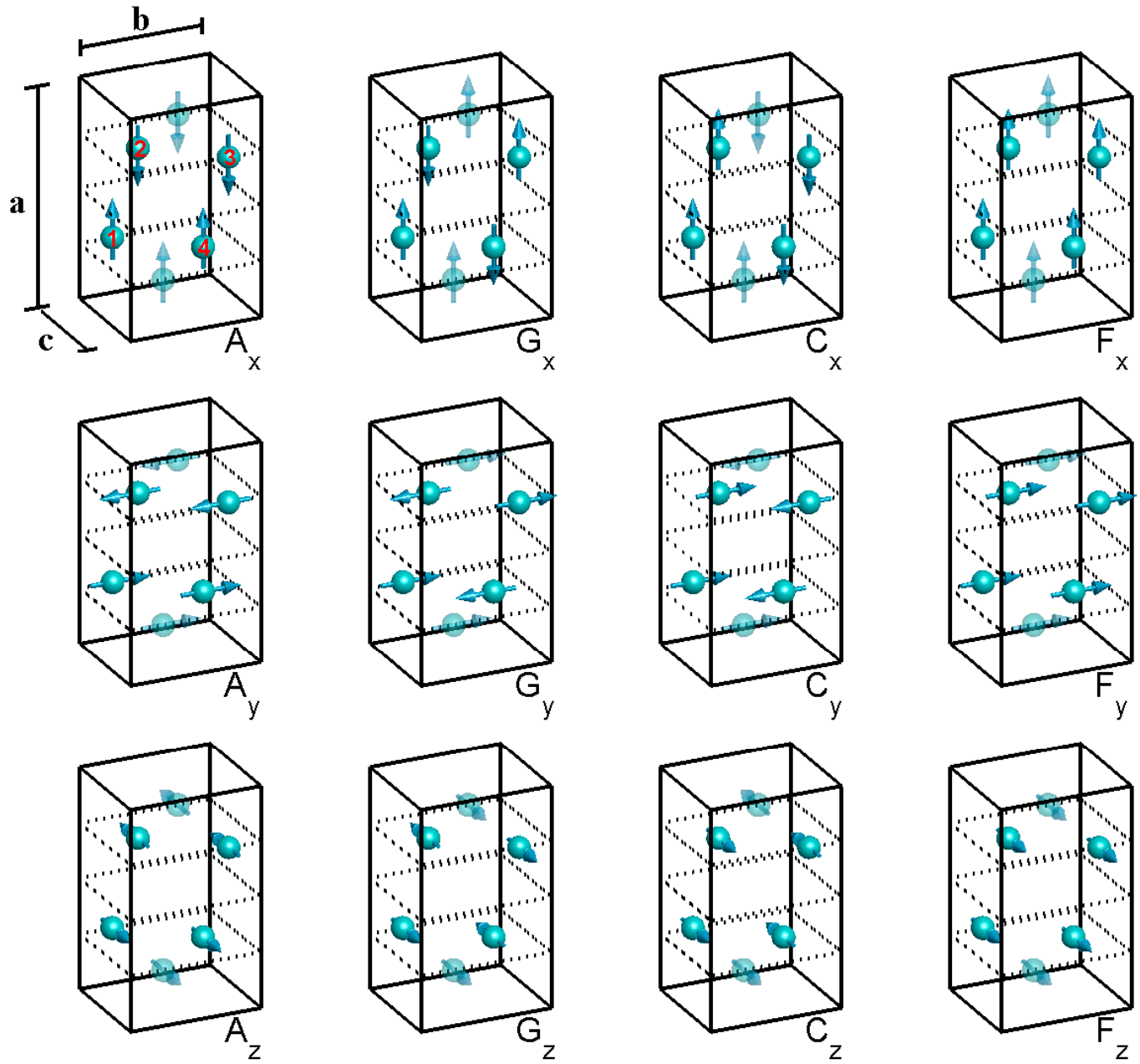

Figure 3.3: The magnetic structures connected to the commensurate A,G,C and F irreducible basis vectors.

Since $\mathbf{k} = 0$, the Fourier and spatial components of the magnetic moments are identical. Therefore (3.88) describes a spatial magnetic structure, which we can call an A_x structure, with the spins (magnetic moments) pointing along the x-axis, and $\langle S_{1x}\rangle = -\langle S_{2x}\rangle = -\langle S_{3x}\rangle = \langle S_{4x}\rangle$. The following spatial magnetic structures correspond to the commensurate A, C, G, F irreducible basis vectors

$$\begin{aligned}
&\langle A_\mu\rangle \neq 0: \quad \langle S_{1\mu}\rangle = -\langle S_{2\mu}\rangle = -\langle S_{3\mu}\rangle = \langle S_{4\mu}\rangle,\\
&\langle C_\mu\rangle \neq 0: \quad \langle S_{1\mu}\rangle = \langle S_{2\mu}\rangle = -\langle S_{3\mu}\rangle = -\langle S_{4\mu}\rangle,\\
&\langle F_\mu\rangle \neq 0: \quad \langle S_{1\mu}\rangle = \langle S_{2\mu}\rangle = \langle S_{3\mu}\rangle = \langle S_{4\mu}\rangle,\\
&\langle G_\mu\rangle \neq 0: \quad \langle S_{1\mu}\rangle = -\langle S_{2\mu}\rangle = \langle S_{3\mu}\rangle = -\langle S_{4\mu}\rangle, \quad \mu = x, y, z,
\end{aligned} \tag{3.89}$$

and are depicted in figure 3.3.

3.4.2 Magnetic basis structures in the incommensurate phase, $\mathbf{k} = (0, k_y, 0)$

For $\mathbf{k} = (0, k_y, 0)$

$$\begin{aligned}
\langle A_\mu(\mathbf{k})\rangle &= \langle S_{1\mu}(\mathbf{k})\rangle - \langle S_{2\mu}(\mathbf{k})\rangle - \beta^{-1}\langle S_{3\mu}(\mathbf{k})\rangle + \beta^{-1}\langle S_{4\mu}(\mathbf{k})\rangle, \quad \mu = x, y, z,\\
\langle C_\mu(\mathbf{k})\rangle &= \langle S_{1\mu}(\mathbf{k})\rangle + \langle S_{2\mu}(\mathbf{k})\rangle - \beta^{-1}\langle S_{3\mu}(\mathbf{k})\rangle - \beta^{-1}\langle S_{4\mu}(\mathbf{k})\rangle, \quad \mu = x, y, z,\\
\langle F_\mu(\mathbf{k})\rangle &= \langle S_{1\mu}(\mathbf{k})\rangle + \langle S_{2\mu}(\mathbf{k})\rangle + \beta^{-1}\langle S_{3\mu}(\mathbf{k})\rangle + \beta^{-1}\langle S_{4\mu}(\mathbf{k})\rangle, \quad \mu = x, y, z,\\
\langle G_\mu\rangle(\mathbf{k}) &= \langle S_{1\mu}(\mathbf{k})\rangle - \langle S_{2\mu}(\mathbf{k})\rangle + \beta^{-1}\langle S_{3\mu}(\mathbf{k})\rangle - \beta^{-1}\langle S_{4\mu}(\mathbf{k})\rangle, \quad \mu = x, y, z,
\end{aligned} \tag{3.90}$$

giving

$$\begin{aligned}
\langle S_{1\mu}(\mathbf{k})\rangle &= \frac{1}{4}\Big(\langle A_\mu(\mathbf{k})\rangle + \langle C_\mu(\mathbf{k})\rangle + \langle F_\mu(\mathbf{k})\rangle + \langle G_\mu(\mathbf{k})\rangle\Big), \quad \mu = x, y, z,\\
\langle S_{2\mu}(\mathbf{k})\rangle &= \frac{1}{4}\Big(-\langle A_\mu(\mathbf{k})\rangle + \langle C_\mu(\mathbf{k})\rangle + \langle F_\mu(\mathbf{k})\rangle - \langle G_\mu(\mathbf{k})\rangle\Big), \quad \mu = x, y, z,\\
\langle S_{3\mu}(\mathbf{k})\rangle &= \frac{\beta}{4}\Big(-\langle A_\mu(\mathbf{k})\rangle - \langle C_\mu(\mathbf{k})\rangle + \langle F_\mu(\mathbf{k})\rangle + \langle G_\mu(\mathbf{k})\rangle\Big), \quad \mu = x, y, z,\\
\langle S_{4\mu}(\mathbf{k})\rangle &= \frac{\beta}{4}\Big(\langle A_\mu(\mathbf{k})\rangle - \langle C_\mu(\mathbf{k})\rangle + \langle F_\mu(\mathbf{k})\rangle - \langle G_\mu(\mathbf{k})\rangle\Big), \quad \mu = x, y, z.
\end{aligned} \tag{3.91}$$

with $\beta = e^{-i\pi k_y}$. The characteristic structures have the following Fourier components

$$\begin{aligned}
&\langle A_\mu(\mathbf{k})\rangle = 2\langle S_\mu\rangle: \quad \langle S_{1\mu}(\mathbf{k})\rangle = \frac{\langle S_\mu\rangle}{2},\ \langle S_{2\mu}(\mathbf{k})\rangle = -\frac{\langle S_\mu\rangle}{2},\ \langle S_{3\mu}(\mathbf{k})\rangle = -\beta\frac{\langle S_\mu\rangle}{2},\ \langle S_{4\mu}(\mathbf{k})\rangle = \beta\frac{\langle S_\mu\rangle}{2},\\
&\langle C_\mu(\mathbf{k})\rangle = 2\langle S_\mu\rangle: \quad \langle S_{1\mu}(\mathbf{k})\rangle = \frac{\langle S_\mu\rangle}{2},\ \langle S_{2\mu}(\mathbf{k})\rangle = \frac{\langle S_\mu\rangle}{2},\ \langle S_{3\mu}(\mathbf{k})\rangle = -\beta\frac{\langle S_\mu\rangle}{2},\ \langle S_{4\mu}(\mathbf{k})\rangle = -\beta\frac{\langle S_\mu\rangle}{2},\\
&\langle F_\mu(\mathbf{k})\rangle = 2\langle S_\mu\rangle: \quad \langle S_{1\mu}(\mathbf{k})\rangle = \frac{\langle S_\mu\rangle}{2},\ \langle S_{2\mu}(\mathbf{k})\rangle = \frac{\langle S_\mu\rangle}{2},\ \langle S_{3\mu}(\mathbf{k})\rangle = \beta\frac{\langle S_\mu\rangle}{2},\ \langle S_{4\mu}(\mathbf{k})\rangle = \beta\frac{\langle S_\mu\rangle}{2},\\
&\langle G_\mu(\mathbf{k})\rangle = 2\langle S_\mu\rangle: \quad \langle S_{1\mu}(\mathbf{k})\rangle = \frac{\langle S_\mu\rangle}{2},\ \langle S_{2\mu}(\mathbf{k})\rangle = -\frac{\langle S_\mu\rangle}{2},\ \langle S_{3\mu}(\mathbf{k})\rangle = \beta\frac{\langle S_\mu\rangle}{2},\ \langle S_{4\mu}(\mathbf{k})\rangle = -\beta\frac{\langle S_\mu\rangle}{2},
\end{aligned} \tag{3.92}$$

where $\langle S_\mu\rangle$ is a constant that may be complex, and $\mu = x, y, z$. The spatial structures are found using (3.5) and (3.92)

$$\begin{aligned}
\langle S_{1\mu}(\mathbf{R}_n)\rangle &= \sigma_1\left[\frac{\langle S_\mu\rangle^*}{2}e^{i\mathbf{k}\cdot\mathbf{R}_n} + \frac{\langle S_\mu\rangle}{2}e^{-i\mathbf{k}\cdot\mathbf{R}_n}\right],\\
\langle S_{2\mu}(\mathbf{R}_n)\rangle &= \sigma_2\left[\frac{\langle S_\mu\rangle^*}{2}e^{i\mathbf{k}\cdot\mathbf{R}_n} + \frac{\langle S_\mu\rangle}{2}e^{-i\mathbf{k}\cdot\mathbf{R}_n}\right],\\
\langle S_{3\mu}(\mathbf{R}_n)\rangle &= \sigma_3\left[\frac{\beta^{-1}\langle S_\mu\rangle^*}{2}e^{i\mathbf{k}\cdot\mathbf{R}_n} + \frac{\beta\langle S_\mu\rangle}{2}e^{-i\mathbf{k}\cdot\mathbf{R}_n}\right],\\
\langle S_{4\mu}(\mathbf{R}_n)\rangle &= \sigma_4\left[\frac{\beta^{-1}\langle S_\mu\rangle^*}{2}e^{i\mathbf{k}\cdot\mathbf{R}_n} + \frac{\beta\langle S_\mu\rangle}{2}e^{-i\mathbf{k}\cdot\mathbf{R}_n}\right],
\end{aligned} \tag{3.93}$$

where

$$\begin{aligned} A_\mu(\mathbf{k}): &\quad (\sigma_1,\sigma_2,\sigma_3,\sigma_4)=(1,-1,-1,1),\\ C_\mu(\mathbf{k}): &\quad (\sigma_1,\sigma_2,\sigma_3,\sigma_4)=(1,1,-1,-1),\\ F_\mu(\mathbf{k}): &\quad (\sigma_1,\sigma_2,\sigma_3,\sigma_4)=(1,1,1,1),\\ G_\mu(\mathbf{k}): &\quad (\sigma_1,\sigma_2,\sigma_3,\sigma_4)=(1,-1,1,-1), \end{aligned} \tag{3.94}$$

If $\langle S_\mu\rangle$ is a real number, then

$$\begin{aligned} \langle S_{1\mu}(\mathbf{R}_n)\rangle &= \sigma_1\langle S_\mu\rangle\cos(\mathbf{k}\cdot\mathbf{R_n}),\\ \langle S_{2\mu}(\mathbf{R}_n)\rangle &= \sigma_2\langle S_\mu\rangle\cos(\mathbf{k}\cdot\mathbf{R_n}),\\ \langle S_{3\mu}(\mathbf{R}_n)\rangle &= \sigma_3\langle S_\mu\rangle\cos(\mathbf{k}\cdot\mathbf{R_n}+\varphi_\beta), \quad \varphi_\beta=\pi k_y,\\ \langle S_{4\mu}(\mathbf{R}_n)\rangle &= \sigma_4\langle S_\mu\rangle\cos(\mathbf{k}\cdot\mathbf{R_n}+\varphi_\beta), \quad \varphi_\beta=\pi k_y. \end{aligned} \tag{3.95}$$

The spatial structures corresponding to (3.95) for the A, C, F, G irreducible basis vectors, are very similar to the commensurate structures shown in figure 3.3. The only difference is that the length of the moments in the incommensurate structures is modulated with the phase factor $\beta = e^{-i\pi k_y}$ along the **b** axis.

3.5 The magnetic scattering cross-section

In the following we are considering a magnetic crystal (we are of course thinking of $LiNiPO_4$) with 4 identical magnetic ions per unit cell. Each of these 4 magnetic ions have an equilibrium position $\mathbf{r}_d$ relative to the unit cell and are located at the same crystallographic site[9]. If $\mathbf{R}_n$ is the position of a certain unit cell and $\mathbf{r}_{nd}$ is the equilibrium position of a given magnetic ion in this unit cell, then obviously $\mathbf{r}_d = \mathbf{r}_{nd} - \mathbf{R}_n$.

Quite generally the magnetic elastic cross section for a crystal can be written [29]

$$\frac{d\sigma_M}{d\Omega}(\mathbf{Q}) = \left(\frac{\gamma r_0}{2\mu_B}\right)^2 |\widehat{\mathbf{Q}}\times[\langle\mathbf{M}(\mathbf{Q})\rangle\times\widehat{\mathbf{Q}}]|^2, \tag{3.96}$$

where $r_0 = \frac{\mu_0 e^2}{4\pi m_e} \simeq 2.8$ fm, $\widehat{\mathbf{Q}} = \mathbf{Q}/Q$ is a unit vector directed in the direction of the scattering vector and $\langle\mathbf{M}(\mathbf{Q})\rangle$ is the thermal average of the Fourier component

$$\mathbf{M}(\mathbf{Q}) = \sum_n\sum_d \mathbf{m}_d(\mathbf{R}_n)e^{i\mathbf{Q}\cdot\mathbf{R}_{nd}}, \tag{3.97}$$

of the magnetization operator $\mathbf{M}(\mathbf{r})$.

3.5.1 The polarization factor

The geometrical significance of the cross products in (3.96) is easy to deduce. Considering an arbitrary magnetic moment, **M**, and scattering vector, **Q**, we introduce the expression

$$\mathbf{M}_\perp(\mathbf{Q}) = \widehat{\mathbf{Q}}\times(\mathbf{M}\times\widehat{\mathbf{Q}}). \tag{3.98}$$

We note that if $\mathbf{M}||(\mathbf{Q})$ then $\mathbf{M}_\perp(\mathbf{Q}) = 0$. Generally

(a) $|\mathbf{M}_\perp(\mathbf{Q})| = M\sin\theta$, where θ is the angle between **M** and **Q**.

(b) $\mathbf{M}_\perp(\mathbf{Q}) \perp \mathbf{Q}$.

(c) $\mathbf{M}_\perp(\mathbf{Q}) \perp \mathbf{n}$, where $\mathbf{n} = \mathbf{M}\times\mathbf{Q}$, i.e. $\mathbf{M}_\perp(\mathbf{Q})$ is in the plane spanned by **M** and **Q**.

[9] Ions are said to be located at the same site in a unit cell if their positions can be transformed into one another by the symmetry elements of the crystal.

(d) The direction of $\mathbf{M}_\perp(\mathbf{Q})$ is found by using the right hand rule twice.

From (a)-(d) we see that $\mathbf{M}_\perp(\mathbf{Q})$ is the component of $\mathbf{M}(\mathbf{Q})$ which is perpendicular to the scattering vector $\mathbf{Q}$. The magnetic scattering cross-section (3.96) therefore measures only the magnetic components of $\mathbf{M}$ that are perpendicular to $\mathbf{Q}$.

For later use we define the polarization factors[10] as

$$\begin{aligned}\mathbf{P}_x(\mathbf{Q}) &= \widehat{\mathbf{Q}} \times (\mathbf{e}_x \times \widehat{\mathbf{Q}}) = (1-\widehat{Q}_x^2, -\widehat{Q}_x\widehat{Q}_y, -\widehat{Q}_x\widehat{Q}_z),\\ \mathbf{P}_y(\mathbf{Q}) &= \widehat{\mathbf{Q}} \times (\mathbf{e}_y \times \widehat{\mathbf{Q}}) = (-\widehat{Q}_x\widehat{Q}_y, 1-\widehat{Q}_y^2, -\widehat{Q}_y\widehat{Q}_z),\\ \mathbf{P}_z(\mathbf{Q}) &= \widehat{\mathbf{Q}} \times (\mathbf{e}_z \times \widehat{\mathbf{Q}}) = (-\widehat{Q}_x\widehat{Q}_z, -\widehat{Q}_y\widehat{Q}_z, 1-\widehat{Q}_z^2).\end{aligned} \tag{3.99}$$

The polarization factors at different scattering vectors $\mathbf{Q}$ are given for $LiNiPO_4$ in table 3.6. In the data analysis of the magnetic structures, the polarization factors are used for determining the direction of the magnetic moments, as we shall demonstrate later.

3.5.2 The commensurate structure factor

Evaluating the magnetic scattering cross-section for a commensurate structure with a single magnetic site one may write [30]

$$\frac{d\sigma_M}{d\Omega}(\mathbf{Q}) = N\frac{(2\pi)^3}{V_0}\sum_{\boldsymbol{\tau}}(pf(\mathbf{Q})e^{-W})^2|\mathbf{F}_{M\perp}(\mathbf{Q})|^2\delta(\mathbf{Q}-\boldsymbol{\tau}), \tag{3.100}$$

with $V_0 = abc$ being the volume of a unit cell. We have defined

$$\mathbf{F}_{M\perp}(\mathbf{Q}) = \widehat{\mathbf{Q}} \times [\mathbf{F}_M(\mathbf{Q}) \times \widehat{\mathbf{Q}}] = \mathbf{P}_x(\mathbf{Q})F_M^x(\mathbf{Q}) + \mathbf{P}_y(\mathbf{Q})F_M^y(\mathbf{Q}) + \mathbf{P}_z(\mathbf{Q})F_M^z(\mathbf{Q}), \tag{3.101}$$

where

$$\mathbf{F}_M(\mathbf{Q}) = (F_M^x(\mathbf{Q}), F_M^y(\mathbf{Q}), F_M^z(\mathbf{Q})) = \sum_d \mathbf{m}_d e^{i\mathbf{Q}\cdot\mathbf{r}_d} \tag{3.102}$$

is called the magnetic structure factor. Here $f(\mathbf{Q})$ is the magnetic form-factor for the magnetic ions, we have assumed that the Debye-Waller factor W is isotropic in reciprocal space, and the neutron gyromagnetic ratio $\gamma = 1.913$ has been introduced in the parameter $p = \frac{\gamma r_0}{2}$. Also, $\mathbf{m}_d \equiv \langle \mathbf{S}_d \rangle$ is the thermal average of the magnetic moment[11] at $\mathbf{r}_d$, and $\boldsymbol{\tau}$ are reciprocal lattice vectors. Since the structure is commensurate the magnetic moments $\mathbf{m}_d$ are independent of the position $\mathbf{R}_n$ of their corresponding unit cell.

The magnetic structure factor can be written

$$\begin{aligned}\mathbf{F}_M(\mathbf{Q}) &= \mathbf{m}_1 e^{i\mathbf{Q}\cdot\mathbf{r}_1} + \mathbf{m}_2 e^{i\mathbf{Q}\cdot\mathbf{r}_2} + \mathbf{m}_3 e^{i\mathbf{Q}\cdot\mathbf{r}_3} + \mathbf{m}_4 e^{i\mathbf{Q}\cdot\mathbf{r}_4}\\ &= \mathbf{m}_A F_A^c(\mathbf{Q}) + \mathbf{m}_G F_G^c(\mathbf{Q}) + \mathbf{m}_C F_C^c(\mathbf{Q}) + \mathbf{m}_F F_F^c(\mathbf{Q}),\end{aligned} \tag{3.103}$$

where

$$\begin{aligned}F_A^c(\mathbf{Q}) &= e^{i\mathbf{Q}\cdot\mathbf{r}_1} - e^{i\mathbf{Q}\cdot\mathbf{r}_2} - e^{i\mathbf{Q}\cdot\mathbf{r}_3} + e^{i\mathbf{Q}\cdot\mathbf{r}_4},\\ F_G^c(\mathbf{Q}) &= e^{i\mathbf{Q}\cdot\mathbf{r}_1} - e^{i\mathbf{Q}\cdot\mathbf{r}_2} + e^{i\mathbf{Q}\cdot\mathbf{r}_3} - e^{i\mathbf{Q}\cdot\mathbf{r}_4},\\ F_C^c(\mathbf{Q}) &= e^{i\mathbf{Q}\cdot\mathbf{r}_1} + e^{i\mathbf{Q}\cdot\mathbf{r}_2} - e^{i\mathbf{Q}\cdot\mathbf{d}_3} - e^{i\mathbf{Q}\cdot\mathbf{d}_4},\\ F_F^c(\mathbf{Q}) &= e^{i\mathbf{Q}\cdot\mathbf{r}_1} + e^{i\mathbf{Q}\cdot\mathbf{r}_2} + e^{i\mathbf{Q}\cdot\mathbf{r}_3} + e^{i\mathbf{Q}\cdot\mathbf{r}_4},\end{aligned} \tag{3.104}$$

are the structure factors of the magnetic A, G, C and F structures from figure 3.3. We see that

$$\begin{aligned}\mathbf{m}_1 &= \mathbf{m}_A + \mathbf{m}_G + \mathbf{m}_C + \mathbf{m}_F, \quad \mathbf{m}_2 = -\mathbf{m}_A - \mathbf{m}_G + \mathbf{m}_C + \mathbf{m}_F,\\ \mathbf{m}_3 &= -\mathbf{m}_A + \mathbf{m}_G - \mathbf{m}_C + \mathbf{m}_F, \quad \mathbf{m}_4 = \mathbf{m}_A + \mathbf{m}_G + \mathbf{m}_C + \mathbf{m}_F,\end{aligned} \tag{3.105}$$

[10] It is easy to rewrite $\mathbf{P}_\alpha(\mathbf{Q}) = \mathbf{e}_\alpha - (\mathbf{e}_\alpha \cdot \widehat{\mathbf{Q}})\widehat{\mathbf{Q}}$, once again demonstrating the geometrical meaning of the term. We note that $\mathbf{P}_\alpha(\mathbf{Q})$ and $\mathbf{P}_\beta(\mathbf{Q})$ are not necessarily orthogonal for $\alpha \neq \beta$, since $\mathbf{P}_\alpha(\mathbf{Q}) \cdot \mathbf{P}_\beta(\mathbf{Q}) = \widehat{Q}_\alpha\widehat{Q}_\beta$.

[11] Again we do not distinguish between spin operators and operators measuring magnetic moments.

$\mathbf{Q}$	$F_A^c(\mathbf{Q})$	$F_G^c(\mathbf{Q})$	$F_C^c(\mathbf{Q})$	$F_F^c(\mathbf{Q})$	$\|P_x(\mathbf{Q})\|^2$	$\|P_y(\mathbf{Q})\|^2$	$\|P_z(\mathbf{Q})\|^2$
(0,1,0)	0	0	$4i$	0	1	0	1
(1,1,0)	0	-4	0	0	0.75	0.25	1
(1,2,0)	-4i	0	0	0	0.92	0.08	1
(0,2,0)	0	0	0	-4	1	0	1
(2,2,0)	0	0	0	4	0.75	0.25	1
(4,0,0)	0	0	0	4	0	1	1
(2,1,0)	0	0	-4i	0	0.42	0.58	1
(0,1,1)	4i	0	0	0	1	0.61	0.39
(1,1,1)	0	0	0	-4	0.88	0.66	0.46
(1,2,1)	0	0	-4i	0	0.94	0.32	0.73
(0,2,1)	0	-4	0	0	1	0.28	0.72

Table 3.5: Commensurate magnetic structure- and polarization factors - simple case.

and conversely

$$\begin{aligned} \mathbf{m}_A &= \frac{1}{4}(\mathbf{m}_1 - \mathbf{m}_2 - \mathbf{m}_3 + \mathbf{m}_4), \quad \mathbf{m}_G = \frac{1}{4}(\mathbf{m}_1 - \mathbf{m}_2 + \mathbf{m}_3 - \mathbf{m}_4), \\ \mathbf{m}_C &= \frac{1}{4}(\mathbf{m}_1 + \mathbf{m}_2 - \mathbf{m}_3 - \mathbf{m}_4), \quad \mathbf{m}_F = \frac{1}{4}(\mathbf{m}_1 + \mathbf{m}_2 + \mathbf{m}_3 + \mathbf{m}_4). \end{aligned} \tag{3.106}$$

Expressing the structure factor as (3.103) has two advantages. As previously discussed, the quadratic terms in the spin Hamiltonian are products of irreducible basis vectors belonging to the same irreducible representation. Of these combinations, one is probably favored by the Hamiltonian, and consequently the magnetic structure will be described by only a few irreducible components. Furthermore, as the following examples will show, the structure factors of the **A**, **G**, **C** and **F** structures are especially simple, and well suited for data analysis. The structures **A**, **G**, **C** and **F** are (more or less) reflected at different scattering vectors, making it relatively easy to detect which components belong to the magnetic structure and which do not.

Example: Magnetic ions in high-symmetry points (simple case)

Let us assume the 4 magnetic ions in the unit cell are situated at

$$\mathbf{d}_1 = (0.25, 0.25, 1), \mathbf{d}_2 = (0.75, 0.25, 0.5), \mathbf{d}_3 = (0.75, 0.75, 0), \mathbf{d}_4 = (0.25, 0.75, 0.5). \tag{3.107}$$

According to (3.100)-(3.103) the magnetic scattering cross-section for a single irreducible structure is proportional to $|F_\Gamma^c|^2$, where

$$\begin{aligned} F_A^c(\mathbf{Q}) &= e^{i\mathbf{Q}\cdot\mathbf{d}_1} - e^{i\mathbf{Q}\cdot\mathbf{d}_2} - e^{i\mathbf{Q}\cdot\mathbf{d}_3} + e^{i\mathbf{Q}\cdot\mathbf{d}_4}, \\ F_G^c(\mathbf{Q}) &= e^{i\mathbf{Q}\cdot\mathbf{d}_1} - e^{i\mathbf{Q}\cdot\mathbf{d}_2} + e^{i\mathbf{Q}\cdot\mathbf{d}_3} - e^{i\mathbf{Q}\cdot\mathbf{d}_4}, \\ F_C^c(\mathbf{Q}) &= e^{i\mathbf{Q}\cdot\mathbf{d}_1} + e^{i\mathbf{Q}\cdot\mathbf{d}_2} - e^{i\mathbf{Q}\cdot\mathbf{d}_3} - e^{i\mathbf{Q}\cdot\mathbf{d}_4}, \\ F_F^c(\mathbf{Q}) &= e^{i\mathbf{Q}\cdot\mathbf{d}_1} + e^{i\mathbf{Q}\cdot\mathbf{d}_2} + e^{i\mathbf{Q}\cdot\mathbf{d}_3} + e^{i\mathbf{Q}\cdot\mathbf{d}_4}. \end{aligned} \tag{3.108}$$

In table 3.5 the structure factor is calculated for various $\mathbf{Q} = (H, K, L)$. We see from the table that the different magnetic structures, A, G, C, F, gives intensities at different scattering vectors. For $\mathbf{Q} = (H, K, L)$ we note that

$$e^{i\mathbf{Q}\cdot\mathbf{d}_1} = e^{i\frac{\pi}{2}(H+K)} = \begin{cases} 1, & \text{when } H+K = 0 \pmod 4, \\ i, & \text{when } H+K = 1 \pmod 4, \\ -1, & \text{when } H+K = 2 \pmod 4, \\ -i, & \text{when } H+K = 3 \pmod 4, \end{cases} \tag{3.109}$$

and

$$\left(e^{i\mathbf{Q}\cdot\mathbf{d}_1}, e^{i\mathbf{Q}\cdot\mathbf{d}_2}, e^{i\mathbf{Q}\cdot\mathbf{d}_3}, e^{i\mathbf{Q}\cdot\mathbf{d}_4}\right) = e^{i\mathbf{Q}\cdot\mathbf{d}_1}(1, e^{i\pi H}e^{i\pi L}, [e^{i\mathbf{Q}\cdot\mathbf{d}_1}]^2, e^{i\pi K}e^{i\pi L}). \tag{3.110}$$

From (3.109) and (3.110) the following selection rules are easily deduced.

- (H,K,L)=(odd,even,even) or (H,K,L)=(even,odd,odd): $|F_A^c|^2 = 16$, and $|F_G^c|^2 = |F_C^c|^2 = |F_F^c|^2 = 0$,
- (H,K,L)=(odd,odd,even) or (H,K,L)=(even,even,odd): $|F_G^c|^2 = 16$, and $|F_A^c|^2 = |F_C^c|^2 = |F_F^c|^2 = 0$,
- (H,K,L)=(even,odd,even) or (H,K,L)=(odd,even,odd): $|F_C^c|^2 = 16$, and $|F_A^c|^2 = |F_G^c|^2 = |F_F^c|^2 = 0$,
- (H,K,L)=(even,even,even) or (H,K,L)=(odd,odd,odd): $|F_F^c|^2 = 16$, and $|F_A^c|^2 = |F_G^c|^2 = |F_C^c|^2 = 0$.

Example: $LiNiPO_4$

In $LiNiPO_4$ the magnetic Ni^{2+} ions are *not* situated as above. Compared to the simple case the ions in $LiNiPO_4$ are slightly displaced, and have equilibrium positions at

$$\mathbf{r}_1 = (0.25+x, 0.25, 1-z), \mathbf{r}_2 = (0.75+x, 0.25, 0.5+z), \mathbf{r}_3 = (0.75-x, 0.75, z), \mathbf{r}_4 = (0.25-x, 0.75, 0.5-z), \tag{3.111}$$

where $x \approx 0.0256$ and $z \approx 0.0175$. As a consequence of this displacement the basis vector contributions will mix as shown in table 3.6. The commensurate case is complicated by the fact that there can be both nuclear and magnetic neutron scattering occurring at the same scattering vectors $\mathbf{Q}$. Therefore the nuclear neutron scattering cross-section, $|F|^2$, for $LiNiPO_4$, calculated in MATLAB, is also given in the table. In an experimental setup, one must of course measure the peak intensities for both the paramagnetic and the magnetically ordered phase to accurately distinguish between nuclear and magnetic contributions.

$\mathbf{Q}$	$F_A^c(\mathbf{Q})$	$F_G^c(\mathbf{Q})$	$F_C^c(\mathbf{Q})$	$F_F^c(\mathbf{Q})$	$\lvert P_x(\mathbf{Q})\rvert^2$	$\lvert P_y(\mathbf{Q})\rvert^2$	$\lvert P_z(\mathbf{Q})\rvert^2$	$\lvert F_N(\mathbf{Q})\rvert^2$
(0,1,3)	$3.78i$	0	0	1.30	1	0.93	0.07	32.53
(1,2,0)	$-3.95i$	0.64	0	0	0.92	0.08	1	0
(0,0,-1)	0	3.98	$0.44i$	0	1	1	0	0
(1,1,0)	$-0.64i$	-3.95	0	0	0.75	0.25	1	0
(0,1,0)	0	0	$4i$	0	1	0	1	0
(0,1,4)	0	1.70	$3.62i$	0	1	0.96	0.04	0
(0,2,0)	0	0	0	-4	1	0	1	5748.20
(2,0,0)	0	0	-1.26	-3.79	0	1	1	1261.45

Table 3.6: Commensurate magnetic structure- and polarization factors for $LiNiPO_4$ with $x \simeq 0.0256$ and $z \approx 0.0175$. The nuclear structure factor $|F_N|^2$ is calculated in MATLAB using the expression given in (5.2), neglecting the Debye-Waller factors, and are in units of fm^2. To compare nuclear and magnetic scattering cross-sections, we compare $p^2|F_M|^2$ with $|F_N|^2$, where $p^2 \approx 7.8$ fm^2.

3.5.3 The incommensurate structure factor

For an incommensurate magnetic structure

$$\mathbf{m}_d(\mathbf{R}_n) = \sum_{\mathbf{k}} \mathbf{m}_d(\mathbf{k}) e^{-i\mathbf{k}\cdot\mathbf{R}_n}, \tag{3.112}$$

the magnetic scattering cross section can be written as

$$\frac{d\sigma_M}{d\Omega}(\mathbf{Q}) = N\frac{(2\pi)^3}{V_0}\sum_{\boldsymbol{\tau}}\sum_{\mathbf{k}}(pf(\mathbf{Q})e^{-W})^2|\mathbf{F}_{M\perp}(\mathbf{Q},\mathbf{k})|^2\delta(\mathbf{Q}-\mathbf{k}-\boldsymbol{\tau}), \tag{3.113}$$

where

$$\mathbf{F}_{M\perp}(\mathbf{Q},\mathbf{k}) = \widehat{\mathbf{Q}} \times [\mathbf{F}_M(\mathbf{Q},\mathbf{k}) \times \widehat{\mathbf{Q}}], \tag{3.114}$$

and

$$\mathbf{F}_M(\mathbf{Q},\mathbf{k}) = \sum_d \mathbf{m}_d(\mathbf{k}) e^{i\mathbf{Q}\cdot\mathbf{r}_d}. \tag{3.115}$$

In our case $\mathbf{k} = \pm(0, k_y, 0)$, but since these two wave vectors are connected by symmetry we need only consider $\mathbf{k} = (0, k_y, 0)$. As before the magnetic structure factor is rewritten as

$$\begin{aligned}\mathbf{F}_M(\mathbf{Q},\mathbf{k}) &= \mathbf{m}_1(\mathbf{k})e^{i\mathbf{Q}\cdot\mathbf{r}_1} + \mathbf{m}_2(\mathbf{k})e^{i\mathbf{Q}\cdot\mathbf{r}_2} + \mathbf{m}_3(\mathbf{k})e^{i\mathbf{Q}\cdot\mathbf{r}_3} + \mathbf{m}_4(\mathbf{k})e^{i\mathbf{Q}\cdot\mathbf{r}_4} \\ &= \mathbf{m}_A(\mathbf{k})F_A^c(\mathbf{Q}) + \mathbf{m}_G(\mathbf{k})F_G^c(\mathbf{Q}) + \mathbf{m}_C(\mathbf{k})F_C^c(\mathbf{Q}) + \mathbf{m}_F(\mathbf{k})F_F^c(\mathbf{Q}),\end{aligned} \tag{3.116}$$

where we define

$$\begin{aligned}F_A^{ic}(\boldsymbol{\tau}+\mathbf{k}) &= e^{i(\boldsymbol{\tau}+\mathbf{k})\cdot\mathbf{r}_1} - e^{i(\boldsymbol{\tau}+\mathbf{k})\cdot\mathbf{r}_2} - \beta e^{i(\boldsymbol{\tau}+\mathbf{k})\cdot\mathbf{r}_3} + \beta e^{i(\boldsymbol{\tau}+\mathbf{k})\cdot\mathbf{r}_4}, \\ F_G^{ic}(\boldsymbol{\tau}+\mathbf{k}) &= e^{i(\boldsymbol{\tau}+\mathbf{k})\cdot\mathbf{r}_1} - e^{i(\boldsymbol{\tau}+\mathbf{k})\cdot\mathbf{r}_2} + \beta e^{i(\boldsymbol{\tau}+\mathbf{k})\cdot\mathbf{r}_3} - \beta e^{i(\boldsymbol{\tau}+\mathbf{k})\cdot\mathbf{r}_4}, \\ F_C^{ic}(\boldsymbol{\tau}+\mathbf{k}) &= e^{i(\boldsymbol{\tau}+\mathbf{k})\cdot\mathbf{r}_1} + e^{i(\boldsymbol{\tau}+\mathbf{k})\cdot\mathbf{r}_2} - \beta e^{i(\boldsymbol{\tau}+\mathbf{k})\cdot\mathbf{r}_3} - \beta e^{i(\boldsymbol{\tau}+\mathbf{k})\cdot\mathbf{r}_4}, \\ F_F^{ic}(\boldsymbol{\tau}+\mathbf{k}) &= e^{i(\boldsymbol{\tau}+\mathbf{k})\cdot\mathbf{r}_1} + e^{i(\boldsymbol{\tau}+\mathbf{k})\cdot\mathbf{r}_2} + \beta e^{i(\boldsymbol{\tau}+\mathbf{k})\cdot\mathbf{r}_3} + \beta e^{i(\boldsymbol{\tau}+\mathbf{k})\cdot\mathbf{r}_4},\end{aligned} \tag{3.117}$$

for $\mathbf{Q} = \boldsymbol{\tau} + \mathbf{k}$ and $\beta = e^{-i\pi k_y}$.

Example: Magnetic ions in high-symmetry points (simple case)

Once again we begin by seeing what would happen if the 4 magnetic ions in the unit cell were situated at

$$\mathbf{d}_1 = (0.25, 0.25, 1),\ \mathbf{d}_2 = (0.75, 0.25, 0.5),\ \mathbf{d}_3 = (0.75, 0.75, 0),\ \mathbf{d}_4 = (0.25, 0.75, 0.5). \tag{3.118}$$

Since $\mathbf{k} = (0, k_y, 0)$ we have that

$$\begin{aligned}e^{i(\boldsymbol{\tau}+\mathbf{k})\cdot\mathbf{d}_1} &= e^{i\pi k_y/2} e^{i\boldsymbol{\tau}\cdot\mathbf{d}_1}, \\ e^{i(\boldsymbol{\tau}+\mathbf{k})\cdot\mathbf{d}_2} &= e^{i\pi k_y/2} e^{i\boldsymbol{\tau}\cdot\mathbf{d}_2}, \\ \beta e^{i(\boldsymbol{\tau}+\mathbf{k})\cdot\mathbf{d}_3} &= e^{-i\pi k_y} e^{i3\pi k_y/2} e^{i\boldsymbol{\tau}\cdot\mathbf{d}_3} = e^{i\pi k_y/2} e^{i\boldsymbol{\tau}\cdot\mathbf{d}_3}, \\ \beta e^{i(\boldsymbol{\tau}+\mathbf{k})\cdot\mathbf{d}_4} &= e^{-i\pi k_y} e^{i3\pi k_y/2} e^{i\boldsymbol{\tau}\cdot\mathbf{d}_4} = e^{i\pi k_y/2} e^{i\boldsymbol{\tau}\cdot\mathbf{d}_4}.\end{aligned} \tag{3.119}$$

Inserting (3.119) into (3.117), we see that $F_\Gamma^{ic}(\boldsymbol{\tau}+\mathbf{k}) = e^{i\pi k/2} F_\Gamma^c(\boldsymbol{\tau})$. Since the overall phase factor does not play a role, the incommensurate result, given in table 3.7, is identical to the commensurate structure factors from table 3.5.

$\mathbf{Q}$	$F_A^{ic}(\mathbf{Q})$	$F_G^{ic}(\mathbf{Q})$	$F_C^{ic}(\mathbf{Q})$	$F_F^{ic}(\mathbf{Q})$
$(0, 1 \pm k_y, 0)$	0	0	$4i$	0
$(1, 1 \pm k_y, 0)$	0	-4	0	0
$(1, 2 \pm k_y, 0)$	$-4i$	0	0	0
$(0, 2 \pm k_y, 0)$	0	0	0	-4
$(2, 2 \pm k_y, 0)$	0	0	0	4
$(4, 0 \pm k_y, 0)$	0	0	0	4
$(2, 1 \pm k_y, 0)$	0	0	-4i	0
$(0, 1 \pm k_y, 1)$	4i	0	0	0
$(1, 1 \pm k_y, 1)$	0	0	0	-4
$(1, 2 \pm k_y, 1)$	0	0	-4i	0
$(0, 2 \pm k_y, 1)$	0	-4	0	0

Table 3.7: Incommensurate magnetic structure factors - simple case.

Example: $LiNiPO_4$

Having

$$\begin{aligned}\mathbf{r}_1 &= (0.25+x, 0.25, 1-z), \mathbf{r}_2 = (0.75-x, 0.75, z),\\ \mathbf{r}_3 &= (0.25-x, 0.75, 0.5-z), \mathbf{r}_4 = (0.75+x, 0.25, 0.5+z),\end{aligned} \tag{3.120}$$

does not complicate the things much. Also here we find that

$$\begin{aligned}e^{i(\boldsymbol{\tau}+\mathbf{k})\cdot\mathbf{r}_1} &= e^{i\pi k_y/2}e^{i\boldsymbol{\tau}\cdot\mathbf{r}_1},\\ e^{i(\boldsymbol{\tau}+\mathbf{k})\cdot\mathbf{r}_2} &= e^{i\pi k_y/2}e^{i\boldsymbol{\tau}\cdot\mathbf{r}_2},\\ \beta e^{i(\boldsymbol{\tau}+\mathbf{k})\cdot\mathbf{r}_3} &= e^{-i\pi k_y}e^{i3\pi k_y/2}e^{i\boldsymbol{\tau}\cdot\mathbf{r}_3} = e^{i\pi k_y/2}e^{i\boldsymbol{\tau}\cdot\mathbf{r}_3},\\ \beta e^{i(\boldsymbol{\tau}+\mathbf{k})\cdot\mathbf{r}_4} &= e^{-i\pi k_y}e^{i3\pi k_y/2}e^{i\boldsymbol{\tau}\cdot\mathbf{r}_4} = e^{i\pi k_y/2}e^{i\boldsymbol{\tau}\cdot\mathbf{r}_4}.\end{aligned} \tag{3.121}$$

and therefore $F^{ic}_\Gamma(\boldsymbol{\tau}+\mathbf{k}) = e^{i\pi k/2}F^c_\Gamma(\boldsymbol{\tau})$. Using this relation, and table 3.6, we can immediately evaluate F^{ic}_Γ. Neglecting the overall phase factor, the result is given in table 3.8.

$\mathbf{Q}$	$F^{ic}_A(\mathbf{Q})$	$F^{ic}_G(\mathbf{Q})$	$F^{ic}_C(\mathbf{Q})$	$F^{ic}_F(\mathbf{Q})$
(0,1±k_y,3)	$3.78i$	0	0	1.30
(1,2±k_y,0)	$-3.95i$	0.64	0	0
(0,0±k_y,-1)	0	3.98	$0.44i$	0
(1,1±k_y,0)	$-0.64i$	-3.95	0	0
(0,1±k_y,0)	0	0	$4i$	0
(0,1±k_y,4)	0	1.70	$3.62i$	0
(0,2±k_y,0)	0	0	0	-4
(2,0±k_y,0)	0	0	-1.26	-3.79

Table 3.8: Incommensurate magnetic structure factors for $LiNiPO_4$ with $x \simeq 0.0256$ and $z \approx 0.0175$.

Chapter 4

Magnetic phase diagram

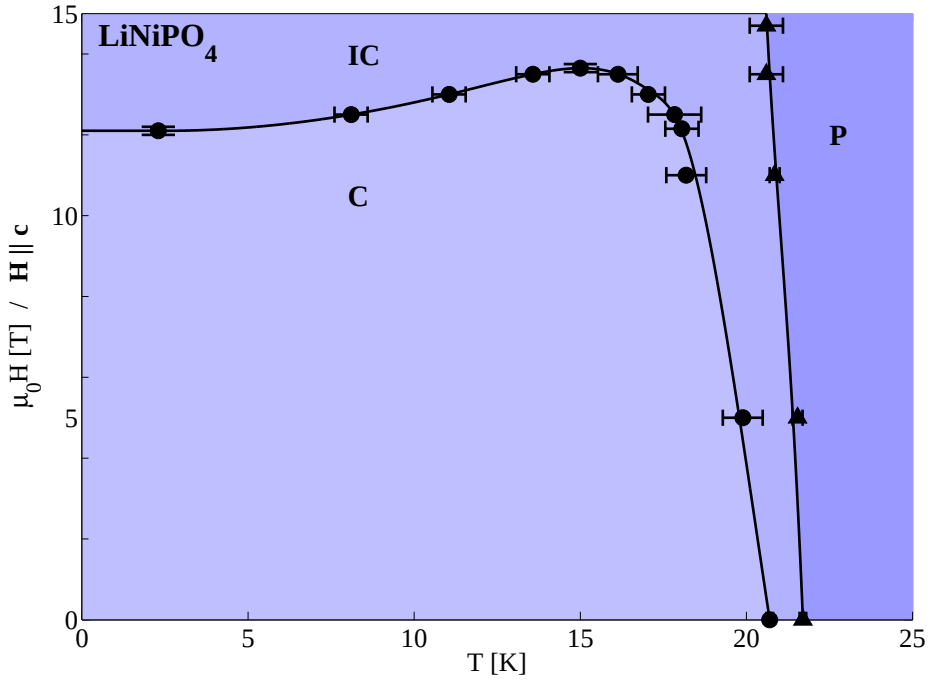

Figure 4.1: HT-magnetic phase diagram of $LiNiPO_4$ determined for $\mathbf{H}||\mathbf{c}$ at RITA-II. The phase diagram include commensurate (C) and incommensurate (IC) magnetically ordered phases, and a paramagnetic (P) phase.

4.1 Introduction

A major experimental result of this project is the phase diagram shown in figure 4.1. This phase diagram was determined by a combination of temperature and field scans, tracking the field- and temperature dependence of the commensurate (C) and incommensurate (IC) order parameters (this will be described in more detail below). We have defined the paramagnetic (P) phase as the regions where there is no long range magnetic order.

All the measurements discussed in this chapter were conducted on the cold source triple axis spectrometer RITA-II. The instrument was in the 7 blade imaging mode, but the resulting data were analyzed taking only

the intensity of the center blade into account. Both the monochromator and the analyzer was set to reflect 5 meV neutrons. A radial Be filter inserted between the sample and the analyzer prevented the detection of higher order neutrons. The sample was an irregularly shaped single $LiNiPO_4$ crystal of dimension $5 \times 5 \times 9$ mm^3, mounted in a Oxford 15 T vertical magnet with the crystallographic *ab*-plane as scattering plane. During the experiment the sample was subjected to magnetic fields directed along the crystallographic *c*-axis, with field strengths ranging from 0-14.7 T.

4.2 Commensurate phase

In their zero field measurements, Vaknin *et al.* [9] used the commensurate (0,1,0) Bragg peak as commensurate order parameter. This is a natural choice, since the nuclear structure factor for this scattering vector is zero, and because it strongly reflects the dominant antiferromagnetic structure already determined by powder diffraction. We have investigated the field and temperature dependence of other commensurate peaks, but it is the (0,1,0) peak intensity we consider as the primary commensurate order parameter throughout the experiment. Accordingly, the commensurate phase boundary was mostly mapped out by temperature and field scans where the scattering vector was fixed at $\mathbf{Q} = (0, 1, 0)$.

Temperature scans

Figure 4.2 show the (0,1,0) peak intensity in a series of temperature scans at fixed magnetic fields. The system is in the commensurate phase when the measured peak intensity is much higher than the background. The

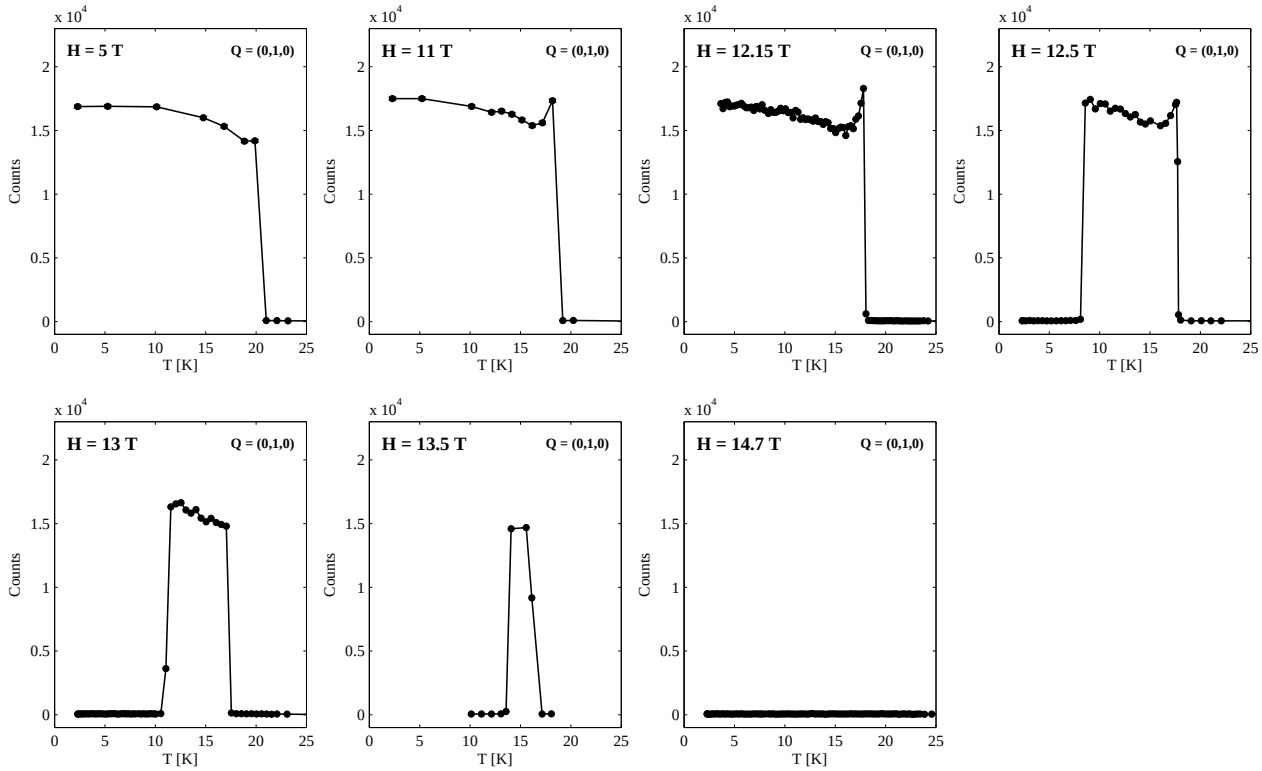

Figure 4.2: Temperature scans of the (0,1,0) peak intensity for various fields (counting time was 30 seconds per point). These scans have been used to map out the C-IC phase boundary. In the commensurate phase the peak intensity of (0,1,0) is large, while it is small in the incommensurate (and paramagnetic) phase.

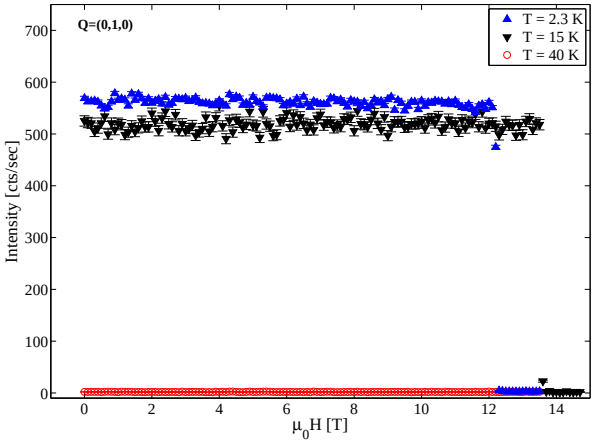

Figure 4.3: Field scans sitting on the (0,1,0) peak (counting time was 10 seconds per point). At 2.3 K the C-IC phase transition takes place around 12.1 T, while at 15 K the transition temperature is around 13.6 T. At 40 K the system is paramagnetic.

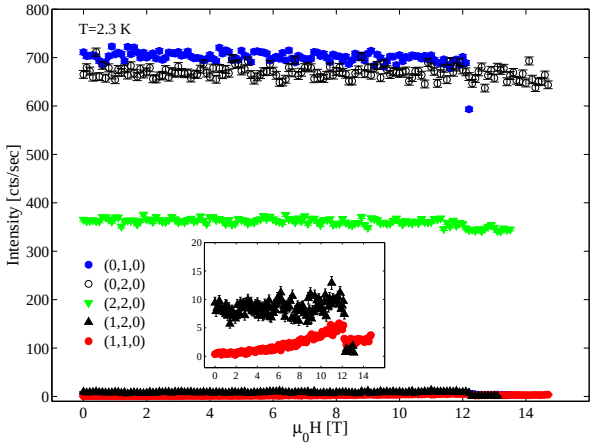

Figure 4.4: Field scans of various commensurate peak intensities at 2.3 K (10 seconds per point for large peaks, and 30 seconds per point for smaller peaks). The inset is a closeup of the (1,2,0) and (1,1,0) peak intensities.

temperatures where the (0,1,0) signal drops to the background intensity, mark the C phase boundary and are inserted in figure 4.1.

The high-field commensurate phase boundary has a "dome-like" feature, which is reflected in the 12.5, 13 and 13.5 T measurements. Here the commensurate region is restricted from both above and below in temperature. At 5, 11 and 12.15 T the commensurate phase has no lower bound. For these fields there is a distinct upturn in the peak intensity when approaching the phase boundary from low temperatures. Such an upturn is also observed at 12.5 T, but not at 13 or 13.5 T. At 14.7 T the (0,1,0) peak intensity is small for all temperatures and the system is never in the commensurate phase.

Field scans

Figure 4.3 show the (0,1,0) peak intensity for three field scans at various temperatures. It is readily seen that $LiNiPO_4$ is in the commensurate phase for fields below 12.1 T at 2.3 K, and below 13.6 T at 15 K. These two transition fields are marked in figure 4.1. For T = 40 K the system is paramagnetic at all fields.

Field scans at T = 2.3 K for different commensurate peaks are shown in figure 4.4. The strongest intensities are those belonging to the (0,1,0) and (0,2,0) scattering vectors. As already mentioned, the peak at $\mathbf{Q} = (0, 1, 0)$ reflects the dominant anti-ferromagnetic C structure at zero field. The (0,1,0) intensity remains almost constant until 12.1 T, suggesting that field induced changes in the magnetic structure are small below the phase transition. The field dependence of the magnetic structures will be discussed further in chapter 5. The (0,2,0) and (2,2,0) peaks are primarily nuclear peaks and do not reflect the anti-ferromagnetic structure. Therefore there is no noticeable change in their peak intensities when crossing the C phase boundary at 12.1 T. The (1,2,0) and (1,1,0) peak intensities are on the other hand clearly affected by the magnetic phase transition at 12.1 T (see inset of figure 4.4). These peaks play a substantial role in our magnetic structure determination and will be analyzed in more detail in chapter 5.

4.3 Incommensurate phase

As we have just discussed, the commensurate scans outline the magnetic commensurate phase boundary as function of temperature and field. However, these scans do not reveal the nature of the phase (or phases)

in the non-commensurate *HT*-regions. In order to do this we have performed series of **Q** scans at different fields and temperatures.

The magnetic ordering vector at 13.5 T and 2.3 K

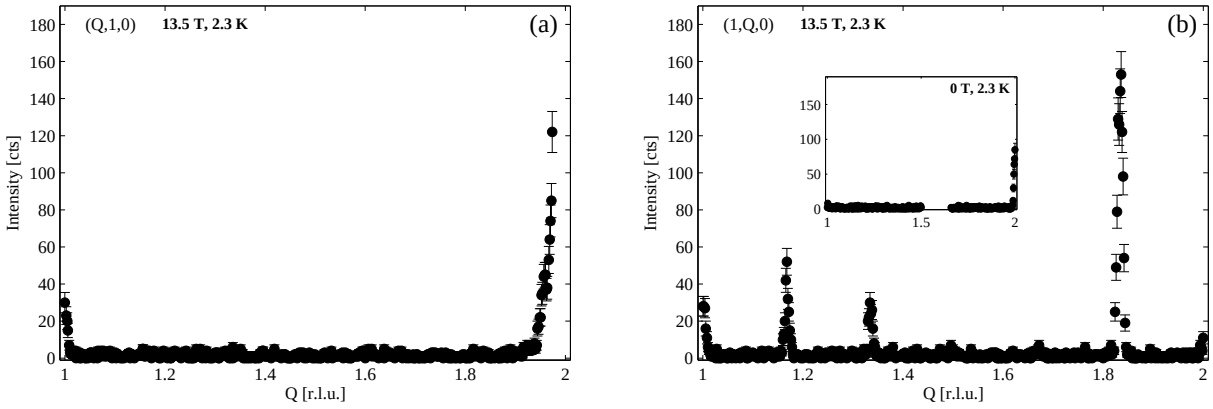

Figure 4.5: (a) Q_H scan at 13.5 T and 2.3 K. (b) Q_L scan at 13.5 T and 2.3 K showing three IC peaks at (1,1.18,0), (1,1.36,0) and (1,1.82,0). Inset shows a Q_L scan at 0 T and 2.3 K for comparison. All scans with counting times 10 seconds per point.

Figure 4.5 show Q_H and Q_K scans at 13.5 T and 2.3 K, measuring from $\mathbf{Q} = (1,1,0)$ to (2,1,0) and (1,2,0), respectively. Apart from the commensurate (1,1,0) and (2,1,0) peaks, only background intensity was observed in the Q_H scan (figure 4.5(a)). However, in the Q_K scan (figure 4.5(b)) there are additional peaks at the incommensurate positions $(1, 1+q, 0)$, $(1, 1+2q, 0)$ and $(1, 2-q, 0)$, where q is approximately 0.18 r.l.u. This shows that the phase at 2.3 K and 13.5 T is magnetically[1] ordered with an incommensurate ordering vector $\mathbf{q} = (0, q, 0)$. We note that this direction of this modulation is the same as the zero field IC ordering vector determined by Vaknin *et al* [9].

A second order peak appears at $(1, 1.36, 0)$ in figure 4.5(b). It would have been interesting to track the temperature dependence of this second order peak, but unfortunately we have not done this satisfactorily. A series of Q_K scans for different temperatures at 13.5 T indicate that the second order peak is present in the IC region below the commensurate "dome" (i.e. at temperatures below 14.5 K), but not above the dome (at temperatures above 15.5 K). However, the data are far from conclusive since we never successfully scanned the $1 + 2q$ position for temperatures above 17 K. I shall not be discussing the higher order features further in this thesis.

Field and temperature dependence

In our initial measurements at 13.5 T we had used the $(1, 1 + q, 0)$ peak as IC order parameter. In fact this was not the best choice since we found the $(0, 1 + q, 0)$ peak to be a much stronger peak (compare figure 4.8(a) and (c)). In the remaining experiment we therefore used the $(0, 1 + q, 0)$ peak as primary IC order parameter. At 13.5 T, however, we had already performed a long series of $(1, 1 + q, 0)$ scans as function of temperature. Since the behavior of the $(1, 1 + q, 0)$ and the $(0, 1 + q, 0)$ peaks seems to be identical (see for instance figure 4.9 and 4.10), we use the $(1, 1 + q, 0)$ peak intensity as primary order parameter at 13.5 T, and the $(0, 1 + q, 0)$ peak intensity as order parameter for all other fields.

[1]The reason we know that the IC peaks signals magnetic and not structural ordering, is because the phase transition is visible in the magnetization measurements (section 2.2.2), and because the measured data can be satisfactory fitted by the magnetic structure calculations (chapter 5). Furthermore, in x-ray experiments performed on the beamline BW5 at HASYLAB, the IC phase was not observed.

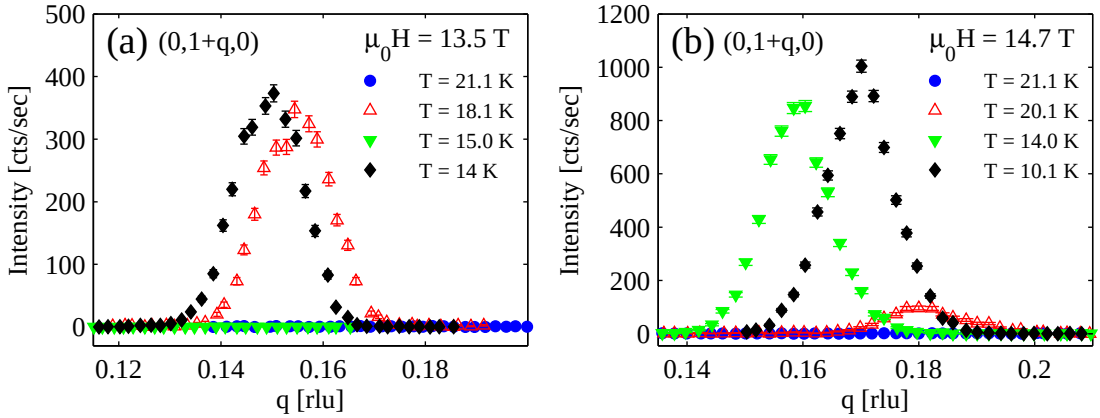

Figure 4.6: (a) QK scans of (0,1+q,0) at 13.5 T. For T = 21.1 K the system is paramagnetic and there is no peak. At T = 18.1 K and 14 K the visible peaks indicate that the system is incommensurate. At 15 K the system is commensurate and therefore has no IC peak. (b) QK scans of (0,1+q,0) at 14.7 T. Also here the system is paramagnetic at 21.1 K. At 20.1 K the system is incommensurate and a peak has appeared. At 14.7 T there is no commensurate region causing the peak to disappear below 20.1 K. All scans with counting time 10 seconds per point.

Scanning the peaks as function of **H** and T we observed that the IC peak position changed a great deal. Figure 4.6(a) and (b) show a couple of scans at 13.5 T and 14.7 T, respectively. At 13.5 T, in figure 4.6 (a), it is seen how the the commensurate "dome" cause the IC peak to vanish at 15 K. Figure 4.6(b) demonstrates how the IC peak at 14.7 T shifts back and forth in position when the temperature is decreased. The IC phase boundary, depicted in figure 4.1, was measured by mapping out the fields and temperatures where the measured IC peaks first appeared or disappeared.

The incommensurate peak behavior is summarized in figure 4.7(a) and (b). Here the IC peak positions are shown as function of field and temperature in (a), and the integrated peak intensities in (b). The 13.5

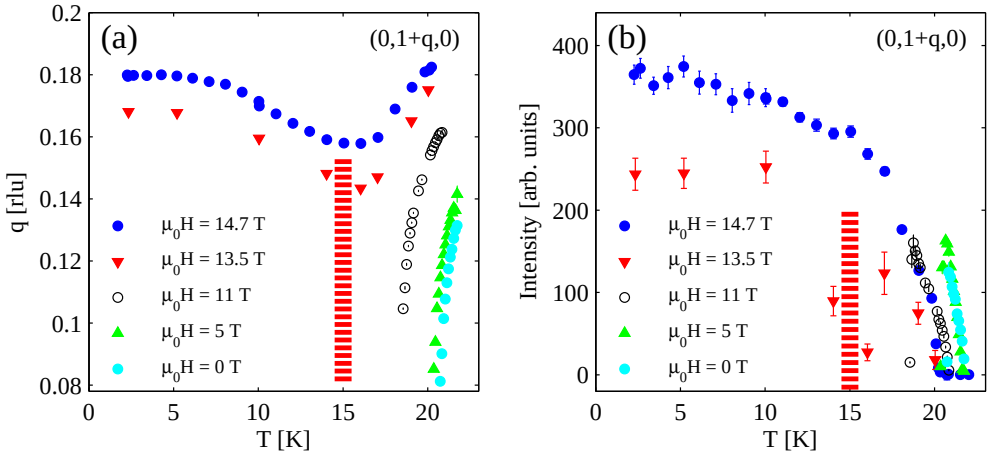

Figure 4.7: (a) Incommensurate wave vector q from (0,1+q,0) scans at different fields and temperatures. The 13.5 T data are from (1,1+q,0) incommensurate scans. The region marked by red lines is the (commensurate) temperature region where the incommensurate peaks at 13.5 T disappear. (b) Integrated intensity of the (0,1+q,0) incommensurate peak at different fields and temperatures. The 13.5 T data are from (1,1+q,0) incommensurate scans. The region marked by red lines is the (commensurate) temperature region where the incommensurate peaks at 13.5 T disappear.

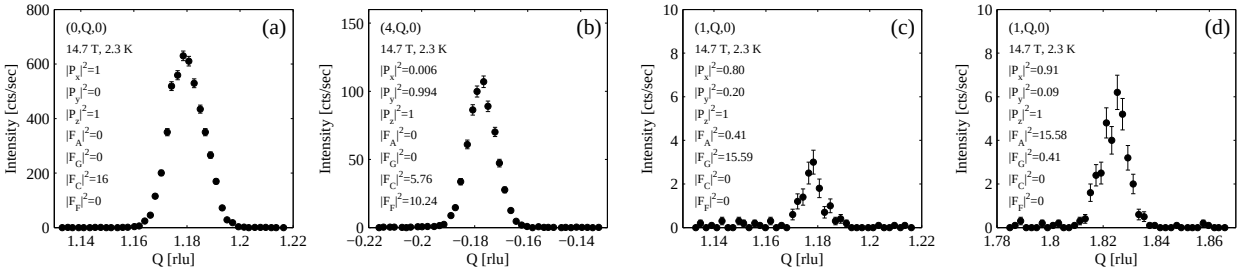

Figure 4.8: Incommensurate peaks with different symmetries at 2.3 K and 14.7 T. (a) The $(0, 1+q, 0)$ peak. (b) The $(4, -q, 0)$ peak. (c) The $(1, 1+q, 0)$ peak. (d) The $(1, 2-q, 0)$ peak.

T peak intensities in (b) are actually $(1, 1+q, 0)$ intensities scaled to correspond to $(0, 1+q, 0)$ intensities. This was done by estimating the relative intensities of the $(0, 1+q, 0)$ and $(1, 1+q, 0)$ peaks at 13.5 T, by comparing with $(0, 1+q, 0)$ and $(1, 1+q, 0)$ scans taken at 2.3 K and 13.5 T.

Peaks of different symmetry

One important consequence of the magnetic scattering cross-section is that the measured neutron intensities at various $\mathbf{Q}$ will probe different aspects of the magnetic structure, both regarding to the direction and to the symmetry of the magnetic moments. By comparing the behavior of several peaks one can therefore hope to find additional phase transitions. For instance, suppose two peaks, reflecting different magnetic symmetries, have different onset temperatures $T_1 \neq T_2$ at a given field. Then these two peaks represent two non-equivalent magnetic order parameters, and the system will experience a phase transition both at T_1 and T_2.

Hoping to gain such additional information, we scanned a variety of $\mathbf{Q} = (H, K \pm q, 0)$ positions at 14.7 T. Four such scans are shown in figure 4.8. The temperature dependence of the modulation vector q and the integrated peak intensity for the $(0, 1+q, 0)$, $(1, 1+q, 0)$, $(1, 2-q, 0)$ and $(4, -q, 0)$ peaks are shown in figure 4.9 and 4.10. The fits have been done rather uncritically using a gaussian fitting function and the integrated intensities have been scaled in order to compare the temperature dependencies more easily. It is hard to see a difference in the temperature behavior of the different peaks, apart perhaps from a faster development in the $(1, 2-q, 0)$ intensity. The onset temperatures are also the same for all four IC peaks, and the measurements did therefore not reveal the presence of additional phase transitions at 14.7 T.

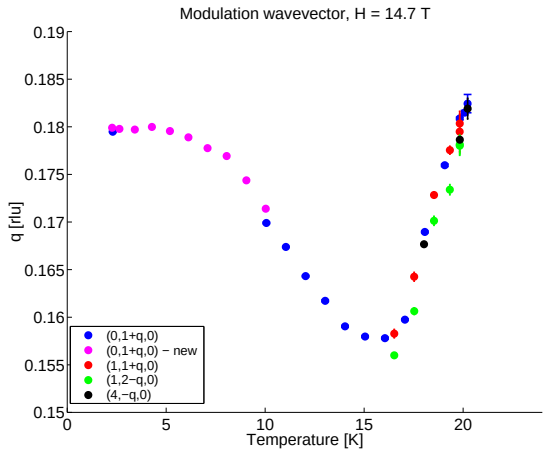

Figure 4.9: The incommensurate wave vector q for four incommensurate peaks of different symmetry at 14.7 T.

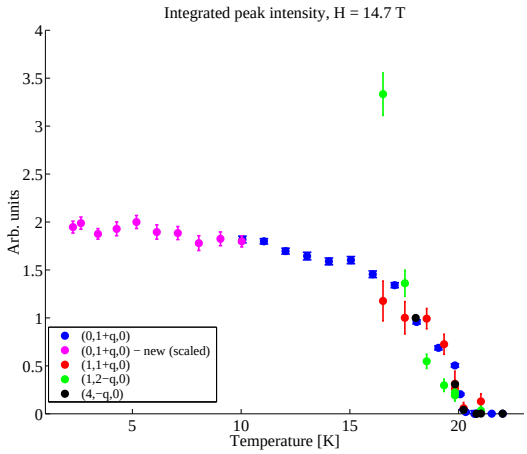

Figure 4.10: Integrated intensity (scaled) of the four incommensurate peaks with different symmetry peak at 14.7 T.

Chapter 5

Magnetic structure determination Part B

Experimental results

5.1 Introduction

In this chapter we present the magnetic structures of the commensurate and incommensurate ordered phases; both at zero field and at $\mathbf{H}||\mathbf{c}$ below 14.7 T. The magnetic structures have been determined by analyzing elastic neutron data from experiments at the single crystal diffractometer, TriCS, and the triple axis spectrometer RITA-II.

The chapter is organized as follows. We start out with a small example, manually inspecting a few commensurate scans from TriCS and deduce the primary elements of the commensurate magnetic structure "just by looking". After this example we turn our attention to the measurements at RITA, where we discuss some scans providing additional information. In section 5.4, the results of the full structural analysis is given. We then (section 5.5) relate the symmetry of the observed zero field commensurate structure, with the Dzyaloshinsky-Moriya interaction terms that may appear in the spin Hamiltonian. In section 5.6, we extract the field induced magnetization from the neutron data, and compare to macroscopic bulk measurements reported in the literature. We end this chapter with a few considerations concerning the symmetries of the magnetic phases and the magnetoelectric effect in $LiNiPO_4$.

5.2 The TRiCS experiments

The experiments on TriCS were all performed in zero field. We have analyzed data from 112 scans around commensurate positions at 5 K, and from 154 scans around incommensurate scattering vectors at 21 K. Both the 5 K and the 21 K series were accompanied by background measurements at 50 K. The commensurate scans were all performed with neutrons of wavelength $\lambda = 1.18$ Å, while neutrons with $\lambda = 2.3$ Å was used for the incommensurate scans.

In order to extract all the details of the zero field magnetic structure, the TriCS measurements had to be supplemented by data from RITA. Doing so, we combine the advantage of collecting a large number of magnetic peaks at TriCS, with a better signal-to-noise ratio at RITA. Before giving the result of the full analysis of all the TriCS and RITA data, we shall consider the following instructional example.

5.2.1 Calculating by hand - an example

In this example we show that the main features of the magnetic structure in $LiNiPO_4$ can be determined by a few fast and simple considerations on a limited number of peaks. We do so for the commensurate structure,

but the incommensurate case is just as easily inspected. This "hands on" approach demonstrates the use of the structure- and polarization factors introduced earlier, and will illustrate the benefits of decomposing the magnetic structure factor into A, G, C and F components.

G type components: (H, K, L)=(odd,odd,even) or (even,even,odd)

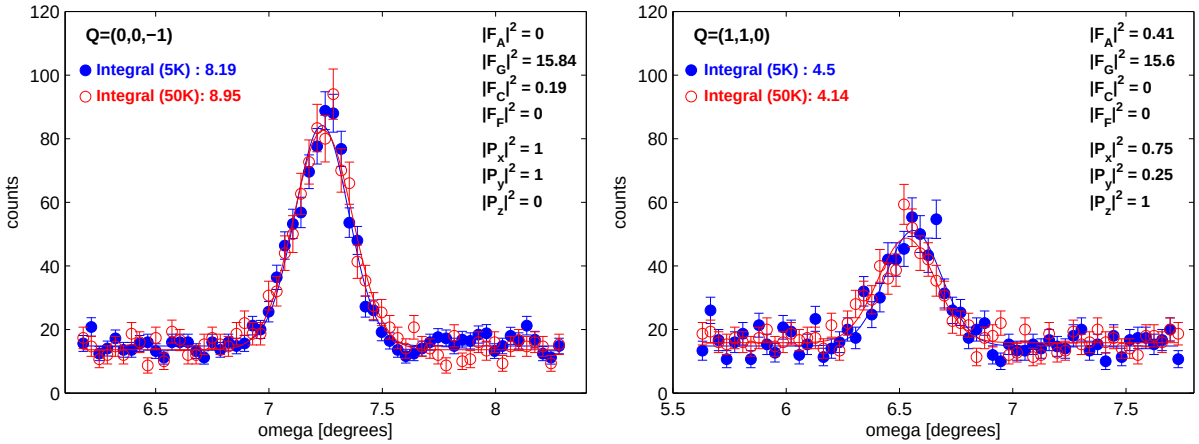

Figure 5.1: TriCS data reflecting and distinguishing between G_x, G_y and G_z components (counting time approximately 5 seconds per point for all the TriCS data depicted here and below).

Consider the omega scans in figure 5.1. From the structure- and polarization factors we see that G_x and G_y would be strongly reflected in $(0, 0, -1)$, and G_x and G_z would be strongly reflected in (1,1,0). Both for $\mathbf{Q} = (0, 0, -1)$ and $\mathbf{Q} = (1, 1, 0)$, the measured intensities are identical at T = 5 K and 50 K. This means that there is no magnetic signal at the two scattering vectors, and we can conclude that the commensurate magnetic structure at zero field do not have any G components.

F type components: (H, K, L)=(even,even,even) or (odd,odd,odd)

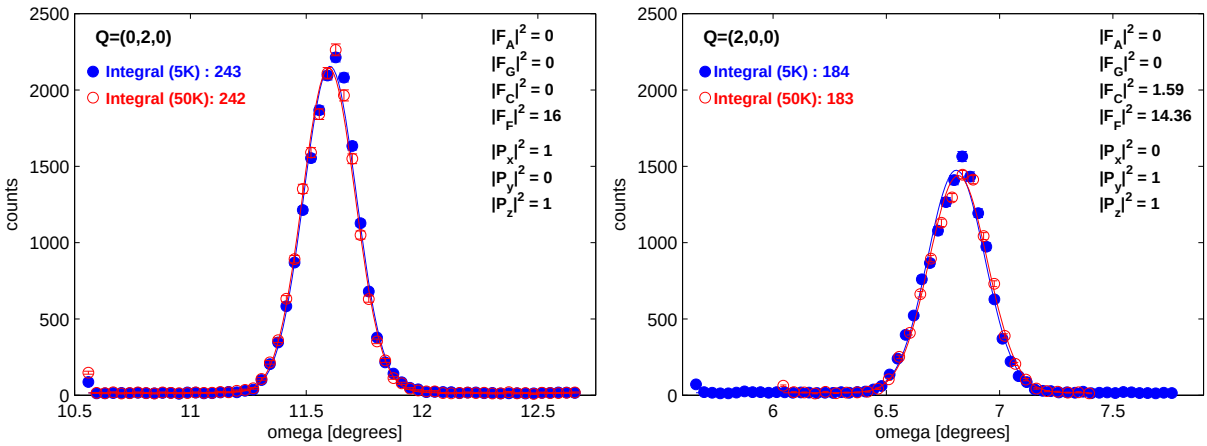

Figure 5.2: TriCS data reflecting and distinguishing between F_x, F_y and F_z components.

The scans in figure 5.2 are of scattering vectors that reflect F components. Also here the peaks are

undistinguishable at 5 and 50 K. The situation is somewhat complicated by the fact that scattering vectors reflecting magnetic F components are often also strong nuclear peaks, making small magnetic signals hard to detect. However, from figure 5.2, there is no indication of magnetic F components in the zero field commensurate structure.

A type components: (H, K, L)=(odd,even,even) or (even,odd,odd)

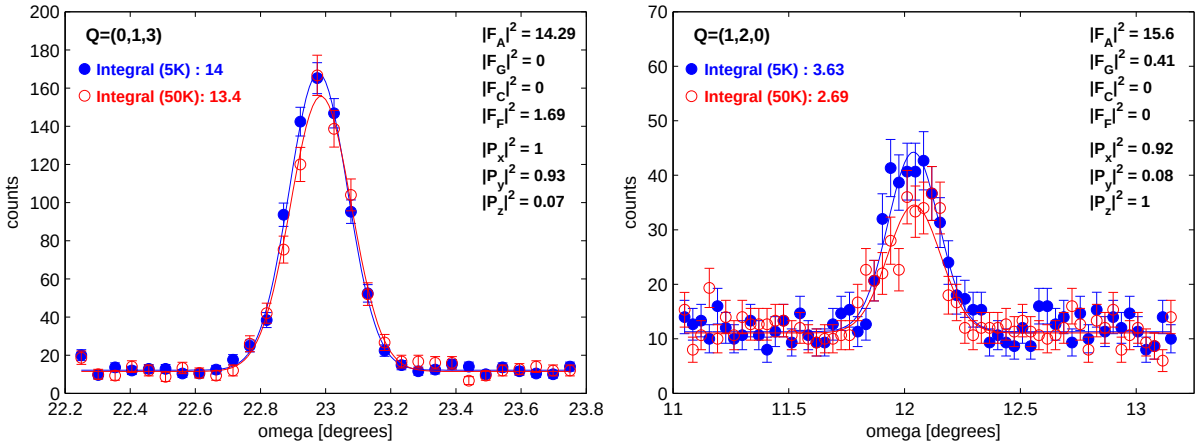

Figure 5.3: TriCS data reflecting and distinguishing between A_x, A_y and A_z components.

In the scans at $\mathbf{Q} = (0, 1, 3)$ and $\mathbf{Q} = (1, 2, 0)$, shown in figure 5.3, the intensities at 5 K seems to be slightly higher than at 50 K. The structure factor at $\mathbf{Q} = (0, 1, 3)$ is large for A, small for F, and zero for G and C. For $\mathbf{Q} = (1, 2, 0)$ the structure factor of A is large, it is small for G while being zero for C and F.

We have already concluded that both the F and G magnetic components are zero (or at least very small), and will not cause a magnetic signal at (1,2,0) and (0,1,3). The small magnetically induced signal, indicated by both scans of figure 5.3, therefore comes from an A component. The A_x, A_y and A_z components do not belong to the same irreducible representations (table 3.4), and are therefore not *a priori* expected to co-exist. Inspecting the polarization factors, we see that the A_x component is strongly reflected at both peaks, while the A_y and A_z components are reflected in only one of the two peaks each. So, assuming only one A component, and noting that a small magnetic signal seems to be present at both peaks, the scans suggest the existence of an A_x component in the commensurate magnetic structure.

It must be mentioned that the observed differences between the 5 and 50 K peaks at TriCS are too small to be conclusive. In the computer analysis of 112 commensurate peaks from TriCS, the presence of an A_x component was not determined with certainty. However, data measured at RITA (section 5.3) confirms that a small A_x component is present in the zero field commensurate phase.

C type components: (H, K, L)=(even,odd,even) or (odd,even,odd)

From the (0,1,0) scans in figure 5.4 we immediately see that the magnetic structure has a large C_x or a C_z component. The polarization factor shows that the C_z component is not reflected in the (0,1,4) peak, while C_x and C_y are. There is almost no magnetic intensity at $\mathbf{Q} = (0, 1, 4)$, so we conclude that the commensurate magnetic structure at zero field has a very large C_z component, and no C_x or C_y components.

Manually estimating the size of the C_z moments

To determine a magnetic structure accurately one must consider a very large number of magnetic peaks (the more the better) and in the analysis take the Lorentz factor, form factor and so on into account. However, knowledge of the irreducible basis vectors has allowed us to extract the main features of the magnetic

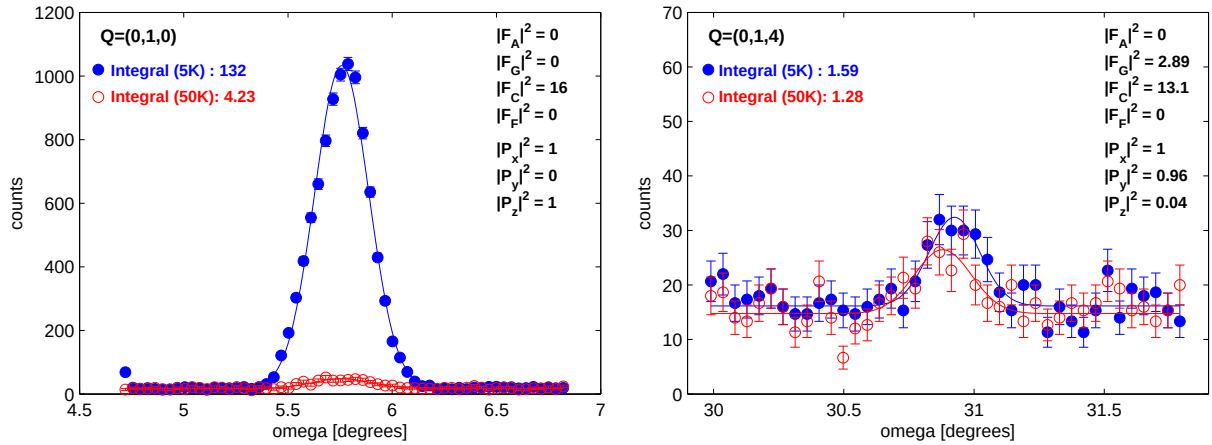

Figure 5.4: TriCS data reflecting and distinguishing between C_x, C_y and C_z components.

structure just by looking at a few well chosen scans, and without doing much calculating. As a result, we already now know that the zero field commensurate magnetic structure probably consist of a large C_z component, and a smaller A_x component. It is rewarding to note that these two components belong to the same irreducible representation (Γ_7 in table 3.4), effectively illustrating the considerations of section 3.3.4.

The size of the magnetic moments can be calculated by comparing magnetic and nuclear intensities, and we end this "hands on" example by the following rough estimation. The nuclear scattering cross-section for coherent elastic scattering can be written [30] as

$$\frac{d\sigma_N}{d\Omega}(\mathbf{Q}) = N\frac{(2\pi)^3}{V_0}\sum_{\tau}|F_N(\mathbf{Q})|^2\delta(\mathbf{Q}-\boldsymbol{\tau}), \tag{5.1}$$

where

$$F_N(\mathbf{Q}) = \sum_{\mathbf{d}}\overline{b}_d e^{i\mathbf{Q}\cdot\mathbf{d}}e^{-W_d}, \tag{5.2}$$

is called the nuclear structure factor. Here $\overline{b}_d$ is the coherent scattering length and W_d the Debye-Waller factor of the ion positioned at $\mathbf{d}$. The tabulated scattering lengths of the ions in $LiNiPO_4$ are [36]

$$\overline{b}_{Li} = -1.90 \text{ fm}, \quad \overline{b}_{Ni} = 10.3 \text{ fm}, \quad \overline{b}_P = 5.13 \text{ fm}, \quad \overline{b}_0 = 5.805 \text{ fm}. \tag{5.3}$$

$\mathbf{Q}$	$I_N(\mathbf{Q})$	$I_M(\mathbf{Q})$	$p^2\lvert F_C^c(\mathbf{Q})\rvert^2/(\text{fm})^2$	$F_N(\mathbf{Q})/(\text{fm})^2$	$\lvert P_z(\mathbf{Q})\rvert^2$	2θ	$\sin 2\theta$
(0,1,0)	4	128	123.2	–	1	11.61°	0.201
(2,0,0)	183	–	–	1261.4	–	13.53°	0.234
(0,2,0)	242	–	–	5748.2	–	23.35°	0.396

Table 5.1: Values used for the rough manual estimate of the commensurate C_z moments at zero field. The scattering angles are given for neutrons with $\lambda = 1.18$ Å. The nuclear structure factors was calculated in MATLAB, neglecting the Debye-Waller factors.

Let us compare the measured magnetic intensity at $\mathbf{Q}_M = (0,1,0)$ (figure 5.4), with the nuclear intensities $\mathbf{Q}_N = (2,0,0)$ and $\mathbf{Q}_N = (0,2,0)$ (figure 5.3). From (3.103) and (5.2), we find that

$$\frac{I_M(\mathbf{Q}_M)}{I_N(\mathbf{Q}_N)} = \frac{(pf(\mathbf{Q}_M)e^{-W_{Ni}})^2|\mathbf{F}_{M\perp}(\mathbf{Q}_M)|^2\sin 2\theta_N}{|\mathbf{F}_N(\mathbf{Q}_N)|^2\sin 2\theta_M}, \tag{5.4}$$

using that $|\mathbf{P}_z(\mathbf{Q}_M)|^2 = 1$ for $\mathbf{Q}_M = (0,1,0)$. The Lorentz factors, $1/\sin 2\theta_M$ and $1/\sin 2\theta_N$, are included in (5.4), since we are considering omega scans. Just wanting to illustrate the general idea, we neglect the form factors and Debye-Waller factors, and find from (5.4) that

$$m_z^2 = \frac{|F_N(\mathbf{Q}_N)|^2 I_M(\mathbf{Q}_M)\sin 2\theta_M}{p^2|F_C(\mathbf{Q}_M)|^2 I_N(\mathbf{Q}_N)\sin 2\theta_N}. \tag{5.5}$$

Inserting the values given in table 5.1, we get the following estimates:

- Comparing to the $\mathbf{Q} = (2,0,0)$ nuclear peak gives

$$m_z^2 = \frac{|F_N(2,0,0)|^2 I_M(0,1,0)\sin 2\theta_M}{p^2|F_C(0,1,0)|^2 I_N(2,0,0)\sin 2\theta_N} \simeq 6.15, \tag{5.6}$$

  which is equivalent to a magnetic moment

$$m_z \simeq 2.48\mu_B. \tag{5.7}$$

- Comparing to the $\mathbf{Q} = (0,2,0)$ nuclear peak gives

$$m_z^2 = \frac{|F_N(2,0,0)|^2 I_M(0,1,0)\sin 2\theta_M}{p^2|F_C(0,1,0)|^2 I_N(2,0,0)\sin 2\theta_N} \simeq 12.52, \tag{5.8}$$

  which is equivalent to a magnetic moment

$$m_z \simeq 3.54\mu_B. \tag{5.9}$$

We see that the two estimates, (5.7) and (5.9), differ significantly in size. To get a more precise value we[1] performed a full analysis of all the peaks measured on TriCS, also correcting for extinction ect. Here the size of the C_z moments was found to be

$$m_z \simeq 2.2\mu_B. \tag{5.10}$$

This value is relatively close to the estimated value in (5.7), at least compared to that of (5.9). This can be understood by noting that the angles, omega and 2θ, are much closer to the (0,1,0) values at the (2,0,0) position, than for the (0,2,0) position. The effect of extinction crucially depend on the length of the neutron path through the crystal, and is therefore very sensitive to the relative orientation between the crystal and the instrument. This orientation is ultimately determined by omega and 2θ, so it is not surprising that the measured intensities at (0,1,0) are more comparable to (2,0,0) than to (0,2,0) when we have not corrected for extinction.

5.3 The Rita experiment - supplementary data

The measurements in applied magnetic fields, $\mathbf{H}||c$, were performed in an Oxford 15 Tesla vertical magnet on RITA. For most parts of the experiment 5 meV neutrons were used, but we also collected a large number of peaks using second order neutrons with energy 20 meV. This was done by keeping the monochromater reflecting 5 meV neutrons (having 20 meV neutrons as an unavoidable bi-product[2]), while setting the analyzer to reflect neutrons with energy 20 meV. The use of second order neutrons allows for a larger portion of the reciprocal space to be investigated, but at great cost of neutron intensity.

Besides providing the possibility of applying magnetic fields up to 15 Tesla, the 5 meV data from RITA has a better signal-to-noise ratio than the TriCS data. We could therefore determine structural details that were left unresolved by the TriCS experiment. Here we present data from RITA, revealing that the magnetic structure has components other than C_z, both in zero field and in non-zero field.

[1] The magnetic structure refinement was done by Michel Kenzelmann, ETH Zurich and PSI Villigen. The software used for the refinement is written in MATLAB.

[2] Usually we remove these higher order neutrons by inserting a Beryllium filter between the sample and the analyzer. Wanting to use 20 meV neutrons in this part of the experiment the filter was of course taken out.

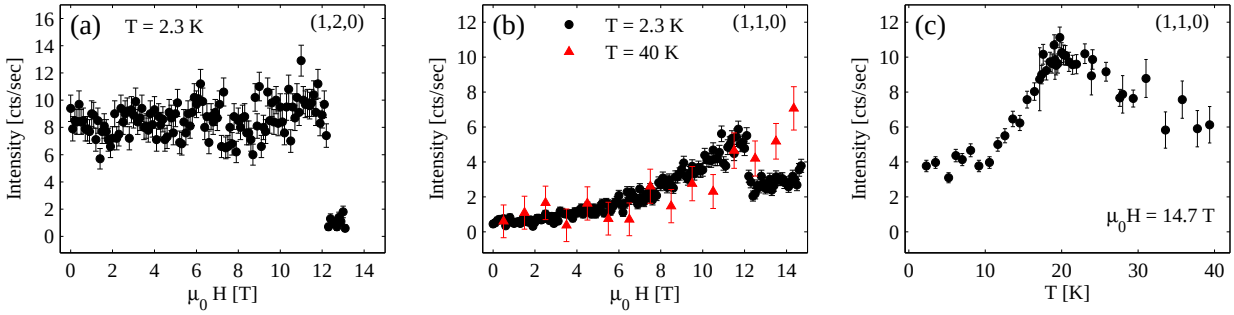

Figure 5.5: (a) Field scan of the (1,2,0) peak intensity for $\mathbf{H}||\mathbf{c}$, showing the presence of a field independent A_x component in the commensurate phase. Once the system becomes incommensurate, the commensurate A_x component disappear. (b) Field dependence of the (1,1,0) peak intensity at 2.3 K and 40 K, giving evidence of a field induced magnetic moment along **a** for $\mathbf{H}||\mathbf{c}$. The induced moments have G_x symmetry and are suppressed, but do not disappear, when the system enters the incommensurate phase. (c) Temperature dependence of the (1,1,0) peak intensity at 14.7 T. As function of temperature the commensurate G_x component is suppressed for T below 20 K, where the system is incommensurate.

Commensurate A_x structure, and field induced G_x structure

A series of field- and temperature scans, performed at the $(1,2,0)$ and $(1,1,0)$ peak positions, are shown in figure 5.5. The peak intensity of (1,2,0) at T = 2.3 K, depicted in (a), remain virtually unaffected by the field as long as the system is in the commensurate phase. Once the applied field is above 12.1 T, the system becomes incommensurate and the (1,2,0) intensity drops to zero. From the omega scans of (1,0,0) and (1,2,0), shown in figure 5.6, it is obvious that the (1,2,0) peak reflects a non-zero A_x component. So, a magnetic A_x component, resistent to changes in the applied field, is part of the magnetic structure as long as the system is commensurate.

The (1,1,0) has a very different field and temperature dependence, as figure 5.5(b) and (c) clearly shows. At 2.3 K, the (1,1,0) intensity grows as $(\mu_0 H)^2$ for fields below 12.1 T. When the system enters the incommensurate phase, at 12.1 T, the signal is suppressed, but it does not disappear. At 40 K, where the system is paramagnetic at zero field, the field induced (1,1,0) intensity grows as $(\mu_0 H)^2$ for all measured fields. Wanting to make sure that the field induced (1,1,0) signal is magnetic, we investigated the field dependence of the (1,1,0) peak by synchrotron x-ray scattering. We did this on the beamline BW5 at HASYLAB, DESY in Hamburg. Applying fields up to 10 T, we did not observe any field dependence at the (1,1,0) position. Since the performed x-ray experiment is extremely sensitive to structural changes, and do not measure magnetic signals, we conclude that the field induced (1,1,0) intensity, observed by neutrons, is magnetic in origin. Comparing the (1,1,0) and (3,1,0) scans in figure 5.6 clearly proves that the field induced magnetic intensity at (1,1,0) reflects a commensurate G_x component. This field induced commensurate G_x component is also present above the magnetic ordering temperature, and even in the high field incommensurate phase, although here it is suppressed.

We mention that there seems to be some inconsistency between the (1,2,0) omega scans from TriCS in figure 5.3, and from RITA in figure 5.6. It is hard, at least for the author, to argue why the (1,2,0) magnetic signal measured at TriCS is so much smaller than at RITA. In this chapter we have chosen to trust the RITA data when evaluating the size of the small A_x (and G_x) moments, while the TriCS data are used to evaluate the size of the large zero field C_z component. We shall not discuss the inconsistency further, but keep in mind that trusting the RITA data blindly may mean overestimating the size of the small magnetic A_x and G_x moments.

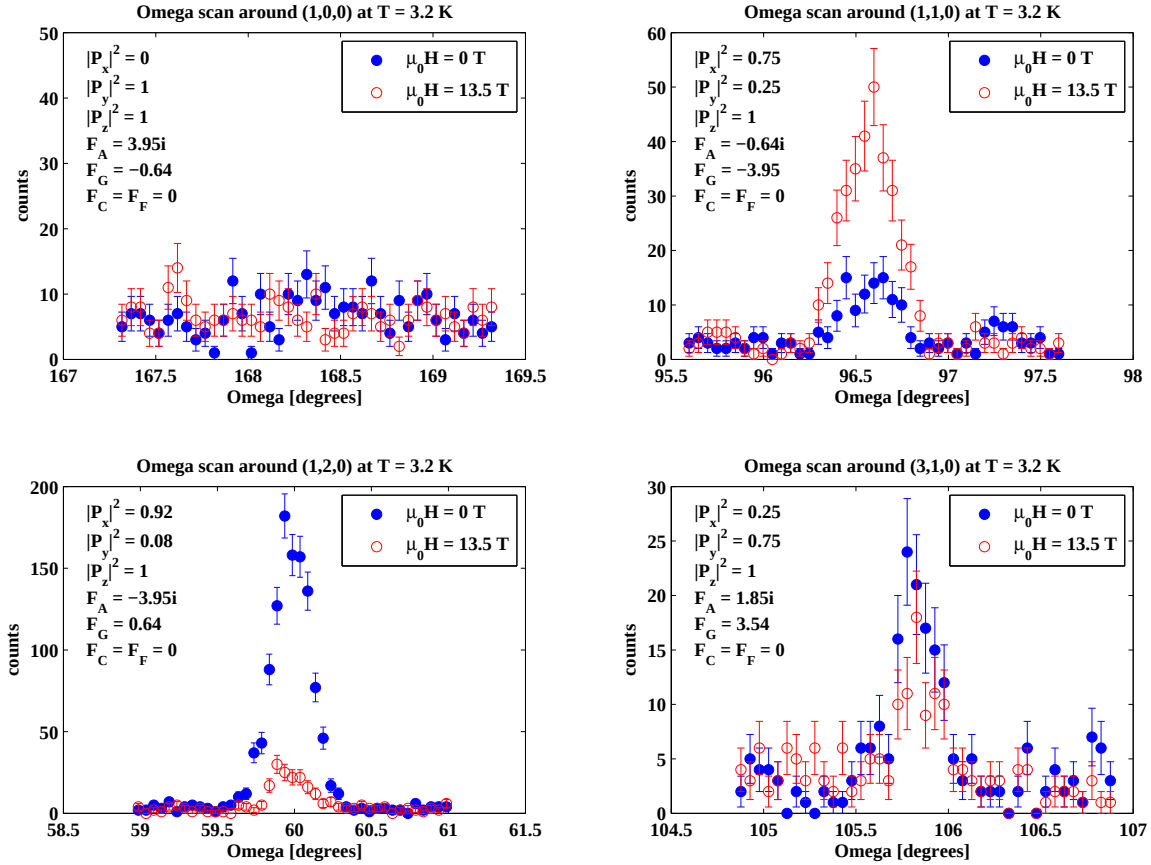

Figure 5.6: Omega scans from RITA, reflecting and distinguishing between, for the (1,0,0) and (1,2,0) peaks, A_x, A_y and A_z, and, for (1,1,0) and (3,1,0), between G_x, G_y and G_z. Counting time approximately 20 seconds per point.

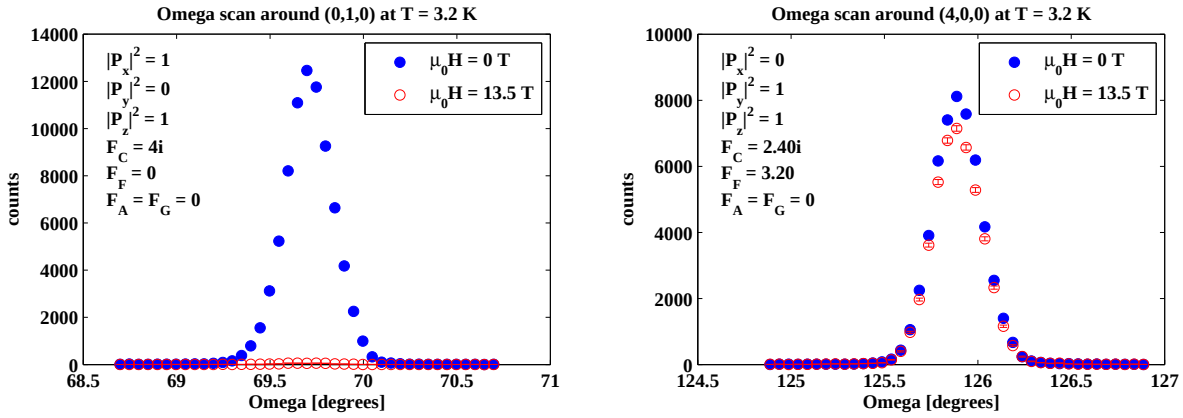

Figure 5.7: Omega scans from RITA, reflecting C and F type structures. The small magnetic intensity at the (4,0,0) position does not signal the presence of an F component, but rather reflect that the C_z component has a non-zero structure factor even here. The scans are mostly shown for comparing the relative size of the measured intensities at RITA. For instance, the integrated (1,2,0) magnetic intensity (figure 5.6) is seen to be approximately 80 times smaller than the integrated (0,1,0) magnetic intensity. Counting time approximately 20 seconds per point.

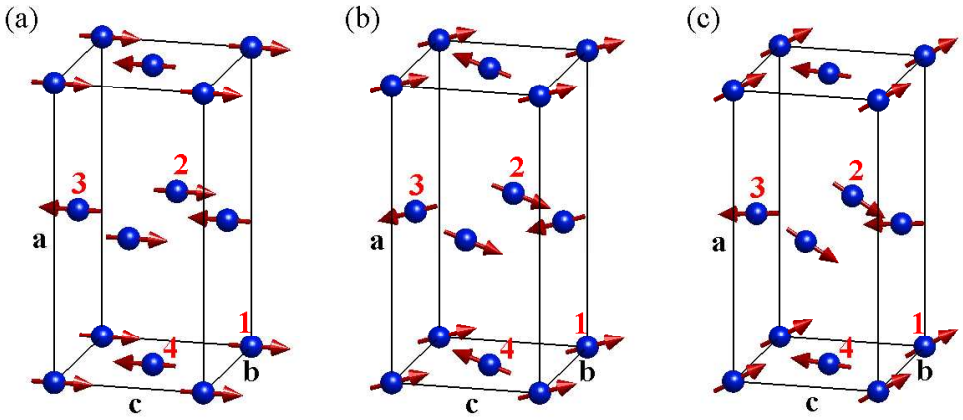

Figure 5.8: (a) The commensurate zero field magnetic structure as previously determined by powder diffraction [7]. This structure is described by a single C_z component. (b) The commensurate zero field structure determined by single crystal data from TriCS and RITA. Here the structure is composed by a large C_z and a smaller A_x component. (c) The commensurate structure of $LiNiPO_4$ in an applied field $\mathbf{H}||\mathbf{c}$. Here an additional G_x component is induced by the applied field.

5.4 Result of the full structural analysis

In the previous sections we have described many of the fundamental ideas and arguments used for the magnetic structure analysis of $LiNiPO_4$. It is now time to present the final results. The detailed refinements were performed by Michel Kenzelmann, ETH Zurich and PSI Villigen, using self-written MATLAB routines to find the structures best fitting the data. In figure 5.9-5.11 the quality of the final refinements are evaluated by comparing the measured integrated intensities with those calculated for the structures described below.

5.4.1 The zero field commensurate structure

The commensurate magnetic structure in zero field, determined from the TriCS and RITA measurements, is shown in figure 5.8(b). Here, the depicted unit cell is the magnetic unit cell, and the angles between the spins and the c-direction have been exaggerated for clarity. The commensurate magnetic moments, $\mathbf{m}_C$, are directed primarily along the c-axis, but are slightly tilted in the a direction. From the structure refinement we find that the zero field commensurate moment at T = 5 K (for an ion at position $\mathbf{r}_1$), is

$$\mathbf{m}_C = (0.3(1), 0, 2.2(2))\mu_B. \tag{5.11}$$

As already discussed, the x-components are ordered according to A_x, so

$$(m_{1x}, m_{2x}, m_{3x}, m_{4x}) = (1, -1, -1, 1)0.3\mu_B. \tag{5.12}$$

Here the index 1-4 refer to Ni^{2+} ions positioned at

$$\begin{aligned} \mathbf{r}_1 &= (0.275, 0.25, 0.98), \quad \mathbf{r}_2 = (0.775, 0.25, 0.52), \\ \mathbf{r}_3 &= (0.725, 0.75, 0.02), \quad \mathbf{r}_4 = (0.225, 0.75, 0.48), \end{aligned} \tag{5.13}$$

within the (chemical) unit cell. The z-components describe, as we already know, a C_z component, and are ordered according to

$$(m_{1z}, m_{2z}, m_{3z}, m_{4z}) = (1, 1, -1, -1)2.2\mu_B. \tag{5.14}$$

For reference we show, in figure 5.8(a), the magnetic structure which until now [7] has been considered as the zero field structure. This was based on powder diffraction data, which, although successful in determining the large C_z moments, did not detect the smaller A_x component.

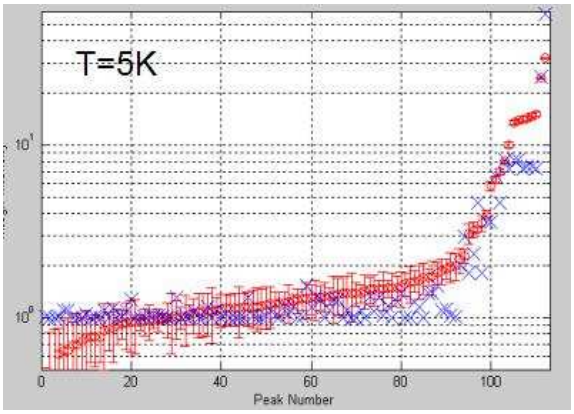

Figure 5.9: Comparing calculated (blue crosses) and measured (red circles) integrated magnetic intensities for the commensurate phase at T = 5 K and $\mu_0 H = 0$ T. The depicted data are from TriCS, and the resulting fit has a $\chi^2 = 20$. Figure from [42].

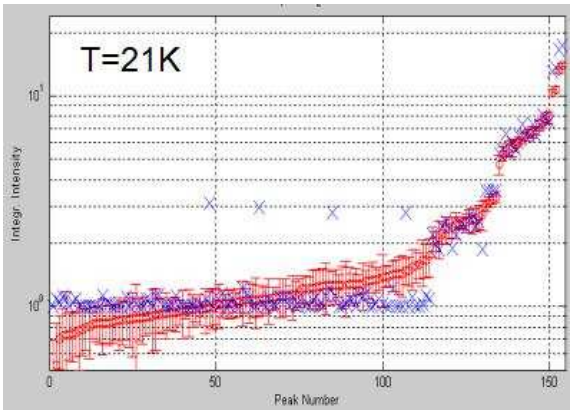

Figure 5.10: Comparing calculated (blue crosses) and measured (red circles) integrated magnetic intensities for the incommensurate phase at T = 21 K and $\mu_0 H = 0$ T. The depicted data are from TriCS, and the resulting fit has a $\chi^2 = 5.9$. Figure from [42].

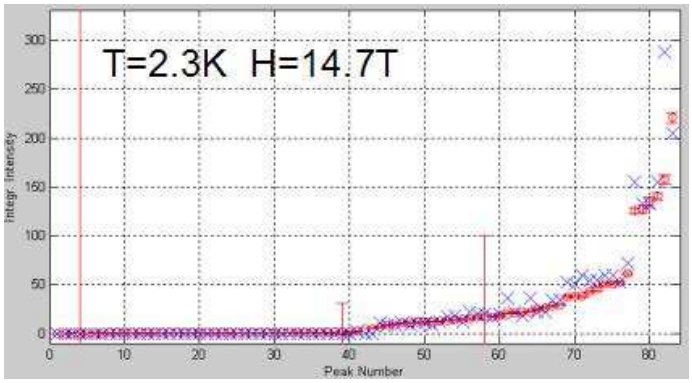

Figure 5.11: Comparing calculated (blue crosses) and measured (red circles) integrated magnetic intensities for the high field incommensurate phase at T = 2.3 K and $\mu_0 H = 14.7$ T. The depicted data are from RITA, and the resulting fit has a $\chi^2 = 25$. Figure from [42].

5.4.2 The commensurate structure in applied field, H||c

The commensurate magnetic structure in an applied field, $\mathbf{H}||c$, is shown in figure 5.8(c). The structure is a superposition of the zero field structure, described in section 5.4.1, and field induced G_x moments, of the form

$$\mathbf{m}_1 = \mathbf{m}_{st}, \quad \mathbf{m}_2 = -\mathbf{m}_{st}, \quad \mathbf{m}_3 = \mathbf{m}_{st}, \quad \mathbf{m}_4 = -\mathbf{m}_{st}, \tag{5.15}$$

with

$$\mathbf{m}_{st} = (m_{st}, 0, 0). \tag{5.16}$$

We have seen (figure 5.5) that the (1,1,0) intensity is proportional to $(\mu_0 H)^2$ for fields below 12.1 T. Since the integrated peak intensity depend on the size of the squared magnetic moment, the field induced moment, m_{st}, must be proportional to the applied field. We have evaluated the size of m_{st}, by comparing the integrated intensity of (1,1,0) with that of other magnetic peaks, and find that $m_{st} \approx 0.17\mu_B$ at 12 T. We can therefore write

$$m_{st} = \alpha_{st}\mu_0 H, \tag{5.17}$$

where

$$\alpha_{st} \approx 0.014 \ \mu_B \mathrm{T}^{-1}, \tag{5.18}$$

in the commensurate phase at low temperatures.

In figure 5.12, the low temperature commensurate structures are shown projected on the ac-plane. In zero field (a) the sum of all the magnetic components cancel out. However, when applying a field (b) along the c-axis, the spin configuration appears to have a net magnetic moment per unit cell, pointing in the direction of the applied field. A net magnetic moment requires an F component, but, as we have already discussed, small ferromagnetic signals are hard to detect due to the large nuclear peaks. If the effect of the applied field is to rotate the spins according to the symmetry of G_x, but without changing the size of the moments, an F_z component will automatically be induced. Under this assumption, we have calculated the resulting magnetic moment per unit cell in section 5.6, and compared the result with bulk magnetization data found in the literature. The analysis of the neutron data (section 5.6) and the bulk magnetization data [43] are in perfect agreement, both giving a magnetization that is near linear to the applied field in the commensurate phase, and of size 0.027 G (neutron data) and 0.03 G (bulk measurements from [43]) at 0.1 T.

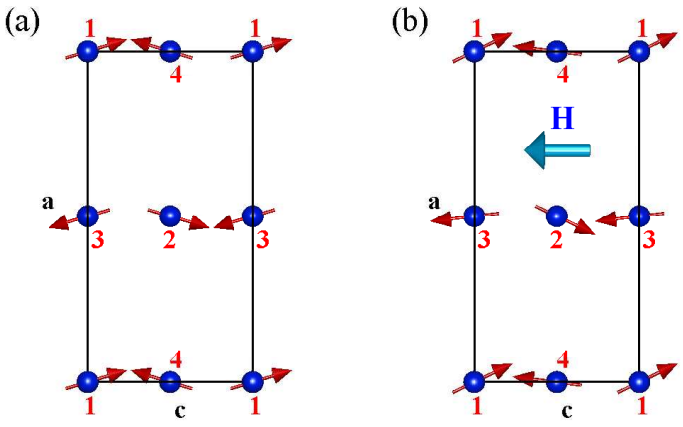

Figure 5.12: (a) The commensurate zero field structure determined by the single crystal data from TriCS and RITA, projected on the ac-plane. Here there is no net magnetic moment per unit cell. (b) The commensurate structure for $LiNiPO_4$ in an applied field $\mathbf{H}||\mathbf{c}$, projected on the ac-plane. The additional G_x component, induced by the applied field, is a result of the moments turning in a way that gives a net magnetic moment in the field direction.

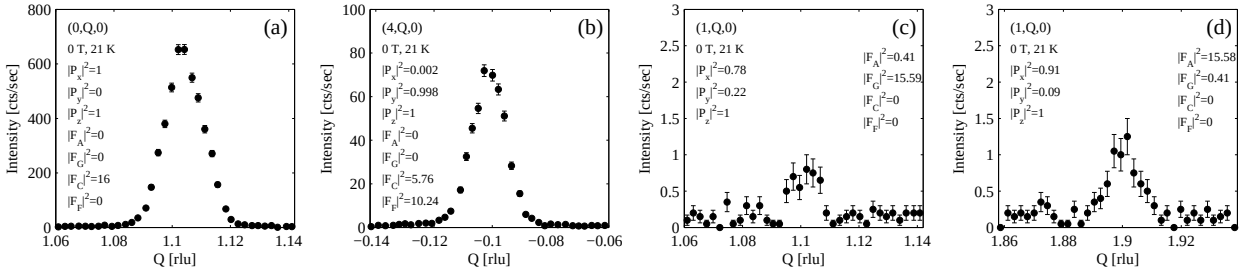

Figure 5.13: Incommensurate peaks with different symmetries at 21 K and 0 T.The scans were measured on RITA with 5 meV neutrons. (a) The $(0, 1+q, 0)$ peak. (b) The $(4, -q, 0)$ peak. (c) The $(1, 1+q, 0)$ peak. (d) The $(1, 2-q, 0)$ peak.

5.4.3 The incommensurate structure in zero field

The best fit, with $\chi^2 = 5.9$, from the 154 incommensurate scans measured on TriCS at T = 21 K, gives a single $C_z(\mathbf{k})$ structure as result. The co-linear magnetic moments are given as

$$\mathbf{m_1} = \mathbf{m}_{IC}, \mathbf{m_2} = \mathbf{m}_{IC}, \mathbf{m_3} = -\beta\mathbf{m}_{IC}, \mathbf{m_4} = -\beta\mathbf{m}_{IC}, \tag{5.19}$$

with

$$\mathbf{m}_{IC} = (0, 0, 1.2(2))\mu_B, \tag{5.20}$$

and $\beta = e^{-i\pi k_y}$. Here $\mathbf{k} = (0, k_y, 0)$ is the experimentally determined modulation vector, and the phase factor β describes the incommensurate modulation of the spins within a single unit cell. The moments are of course also modulated from one unit cell to the next. As we have already discussed (chapter 3), the modulation between unit cells is given as $e^{-i\mathbf{k}\cdot\mathbf{R_n}}$, where $\mathbf{R}_n$ is the position of the unit cell.

Figure 5.13 show scans reflecting different irreducible components measured on RITA with 5 meV neutrons. The integrated intensity of the (1,2-q,0) peak, reflecting the incommensurate $A_x(\mathbf{k})$ structure, is almost

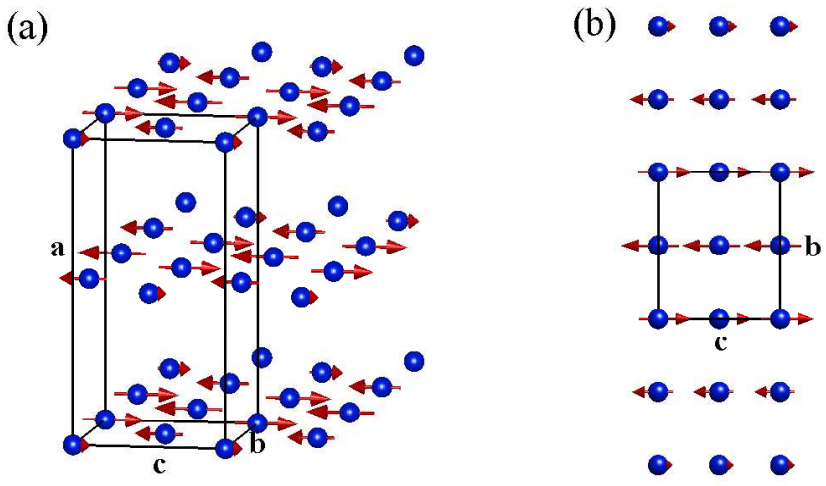

Figure 5.14: (a) The incommensurate magnetic structure at zero field, determined by single crystal data from TriCS and RITA. The structure is composed by a large $C_z(\mathbf{k})$ and a very small $A_x(\mathbf{k})$ component. The incommensurable $A_x(\mathbf{k})$ component is negligible at zero field, and has not been depicted in the figure. (b) The incommensurate zero field structure projected onto a bc plane.

500 times smaller than the (0,1+q,0) peak reflecting $C_x(\mathbf{k})$. This is much smaller (almost negligible) than the commensurate A_x component at 5 K, as seen by comparing to the (1,2,0) and (0,1,0) scans from figure 5.6 and 5.7. The zero field incommensurate structure is sketched in figure 5.14.

5.4.4 The incommensurate structure in high field and T = 2.3 K

The incommensurate part of the magnetic structure at high fields was found by analyzing 83 magnetic peaks at 14.7 T and 2.3 K, measured at RITA using second order 20 meV neutrons. The best fit, with $\chi^2 = 25$, is for a $C_z(\mathbf{k})$ structure, with moments of size $2.0(2)\mu_B$. The (1,2-q,0) scan in figures 4.8(d) shows that there is a small incommensurate $A_x(\mathbf{k})$ component at 14.7 T. The size of the integrated (1,2-q,0) intensity compared to that of the (0,1+q,0) peak, is approximately the same as that of the (1,2,0) peak compared to (0,1,0) in figure 5.6 and 5.7. This indicates that, at low temperatures, the high field incommensurate $A_x(\mathbf{k})$ and $C_z(\mathbf{k})$ moments have the same relative size as the commensurate A_x and C_z moments have at zero field. Since $\mathbf{m}_C = (0.3, 0, 2.2)\mu_B$ at zero field and 5 K, we deduce that at 14.7 T and 2.3 K the incommensurate structure is described by

$$\mathbf{m}_{IC} = (0.27, 0, 2.0)\mu_B, \tag{5.21}$$

where the x components are ordered according to

$$(m_{1x}, m_{2x}, m_{3x}, m_{4x}) = (1, -1, -\beta, \beta)0.27\mu_B, \tag{5.22}$$

and the z component according to

$$(m_{1z}, m_{2z}, m_{3z}, m_{4z}) = (1, 1, -\beta, -\beta)2.0\mu_B. \tag{5.23}$$

An additional commensurate G_x component is superposed on the incommensurate structure at 14.7 T, as witnessed by the non-zero intensity in the (1,1,0) commensurate peak in figure 5.5. Evaluating the integrated intensities, we estimate the size of the commensurate G_x moment to be approximately $0.11\mu_B$. There is probably also an accompanying F_z component, due to the magnetization of the system by the applied field. We shall not evaluate this component, but merely refer the reader to the discussion of the induced commensurate magnetization, given in section 5.6. In figure 5.15 we depict the high field incommensurate structure as described above.

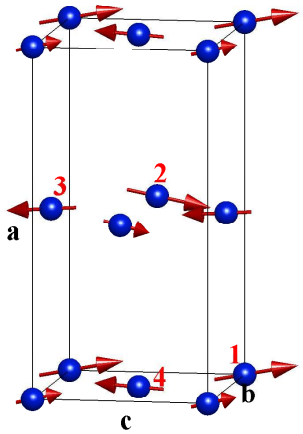

Figure 5.15: The high field incommensurate structure for $LiNiPO_4$ in an applied field $\mathbf{H}||\mathbf{c}$ at T = 2.3 K.

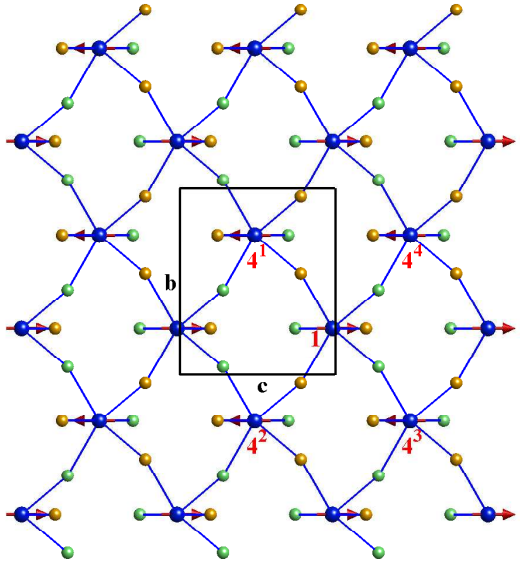

Figure 5.16: A buckled nickel-oxide plane seen from above. Neighboring Ni ions (blue) are connected via Ni-O-Ni bonds. The yellow ions represent oxygen lying above the Ni plane, while the green ions represent oxygen lying below the plane. We see that the paths between a Ni ion (1) and each of its 4 nearest neighboring Ni ions (4^1)-(4^4) are not the same. The difference between "up" and "down" in the environment of two neighboring Ni ions allows for DM interactions between (1) and (4).

5.5 Dzyaloshinsky-Moriya interactions

In this section, we discuss the possible origin of the small magnetic A_x component in the commensurate structure. We show that the allowed Dzyaloshinsky-Moriya (DM) interactions in $LiNiPO_4$, have symmetries that support the A_x component. This could indicate, but of course does not prove, that small DM interactions are the reason for the A_x components.

5.5.1 Microscopic considerations

The Dzyaloshinsky-Moriya (DM) interaction [24, 28] between two ions (1) and (2) can be written

$$\mathcal{H}_{DM} = \mathbf{D}_{12} \cdot (\mathbf{S}_1 \times \mathbf{S}_2), \tag{5.24}$$

where

$$\mathbf{D}_{12} = -2i\lambda \left(\sum_{n_1} \frac{\langle g_1|\mathbf{L}_1|n_1\rangle}{E_{n_1} - E_{g_1}} J(n_1 g_2, g_1 g_2) - \sum_{n_2} \frac{\langle g_2|\mathbf{L}_2|n_2\rangle}{E_{n_2} - E_{g_2}} J(n_2 g_1, g_2 g_1) \right) \equiv \widehat{\mathbf{L}}_{12} - \widehat{\mathbf{L}}_{21}. \tag{5.25}$$

Here we have defined the pseudo-vector

$$\widehat{\mathbf{L}}_{12} = (\widehat{L}^x_{12}, \widehat{L}^y_{12}, \widehat{L}^z_{12}) = -2i\lambda \sum_{n_1} \frac{\langle g_1|\mathbf{L}_1|n_1\rangle}{E_{n_1} - E_{g_1}} J(n_1 g_2, g_1 g_2), \tag{5.26}$$

where $|g_1\rangle$ is the ground state and $|n_1\rangle$ exited states of ion (1), while $J(n_1 g_2, g_1 g_2)$ are super-exchange matrix elements between (1) and (2). From (5.25) it is clear that if the environments of (1) and (2) are identical then $\widehat{\mathbf{L}}_{12} = \widehat{\mathbf{L}}_{21}$ and there will be no DM interaction between the two ions.

Let us consider the case of $LiNiPO_4$. Here there are 4 magnetic Ni^{2+} ions per unit cell, situated at positions

$$\begin{aligned}\mathbf{r}_1 &= (0.275, 0.25, 0.98), \mathbf{r}_2 = (0.775, 0.25, 0.52),\\ \mathbf{r}_3 &= (0.725, 0.75, 0.02), \mathbf{r}_4 = (0.225, 0.75, 0.48).\end{aligned} \tag{5.27}$$

The nickel ion (1) has four nearest Ni neighbors, shown as (4^1)-(4^4) in figure 5.16. The figure shows that the positions of oxygen around (1) are different from those around $(4^{1\text{-}4})$. Therefore we can not exclude that, for instance, the vectors $\widehat{\mathbf{L}}_{14^1}$ and $\widehat{\mathbf{L}}_{4^11}$ are pointing in different directions (although they have the same length), thus causing non-zero DM interactions between (1) and (4^1). Inspecting (5.26) we see that in general $\widehat{\mathbf{L}}_{14^m}$ must be the same[3] for $m =$ 1-4. Therefore

$$\mathbf{D}_{14^1} = \widehat{\mathbf{L}}_{14^1} - \widehat{\mathbf{L}}_{4^11} = \widehat{\mathbf{L}}_{14^2} - \widehat{\mathbf{L}}_{4^21} = \mathbf{D}_{14^2}. \tag{5.28}$$

This holds true also for the two other nearest neighbors, and we have

$$\mathbf{D}_{14^1} = \mathbf{D}_{14^2} = \mathbf{D}_{14^3} = \mathbf{D}_{14^4}. \tag{5.29}$$

In the adjacent NiO plane the Ni ions numbered as (2) have the four neighbors $(3^{1\text{-}4})$. The same considerations hold for these ions, so

$$\mathbf{D}_{23^1} = \mathbf{D}_{23^2} = \mathbf{D}_{23^3} = \mathbf{D}_{23^4}. \tag{5.30}$$

5.5.2 Symmetry considerations

The space group of $LiNiPO_4$ is *Pnma*, with the symmetry group[4]

$$\mathbf{G} = \{1, 2'_x, 2'_y, 2'_z, \bar{1}, m'_{xy}, m'_{xz}, m'_{yz}\}, \tag{5.31}$$

where

1 is the identity :	$1(x,y,z) = (x,y,z),$	(5.32a)
$2'_x$ is a 180° screw axis around $(x, 0.25, 0.25)$:	$2'_x(x,y,z) = (x+0.5, 0.5-y, 0.5-z),$	(5.32b)
$2'_y$ is a 180° screw axis around $(0, y, 0)$:	$2'_y(x,y,z) = (-x, y+0.5, -z),$	(5.32c)
$2'_z$ is a 180° screw axis around $(0.25, 0, z)$:	$2'_z(x,y,z) = (0.5-x, -y, z+0.5),$	(5.32d)
$\bar{1}$ is inversion in $(0,0,0)$:	$\bar{1}(x,y,z) = (-x,-y,-z),$	(5.32e)
m'_{xy} is a glide plane $z = 0.25$ with glide vector $(0.5,0,0)$:	$m'_{xy}(x,y,z) = (x+0.5, y, 0.5-z),$	(5.32f)
m'_{xz} is a mirror plane $y = 0.25$ without glide vector :	$m'_{xz}(x,y,z) = (x, 0.5-y, z),$	(5.32g)
m'_{yz} is a glide plane $x = 0.25$ with glide vector $(0, 0.5, 0.5)$:	$m'_{yz}(x,y,z) = (0.5-x, y+0.5, z+0.5).$	(5.32h)

In the following we want to check which DM terms are allowed by symmetry. This requires finding all DM contributions that are invariant under both the full symmetry group G and all lattice translations. First of all we must see how a term

$$\mathbf{D}_{ij} \cdot [\mathbf{S}_i \times \mathbf{S}_j], \tag{5.33}$$

[3]Here we assume that $J(n_1 g_{4^m}, g_1 g_{4^m})$ and $J(n_{4^m} g_1, g_{4^m} g_1)$, given in section 2.3.3, are the same for $m =$1-4.
[4]Strictly speaking G is not a group before being combined with the group of lattice translations.

	1	$2'_x$	$2'_y$	$2'_z$	$\bar{1}$	m'_{xy}	m'_{xz}	m'_{yz}
$\mathbf{r}_1$	$\mathbf{r}_1$	$\mathbf{r}_2+00\bar{1}$	$\mathbf{r}_3+\bar{1}0\bar{1}$	$\mathbf{r}_4+0\bar{1}1$	$\mathbf{r}_3+\bar{1}\bar{1}\bar{1}$	$\mathbf{r}_2+00\bar{1}$	$\mathbf{r}_1$	$\mathbf{r}_4+001$
$\mathbf{r}_2$	$\mathbf{r}_2$	$\mathbf{r}_1+10\bar{1}$	$\mathbf{r}_4+\bar{1}0\bar{1}$	$\mathbf{r}_3+\bar{1}\bar{1}1$	$\mathbf{r}_4+\bar{1}\bar{1}\bar{1}$	$\mathbf{r}_1+10\bar{1}$	$\mathbf{r}_2$	$\mathbf{r}_3+\bar{1}01$
$\mathbf{r}_3$	$\mathbf{r}_3$	$\mathbf{r}_4+1\bar{1}0$	$\mathbf{r}_1+\bar{1}1\bar{1}$	$\mathbf{r}_2+\bar{1}\bar{1}0$	$\mathbf{r}_1+\bar{1}\bar{1}\bar{1}$	$\mathbf{r}_4+100$	$\mathbf{r}_3+0\bar{1}0$	$\mathbf{r}_2+\bar{1}10$
$\mathbf{r}_4$	$\mathbf{r}_4$	$\mathbf{r}_3+0\bar{1}0$	$\mathbf{r}_2+\bar{1}1\bar{1}$	$\mathbf{r}_1+0\bar{1}0$	$\mathbf{r}_2+\bar{1}\bar{1}\bar{1}$	$\mathbf{r}_3$	$\mathbf{r}_4+0\bar{1}0$	$\mathbf{r}_1+010$
S_x	S_x	S_x	$-S_x$	$-S_x$	S_x	$-S_x$	$-S_x$	S_x
S_y	S_y	$-S_y$	S_y	$-S_y$	S_y	$-S_y$	S_y	$-S_y$
S_z	S_z	$-S_z$	$-S_z$	S_z	S_z	S_z	$-S_z$	$-S_z$

Table 5.2: The transformed positions of $\mathbf{r}_1$-$\mathbf{r}_4$ and transformed spin components S_x, S_y, S_z under the symmetry elements in G. For the readers convenience we reproduce this table (and the list of symmetry elements) here, although it has already been given in section 3.2.2.

where $\mathbf{D}_{ij}$ is a constant pseudo-vector, transforms under the symmetry operations. Let us for instance consider $2'_z$. Using table 5.2 we write

$$\begin{aligned} 2'_z(\mathbf{D}_{ij}\cdot[\mathbf{S}_i\times\mathbf{S}_j]) = \mathbf{D}_{ij}\cdot(2'_z[\mathbf{S}_i\times\mathbf{S}_j]) &= \begin{vmatrix} D^x_{ij} & D^y_{ij} & D^z_{ij} \\ -S^x_{2'_z(\mathbf{r}_i)} & -S^y_{2'_z(\mathbf{r}_i)} & S^z_{2'_z(\mathbf{r}_i)} \\ -S^x_{2'_z(\mathbf{r}_j)} & -S^y_{2'_z(\mathbf{r}_j)} & S^z_{2'_z(\mathbf{r}_j)} \end{vmatrix} \\ &= \begin{vmatrix} -D^x_{ij} & -D^y_{ij} & D^z_{ij} \\ S^x_{2'_z(\mathbf{r}_i)} & S^y_{2'_z(\mathbf{r}_i)} & S^z_{2'_z(\mathbf{r}_i)} \\ S^x_{2'_z(\mathbf{r}_j)} & S^y_{2'_z(\mathbf{r}_j)} & S^z_{2'_z(\mathbf{r}_j)} \end{vmatrix} = 2'_z(\mathbf{D}_{ij})\cdot[\mathbf{S}_{2'_z(\mathbf{r}_i)}\times\mathbf{S}_{2'_z(\mathbf{r}_j)}], \end{aligned} \tag{5.34}$$

where

$$2'_z(\mathbf{D}_{ij}) = (-D^x_{ij}, -D^y_{ij}, D^z_{ij}). \tag{5.35}$$

Doing this for all symmetries $R\in G$ it is easily seen that

$$R(\mathbf{D}_{ij}\cdot[\mathbf{S}_i\times\mathbf{S}_j]) = R(\mathbf{D}_{ij})\cdot[\mathbf{S}_{R(\mathbf{r}_i)}\times\mathbf{S}_{R(\mathbf{r}_j)}], \tag{5.36}$$

where $\mathbf{D}_{ij}$ now transforms under R as a pseudo-vector, i.e. like an angular momentum.

Let R be any symmetry operation (including lattice translations) of $LiNiPO_4$, and let $R(\mathbf{r}_i)\equiv R(i)$. An invariant with the term $\mathbf{D}_{ij}\cdot[\mathbf{S}_i\times\mathbf{S}_j]$, must also include $R(\mathbf{D}_{ij}\cdot[\mathbf{S}_i\times\mathbf{S}_j])$. This is possible if and only if

$$R(\mathbf{D}_{ij}\cdot[\mathbf{S}_i\times\mathbf{S}_j]) = \mathbf{D}_{R(i)R(j)}\cdot[\mathbf{S}_{R(i)}\times\mathbf{S}_{R(j)}], \tag{5.37}$$

which is equivalent to the requirement

$$R(\mathbf{D}_{ij}) = \mathbf{D}_{R(i)R(j)}, \tag{5.38}$$

for all symmetry operations R. Remembering the microscopic conditions (5.29) and (5.30), we therefore have the following three conditions (in a system with only one type of magnetic ions):

1) *For any two magnetic ions i and j*

$$\mathbf{D}_{ij} = -\mathbf{D}_{ji}. \tag{5.39}$$

2) *If the ions i and i' have identical surroundings, and if the ions j and j' have identical surroundings, then*

$$\mathbf{D}_{ij} = \mathbf{D}_{i'j'}, \tag{5.40}$$

if the path between i and j is equivalent to (but not necessarily identical with) the path between i' and j'.

3) *For any symmetry operation R and for any two magnetic ions i and j*

$$R(\mathbf{D}_{ij}) = \mathbf{D}_{R(i)R(j)}, \tag{5.41}$$

where $\mathbf{D}_{ij}$ transforms under R as a pseudo-vector.

DM interactions between $1 \leftrightarrow 4$, and $2 \leftrightarrow 3$

	1	$2'_x$	$2'_y$	$2'_z$	$\bar{1}$	m'_{xy}	m'_{xz}	m'_{yz}
$R(D^y_{14})$	D^y_{14}	$-D^y_{14}$	D^y_{14}	$-D^y_{14}$	D^y_{14}	$-D^y_{14}$	D^y_{14}	$-D^y_{14}$
$D^y_{R(1)R(4)}$	D^y_{14}	D^y_{23}	D^y_{32}	D^y_{41}	D^y_{32}	D^y_{23}	D^y_{14}	D^y_{41}

Table 5.3: Symmetry transformations of D^y_{14}.

We begin by investigating the possible DM interactions between ions of type (1) and (4), and (2) and (3) respectively. These include the interactions between nearest neighboring Ni ions. We want to construct an invariant

$$\begin{aligned}\mathcal{H}_{DM} = \sum_{1,2} \Big(&\mathbf{D}_{14} \cdot [\mathbf{S}_1 \times \mathbf{S}_{4^1} + \mathbf{S}_1 \times \mathbf{S}_{4^2} + \mathbf{S}_1 \times \mathbf{S}_{4^3} + \mathbf{S}_1 \times \mathbf{S}_{4^4}] \\ &+ \mathbf{D}_{23} \cdot [\mathbf{S}_2 \times \mathbf{S}_{3^1} + \mathbf{S}_2 \times \mathbf{S}_{3^2} + \mathbf{S}_2 \times \mathbf{S}_{3^3} + \mathbf{S}_2 \times \mathbf{S}_{3^4}] \Big).\end{aligned} \tag{5.42}$$

Using the rules (5.39)-(5.41) and table 5.2 we find that

$$\left.\begin{aligned} m'_{xz}(\mathbf{D}_{14}) =& (-D^x_{14}, D^y_{14}, -D^z_{14}) \\ m'_{xz}(\mathbf{D}_{14}) =& \mathbf{D}_{m'_{xz}(1)m'_{xz}(4)} = \mathbf{D}_{14'} = \mathbf{D}_{14} = (D^x_{14}, D^y_{14}, D^z_{14}) \end{aligned}\right\} \Rightarrow \mathbf{D}_{14} = (0, D^y_{14}, 0). \tag{5.43}$$

Similarly one finds that $\mathbf{D}_{23} = (0, D^y_{23}, 0)$. Checking the other symmetry operations (table 5.3) we see that (5.42) is invariant if $\mathbf{D}_{14} = (0, D, 0)$, and $\mathbf{D}_{14} = -\mathbf{D}_{23}$. Writing the invariant explicitly

$$\begin{aligned}\mathcal{H}_{DM} = \sum_{1,2} \Big\{ &(0, D, 0) \cdot [\mathbf{S}_1 \times \mathbf{S}_{4^1} + \mathbf{S}_1 \times \mathbf{S}_{4^2} + \mathbf{S}_1 \times \mathbf{S}_{4^3} + \mathbf{S}_1 \times \mathbf{S}_{4^4}] \\ &- (0, D, 0) \cdot [\mathbf{S}_2 \times \mathbf{S}_{3^1} + \mathbf{S}_2 \times \mathbf{S}_{3^2} + \mathbf{S}_2 \times \mathbf{S}_{3^3} + \mathbf{S}_2 \times \mathbf{S}_{3^4}] \Big\},\end{aligned} \tag{5.44}$$

we can inspect the terms between the ions in a single unit cell. Remembering that the dominant magnetic structure has the following spin configuration $(S^z_1, S^z_2, S^z_3, S^z_4) = (S, S, -S, -S)$ for the ions in a unit cell, we find for a single unit cell

$$\mathcal{H}'_{DM} = \mathbf{D} \cdot [\mathbf{S}_1 \times \mathbf{S}_4] - \mathbf{D} \cdot [\mathbf{S}_2 \times \mathbf{S}_3] = D(S^z_1 S^x_4 - S^x_1 S^z_4 - (S^z_2 S^x_3 - S^x_2 S^z_3)) = DS(S^x_1 - S^x_2 - S^x_3 + S^x_4). \tag{5.45}$$

Clearly $\mathcal{H}'_{DM}$ favors a spin configuration with $(S^x_1, S^x_2, S^x_3, S^x_4) = (S', -S', -S', S')$, which is exactly what we have measured experimentally.

DM interactions between $1 \leftrightarrow 2$, and $3 \leftrightarrow 4$

	1	$2'_x$	$2'_y$	$2'_z$	$\bar{1}$	m'_{xy}	m'_{xz}	m'_{yz}
$R(D^y_{12})$	D^y_{12}	$-D^y_{12}$	D^y_{12}	$-D^y_{12}$	D^y_{12}	$-D^y_{12}$	D^y_{12}	$-D^y_{12}$
$D^y_{R(1)R(2)}$	D^y_{12}	D^y_{21}	D^y_{34}	D^y_{43}	D^y_{34}	D^y_{21}	D^y_{12}	D^y_{43}

Table 5.4: Symmetry transformations of D^y_{12}.

We investigate the possibility of DM interactions between ions of type (1) and (2), and (3) and (4) in the same way as above. Since

$$\left.\begin{aligned} m'_{xz}(\mathbf{D}_{12}) =& (-D^x_{12}, D^y_{12}, -D^z_{12}) \\ m'_{xz}(\mathbf{D}_{12}) =& \mathbf{D}_{m'_{xz}(1)m'_{xz}(2)} = \mathbf{D}_{12} = (D^x_{12}, D^y_{12}, D^z_{12}) \end{aligned}\right\} \Rightarrow \mathbf{D}_{12} = (0, D^y_{12}, 0), \tag{5.46}$$

and using table 5.4 we see that the interactions are only possible if $D_{12} = D_{34} = (0, D, 0)$.

Using $(S_1^z, S_2^z, S_3^z, S_4^z) = (S, S, -S, -S)$ for the ions in a unit cell, we now find

$$\mathcal{H}'_{DM} = \mathbf{D}\cdot[\mathbf{S}_1 \times \mathbf{S}_2] + \mathbf{D}\cdot[\mathbf{S}_3 \times \mathbf{S}_4] = D(S_1^z S_2^x - S_1^x S_2^z + (S_3^z S_4^x - S_3^x S_4^z)) = -DS(S_1^x - S_2^x - S_3^x + S_4^x), \quad (5.47)$$

which also favors $(S_1^x, S_2^x, S_3^x, S_4^x) = (S', -S', -S', S')$.

DM interactions between $1 \leftrightarrow 3$, and $2 \leftrightarrow 4$

Here there are no possible DM interactions, since

$$\left.\begin{array}{l} \bar{1}(\mathbf{D}_{13}) = (D_{13}^x, D_{13}^y, D_{13}^z) = \mathbf{D}_{13} \\ \bar{1}(\mathbf{D}_{13}) = \mathbf{D}_{\bar{1}(1)\bar{1}(3)} = \mathbf{D}_{31} = -\mathbf{D}_{13} \end{array}\right\} \Rightarrow \mathbf{D}_{13} = 0. \quad (5.48)$$

DM interactions between $1 \leftrightarrow 1'$, $2 \leftrightarrow 2'$, $3 \leftrightarrow 3'$, and $4 \leftrightarrow 4'$

Here there are no possible DM interactions, since according to (5.39) and (5.40)

$$\mathbf{D}_{11'} = -\mathbf{D}_{1'1} = -\mathbf{D}_{11'}, \quad (5.49)$$

which is only possible if $\mathbf{D}_{11'} = 0$. Similarly with $\mathbf{D}_{22'}$, $\mathbf{D}_{33'}$ and $\mathbf{D}_{44'}$.

5.6 Field induced magnetization

We know from our neutron diffraction experiments that the four Ni^2 ions in a unit cell has the following magnetic moments in the commensurate (C) phase at zero field

$$\begin{array}{l} \mathbf{m}_C(1) = m(\sin\theta_C, 0, \cos\theta_C), \\ \mathbf{m}_C(2) = m(-\sin\theta_C, 0, \cos\theta_C), \\ \mathbf{m}_C(3) = m(-\sin\theta_C, 0, -\cos\theta_C), \\ \mathbf{m}_C(4) = m(\sin\theta_C, 0, -\cos\theta_C), \end{array} \quad (5.50)$$

as shown in figure 5.17(a). Here $m \simeq 2.2\mu_B$ and

$$\theta_C \simeq \tan\theta_C \simeq \frac{0.3\mu_B}{2.2\mu_B} = 0.14 \Rightarrow \theta_C \approx 7.8^\circ. \quad (5.51)$$

Applying a magnetic field $\mathbf{H}||\mathbf{c}$ induces staggered magnetic moments

$$\begin{array}{l} \mathbf{m}_{st}(1) = (m_{st}, 0, 0), \\ \mathbf{m}_{st}(2) = (-m_{st}, 0, 0), \\ \mathbf{m}_{st}(3) = (m_{st}, 0, 0), \\ \mathbf{m}_{st}(4) = (-m_{st}, 0, 0), \end{array} \quad (5.52)$$

as witnessed by the (1,1,0) magnetic neutron peak. Macroscopic bulk measurements show that the field also induce a non-zero magnetization. This magnetization should be reflected in the neutron diffraction experiment as a field induced ferromagnetic component. Unfortunately such a ferromagnetic component is reflected only in the large structural peaks making these magnetic peaks nearly impossible to measure.

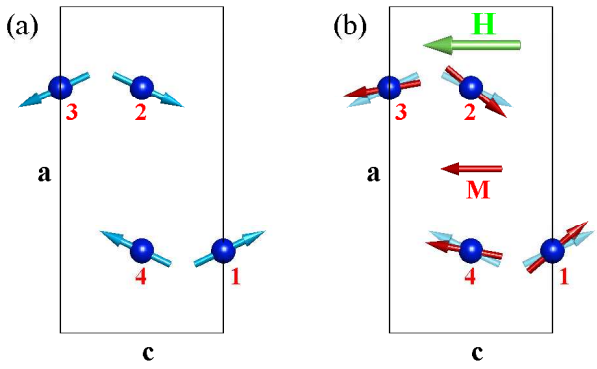

Figure 5.17: (a) Spin configuration (blue arrows) in the commensurate phase of $LiNiPO_4$ in zero field. Angles have been exaggerated for clarity. (b) Spin configuration (red arrows) in the commensurate phase of $LiNiPO_4$ when a field $\mathbf{H}||\mathbf{c}$ is applied (the blue semitransparent arrows depict the zero field moments). It is assumed that the field does not alter the size of the localized moments. If this is the case the moments are rotated by $\mathbf{H}$ in a manor that induce a net magnetization $\mathbf{M}||\mathbf{c}$. The calculated size and field dependence of $\mathbf{M}$ is consistent to that of bulk magnetization measurements.

5.6.1 Calculating the magnetization

From the neutron diffraction experiment we are able to calculate the magnetization (and thereby the ferromagnetic component), if the field rotates the localized moments $\mathbf{m}_H$ in the ac-plane, but does not change the size of the moments (figure 5.17(b)). Assuming that this is the case we have

$$\begin{aligned}
\mathbf{m}_H(1) &= m(\sin\theta_1, 0, \cos\theta_1),\\
\mathbf{m}_H(2) &= m(-\sin\theta_2, 0, \cos\theta_2),\\
\mathbf{m}_H(3) &= m(-\sin\theta_3, 0, -\cos\theta_3),\\
\mathbf{m}_H(4) &= m(\sin\theta_4, 0, -\cos\theta_4),
\end{aligned} \tag{5.53}$$

where $m = 2.2\mu_B$ as in zero field. The total magnetic moment $\mathbf{m}_{uc}$ per unit cell is

$$\begin{aligned}
\mathbf{m}_{uc} &= \mathbf{m}_H(1) + \mathbf{m}_H(2) + \mathbf{m}_H(3) + \mathbf{m}_H(4)\\
&= m(\sin\theta_1 - \sin\theta_2 - \sin\theta_3 + \sin\theta_4, 0, \cos\theta_1 + \cos\theta_2 - \cos\theta_3 - \cos\theta_4),
\end{aligned} \tag{5.54}$$

where

$$\begin{aligned}
m\sin\theta_1 &= m(\sin\theta_C + \frac{m_{st}}{m}),\\
-m\sin\theta_2 &= -m(\sin\theta_C + \frac{m_{st}}{m}),\\
-m\sin\theta_3 &= -m(\sin\theta_C - \frac{m_{st}}{m}),\\
m\sin\theta_4 &= m(\sin\theta_C - \frac{m_{st}}{m}).
\end{aligned} \tag{5.55}$$

Eq. (5.55) reflects that the only magnetic moments in the x-direction are expected to be those coming from the observed A and G type structures. This is equivalent to assuming the induced macroscopic magnetization is directed parallel to the applied field. From (5.55) we see that $\theta_1 = \theta_2$ and $\theta_3 = \theta_4$, and therefore

$$\mathbf{m}_{uc} = 2m(0, 0, \cos\theta_1 - \cos\theta_3). \tag{5.56}$$

Since θ_1-θ_4 and θ_C are all relatively small angles we rewrite (5.55) as

$$\begin{aligned}
\theta_1 = \theta_2 &\simeq \theta_C + \theta_{st},\\
\theta_3 = \theta_4 &\simeq \theta_C - \theta_{st},
\end{aligned} \tag{5.57}$$

with

$$\theta_{st} = \frac{m_{st}}{m}. \tag{5.58}$$

Inserting

$$\cos\theta_1 - \cos\theta_3 = \cos(\theta_C + \theta_{st}) - \cos(\theta_C - \theta_{st}) = -2\sin\theta_C \sin\theta_{st} \simeq -2\theta_C\theta_{st}, \tag{5.59}$$

into (5.56), and using (5.51) and (5.58), we find that the magnetic moment per unit cell is

$$\mathbf{m}_{uc} \simeq -4m(0, 0, \theta_C\theta_{st}) \simeq -(0, 0, 0.55m_{st}). \tag{5.60}$$

At 12 T we have found $m_{st} \simeq 0.17\mu_B$, so the total magnetic moment per unit cell is $m_{uc} = 0.094\mu_B$. The volume of a unit cell is approximately $V \simeq 270$ Å^{-1}, giving a magnetization $\mathbf{M}$ of

$$|\mathbf{M}| = \frac{|\mathbf{m}_{uc}|}{V} \simeq \frac{0.094 \cdot 0.927 \cdot 10^{-23}\mathrm{Am}^2}{270 \cdot 10^{-30}\mathrm{m}^3} = 3227\mathrm{A/m} = 3.2 \text{ G}, \tag{5.61}$$

at 12 T. We estimate the field dependence of $\mathbf{M}$ by noting that the intensity of the (1,1,0) peak is proportional to $(\mu_0 H)^2$. Since the intensity is also proportional to m_{st}^2, we have that $m_{st} \propto \mu_0 H$, and therefore $\mathbf{M} \propto \mathbf{H}$. Bulk measurements, performed by Kharchenco *et al.* [43], reports of a magnetization that is around 0.03 G at 0.1 T and 5 K, and has a nearly linear dependence on $\mathbf{H}$. This is consistent with the size and field behavior of $\mathbf{M}$ calculated in this section.

5.7 Magnetic structures and the ME effect

We end this chapter by a few considerations concerning the ME effect in $LiNiPO_4$. Inspecting the symmetry of the commensurate and incommensurate magnetic structures, we argue that only the commensurate structures support a spontaneous electric polarization, and only in presence of an external magnetic field.

To briefly explain this conclusion, we note that the incommensurate structures are invariant under inversion in certain points, while the commensurate structures are not. An electric polarization requires a system without inversion symmetry, so the incommensurate phases do not favor electric polarizations. Furthermore, the zero field magnetic structures has a 180° screw axis along the b direction. This symmetry is not consistent with that of an electric polarization with a component along the a axis. However, when a field is applied along the c direction, the overall symmetry of the Hamiltonian is changed and the screw axis symmetry along b is broken. This allows for an electric polarization along a. Arguments such as these lead to the conclusion given above.

Chapter 6

Spin wave calculations

6.1 Introduction

This is an account of the dispersion and intensity calculations of spin waves in $LiNiPO_4$ using linear spin wave theory. Here, in the introduction, we outline the general approach described in the following sections.

We start off by expressing the spin Hamiltonian as a quadratic form

$$= \sum_{\mathbf{q}} H_{\mathbf{q}} = \frac{1}{2} \sum_{\mathbf{q}} \mathbf{a}^{+} \mathbf{H} \mathbf{a}, \tag{6.1}$$

where $\mathbf{H}$ and $\mathbf{a}$ are defined in (6.4). The derivation of this Hamiltonian for $LiNiPO_4$ is given in section 6.5.

Solving the following 4×4 eigenvalue problem

$$\mathbf{I}_1 \mathbf{H} \begin{bmatrix} \widetilde{T}_1 \\ \widetilde{T}_2 \\ \widetilde{T}_3 \\ \widetilde{T}_4 \end{bmatrix} = \omega \begin{bmatrix} \widetilde{T}_1 \\ \widetilde{T}_2 \\ \widetilde{T}_3 \\ \widetilde{T}_4 \end{bmatrix}, \tag{6.2}$$

where $\mathbf{I}_1$ is defined in (6.20), is shown (section 6.2.1) to give the eigenenergies of $H_{\mathbf{q}}$. Solving (6.2) is an easy task for a computer (an analytical expression for the eigenenergies of $LiNiPO_4$ is given in section 6.5.1). Besides computing the eigenvalues we also find the corresponding eigenvectors. The matrix having four arbitrary computer generated eigenvectors as columns is called $\widetilde{\mathbf{T}}$. From $\widetilde{\mathbf{T}}$ we find the transformation matrix $\mathbf{T}$ which is needed for calculating the intensities. The relation between $\widetilde{\mathbf{T}}$ and $\mathbf{T}$ is explained in section 6.2.2.

The intensity calculation is sketched in section 6.3, and the resulting scattering cross-sections of the predicted magnon branches are summarized in section 6.3.2. Section 6.4 introduces the concept of the universal first Brillouin zone, which is the region of reciprocal space used for the Fourier transforms. This section also connects the symmetry of the spin wave dispersions to that of the universal Brillouin zones. Finally, section 6.6 provides a very short description of the m-files used for the numerical simulation.

The approach taken in this chapter is equivalent to the method described by Per Anker Lindgård *et. al* in [44]. The most significant differences between the method presented here and that of [44], lies in the use of matrices I_1 and I_2, the algorithm for finding the transformation matrix, and the introduction of the universal first Brillouin zone.

We end this introduction by mentioning that we have successfully tested our MATLAB scripts using the theory developed here, by reproducing already published results [45] on the entirely different system of La_2CuO_4. The results of the test are shown in appendix D.

6.2 Basic theory

Let us consider a Hamiltonian, , that can be written as

$$= \sum_{\mathbf{q}} H_{\mathbf{q}} = \frac{1}{2} \sum_{\mathbf{q}} \mathbf{a}^{+} \mathbf{H} \mathbf{a}, \tag{6.3}$$

where $\mathbf{H}$ and $\mathbf{a}$ are given as

$$\mathbf{H} = \begin{bmatrix} A & B & C & D \\ B & A & D & C \\ C & D & A & B \\ D & C & B & A \end{bmatrix}, \quad \mathbf{a} = \begin{bmatrix} a_{\mathbf{q}} \\ a^{+}_{-\mathbf{q}} \\ b_{\mathbf{q}} \\ b^{+}_{-\mathbf{q}} \end{bmatrix}, \quad \mathbf{a}^{+} = \left[a^{+}_{\mathbf{q}}, a_{-\mathbf{q}}, b^{+}_{\mathbf{q}}, b_{-\mathbf{q}} \right]. \tag{6.4}$$

Here $a_{\mathbf{q}}$ and $b_{\mathbf{q}}$ are Bose operators and $\mathbf{H}$ is a real matrix[1].

We are looking for a transformation

$$\mathbf{a} = \mathbf{T} \boldsymbol{\alpha}, \tag{6.5}$$

so that

$$H_{\mathbf{q}} = \frac{1}{2}\, \mathbf{a}^{+} \mathbf{H} \mathbf{a} = \frac{1}{2}\, \boldsymbol{\alpha}^{+} \mathbf{T}^{+} \mathbf{H} \mathbf{T} \boldsymbol{\alpha} = \frac{1}{2}\, \boldsymbol{\alpha}^{+} \boldsymbol{\omega} \boldsymbol{\alpha}, \tag{6.6}$$

with

$$\boldsymbol{\omega} = \begin{bmatrix} \omega_1 & 0 & 0 & 0 \\ 0 & \omega_2 & 0 & 0 \\ 0 & 0 & \omega_3 & 0 \\ 0 & 0 & 0 & \omega_4 \end{bmatrix}. \tag{6.7}$$

We have introduced

$$\mathbf{T} = \begin{bmatrix} T_{11} & T_{12} & T_{13} & T_{14} \\ T_{21} & T_{22} & T_{23} & T_{24} \\ T_{31} & T_{32} & T_{33} & T_{34} \\ T_{41} & T_{42} & T_{43} & T_{44} \end{bmatrix}, \quad \boldsymbol{\alpha} = \begin{bmatrix} \alpha_{\mathbf{q}} \\ \alpha^{+}_{-\mathbf{q}} \\ \beta_{\mathbf{q}} \\ \beta^{+}_{-\mathbf{q}} \end{bmatrix}, \quad \boldsymbol{\alpha}^{+} = \left[\alpha^{+}_{\mathbf{q}}, \alpha_{-\mathbf{q}}, \beta^{+}_{\mathbf{q}}, \beta_{-\mathbf{q}} \right], \tag{6.8}$$

where $\alpha_{\mathbf{q}}$ and $\beta_{\mathbf{q}}$ are required to be Bose operators. If such a transformation exist, the diagonal elements in the matrix $\boldsymbol{\omega}$ will be the eigenenergies of the system and therefore non-negative. Let us assume that (6.6) is possible and that the transformation matrix $\mathbf{T}$ can be chosen to be real. Equation (6.6) immediately gives that

$$\mathbf{T}^{+} \mathbf{H} \mathbf{T} = \boldsymbol{\omega} \Rightarrow \mathbf{H} \mathbf{T} = (\mathbf{T}^{+})^{-1} \boldsymbol{\omega}. \tag{6.9}$$

Normally transformation matrices $\mathbf{U}$ are unitary ($\mathbf{U}^{+} = \mathbf{U}^{-1}$), but $\mathbf{T}$ will *not* be unitary. This is a consequence of $a_{\mathbf{q}}$, $b_{\mathbf{q}}$, $\alpha_{\mathbf{q}}$ and $\beta_{\mathbf{q}}$ being Bose operators. Since

$$\begin{aligned} a_{\mathbf{q}} &= T_{11} \alpha_{\mathbf{q}} + T_{12} \alpha^{+}_{-\mathbf{q}} + T_{13} \beta_{\mathbf{q}} + T_{14} \beta^{+}_{-\mathbf{q}}, \\ a^{+}_{\mathbf{q}} &= T_{11} \alpha^{+}_{\mathbf{q}} + T_{12} \alpha_{-\mathbf{q}} + T_{13} \beta^{+}_{\mathbf{q}} + T_{14} \beta_{-\mathbf{q}}, \\ b_{\mathbf{q}} &= T_{31} \alpha_{\mathbf{q}} + T_{32} \alpha^{+}_{-\mathbf{q}} + T_{33} \beta_{\mathbf{q}} + T_{34} \beta^{+}_{-\mathbf{q}}, \\ &\vdots \end{aligned} \tag{6.10}$$

the Bose commutation rules gives that

$$\begin{aligned} 1 &= [a_{\mathbf{q}}, a^{+}_{\mathbf{q}}] = T^2_{11} [\alpha_{\mathbf{q}}, \alpha^{+}_{\mathbf{q}}] + T^2_{12} [\alpha^{+}_{-\mathbf{q}}, \alpha_{-\mathbf{q}}] + T^2_{13} [\beta_{\mathbf{q}}, \beta^{+}_{\mathbf{q}}] + T^2_{14} [\beta^{+}_{-\mathbf{q}}, \beta_{-\mathbf{q}}] = T^2_{11} - T^2_{12} + T^2_{13} - T^2_{14}, \\ 0 &= [a_{\mathbf{q}}, a_{-\mathbf{q}}] = T_{11} T_{21} - T_{12} T_{22} + T_{13} T_{23} - T_{14} T_{24}, \\ &\vdots \end{aligned} \tag{6.11}$$

[1] The Hamilton matrix, $\mathbf{H}$, in our model for $LiNiPO_4$ is a real matrix, but we could easily extend the theory to include complex $\mathbf{H}$. In fact, the results given in section 6.3 apply also for complex matrices.

We can collect the equations from (6.11) in the following matrix equation

$$\begin{bmatrix} T_{11} & -T_{12} & T_{13} & -T_{14} \\ -T_{21} & T_{22} & -T_{23} & T_{24} \\ T_{31} & -T_{32} & T_{33} & -T_{34} \\ -T_{41} & T_{42} & -T_{43} & T_{44} \end{bmatrix} \begin{bmatrix} T_{11} & T_{21} & T_{31} & T_{41} \\ T_{12} & T_{22} & T_{32} & T_{42} \\ T_{13} & T_{23} & T_{33} & T_{43} \\ T_{14} & T_{24} & T_{34} & T_{44} \end{bmatrix} = \begin{bmatrix} 1 & 0 & 0 & 0 \\ 0 & 1 & 0 & 0 \\ 0 & 0 & 1 & 0 \\ 0 & 0 & 0 & 1 \end{bmatrix}. \tag{6.12}$$

Since

$$\mathbf{T}^{+} = \begin{bmatrix} T_{11} & T_{21} & T_{31} & T_{41} \\ T_{12} & T_{22} & T_{32} & T_{42} \\ T_{13} & T_{23} & T_{33} & T_{43} \\ T_{14} & T_{24} & T_{34} & T_{44} \end{bmatrix}, \tag{6.13}$$

it follows from (6.12) that

$$(\mathbf{T}^{+})^{-1} = \begin{bmatrix} T_{11} & -T_{12} & T_{13} & -T_{14} \\ -T_{21} & T_{22} & -T_{23} & T_{24} \\ T_{31} & -T_{32} & T_{33} & -T_{34} \\ -T_{41} & T_{42} & -T_{43} & T_{44} \end{bmatrix}. \tag{6.14}$$

6.2.1 Finding the eigenenergies

Inserting (6.14) into (6.9) we find

$$\begin{aligned} \mathbf{HT} = (\mathbf{T}^{+})^{-1}\boldsymbol{\omega} &= \begin{bmatrix} T_{11} & -T_{12} & T_{13} & -T_{14} \\ -T_{21} & T_{22} & -T_{23} & T_{24} \\ T_{31} & -T_{32} & T_{33} & -T_{34} \\ -T_{41} & T_{42} & -T_{43} & T_{44} \end{bmatrix} \begin{bmatrix} \omega_1 & 0 & 0 & 0 \\ 0 & \omega_2 & 0 & 0 \\ 0 & 0 & \omega_3 & 0 \\ 0 & 0 & 0 & \omega_4 \end{bmatrix} \\ &= \left(\omega_1 \begin{bmatrix} T_{11} \\ -T_{21} \\ T_{31} \\ -T_{41} \end{bmatrix}, \omega_2 \begin{bmatrix} -T_{12} \\ T_{22} \\ -T_{32} \\ T_{42} \end{bmatrix}, \omega_3 \begin{bmatrix} T_{13} \\ -T_{23} \\ T_{33} \\ -T_{43} \end{bmatrix}, \omega_4 \begin{bmatrix} -T_{14} \\ T_{24} \\ -T_{34} \\ T_{44} \end{bmatrix} \right). \end{aligned} \tag{6.15}$$

Equation (6.15) gives the following four eigenvalue equations

$$\mathbf{H} \begin{bmatrix} T_{11} \\ T_{21} \\ T_{31} \\ T_{41} \end{bmatrix} = \omega_1 \begin{bmatrix} T_{11} \\ -T_{21} \\ T_{31} \\ -T_{41} \end{bmatrix} = \begin{bmatrix} 1 & 0 & 0 & 0 \\ 0 & -1 & 0 & 0 \\ 0 & 0 & 1 & 0 \\ 0 & 0 & 0 & -1 \end{bmatrix} \omega_1 \begin{bmatrix} T_{11} \\ T_{21} \\ T_{31} \\ T_{41} \end{bmatrix} = \mathbf{I}_1\omega_1\mathbf{T}_1 \Rightarrow \mathbf{I}_1\mathbf{H}\mathbf{T}_1 = \omega_1\mathbf{T}_1, \tag{6.16}$$

$$\mathbf{HT}_2 = \mathbf{I}_2\omega_2\mathbf{T}_2 \Rightarrow \mathbf{I}_2\mathbf{H}\mathbf{T}_2 = \omega_2\mathbf{T}_2, \tag{6.17}$$

$$\mathbf{HT}_3 = \mathbf{I}_1\omega_3\mathbf{T}_3 \Rightarrow \mathbf{I}_1\mathbf{H}\mathbf{T}_3 = \omega_3\mathbf{T}_3, \tag{6.18}$$

$$\mathbf{HT}_4 = \mathbf{I}_2\omega_4\mathbf{T}_4 \Rightarrow \mathbf{I}_2\mathbf{H}\mathbf{T}_4 = \omega_4\mathbf{T}_4, \tag{6.19}$$

where

$$\mathbf{I}_1 = \begin{bmatrix} 1 & 0 & 0 & 0 \\ 0 & -1 & 0 & 0 \\ 0 & 0 & 1 & 0 \\ 0 & 0 & 0 & -1 \end{bmatrix}, \quad \mathbf{I}_2 = \begin{bmatrix} -1 & 0 & 0 & 0 \\ 0 & 1 & 0 & 0 \\ 0 & 0 & -1 & 0 \\ 0 & 0 & 0 & 1 \end{bmatrix}, \quad \mathbf{T}_n = \begin{bmatrix} T_{1n} \\ T_{2n} \\ T_{3n} \\ T_{4n} \end{bmatrix}. \tag{6.20}$$

We immediately have that (6.16) is identical to (6.18), and that (6.17) is identical to (6.19). It is also easy to see that (6.16) is equivalent to (6.17), since

$$\mathbf{I}_1\mathbf{H}\mathbf{T}_n = \omega\mathbf{T}_n \Rightarrow \mathbf{H}\mathbf{T}_n = \mathbf{I}_1\omega\mathbf{T}_n = \mathbf{I}_2(-\omega)\mathbf{T}_n \Rightarrow \mathbf{I}_2\mathbf{H}\mathbf{T}_n = (-\omega)\mathbf{T}_n. \tag{6.21}$$

This means that if ω is an eigenvalue to (6.16), then $-\omega$ will be an eigenvalue to (6.17). All in all we see that the eigenvalues to (6.16) will be $\omega_1 \geq 0$, $-\omega_2 \leq 0$, $\omega_3 \geq 0$, and $-\omega_4 \leq 0$, where ω_1, ω_2, ω_3, and ω_4 are the eigenenergies appearing in (6.7).

If ω is an eigenvalue to (6.16), then

$$(\mathbf{I}_1\mathbf{H} - \omega\mathbf{E}) \begin{bmatrix} T_1 \\ T_2 \\ T_3 \\ T_4 \end{bmatrix} = \begin{bmatrix} A-\omega & B & C & D \\ -B & -A-\omega & -D & -C \\ C & D & A-\omega & B \\ -D & -C & -B & -A-\omega \end{bmatrix} \begin{bmatrix} T_1 \\ T_2 \\ T_3 \\ T_4 \end{bmatrix} = 0 \Rightarrow$$

$$\begin{bmatrix} -A+\omega & -B & -C & -D \\ B & A+\omega & D & C \\ -C & -D & -A+\omega & -B \\ D & C & B & A+\omega \end{bmatrix} \begin{bmatrix} T_1 \\ T_2 \\ T_3 \\ T_4 \end{bmatrix} = 0 \Rightarrow \begin{bmatrix} A+\omega & B & C & D \\ -B & -A+\omega & -D & -C \\ C & D & A+\omega & B \\ -D & -C & -B & -A+\omega \end{bmatrix} \begin{bmatrix} T_2 \\ T_1 \\ T_4 \\ T_3 \end{bmatrix} = 0 \Rightarrow$$

$$\begin{bmatrix} A & B & C & D \\ -B & -A & -D & -C \\ C & D & A & B \\ -D & -C & -B & -A \end{bmatrix} \begin{bmatrix} T_2 \\ T_1 \\ T_4 \\ T_3 \end{bmatrix} = (-\omega) \begin{bmatrix} T_2 \\ T_1 \\ T_4 \\ T_3 \end{bmatrix}. \tag{6.22}$$

This shows that if ω is an eigenvalue to (6.16) with eigenvector (T_1, T_2, T_3, T_4), then $(-\omega)$ will also be an eigenvalue to (6.16) with eigenvector (T_2, T_1, T_4, T_3).

All in all we only need to solve one eigenvalue problem, namely (6.16). This eigenvalue equation, $\mathbf{I}_1\mathbf{H}\mathbf{T}_1 = \omega\mathbf{T}_1$, has four eigenvalues $\pm\omega_1$ and $\pm\omega_3$, where $\omega_1, \omega_3 \geq 0$. The eigenenergies of $H_{\mathbf{q}}$ are connected to the eigenvalues of (6.16) through the relations $\omega^{\alpha}_{\mathbf{q}} = \omega^{\alpha}_{-\mathbf{q}} = \omega_1$ and $\omega^{\beta}_{\mathbf{q}} = \omega^{\beta}_{-\mathbf{q}} = \omega_3$.

6.2.2 Finding the correct transformation matrix

The transformation matrix $\mathbf{T}$ is a 4×4 matrix with columns that are eigenvectors to (6.16). Furthermore, $\mathbf{T}$ must ensure that the Bose commutation rules hold for both $\mathbf{a}$ and $\boldsymbol{\alpha}$.

Let us assume that our computer has found four eigenvectors $\widetilde{\mathbf{T}}_1$, $\widetilde{\mathbf{T}}_2$, $\widetilde{\mathbf{T}}_3$ and $\widetilde{\mathbf{T}}_4$ corresponding to the eigenvalue problem (6.16). It is more than likely that the computer generated matrix

$$\widetilde{\mathbf{T}} = \left[\widetilde{\mathbf{T}}_1, \widetilde{\mathbf{T}}_2, \widetilde{\mathbf{T}}_3, \widetilde{\mathbf{T}}_4\right] = \begin{bmatrix} \widetilde{T}_{11} & \widetilde{T}_{12} & \widetilde{T}_{13} & \widetilde{T}_{14} \\ \widetilde{T}_{21} & \widetilde{T}_{22} & \widetilde{T}_{23} & \widetilde{T}_{24} \\ \widetilde{T}_{31} & \widetilde{T}_{32} & \widetilde{T}_{33} & \widetilde{T}_{34} \\ \widetilde{T}_{41} & \widetilde{T}_{42} & \widetilde{T}_{43} & \widetilde{T}_{44} \end{bmatrix}, \tag{6.23}$$

does not respect the Bose commutation rules. We therefore need an algorithm that will transform $\widetilde{\mathbf{T}}$ into a transformation matrix $\mathbf{T}$ that respects the Bose requirements.

The correct transformation matrix $\mathbf{T}$ must fulfil[2] that

$$\mathbf{T}\mathbf{I}_1\mathbf{T}^+ = \begin{bmatrix} T_{11} & T_{12} & T_{13} & T_{14} \\ T_{21} & T_{22} & T_{23} & T_{24} \\ T_{31} & T_{32} & T_{33} & T_{34} \\ T_{41} & T_{42} & T_{43} & T_{44} \end{bmatrix} \begin{bmatrix} 1 & 0 & 0 & 0 \\ 0 & -1 & 0 & 0 \\ 0 & 0 & 1 & 0 \\ 0 & 0 & 0 & -1 \end{bmatrix} \begin{bmatrix} T_{11} & T_{21} & T_{31} & T_{41} \\ T_{12} & T_{22} & T_{32} & T_{42} \\ T_{13} & T_{23} & T_{33} & T_{43} \\ T_{14} & T_{24} & T_{34} & T_{44} \end{bmatrix} = \tag{6.24}$$

$$\begin{bmatrix} T_{11} & T_{12} & T_{13} & T_{14} \\ T_{21} & T_{22} & T_{23} & T_{24} \\ T_{31} & T_{32} & T_{33} & T_{34} \\ T_{41} & T_{42} & T_{43} & T_{44} \end{bmatrix} \begin{bmatrix} T_{11} & T_{21} & T_{31} & T_{41} \\ -T_{12} & -T_{22} & -T_{32} & -T_{42} \\ T_{13} & T_{23} & T_{33} & T_{43} \\ -T_{14} & -T_{24} & -T_{34} & -T_{44} \end{bmatrix} = \begin{bmatrix} 1 & 0 & 0 & 0 \\ 0 & -1 & 0 & 0 \\ 0 & 0 & 1 & 0 \\ 0 & 0 & 0 & -1 \end{bmatrix} = \mathbf{I}_1,$$

because of the Bose rules in (6.11). Since the eigenvectors to (6.16) are determined only within a multiplicative constant we can write

$$\mathbf{T} = [\mathbf{T}_1, \mathbf{T}_2, \mathbf{T}_3, \mathbf{T}_4], = \left[s\widetilde{\mathbf{T}}_1, t\widetilde{\mathbf{T}}_2, u\widetilde{\mathbf{T}}_3, v\widetilde{\mathbf{T}}_4\right] = \widetilde{\mathbf{T}} \begin{bmatrix} s & 0 & 0 & 0 \\ 0 & t & 0 & 0 \\ 0 & 0 & u & 0 \\ 0 & 0 & 0 & v \end{bmatrix} = \widetilde{\mathbf{T}}\mathbf{N}, \tag{6.25}$$

where the normalization matrix

$$\mathbf{N} = \begin{bmatrix} s & 0 & 0 & 0 \\ 0 & t & 0 & 0 \\ 0 & 0 & u & 0 \\ 0 & 0 & 0 & v \end{bmatrix}, \tag{6.26}$$

is assumed (chosen) to be real (we may in fact chose it to be positive definite). To find $\mathbf{N}$ we use the fact that two diagonal matrices always commute, and rewrite (6.24)

$$\mathbf{I}_1 = \mathbf{T}\mathbf{I}_1\mathbf{T}^+ = \widetilde{\mathbf{T}}\mathbf{N}\mathbf{I}_1\mathbf{N}^+\widetilde{\mathbf{T}}^+ = \widetilde{\mathbf{T}}\mathbf{I}_1\mathbf{N}^2\widetilde{\mathbf{T}}^+ \Rightarrow \mathbf{N}^2 = \mathbf{I}_1\widetilde{\mathbf{T}}^{-1}\mathbf{I}_1(\widetilde{\mathbf{T}}^+)^{-1}. \tag{6.27}$$

From $\widetilde{\mathbf{T}}$ it is easy to find s, t, u and v (within an arbitrary phase) using (6.27), and via (6.25) we can then find the desired transformation matrix $\mathbf{T}$.

6.3 Calculating the spin wave intensities

The differential scattering cross-section for magnetic scattering is given as [29]

$$\left(\frac{d^2\sigma_m}{d\Omega dE'}\right)(\mathbf{Q},\omega) = \frac{k_f}{k_i}(\gamma r_0)^2 \left[\frac{g}{2}F(\mathbf{Q})\right]^2 \frac{e^{-2W(\mathbf{Q})}}{\hbar} \sum_{\mu\nu}(\delta_{\mu\nu} - \widehat{Q}_\mu\widehat{Q}_\nu)S_{\mu\nu}(\mathbf{Q},\omega), \tag{6.28}$$

where

$$S_{\mu\nu}(\mathbf{Q},\omega) = \frac{1}{2\pi}\int dt e^{-i\omega t}S_{\mu\nu}(\mathbf{Q},t), \tag{6.29}$$

and

$$S_{\mu\nu}(\mathbf{Q},t) = \sum_{\mathbf{r},\mathbf{r}'} e^{i\mathbf{Q}\cdot(\mathbf{r}'-\mathbf{r})}\langle S^\mu_{\mathbf{r}}(0)S^\nu_{\mathbf{r}'}(t)\rangle. \tag{6.30}$$

In the magnetic systems we are considering there are two different kind of ions, namely spin up and spin down ions. This is described by introducing Holstein Primakoff [46] operators a, a^+ related to spin up sites and b, b^+ related to spin down sites. Here we will show how to evaluate (6.28) using the Holstein Primakoff operators, the quasi particle operators α, α^+, β and β^+ and the transformation matrix $\mathbf{T}$.

[2]This can be shown more elegantly using that $\mathbf{I}_1 = [\mathbf{a}, \mathbf{a}^+] = [\boldsymbol{\alpha}, \boldsymbol{\alpha}^+]$ since they are bose operators. Using $\mathbf{a} = \mathbf{T}\boldsymbol{\alpha}$ we immediately find that $\mathbf{I}_1 = [\mathbf{T}\boldsymbol{\alpha}, \boldsymbol{\alpha}^+\mathbf{T}^+] = \mathbf{T}[\boldsymbol{\alpha}, \boldsymbol{\alpha}^+]\mathbf{T}^+ = \mathbf{T}\mathbf{I}_1\mathbf{T}^+$

Definition 2 *Introducing the notation i, i' for spin up sites, and j, j' for spin down sites we connect the spin operators $\mathbf{S_r}$ and $\mathbf{S_{r'}}$ to the Holstein Primakoff operators through the following definitions*

$$S^+_{i,j} = S^x_{i,j} + iS^y_{i,j}, \quad S^-_{i,j} = S^x_{i,j} - iS^y_{i,j}, \tag{6.31}$$

and

$$\begin{aligned} S^+_i &= \sqrt{2S}\ (1 - \frac{a^+_i a_i}{2S})^{1/2} a_i, \quad S^-_i = \sqrt{2S}\ a^+_i (1 - \frac{a^+_i a_i}{2S})^{1/2}, \quad S^z_i = S - a^+_i a_i, \\ S^+_j &= \sqrt{2S}\ b^+_j (1 - \frac{b^+_j b_j}{2S})^{1/2}, \quad S^-_j = \sqrt{2S}\ (1 - \frac{b^+_j b_j}{2S})^{1/2} b_j, \quad S^z_j = -S + b^+_j b_j. \end{aligned} \tag{6.32}$$

At low temperatures (6.32) can be written [46, 47] as

$$\begin{aligned} S^+_i &\simeq \sqrt{2S} a_i, \quad S^-_i \simeq \sqrt{2S} a^+_i, \quad S^z_i = S - a^+_i a_i, \\ S^+_j &\simeq \sqrt{2S} b^+_j, \quad S^-_j \simeq \sqrt{2S} b_j, \quad S^z_j = -S + b^+_j b_j, \end{aligned} \tag{6.33}$$

which is what we use in the following. We also introduce the Fourier transforms[3]

$$\begin{aligned} a^+_i &= \sqrt{\frac{2}{N}} \sum_{\mathbf{q}} e^{-i\mathbf{q}\cdot\mathbf{r}_i} a^+_{\mathbf{q}}, \quad b^+_j = \sqrt{\frac{2}{N}} \sum_{\mathbf{q}} e^{-i\mathbf{q}\cdot\mathbf{r}_j} b^+_{\mathbf{q}}, \\ a_i &= \sqrt{\frac{2}{N}} \sum_{\mathbf{q}} e^{i\mathbf{q}\cdot\mathbf{r}_i} a_{\mathbf{q}}, \quad b_j = \sqrt{\frac{2}{N}} \sum_{\mathbf{q}} e^{i\mathbf{q}\cdot\mathbf{r}_j} b_{\mathbf{q}}. \end{aligned} \tag{6.34}$$

The wavevectors $\mathbf{q}$ appearing in (6.34) are not necessarily restricted to the first Brillouin zone, but are situated in a "universal first Brillouin zone". We will discuss this in detail in section 6.4.

The general idea is to express, via definition 2 and (6.5), the thermal mean values $\langle S^\mu_{\mathbf{r}}(0) S^\nu_{\mathbf{r}'}(t)\rangle$ as quasi particle thermal mean values, and use that

$$\begin{aligned} \langle \alpha_{\mathbf{q}}(0)\alpha^+_{\mathbf{q}}(t)\rangle &= \left(n(\omega^\alpha_{\mathbf{q}}) + 1\right) e^{i\omega^\alpha_{\mathbf{q}} t}, \quad \langle \alpha^+_{\mathbf{q}}(0)\alpha_{\mathbf{q}}(t)\rangle = n(\omega^\alpha_{\mathbf{q}}) e^{-i\omega^\alpha_{\mathbf{q}} t}, \\ \langle \beta_{\mathbf{q}}(0)\beta^+_{\mathbf{q}}(t)\rangle &= \left(n(\omega^\beta_{\mathbf{q}}) + 1\right) e^{i\omega^\beta_{\mathbf{q}} t}, \quad \langle \beta^+_{\mathbf{q}}(0)\beta_{\mathbf{q}}(t)\rangle = n(\omega^\beta_{\mathbf{q}}) e^{-i\omega^\beta_{\mathbf{q}} t}. \end{aligned} \tag{6.35}$$

Here $n(\omega) = (e^{\hbar\omega/k_B T} - 1)^{-1}$ is the Bose population factor and the energies $\omega^\alpha_{\mathbf{q}}$ and $\omega^\beta_{\mathbf{q}}$ are those of the spin wave dispersions.

Proof of (6.35)
The identities in (6.35) are easily proved, since for $x = e^{-\hbar\omega/k_B T}$

$$\begin{aligned} \langle \alpha^+(0)\alpha(t)\rangle &= \frac{\sum_{n=0}^\infty x^n \langle n|\alpha^+ e^{iHt/\hbar}\alpha e^{-iHt/\hbar}|n\rangle}{\sum_{n=0}^\infty x^n} = \frac{\sum_{n=1}^\infty n x^n e^{-i\omega t}}{\sum_{n=0}^\infty x^n} = (x + 2x^2 + 3x^3 + \ldots)(1-x)e^{-i\omega t} \\ &= (x + x^2 + x^3 + \ldots)e^{-i\omega t} = \frac{x}{1-x}\ e^{-i\omega t} = n(\omega)e^{-i\omega t}, \end{aligned} \tag{6.36}$$

and

$$\begin{aligned} \langle \alpha(0)\alpha(t)^+\rangle &= \frac{\sum_{n=0}^\infty x^n \langle n|\alpha e^{iHt/\hbar}\alpha^+ e^{-iHt/\hbar}|n\rangle}{\sum_{n=0}^\infty x^n} = \frac{\sum_{n=0}^\infty (n+1) x^n e^{i\omega t}}{\sum_{n=0}^\infty x^n} = (1 + 2x + 3x^2 + \ldots)(1-x)e^{i\omega t} \\ &= (1 + x + x^2 + \ldots)e^{i\omega t} = \frac{1}{1-x}\ e^{i\omega t} = (n(\omega) + 1)e^{i\omega t}. \end{aligned} \tag{6.37}$$

[3] It is customary to define the Fourier transforms of the Holstein Primakoff operators with opposite signs in the exponentials for a_i and b_i. Using (6.34) instead of the conventional definition is important for the formalism, since it allows for the correct form of the $LiNiPO_4$ model Hamiltonian.

The Hamiltonian is diagonal with respect to the quasi particles, so the only non-zero mean values are those where α appears the same number of times as α^+ and β the same number of times as β^+. Therefore, in the linear approximation, only the terms given in (6.35) contribute to the scattering cross-section. Furthermore, $\langle S^\mu_{\mathbf{r}}(0)S^\nu_{\mathbf{r}'}(t)\rangle$ does not contribute to the inelastic scattering cross-section if μ or ν is equal to the preferred spin direction (the z-direction). This is because such terms transform into thermal mean values with an odd number of quasi operators (i.e. with a mean value that is zero), or into mean values where the quasi operators are taken at the same time and only contribute to elastic scattering. So for inelastic scattering we need only consider

$$\begin{aligned}
\langle S^x_{\mathbf{r}}(0)S^x_{\mathbf{r}'}(t)\rangle &= \frac{1}{4}\Big[\langle S^+_{\mathbf{r}}(0)S^+_{\mathbf{r}'}(t)\rangle + \langle S^+_{\mathbf{r}}(0)S^-_{\mathbf{r}'}(t)\rangle + \langle S^-_{\mathbf{r}}(0)S^+_{\mathbf{r}'}(t)\rangle + \langle S^-_{\mathbf{r}}(0)S^-_{\mathbf{r}'}(t)\rangle\Big],\\
\langle S^x_{\mathbf{r}}(0)S^y_{\mathbf{r}'}(t)\rangle &= \frac{1}{4i}\Big[\langle S^+_{\mathbf{r}}(0)S^+_{\mathbf{r}'}(t)\rangle - \langle S^+_{\mathbf{r}}(0)S^-_{\mathbf{r}'}(t)\rangle + \langle S^-_{\mathbf{r}}(0)S^+_{\mathbf{r}'}(t)\rangle - \langle S^-_{\mathbf{r}}(0)S^-_{\mathbf{r}'}(t)\rangle\Big],\\
\langle S^y_{\mathbf{r}}(0)S^x_{\mathbf{r}'}(t)\rangle &= \frac{1}{4i}\Big[\langle S^+_{\mathbf{r}}(0)S^+_{\mathbf{r}'}(t)\rangle + \langle S^+_{\mathbf{r}}(0)S^-_{\mathbf{r}'}(t)\rangle - \langle S^-_{\mathbf{r}}(0)S^+_{\mathbf{r}'}(t)\rangle - \langle S^-_{\mathbf{r}}(0)S^-_{\mathbf{r}'}(t)\rangle\Big],\\
\langle S^y_{\mathbf{r}}(0)S^y_{\mathbf{r}'}(t)\rangle &= \frac{1}{4}\Big[-\langle S^+_{\mathbf{r}}(0)S^+_{\mathbf{r}'}(t)\rangle + \langle S^+_{\mathbf{r}}(0)S^-_{\mathbf{r}'}(t)\rangle + \langle S^-_{\mathbf{r}}(0)S^+_{\mathbf{r}'}(t)\rangle - \langle S^-_{\mathbf{r}}(0)S^-_{\mathbf{r}'}(t)\rangle\Big].
\end{aligned} \tag{6.38}$$

We want to calculate the separate contributions to the cross-section of the α and β creation and annihilation processes, since this is what our neutron experiments are probing. Combining (6.29) to (6.35) we find that

$$\frac{1}{2\pi}\int dt e^{-i\omega t}\langle \alpha_{\mathbf{q}}(0)\alpha^+_{\mathbf{q}}(t)\rangle = \big(n(\omega^\alpha_{\mathbf{q}})+1\big)\,\frac{1}{2\pi}\int dt e^{-i(\omega-\omega^\alpha_{\mathbf{q}})t} = \big(n(\omega^\alpha_{\mathbf{q}})+1\big)\,\delta(\omega-\omega^\alpha_{\mathbf{q}}) \equiv n^+(\omega^\alpha_{\mathbf{q}}), \tag{6.39a}$$

$$\frac{1}{2\pi}\int dt e^{-i\omega t}\langle \alpha^+_{\mathbf{q}}(0)\alpha_{\mathbf{q}}(t)\rangle = n(\omega^\alpha_{\mathbf{q}})\frac{1}{2\pi}\int dt e^{-i(\omega+\omega^\alpha_{\mathbf{q}})t} = n(\omega^\alpha_{\mathbf{q}})\delta(\omega+\omega^\alpha_{\mathbf{q}}) \equiv n^-(\omega^\alpha_{\mathbf{q}}), \tag{6.39b}$$

$$\frac{1}{2\pi}\int dt e^{-i\omega t}\langle \beta_{\mathbf{q}}(0)\beta^+_{\mathbf{q}}(t)\rangle = \big(n(\omega^\beta_{\mathbf{q}})+1\big)\,\frac{1}{2\pi}\int dt e^{-i(\omega-\omega^\beta_{\mathbf{q}})t} = \big(n(\omega^\beta_{\mathbf{q}})+1\big)\,\delta(\omega-\omega^\beta_{\mathbf{q}}) \equiv n^+(\omega^\beta_{\mathbf{q}}), \tag{6.39c}$$

$$\frac{1}{2\pi}\int dt e^{-i\omega t}\langle \beta^+_{\mathbf{q}}(0)\beta_{\mathbf{q}}(t)\rangle = n(\omega^\beta_{\mathbf{q}})\frac{1}{2\pi}\int dt e^{-i(\omega+\omega^\beta_{\mathbf{q}})t} = n(\omega^\beta_{\mathbf{q}})\delta(\omega+\omega^\beta_{\mathbf{q}}) \equiv n^-(\omega^\beta_{\mathbf{q}}). \tag{6.39d}$$

Since magnon creation processes are connected with a positive energy transfer ($\omega > 0$) to the crystal, and destruction processes have negative ω, we see that (6.39a) relates to the creation of an α magnon and (6.39b) to the destruction of one. Similarly (6.39c) describes the creation and (6.39d) the destruction of a β magnon.

6.3.1 The α magnon creation cross-section

Let us in detail calculate the scattering cross-section for creating an α magnon. Remembering the notation i, i' for spin up and j, j' for spin down ions, we begin with

$$\langle S_i^+(0)S_{i'}^+(t)\rangle = 2S\langle a_i(0)a_{i'}(t)\rangle = \frac{4S}{N}\sum_{\mathbf{q},\mathbf{q}'} e^{i\mathbf{q}\cdot\mathbf{r}_i}e^{i\mathbf{q}'\cdot\mathbf{r}_{i'}}\langle a_{\mathbf{q}}(0)a_{\mathbf{q}'}(t)\rangle. \tag{6.40}$$

We are interested in the part of $\langle a_{\mathbf{q}}(0)a_{\mathbf{q}'}(t)\rangle$ that describes the creation of an α magnon, i.e. transforms into $\langle\alpha_{\mathbf{q}}(0)\alpha_{\mathbf{q}}^+(t)\rangle$. Allowing the transformation matrix $\mathbf{T}$ to be complex, we have

$$\begin{aligned}
a_{\mathbf{q}} &= T_{11}\alpha_{\mathbf{q}} + T_{12}\alpha_{-\mathbf{q}}^+ + T_{13}\beta_{\mathbf{q}} + T_{14}\beta_{-\mathbf{q}}^+,\\
a_{\mathbf{q}}^+ &= T_{11}^*\alpha_{\mathbf{q}}^+ + T_{12}^*\alpha_{-\mathbf{q}} + T_{13}^*\beta_{\mathbf{q}}^+ + T_{14}^*\beta_{-\mathbf{q}},\\
a_{-\mathbf{q}}^+ &= T_{21}\alpha_{\mathbf{q}} + T_{22}\alpha_{-\mathbf{q}}^+ + T_{23}\beta_{\mathbf{q}} + T_{24}\beta_{-\mathbf{q}}^+,\\
a_{-\mathbf{q}} &= T_{21}^*\alpha_{\mathbf{q}}^+ + T_{22}^*\alpha_{-\mathbf{q}} + T_{23}^*\beta_{\mathbf{q}}^+ + T_{24}^*\beta_{-\mathbf{q}},\\
b_{\mathbf{q}} &= T_{31}\alpha_{\mathbf{q}} + T_{32}\alpha_{-\mathbf{q}}^+ + T_{33}\beta_{\mathbf{q}} + T_{34}\beta_{-\mathbf{q}}^+,\\
b_{\mathbf{q}}^+ &= T_{31}^*\alpha_{\mathbf{q}}^+ + T_{32}^*\alpha_{-\mathbf{q}} + T_{33}^*\beta_{\mathbf{q}}^+ + T_{34}^*\beta_{-\mathbf{q}},\\
b_{-\mathbf{q}}^+ &= T_{41}\alpha_{\mathbf{q}} + T_{42}\alpha_{-\mathbf{q}}^+ + T_{43}\beta_{\mathbf{q}} + T_{44}\beta_{-\mathbf{q}}^+,\\
b_{-\mathbf{q}} &= T_{41}^*\alpha_{\mathbf{q}}^+ + T_{42}^*\alpha_{-\mathbf{q}} + T_{43}^*\beta_{\mathbf{q}}^+ + T_{44}^*\beta_{-\mathbf{q}},
\end{aligned} \tag{6.41}$$

and see that the transformation of $\langle a_{\mathbf{q}}(0)a_{\mathbf{q}'}(t)\rangle$ into $\langle\alpha_{\mathbf{q}}(0)\alpha_{\mathbf{q}}^+(t)\rangle$ can be done in various ways. One can for instance chose

$$a_{\mathbf{q}} = T_{11}\alpha_{\mathbf{q}} + T_{12}\alpha_{-\mathbf{q}}^+ + T_{13}\beta_{\mathbf{q}} + T_{14}\beta_{-\mathbf{q}}^+, \quad \text{and} \quad a_{\mathbf{q}'} = T_{11}\alpha_{\mathbf{q}'} + T_{12}\alpha_{-\mathbf{q}'}^+ + T_{13}\beta_{\mathbf{q}'} + T_{14}\beta_{-\mathbf{q}'}^+, \tag{6.42}$$

or

$$a_{\mathbf{q}} = T_{11}\alpha_{\mathbf{q}} + T_{12}\alpha_{-\mathbf{q}}^+ + T_{13}\beta_{\mathbf{q}} + T_{14}\beta_{-\mathbf{q}}^+, \quad \text{and} \quad a_{\mathbf{q}'} = T_{21}^*\alpha_{-\mathbf{q}'}^+ + T_{22}^*\alpha_{\mathbf{q}'} + T_{23}^*\beta_{-\mathbf{q}'}^+ + T_{24}^*\beta_{\mathbf{q}'}, \tag{6.43}$$

since $T_{ij} \equiv T_{ij}(\mathbf{q}) = T_{ij}(-\mathbf{q})$ for our system. Both choices (6.42) and (6.43) are equally valid, but here we will always chose the transformations that allow us to express α magnon processes with first column $\mathbf{T}$ matrix elements T_{i1}, and β magnon processes with third column elements T_{i3}. Being interested in $\langle\alpha_{\mathbf{q}}(0)\alpha_{\mathbf{q}}^+(t)\rangle$ we therefore use (6.43) with $\mathbf{q}' = -\mathbf{q}$ and find

$$\langle S_i^+(0)S_{i'}^+(t)\rangle = \frac{4S}{N}\sum_{\mathbf{q},\mathbf{q}'} e^{i\mathbf{q}\cdot\mathbf{r}_i}e^{i\mathbf{q}'\cdot\mathbf{r}_{i'}}\langle a_{\mathbf{q}}(0)a_{\mathbf{q}'}(t)\rangle\delta_{\mathbf{q},-\mathbf{q}'} = \frac{4S}{N}\sum_{\mathbf{q}} e^{i\mathbf{q}\cdot(\mathbf{r}_i-\mathbf{r}_{i'})}T_{11}T_{21}^*\langle\alpha_{\mathbf{q}}(0)\alpha_{\mathbf{q}}^+(t)\rangle + \dots \tag{6.44}$$

This gives an α creation contribution to (6.29) which is

$$S_{\uparrow\uparrow}^{++}(\mathbf{Q},\omega)^{\alpha+} = \frac{4S}{N}\sum_{\mathbf{r}_i,\mathbf{r}_i'} e^{i\mathbf{Q}\cdot(\mathbf{r}_i'-\mathbf{r}_i)}\sum_{\mathbf{q}} e^{i\mathbf{q}\cdot(\mathbf{r}_i-\mathbf{r}_i')}T_{11}T_{21}^*\frac{1}{2\pi}\int dt e^{-i\omega t}\langle\alpha_{\mathbf{q}}(0)\alpha_{\mathbf{q}}^+(t)\rangle. \tag{6.45}$$

Here the indices of $S_{\uparrow\uparrow}^{++}(\mathbf{Q},\omega)^{\alpha+}$ reflect that we are considering the contribution to the scattering cross-section for creating an α magnon (written as $^{\alpha+}$) from the thermal mean value of $\langle S_i^+(0)S_{i'}^+(t)\rangle$. Since i and i' are both spin $\uparrow$ indices we write $_{\uparrow\uparrow}$, and since we are considering two S^+ operators we write $^{++}$.

For a non-Bravais crystal the position of the magnetic ions with spin σ can be written as

$$\mathbf{r} = \mathbf{l} + \boldsymbol{\sigma}. \tag{6.46}$$

Here $\mathbf{l}$ is the position of the unit cell, while $\boldsymbol{\sigma}$ is the position of the magnetic ion relative to the l'th unit cell. Let us define the spin dependent structure factors

$$F_\sigma(\boldsymbol{\tau}) = \sum_{\boldsymbol{\sigma}} e^{-i\boldsymbol{\tau}\cdot\boldsymbol{\sigma}}, \tag{6.47}$$

where the sum extends over all spin σ ions in a single unit cell. Remembering that

$$\sum_{\mathbf{l},\mathbf{l}'} e^{i(\mathbf{Q}-\mathbf{q})\cdot(\mathbf{l}'-\mathbf{l})} = N_u^2 \sum_{\boldsymbol{\tau}} \delta(\mathbf{Q}-\mathbf{q}-\boldsymbol{\tau}), \tag{6.48}$$

with N_u being the number of unit cells in the crystal and $\boldsymbol{\tau}$ being reciprocal lattice vectors, we find that

$$\begin{aligned}\sum_{\mathbf{r},\mathbf{r}'} e^{i\mathbf{Q}\cdot(\mathbf{r}'-\mathbf{r})} \sum_{\mathbf{q}} e^{i\mathbf{q}\cdot(\mathbf{r}-\mathbf{r}')} &= \sum_{\mathbf{q}} \sum_{\boldsymbol{\sigma}} e^{-i(\mathbf{Q}-\mathbf{q})\cdot\boldsymbol{\sigma}} \sum_{\boldsymbol{\sigma}'} e^{i(\mathbf{Q}-\mathbf{q})\cdot\boldsymbol{\sigma}'} \sum_{\mathbf{l},\mathbf{l}'} e^{i(\mathbf{Q}-\mathbf{q})\cdot(\mathbf{l}'-\mathbf{l})} \\ &= N_u^2 \sum_{\mathbf{q},\boldsymbol{\tau}} F_\sigma(\boldsymbol{\tau}) F_{\sigma'}(\boldsymbol{\tau})^* \, \delta(\mathbf{Q}-\mathbf{q}-\boldsymbol{\tau}).\end{aligned} \tag{6.49}$$

Often we will meet the related sum

$$\sum_{\mathbf{r},\mathbf{r}'} e^{i\mathbf{Q}\cdot(\mathbf{r}'-\mathbf{r})} \sum_{\mathbf{q}} e^{-i\mathbf{q}\cdot(\mathbf{r}-\mathbf{r}')} = N_u^2 \sum_{\mathbf{q},\boldsymbol{\tau}} F_\sigma(\boldsymbol{\tau}) F_{\sigma'}(\boldsymbol{\tau})^* \, \delta(\mathbf{Q}+\mathbf{q}-\boldsymbol{\tau}), \tag{6.50}$$

but it turns out, with the choices made in this section, that (6.49) always appears for magnon creation and (6.50) always for magnon destruction processes. The connections between $\mathbf{Q}$, $\mathbf{q}$ and $\boldsymbol{\tau}$ dictated by (6.49) and (6.50) are discussed in section 6.4.

Inserting (6.49) into (6.45) gives

$$S^{++}_{\uparrow\uparrow}(\mathbf{Q},\omega)^{\alpha+} = SN_u \sum_{\mathbf{q},\boldsymbol{\tau}} F_\uparrow(\boldsymbol{\tau}) F_\uparrow(\boldsymbol{\tau})^* T_{11} T_{21}^* n^+(\omega_{\mathbf{q}}^\alpha) \delta(\mathbf{Q}-\mathbf{q}-\boldsymbol{\tau}), \tag{6.51}$$

since $N = 4N_u$ for $LiNiPO_4$. As explained in section 6.4 there may be more than one pair of $(\mathbf{q},\boldsymbol{\tau})$ fulfilling the delta function in (6.51). In the case of primary interest, namely $LiNiPO_4$, there are four pairs of $(\mathbf{q},\boldsymbol{\tau})$ connected to each $\mathbf{Q}$. Two of these pairs have spin dependent structure factors $F_\uparrow(\boldsymbol{\tau})$ that are zero and do not contribute to the scattering cross-section. The two remaining pairs give the exact same results in the numerical MATLAB simulations, both regarding to the dispersions and the intensities. This indicates, although it does not prove, that the two pairs are always equivalent. In any case, evaluating the delta function gives

$$S^{++}_{\uparrow\uparrow}(\mathbf{Q},\omega)^{\alpha+} = SN_u \sum_{\boldsymbol{\tau}_{\boldsymbol{Q}}} F_\uparrow(\boldsymbol{\tau}_{\boldsymbol{Q}}) F_\uparrow(\boldsymbol{\tau}_{\boldsymbol{Q}})^* T_{11} T_{21}^* n^+(\omega_{\mathbf{Q}}^\alpha), \tag{6.52}$$

where $\boldsymbol{\tau}_{\boldsymbol{Q}}$ are the appropriate "surviving" reciprocal lattice points and $T_{ij} = T_{ij}(\mathbf{Q}-\boldsymbol{\tau}_{\boldsymbol{Q}})$.

The calculation we have just performed is almost exactly the same for the other terms needed in the α magnon creation cross-section. The only difference is which T_{ij} elements to use, and these can easily be found by looking at (6.41). This is done in table 6.1 for the α magnon creation cross-section, and in tables 6.2-6.4 for the other cross-sections.

In table 6.1 we define

$$\begin{aligned}\Sigma_1^{\alpha+} = \sum_{\sigma\sigma'} F_\sigma(\boldsymbol{\tau}) F_{\sigma'}(\boldsymbol{\tau})^* S^{++}_{\sigma\sigma'} &= T_{11}T_{21}^* F_\uparrow(\boldsymbol{\tau})F_\uparrow(\boldsymbol{\tau})^* + T_{11}T_{31}^* F_\uparrow(\boldsymbol{\tau})F_\downarrow(\boldsymbol{\tau})^* + T_{41}T_{21}^* F_\downarrow(\boldsymbol{\tau})F_\uparrow(\boldsymbol{\tau})^* \\ &+ T_{41}T_{31}^* F_\downarrow(\boldsymbol{\tau})F_\downarrow(\boldsymbol{\tau})^* = \big[T_{11}F_\uparrow(\boldsymbol{\tau}) + T_{41}F_\downarrow(\boldsymbol{\tau})\big]\big[T_{21}F_\uparrow(\boldsymbol{\tau}) + T_{31}F_\downarrow(\boldsymbol{\tau})\big]^*,\end{aligned} \tag{6.53}$$

and similar for the other columns. We have

$$\Sigma_1^{\alpha+} = \big[T_{11}F_\uparrow(\boldsymbol{\tau}) + T_{41}F_\downarrow(\boldsymbol{\tau})\big]\big[T_{21}F_\uparrow(\boldsymbol{\tau}) + T_{31}F_\downarrow(\boldsymbol{\tau})\big]^* \equiv MN^*, \tag{6.54a}$$

$$\Sigma_2^{\alpha+} = \big[T_{11}F_\uparrow(\boldsymbol{\tau}) + T_{41}F_\downarrow(\boldsymbol{\tau})\big]\big[T_{11}F_\uparrow(\boldsymbol{\tau}) + T_{41}F_\downarrow(\boldsymbol{\tau})\big]^* \equiv MM^*, \tag{6.54b}$$

$$\Sigma_3^{\alpha+} = \big[T_{21}F_\uparrow(\boldsymbol{\tau}) + T_{31}F_\downarrow(\boldsymbol{\tau})\big]\big[T_{21}F_\uparrow(\boldsymbol{\tau}) + T_{31}F_\downarrow(\boldsymbol{\tau})\big]^* \equiv NN^*, \tag{6.54c}$$

$$\Sigma_4^{\alpha+} = \big[T_{11}F_\uparrow(\boldsymbol{\tau}) + T_{41}F_\downarrow(\boldsymbol{\tau})\big]^*\big[T_{21}F_\uparrow(\boldsymbol{\tau}) + T_{31}F_\downarrow(\boldsymbol{\tau})\big] \equiv M^*N, \tag{6.54d}$$

where

$$M = T_{11}F_{\uparrow}(\boldsymbol{\tau}) + T_{41}F_{\downarrow}(\boldsymbol{\tau}), \tag{6.55}$$
$$N = T_{21}F_{\uparrow}(\boldsymbol{\tau}) + T_{31}F_{\downarrow}(\boldsymbol{\tau}). \tag{6.56}$$

Using (6.38), (6.52) and (6.54a)-(6.54d) we now see that

$$S^{\alpha+}_{xx}(\mathbf{Q},\omega) = SN_u \sum_{\boldsymbol{\tau}_{\boldsymbol{Q}}} |M+N|^2 n(\omega^{\alpha}_{\mathbf{Q}})\delta(\omega - \omega^{\alpha}_{\mathbf{Q}}), \tag{6.57}$$
$$S^{\alpha+}_{yy}(\mathbf{Q},\omega) = SN_u \sum_{\boldsymbol{\tau}_{\boldsymbol{Q}}} |M-N|^2 n(\omega^{\alpha}_{\mathbf{Q}})\delta(\omega - \omega^{\alpha}_{\mathbf{Q}}), \tag{6.58}$$
$$S^{\alpha+}_{xy}(\mathbf{Q},\omega) + S^{\alpha+}_{yx}(\mathbf{Q},\omega) = 2SN_u \sum_{\boldsymbol{\tau}_{\boldsymbol{Q}}} \mathrm{Im}\big(MN^*\big) n(\omega^{\alpha}_{\mathbf{Q}})\delta(\omega - \omega^{\alpha}_{\mathbf{Q}}), \tag{6.59}$$

where the $\boldsymbol{\tau}$ appearing in M and N are the appropriate $\boldsymbol{\tau}_{\boldsymbol{Q}}$ dictated by $\delta(\mathbf{Q}-\mathbf{q}-\boldsymbol{\tau})$. Inserting into (6.28) we finally find that the cross-section for creating an α magnon is

$$\begin{aligned}\left(\frac{d^2\sigma^{\alpha+}_m}{d\Omega dE'}\right)(\mathbf{Q},\omega) &= \Gamma(\mathbf{Q},\omega)\big(n(\omega^{\alpha}_{\mathbf{Q}})+1\big)\delta(\omega-\omega^{\alpha}_{\mathbf{Q}}) \\ &\times \sum_{\boldsymbol{\tau}_{\boldsymbol{Q}}} \Big(\big(1-\widehat{\mathbf{Q}}^2_x\big)|M+N|^2 + \big(1-\widehat{\mathbf{Q}}^2_y\big)|M-N|^2 - \widehat{\mathbf{Q}}_x\widehat{\mathbf{Q}}_y 2\mathrm{Im}\big(MN^*\big)\Big),\end{aligned} \tag{6.60}$$

where

$$\Gamma(\mathbf{Q},\omega) = \frac{k_f}{k_i}(\gamma r_0)^2 \left[\frac{g}{2}F(\mathbf{Q})\right]^2 \frac{e^{-2W(\mathbf{Q})}}{4\hbar} SN_u. \tag{6.61}$$

6.3.2 The general one magnon cross-sections

The scattering cross-sections for the other processes are calculated in the same way as the α creation cross-section. Here we summarize the results (F_σ is defined in (6.47) and Γ in (6.61)).

$\underline{\alpha}$ **creation**

$$\begin{aligned}\left(\frac{d^2\sigma_m^{\alpha+}}{d\Omega dE'}\right)(\mathbf{Q},\omega) &= \Gamma(\mathbf{Q},\omega)\big(n(\omega_{\mathbf{Q}}^{\alpha})+1\big)\delta(\omega-\omega_{\mathbf{Q}}^{\alpha}) \\ &\times\sum_{\boldsymbol{\tau}_{\boldsymbol{Q}}}\Big(\big(1-\widehat{\mathbf{Q}}_x^2\big)|M+N|^2+\big(1-\widehat{\mathbf{Q}}_y^2\big)|M-N|^2-\widehat{\mathbf{Q}}_x\widehat{\mathbf{Q}}_y 2\mathrm{Im}\big(MN^*\big)\Big),\end{aligned} \tag{6.62}$$

where

$$M=T_{11}F_\uparrow(\boldsymbol{\tau})+T_{41}F_\downarrow(\boldsymbol{\tau}),\quad N=T_{21}F_\uparrow(\boldsymbol{\tau})+T_{31}F_\downarrow(\boldsymbol{\tau}),\quad \boldsymbol{\tau}_{\boldsymbol{Q}}=\mathbf{Q}-\mathbf{q}. \tag{6.63}$$

$\underline{\beta}$ **creation**

$$\begin{aligned}\left(\frac{d^2\sigma_m^{\beta+}}{d\Omega dE'}\right)(\mathbf{Q},\omega) &= \Gamma(\mathbf{Q},\omega)\big(n(\omega_{\mathbf{Q}}^{\beta})+1\big)\delta(\omega-\omega_{\mathbf{Q}}^{\beta}) \\ &\times\sum_{\boldsymbol{\tau}_{\boldsymbol{Q}}}\Big(\big(1-\widehat{\mathbf{Q}}_x^2\big)|M+N|^2+\big(1-\widehat{\mathbf{Q}}_y^2\big)|M-N|^2-\widehat{\mathbf{Q}}_x\widehat{\mathbf{Q}}_y 2\mathrm{Im}\big(MN^*\big)\Big),\end{aligned} \tag{6.64}$$

where

$$M=T_{13}F_\uparrow(\boldsymbol{\tau})+T_{43}F_\downarrow(\boldsymbol{\tau}),\quad N=T_{23}F_\uparrow(\boldsymbol{\tau})+T_{33}F_\downarrow(\boldsymbol{\tau}),\quad \boldsymbol{\tau}_{\boldsymbol{Q}}=\mathbf{Q}-\mathbf{q}. \tag{6.65}$$

$\underline{\alpha}$ **destruction**

$$\begin{aligned}\left(\frac{d^2\sigma_m^{\alpha-}}{d\Omega dE'}\right)(\mathbf{Q},\omega) &= \Gamma(\mathbf{Q},\omega)n(\omega_{\mathbf{Q}}^{\alpha})\delta(\omega+\omega_{\mathbf{Q}}^{\alpha}) \\ &\times\sum_{\boldsymbol{\tau}_{\boldsymbol{Q}}}\Big(\big(1-\widehat{\mathbf{Q}}_x^2\big)|M+N|^2+\big(1-\widehat{\mathbf{Q}}_y^2\big)|M-N|^2-\widehat{\mathbf{Q}}_x\widehat{\mathbf{Q}}_y 2\mathrm{Im}\big(MN^*\big)\Big),\end{aligned} \tag{6.66}$$

where

$$M=T_{11}F_\uparrow(\boldsymbol{\tau})^*+T_{41}F_\downarrow(\boldsymbol{\tau})^*,\quad N=T_{21}F_\uparrow(\boldsymbol{\tau})^*+T_{31}F_\downarrow(\boldsymbol{\tau})^*,\quad \boldsymbol{\tau}_{\boldsymbol{Q}}=\mathbf{Q}+\mathbf{q}. \tag{6.67}$$

$\underline{\beta}$ **destruction**

$$\begin{aligned}\left(\frac{d^2\sigma_m^{\beta-}}{d\Omega dE'}\right)(\mathbf{Q},\omega) &= \Gamma(\mathbf{Q},\omega)n(\omega_{\mathbf{Q}}^{\beta})\delta(\omega+\omega_{\mathbf{Q}}^{\beta}) \\ &\times\sum_{\boldsymbol{\tau}_{\boldsymbol{Q}}}\Big(\big(1-\widehat{\mathbf{Q}}_x^2\big)|M+N|^2+\big(1-\widehat{\mathbf{Q}}_y^2\big)|M-N|^2-\widehat{\mathbf{Q}}_x\widehat{\mathbf{Q}}_y 2\mathrm{Im}\big(MN^*\big)\Big),\end{aligned} \tag{6.68}$$

where

$$M=T_{13}F_\uparrow(\boldsymbol{\tau})^*+T_{43}F_\downarrow(\boldsymbol{\tau})^*,\quad N=T_{23}F_\uparrow(\boldsymbol{\tau})^*+T_{33}F_\downarrow(\boldsymbol{\tau})^*,\quad \boldsymbol{\tau}_{\boldsymbol{Q}}=\mathbf{Q}+\mathbf{q}. \tag{6.69}$$

$n^+(\omega^\alpha_{\mathbf{q}})$	$\sigma\sigma'$	$S^{++}_{\sigma\sigma'}$	$S^{+-}_{\sigma\sigma'}$	$S^{-+}_{\sigma\sigma'}$	$S^{--}_{\sigma\sigma'}$	
$F_\uparrow(\boldsymbol{\tau})F_\uparrow(\boldsymbol{\tau})^*$	$\uparrow\uparrow$	$T_{11}T^*_{21}$	$T_{11}T^*_{11}$	$T_{21}T^*_{21}$	$T_{21}T^*_{11}$	$\delta(\mathbf{Q}-\mathbf{q}-\boldsymbol{\tau})$
$F_\uparrow(\boldsymbol{\tau})F_\downarrow(\boldsymbol{\tau})^*$	$\uparrow\downarrow$	$T_{11}T^*_{31}$	$T_{11}T^*_{41}$	$T_{21}T^*_{31}$	$T_{21}T^*_{41}$	$\delta(\mathbf{Q}-\mathbf{q}-\boldsymbol{\tau})$
$F_\downarrow(\boldsymbol{\tau})F_\uparrow(\boldsymbol{\tau})^*$	$\downarrow\uparrow$	$T_{41}T^*_{21}$	$T_{41}T^*_{11}$	$T_{31}T^*_{21}$	$T_{31}T^*_{11}$	$\delta(\mathbf{Q}-\mathbf{q}-\boldsymbol{\tau})$
$F_\downarrow(\boldsymbol{\tau})F_\downarrow(\boldsymbol{\tau})^*$	$\downarrow\downarrow$	$T_{41}T^*_{31}$	$T_{41}T^*_{41}$	$T_{31}T^*_{31}$	$T_{31}T^*_{41}$	$\delta(\mathbf{Q}-\mathbf{q}-\boldsymbol{\tau})$
		$\Sigma^{\alpha+}_1$	$\Sigma^{\alpha+}_2$	$\Sigma^{\alpha+}_3$	$\Sigma^{\alpha+}_4$	

Table 6.1: Terms relevant for α magnon creation processes.

$n^+(\omega^\beta_{\mathbf{q}})$	$\sigma\sigma'$	$S^{++}_{\sigma\sigma'}$	$S^{+-}_{\sigma\sigma'}$	$S^{-+}_{\sigma\sigma'}$	$S^{--}_{\sigma\sigma'}$	
$F_\uparrow(\boldsymbol{\tau})F_\uparrow(\boldsymbol{\tau})^*$	$\uparrow\uparrow$	$T_{13}T^*_{23}$	$T_{13}T^*_{13}$	$T_{23}T^*_{23}$	$T_{23}T^*_{13}$	$\delta(\mathbf{Q}-\mathbf{q}-\boldsymbol{\tau})$
$F_\uparrow(\boldsymbol{\tau})F_\downarrow(\boldsymbol{\tau})^*$	$\uparrow\downarrow$	$T_{13}T^*_{33}$	$T_{13}T^*_{43}$	$T_{23}T^*_{33}$	$T_{23}T^*_{43}$	$\delta(\mathbf{Q}-\mathbf{q}-\boldsymbol{\tau})$
$F_\downarrow(\boldsymbol{\tau})F_\uparrow(\boldsymbol{\tau})^*$	$\downarrow\uparrow$	$T_{43}T^*_{23}$	$T_{43}T^*_{13}$	$T_{33}T^*_{23}$	$T_{33}T^*_{13}$	$\delta(\mathbf{Q}-\mathbf{q}-\boldsymbol{\tau})$
$F_\downarrow(\boldsymbol{\tau})F_\downarrow(\boldsymbol{\tau})^*$	$\downarrow\downarrow$	$T_{43}T^*_{33}$	$T_{43}T^*_{43}$	$T_{33}T^*_{33}$	$T_{33}T^*_{43}$	$\delta(\mathbf{Q}-\mathbf{q}-\boldsymbol{\tau})$
		$\Sigma^{\beta+}_1$	$\Sigma^{\beta+}_2$	$\Sigma^{\beta+}_3$	$\Sigma^{\beta+}_4$	

Table 6.2: Terms relevant for β magnon creation processes.

$n^-(\omega^\alpha_{\mathbf{q}})$	$\sigma\sigma'$	$S^{++}_{\sigma\sigma'}$	$S^{+-}_{\sigma\sigma'}$	$S^{-+}_{\sigma\sigma'}$	$S^{--}_{\sigma\sigma'}$	
$F_\uparrow(\boldsymbol{\tau})F_\uparrow(\boldsymbol{\tau})^*$	$\uparrow\uparrow$	$T^*_{21}T_{11}$	$T^*_{21}T_{21}$	$T^*_{11}T_{11}$	$T^*_{11}T_{21}$	$\delta(\mathbf{Q}+\mathbf{q}-\boldsymbol{\tau})$
$F_\uparrow(\boldsymbol{\tau})F_\downarrow(\boldsymbol{\tau})^*$	$\uparrow\downarrow$	$T^*_{21}T_{41}$	$T^*_{21}T_{31}$	$T^*_{11}T_{41}$	$T^*_{11}T_{31}$	$\delta(\mathbf{Q}+\mathbf{q}-\boldsymbol{\tau})$
$F_\downarrow(\boldsymbol{\tau})F_\uparrow(\boldsymbol{\tau})^*$	$\downarrow\uparrow$	$T^*_{31}T_{11}$	$T^*_{31}T_{21}$	$T^*_{41}T_{11}$	$T^*_{41}T_{21}$	$\delta(\mathbf{Q}+\mathbf{q}-\boldsymbol{\tau})$
$F_\downarrow(\boldsymbol{\tau})F_\downarrow(\boldsymbol{\tau})^*$	$\downarrow\downarrow$	$T^*_{31}T_{41}$	$T^*_{31}T_{31}$	$T^*_{41}T_{41}$	$T^*_{41}T_{31}$	$\delta(\mathbf{Q}+\mathbf{q}-\boldsymbol{\tau})$
		$\Sigma^{\alpha-}_1$	$\Sigma^{\alpha-}_2$	$\Sigma^{\alpha-}_3$	$\Sigma^{\alpha-}_4$	

Table 6.3: Terms relevant for α magnon destruction processes.

$n^-(\omega^\beta_{\mathbf{q}})$	$\sigma\sigma'$	$S^{++}_{\sigma\sigma'}$	$S^{+-}_{\sigma\sigma'}$	$S^{-+}_{\sigma\sigma'}$	$S^{--}_{\sigma\sigma'}$	
$F_\uparrow(\boldsymbol{\tau})F_\uparrow(\boldsymbol{\tau})^*$	$\uparrow\uparrow$	$T^*_{23}T_{13}$	$T^*_{23}T_{23}$	$T^*_{13}T_{13}$	$T^*_{13}T_{23}$	$\delta(\mathbf{Q}+\mathbf{q}-\boldsymbol{\tau})$
$F_\uparrow(\boldsymbol{\tau})F_\downarrow(\boldsymbol{\tau})^*$	$\uparrow\downarrow$	$T^*_{23}T_{43}$	$T^*_{23}T_{33}$	$T^*_{13}T_{43}$	$T^*_{13}T_{33}$	$\delta(\mathbf{Q}+\mathbf{q}-\boldsymbol{\tau})$
$F_\downarrow(\boldsymbol{\tau})F_\uparrow(\boldsymbol{\tau})^*$	$\downarrow\uparrow$	$T^*_{33}T_{13}$	$T^*_{33}T_{23}$	$T^*_{43}T_{13}$	$T^*_{43}T_{23}$	$\delta(\mathbf{Q}+\mathbf{q}-\boldsymbol{\tau})$
$F_\downarrow(\boldsymbol{\tau})F_\downarrow(\boldsymbol{\tau})^*$	$\downarrow\downarrow$	$T^*_{33}T_{43}$	$T^*_{33}T_{33}$	$T^*_{43}T_{43}$	$T^*_{43}T_{33}$	$\delta(\mathbf{Q}+\mathbf{q}-\boldsymbol{\tau})$
		$\Sigma^{\beta-}_1$	$\Sigma^{\beta-}_2$	$\Sigma^{\beta-}_3$	$\Sigma^{\beta-}_4$	

Table 6.4: Terms relevant for β magnon destruction processes.

6.4 Fourier transformation and the universal Brillouin zone

A large part of our mathematical framework depends on the Holstein Primakoff operators being Fourier transformed according to (6.34). Here we will discuss exactly which wave vectors **q** are included in the Fourier transforms, and how this is connected to the spin wave dispersions and intensity calculations.

Two identical particles

Let us first look at the simple case of describing two identical particles separated by a distance a along a x-axis and oscillating along a y-axis (figure 6.1). We assume that the particles are oscillating with the same frequency ω and amplitude y_0, so

$$y_1(t) = y_0 e^{i\omega t}, \quad y_2(t) = y_0 e^{i(\omega t - qa)}. \tag{6.70}$$

In order to describe any given oscillation it is clear that the phase difference

$$qa \in]-\pi, \pi] \Rightarrow q \in]-\frac{\pi}{a}, \frac{\pi}{a}]. \tag{6.71}$$

The collective motion of the two particles is called a wave movement and is classified according to

$$qa \in]\frac{\pi}{2}, \pi] \Rightarrow q \in]\frac{\pi}{2a}, \frac{\pi}{a}] : \quad \text{Out of phase oscillation from } 1 \rightarrow 2, \tag{6.72a}$$

$$qa \in]0, \frac{\pi}{2}] \Rightarrow q \in]0, \frac{\pi}{2a}] : \quad \text{In phase oscillation from } 1 \rightarrow 2, \tag{6.72b}$$

$$qa \in]-\frac{\pi}{2}, 0] \Rightarrow q \in]-\frac{\pi}{2a}, 0] : \quad \text{In phase oscillation from } 2 \rightarrow 1, \tag{6.72c}$$

$$qa \in]-\pi, -\frac{\pi}{2}] \Rightarrow q \in]-\frac{\pi}{a}, -\frac{\pi}{2a}] : \quad \text{Out of phase oscillation from } 2 \rightarrow 1. \tag{6.72d}$$

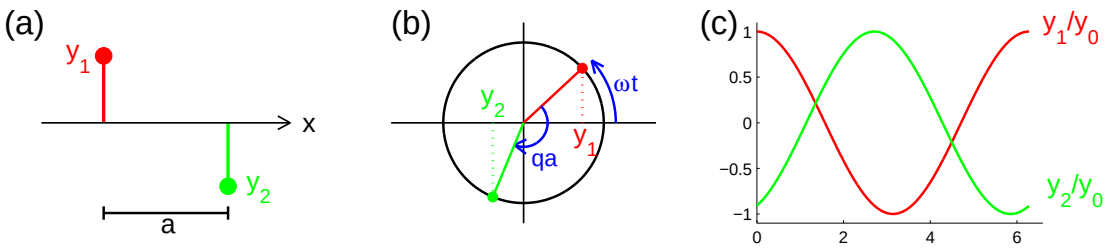

Figure 6.1: (a) Two identical particles separated by a along the x direction and oscillating along the y direction. (b) The complex amplitudes $y_1(t)$ and $y_2(t)$ in the complex plane. The depicted situation has $qa \in]\frac{\pi}{2}, \pi]$ and corresponds to an out of phase wave movement from particle 1 to 2. (c) The real amplitudes as function of time. The situation is the same as in (b) with the two particles being out of phase and particle 1 reaching its maximum ahead of particle 2.

Chain of N identical particles

Next we consider the standard textbook example of a chain with N identical particles (figure 6.2). We assume the particles are uniformly distributed along x with an inter-particle distance a, and consider wave movements that are describable with wave numbers q and frequencies ω. From our example with two particles we know that in order to describe all possible oscillations the Fourier transformation must use

$$q \in]-\frac{\pi}{a}, \frac{\pi}{a}]. \tag{6.73}$$

Considering the N particles as a crystal we proceed by defining a suitable unit cell. The oscillations, or wave movements, are now collective excitations that can be probed by inelastic neutron experiments. Regardless the choice of unit cell the inelastic dispersions must reflect (6.73) and have a periodicity of $\frac{2\pi}{a}$.

It is natural to define the unit cell having length a. In this case the reciprocal lattice vectors are

$$\tau_n = n\frac{2\pi}{a}, \quad n \in \mathbb{Z}. \tag{6.74}$$

Employing periodic boundary conditions leads to discrete values of q, namely

$$q = \frac{2\pi}{Na}, \tag{6.75}$$

and, as is well known, the notion of the first Brillouin zone follows directly from the choice of unit cell. Here the first Brillouin zone is defined as

$$q \in]-\frac{\pi}{a}, \frac{\pi}{a}]. \tag{6.76}$$

This is the same region as (6.73) which means that all possible waves can be described by Fourier transforming with wave vectors from the first Brillouin zone.

Now, assume that we for some reason wish to define our unit cell with length $b = 2a$. Then the reciprocal lattice vectors are

$$\tau_n = n\frac{2\pi}{b} = n\frac{\pi}{a}, \quad n \in \mathbb{Z}, \tag{6.77}$$

and the first Brillouin zone is

$$q \in]-\frac{\pi}{b}, \frac{\pi}{b}] =]-\frac{\pi}{2a}, \frac{\pi}{2a}]. \tag{6.78}$$

Here the first Brillouin zone is smaller than (6.73) and does not suffice to describe all possible oscillations.

If we insist on the Fourier transformations using exclusively wave vectors from the first Brillouin zone we must somehow include the missing wave movements. The standard way of doing this is to fold the part of the dispersion that is lying outside the first Brillouin zone into the zone. This is often called the reduced zone scheme (see figure 6.2(c)). Hereby we get an additional (artificial) branch of the dispersion that describes the out of phase oscillations inside the first Brillouin zone.

The way to mimic the reduced zone scheme in our Holstein Primakoff formalism[4] is somewhat unappealing. We must regard neighboring particles as non identical particles by introducing two different kinds

[4]Even though we are considering spin wave excitations at this point, the considerations are also valid for phonon scattering.

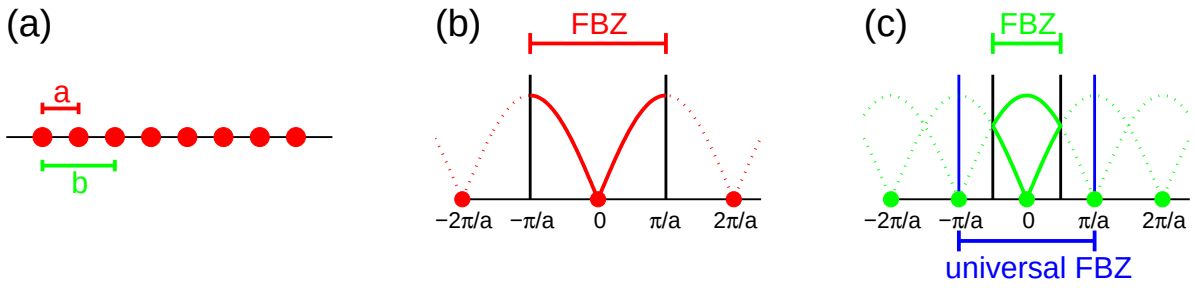

Figure 6.2: (a) N identical particles separated by a along the x direction. (b) The reciprocal lattice points (red full circles), first Brillouin zone (FBZ) and dispersion (red full and dotted line) when choosing a unit cell of length a. Here the first Brillouin zone is large enough to describe any oscillation and the dispersion is fully described within the zone. (c) The reciprocal lattice points (green full circles) and first Brillouin zone (FBZ) when choosing a unit cell of length b. Here the dispersions (green full and dotted line) are folded into the FBZ in the reduced zone picture, giving an extra (acoustic) branch describing the out of phase motion. In our mathematical formalism this requires additional Bose operators which is equivalent to regarding neighboring particles in the chain as different. One can avoid introducing the artificial acoustic branch by including wave vectors from the universal first Brillouin zone in the Fourier transforms (see text).

of Holstein Primakoff operators, a_q, a_q^+ and b_q, b_q^+ in the Hamiltonian. This leads to the existence of two eigenvalues ω_q^α and ω_q^β describing the energies of the in phase and out of phase oscillations, respectively. Since the particles in reality are identical, we would never in an experiment observe two dispersions for any given $\mathbf{Q}$. This is accounted for mathematically when calculating the intensities of the dispersions. In the first Brillouin zone the calculated intensity of the high lying branch (the out of phase oscillations) is zero, while in the neighboring Brillouin zone the low lying branch (the in phase oscillations) have no intensity. This amounts to the exact same results as if we had chosen a unit cell with lattice parameter a.

From a calculational point of view the reduced zone scheme is not the best way to compensate for the choice of unit cell. Instead it is better to use the appropriate wave vectors (6.73) in the Fourier transformations even if this means going outside the first Brillouin zone. Doing this, we let the crystal symmetry govern the Fourier transforms instead of some arbitrary unit cell definition, and avoid having to introduce additional Bose operators. The wave vectors in (6.73) constitutes what we might call a universal (or generalized) first Brillouin zone.

$LiNiPO_4$

Let us generalize the notion of the universal first Brillouin zone (UFBZ) to the magnetic system of $LiNiPO_4$ (figure 6.3(a)). Spin up and down ions are described with different operators a, a^+ and b, b^+, so the universal Brillouin zone is defined by the distances between ions having the same spin. Since Fourier transforming is really just expanding on plane waves, the relevant distances are determined by projecting the magnetic ions on $\mathbf{a}$, $\mathbf{b}$ and $\mathbf{c}$. Figure 6.3(b) show the projection of the Ni ions onto the bc plane. Obviously the projected distance between spin up particles along $\mathbf{b}$ is b, and along the c-direction is $c/2$. Therefore the universal FBZ is lying between $\pm\pi/b$ ($\pm 1/2$ r.l.u.) along the Q_y direction, and between $\pm 2\pi/c$ (± 1 r.l.u.) along the

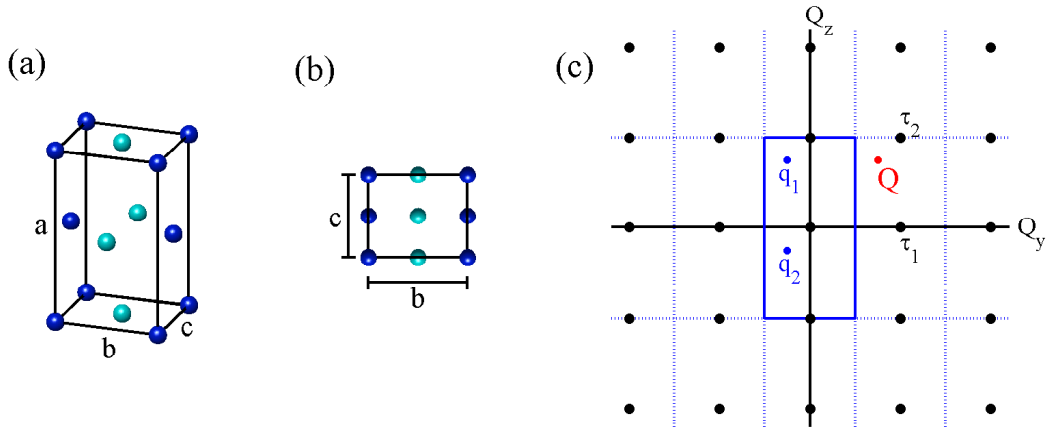

Figure 6.3: (a) Magnetic unit cell for $LiNiPO_4$ showing only the magnetic Ni^{2+} ions. The coloring distinguish between spin up (dark blue) and spin down (light blue) ions. (b) The position of the magnetic ions projected onto the bc plane. (c) The reciprocal Q_yQ_z plane. The reciprocal lattice points (full black circles) follow the choice of the unit cell, while the universal first Brillouin zone (full blue line) is determined by the translation symmetry of the magnetic ions projected onto the bc plane. The dotted blue lines divide the reciprocal plane into several universal zones equivalent with the first universal zone. For the example given in the text we consider a scattering vector $\mathbf{Q} = (0, Q_y, Q_z)$. There are four pairs of $(\mathbf{q}, \boldsymbol{\tau})$ where $\mathbf{q}$ is situated in the universal first Brillouin zone, $\boldsymbol{\tau}$ is a reciprocal lattice vector and $\mathbf{Q} = \mathbf{q} + \boldsymbol{\tau}$. Here we only depict the two pairs for which $q_x, \tau_x = 0$. Since the spin dependent structure factor of $\boldsymbol{\tau}_2$ and $\boldsymbol{\tau}_3$ (not shown) is zero, only the pairs $(\mathbf{q}_1, \boldsymbol{\tau}_1)$ and $(\mathbf{q}_4, \boldsymbol{\tau}_4)$ (not shown) contributes to the scattering cross-section (see text).

Q_z direction (figure 6.3(c)). Since the projected distance is $a/2$ between spin up ions along $\mathbf{a}$, we find that

$$\begin{aligned} \text{UFBZ} &=]-\frac{2\pi}{a},\frac{2\pi}{a}] \times]-\frac{\pi}{b},\frac{\pi}{b}] \times]-\frac{2\pi}{c},\frac{2\pi}{c}] \\ &\equiv]-1,1] \times]-\frac{1}{2},\frac{1}{2}] \times]-1,1]. \end{aligned} \tag{6.79}$$

In section 6.3 we calculated the spin wave intensities for magnon creation processes, and saw that the scattering vector $\mathbf{Q}$ is connected to $\mathbf{q} \in$ UFBZ and a reciprocal lattice vector $\boldsymbol{\tau}$ if

$$\mathbf{Q} = \mathbf{q} + \boldsymbol{\tau}. \tag{6.80}$$

For magnon destruction processes the corresponding relation reads $\mathbf{Q} = -\mathbf{q} + \boldsymbol{\tau}$.

Let us consider an example where the scattering vector, $\mathbf{Q} = (0, 3/4, 3/4)$, is situated in the bc plane (figure 6.3(c)). Focusing on magnon creation processes we note that four pairs of $(\mathbf{q}, \boldsymbol{\tau})$ fulfil (6.80), namely

$$\mathbf{q}_1 = (0, -\frac{1}{4}, \frac{3}{4}), \qquad \boldsymbol{\tau}_1 = (0,1,0), \qquad |F_\sigma(\boldsymbol{\tau}_1)| = 2, \tag{6.81a}$$

$$\mathbf{q}_2 = (0, -\frac{1}{4}, -\frac{1}{4}), \qquad \boldsymbol{\tau}_2 = (0,1,1), \qquad |F_\sigma(\boldsymbol{\tau}_2)| = 0, \tag{6.81b}$$

$$\mathbf{q}_3 = (1, -\frac{1}{4}, \frac{3}{4}), \qquad \boldsymbol{\tau}_3 = (-1,1,0), \qquad |F_\sigma(\boldsymbol{\tau}_3)| = 0, \tag{6.81c}$$

$$\mathbf{q}_4 = (1, -\frac{1}{4}, -\frac{1}{4}), \qquad \boldsymbol{\tau}_4 = (-1,1,1), \qquad |F_\sigma(\boldsymbol{\tau}_4)| = 2. \tag{6.81d}$$

Introducing the spin dependent structure factors (see (6.47))

$$F_\uparrow(\boldsymbol{\tau}) = 1 + e^{i\pi(\tau_x+\tau_z)} = \begin{cases} 2, & \text{if } \tau_x + \tau_z = 2p, \\ 0, & \text{if } \tau_x + \tau_z = 2p+1, \end{cases} \tag{6.82a}$$

$$F_\downarrow(\boldsymbol{\tau}) = e^{i\pi(\tau_y+\tau_z)} F_\uparrow(\boldsymbol{\tau}) = \begin{cases} 2e^{i\pi(\tau_y+\tau_z)}, & \text{if } \tau_x + \tau_z = 2p, \\ 0, & \text{if } \tau_x + \tau_z = 2p+1, \end{cases} \tag{6.82b}$$

we see that $(\mathbf{q}_1, \boldsymbol{\tau}_1)$ and $(\mathbf{q}_4, \boldsymbol{\tau}_4)$ contribute to the cross-section, while $(\mathbf{q}_2, \boldsymbol{\tau}_2)$ and $(\mathbf{q}_3, \boldsymbol{\tau}_3)$ do not. The computer simulations show that $(\mathbf{q}_1, \boldsymbol{\tau}_1)$ gives exactly the same eigenenergies and spin wave intensities as $(\mathbf{q}_4, \boldsymbol{\tau}_4)$. By inspection I have checked that this holds for all the scattering vectors which are included in the computer calculations presented in chapter 7.

In the magnetic system of $LiNiPO_4$ there are two different types of particles, namely spin up and spin down ions, meaning that there are two spin wave dispersions (we have learned to know them as $\omega^\alpha_{\mathbf{q}}$ and $\omega^\beta_{\mathbf{q}}$). Suppose that there were no interactions in the system that distinguishes between α and β quasi particles. Then the two dispersions would be degenerate and $\omega^\alpha_{\mathbf{Q}} = \omega^\beta_{\mathbf{Q}}$ in all of reciprocal space.

We can easily see that this is not the case in $LiNiPO_4$ by comparing the symmetries of the measured spin waves (figure 7.7 in chapter 7) to that of the universal first Brillouin zone (6.79). The Fourier transforms connect every scattering vector $\mathbf{Q}$ with the universal FBZ, so a single dispersion in $LiNiPO_4$ must repeat itself with the symmetry of (6.79). Looking at the measured dispersions along the Q_x and the Q_z direction (figure 7.7(a) and (c)) the spin wave periodicity of 2 r.l.u. matches exactly the size of the universal Brillouin zone. However, along the Q_y direction (figure 7.7(b)), the dispersion has a periodicity that is larger than 1 r.l.u., which is the size of the universal zone along $\hat{\mathbf{y}}$. Since the symmetry of (6.79) cannot be broken by a single dispersion we obviously need (at least) two non-degenerate dispersions to describe the measured data.

In the spin wave calculations of $LiNiPO_4$, we have used a model where the interactions responsible for the non-degeneracy of $\omega^\alpha_{\mathbf{q}}$ and $\omega^\beta_{\mathbf{q}}$ are non-identical single ion anisotropies along $\hat{\mathbf{x}}$ and $\hat{\mathbf{y}}$ ($\hat{\mathbf{z}}$ being the preferred spin direction).

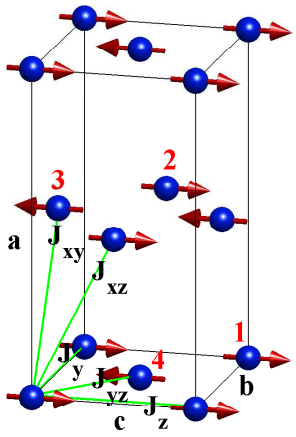

Figure 6.4: The spin structure and Heisenberg interactions used in the spin wave modelling.

6.5 The spin wave model Hamiltonian for $LiNiPO_4$

We analyzed our measured spin wave data in chapter 7, using the theory presented in this chapter on a spin Hamiltonian

$$H = H_{yz} + H_y + H_z + H_{xz} + H_{xy} + A_x + A_y + A_z. \tag{6.83}$$

Here H_α and $H_{\alpha\beta}$ are Heisenberg interactions between pairs of Ni-ions, as shown in figure 6.4, and A_α are single ion anisotropies. The subscripts, α and β, indicate the direction of the interactions, with x, y and z defined along a, b and c. In the model we assume the spins point strictly along the c axis, as depicted in figure 6.4, and thereby neglect the small S_x components found in chapter 5.

Heisenberg terms

Let us consider a spin up ion placed in position (0,0,0). We assume the spin on this ion is interacting with other ionic spins at the following positions:

- In-plane neighboring ions, spin down (J_{yz}) : $(0, b/2, c/2)$, $(0, -b/2, -c/2)$, $(0, b/2, -c/2)$, $(0, -b/2, c/2)$,
- Out of plane neighboring ions, spin down (J_{xy}) : $(a/2, b/2, 0)$, $(-a/2, -b/2, 0)$, $(a/2, -b/2, 0)$, $(-a/2, b/2, 0)$,
- In-plane next-neighboring ions along b, spin up (J_y) : $(0, b, 0)$, $(0, -b, 0)$,
- In-plane next-neighboring ions along c, spin up (J_z) : $(0, 0, c)$, $(0, 0, -c)$,
- Out of plane neighboring ions, spin up (J_{xz}) : $(a/2, 0, c/2)$, $(-a/2, 0, -c/2)$, $(a/2, 0, -c/2)$, $(-a/2, 0, c/2)$.

Using the Holstein Primakoff operators defined by (6.33) and (6.34) we find the corresponding Hamiltonian terms

$$H_{yz} = J_{yz}\sum_i \mathbf{S}_i\cdot\mathbf{S}_j = J_{yz}S\sum_{\mathbf{q}}\Big[4(a^+_{\mathbf{q}}a_{\mathbf{q}}+b^+_{\mathbf{q}}b_{\mathbf{q}})+2(\cos(\mathbf{q}\cdot\mathbf{r}_1)+\cos(\mathbf{q}\cdot\mathbf{r}_2))(a_{\mathbf{q}}b_{-\mathbf{q}}+a^+_{\mathbf{q}}b^+_{-\mathbf{q}})\Big],$$

$$H_{xy} = J_{xy}\sum_i \mathbf{S}_i\cdot\mathbf{S}_j = J_{xy}S\sum_{\mathbf{q}}\Big[4(a^+_{\mathbf{q}}a_{\mathbf{q}}+b^+_{\mathbf{q}}b_{\mathbf{q}})+2(\cos(\mathbf{q}\cdot\mathbf{r}_3)+\cos(\mathbf{q}\cdot\mathbf{r}_4))(a_{\mathbf{q}}b_{-\mathbf{q}}+a^+_{\mathbf{q}}b^+_{-\mathbf{q}})\Big],$$

$$H_y = J_y\frac{1}{2}(\sum_i \mathbf{S}_i\cdot\mathbf{S}_{i'}+\sum_j \mathbf{S}_j\cdot\mathbf{S}_{j'}) = -2J_yS\sum_{\mathbf{q}}(1-\cos(\mathbf{q}\cdot\mathbf{r}_5))(a^+_{\mathbf{q}}a_{\mathbf{q}}+b^+_{\mathbf{q}}b_{\mathbf{q}}), \tag{6.84}$$

$$H_z = J_z\frac{1}{2}(\sum_i \mathbf{S}_i\cdot\mathbf{S}_{i'}+\sum_j \mathbf{S}_j\cdot\mathbf{S}_{j'}) = -2J_zS\sum_{\mathbf{q}}(1-\cos(\mathbf{q}\cdot\mathbf{r}_6))(a^+_{\mathbf{q}}a_{\mathbf{q}}+b^+_{\mathbf{q}}b_{\mathbf{q}}),$$

$$H_{xz} = J_{xz}\frac{1}{2}(\sum_i \mathbf{S}_i\cdot\mathbf{S}_{i'}+\sum_j \mathbf{S}_j\cdot\mathbf{S}_{j'}) = -2J_{xz}S\sum_{\mathbf{q}}(2-\cos(\mathbf{q}\cdot\mathbf{r}_7)-\cos(\mathbf{q}\cdot\mathbf{r}_8))(a^+_{\mathbf{q}}a_{\mathbf{q}}+b^+_{\mathbf{q}}b_{\mathbf{q}}),$$

where

$$\begin{aligned}&\mathbf{r}_1=(0,b/2,c/2),\ \mathbf{r}_2=(0,b/2,-c/2),\ \mathbf{r}_3=(a/2,b/2,0),\ \mathbf{r}_4=(a/2,-b/2,0),\\ &\mathbf{r}_5=(0,b,0),\ \mathbf{r}_6=(0,0,c),\ \mathbf{r}_7=(a/2,0,c/2),\ \mathbf{r}_8=(a/2,0,-c/2).\end{aligned} \tag{6.85}$$

The factor of $1/2$ appearing in H_y, H_z and H_{xz} corrects for double counting.

Single ion anisotropy

In the total spin Hamiltonian we include the three anisotropy terms

$$A_x = D_x(\sum_i (S^x_i)^2+\sum_j (S^x_j)^2) = D_xS\sum_{\mathbf{q}}(a^+_{\mathbf{q}}a_{\mathbf{q}}+b^+_{\mathbf{q}}b_{\mathbf{q}})+\frac{D_xS}{2}\sum_{\mathbf{q}}(a^+_{\mathbf{q}}a^+_{-\mathbf{q}}+a_{\mathbf{q}}a_{-\mathbf{q}}+b^+_{\mathbf{q}}b^+_{-\mathbf{q}}+b_{\mathbf{q}}b_{-\mathbf{q}}),$$

$$A_y = D_y(\sum_i (S^y_i)^2+\sum_j (S^y_j)^2) = D_yS\sum_{\mathbf{q}}(a^+_{\mathbf{q}}a_{\mathbf{q}}+b^+_{\mathbf{q}}b_{\mathbf{q}})-\frac{D_yS}{2}\sum_{\mathbf{q}}(a^+_{\mathbf{q}}a^+_{-\mathbf{q}}+a_{\mathbf{q}}a_{-\mathbf{q}}+b^+_{\mathbf{q}}b^+_{-\mathbf{q}}+b_{\mathbf{q}}b_{-\mathbf{q}}),$$

$$A_z = D_z(\sum_i (S^z_i)^2+\sum_j (S^z_j)^2) = 0, \quad \text{setting } D_z=0 \text{ per definition.}$$

(6.86)

Negligible Dzyaloshinsky-Moriya terms

We have not included DM terms in the spin wave Hamiltonian. This has two reasons. First and foremost, the modelling is extremely successful without including DM terms. It would seem like an unnecessary complication to consider small additional terms that may not even exist. Secondly, even if we did include DM terms into the present model, they would not be reflected in the calculations. From section 5.5, we know that the only allowed DM terms in $LiNiPO_4$ have a DM vector pointing in the b-direction, and are of the form

$$S^x_nS^z_{n'}. \tag{6.87}$$

Such terms do not influence the spin wave spectrum in the model we have set up. This is shown by writing

$$S^x_iS^z_{i'} = \sqrt{\frac{S}{2}}(a_i+a^+_i)(S-a^+_{i'}a_{i'}), \tag{6.88}$$

and similar for entries that also include b operators. We see that these DM terms consist of single operators, a and b, and products of three operators, a^+aa, ect.

The effect of single operators is to shift the overall direction of the spins slightly, but they do not influence the oscillation frequency. This is equivalent to the case of a harmonic oscillator in a constant force field. Formally this can be verified by, after Fourier transforming, applying the following transformation [48, 49, 50] (known as a Cullen transformation)

$$\begin{aligned} a_{\mathbf{q}} &\to a_{\mathbf{q}} + c_{\mathbf{q}}\delta_{\mathbf{q},\mathbf{0}}, \quad a^+_{\mathbf{q}} \to a^+_{\mathbf{q}} + c^+_{\mathbf{q}}\delta_{\mathbf{q},\mathbf{0}}, \\ b_{\mathbf{q}} &\to b_{\mathbf{q}} + d_{\mathbf{q}}\delta_{\mathbf{q},\mathbf{0}}, \quad b^+_{\mathbf{q}} \to b^+_{\mathbf{q}} + d^+_{\mathbf{q}}\delta_{\mathbf{q},\mathbf{0}}, \end{aligned} \tag{6.89}$$

to the Hamiltonian. It is possible to choose c_0 and d_0 so the linear terms introduced by (6.88) disappear. The remaining terms will be exactly those appearing in the Hamilton matrix without including linear terms. Furthermore, in the linear approximation, we generally throw terms with more than two operators away, so the products of three operators are not included in the calculations. Therefore, the considered DM terms are not probed by the spin wave model. Other DM interactions, of the form S^xS^y, may influence the spin wave spectrum, but since they are not allowed in LiNiPO$_4$ we need not consider them.

It has been suggested that taking the canting of the spins into consideration is a way to introduce the effect of DM interactions into the spin wave model. This may be true, but I believe the effect will be very small, since the canting is small and the DM interaction, if at all present, is weak compared to the other considered interactions. In any case, in the approach we take here, the DM interactions do not play a role.

The Hamilton matrix of LiNiPO$_4$

Collecting all the terms, and rearranging, one can write the full spin Hamiltonian in the form (6.3). Here

$$= H_{yz} + H_y + H_z + H_{xz} + H_{xy} + A_x + A_y + A_z = \frac{1}{2}\sum_{\mathbf{q}} \mathbf{a}^+\mathbf{H}\mathbf{a}, \tag{6.90}$$

with

$$\mathbf{H} = \begin{bmatrix} A & B & 0 & D \\ B & A & D & 0 \\ 0 & D & A & B \\ D & 0 & B & A \end{bmatrix}, \tag{6.91}$$

where

$$\begin{aligned} A &= 4S(J_{yz} + J_{xy}) - 2S\Big[J_y(1 - \cos(\mathbf{q}\cdot\mathbf{r}_5)) + J_z(1 - \cos(\mathbf{q}\cdot\mathbf{r}_6)) + J_{xz}(2 - \cos(\mathbf{q}\cdot\mathbf{r}_7) - \cos(\mathbf{q}\cdot\mathbf{r}_8))\Big] + D_xS + D_yS, \\ B &= 2\left(\frac{D_xS}{2} - \frac{D_yS}{2}\right), \\ D &= 2J_{yz}S(\cos(\mathbf{q}\cdot\mathbf{r}_1) + \cos(\mathbf{q}\cdot\mathbf{r}_2)) + 2J_{xy}S(\cos(\mathbf{q}\cdot\mathbf{r}_3) + \cos(\mathbf{q}\cdot\mathbf{r}_4)). \end{aligned} \tag{6.92}$$

6.5.1 Eigenenergies for LiNiPO$_4$.

From section 6.2.1 we see that the spinwave eigenenergies for LiNiPO$_4$ are eigenvalues to the following 4×4 matrix

$$\begin{bmatrix} A & B & 0 & D \\ -B & -A & -D & 0 \\ 0 & D & A & B \\ -D & 0 & -B & -A \end{bmatrix}, \tag{6.93}$$

where A, B and D are given by (6.92). There are two positive and two negative eigenvalues to (6.93), namely

$$\lambda = \pm\sqrt{A^2 - (B \pm D)^2} \ .$$

The two positive values correspond to the two eigenvalues depicted as the blue (full) and red (dashed) curves in figure 7.7 (although in my MATLAB program the eigenenergies are found numerically).

6.6 Overview of Matlab programs used in simulation

I have included 5 Matlab files in appendix C. They are

- **BoguliobovExtended.m**. Calls `tau_LiNiPO4.m` and uses one of the equivalent pairs ($\mathbf{q}$,$\boldsymbol{\tau}$) to calculate the dispersions and the transformation matrix $\mathbf{T}$. Uses $\mathbf{T}$ for calling `intensityBE_alpha.m` and `intensityBE_beta.m`.
- **tau_LiNiPO4.m**. Finds the two reciprocal vectors that connect $\mathbf{Q}$ to the UFBZ and have non-zero structure factors.
- **intensityBE_alpha.m**. Calculates the cross-section for creating an α magnon. Calls `formfactorNi.m`.
- **intensityBE_beta.m**. Calculates the cross-section for creating a β magnon. Calls `formfactorNi.m`.
- **formfactorNi.m**. Calculates the magnetic formfactor for Ni^{2+} ions as tabulated in *International tables for crystallography, Vol. C.*

To run the simulation just run the m-file `BoguliobovExtended.m` with the appropriate interaction parameters.

The calculation only uses one of the equivalent pairs ($\mathbf{q}$,$\boldsymbol{\tau}$) even though in principle one should add the intensities. This is justified by checking that both pairs gives identical results. The equivalence between the pairs are checked by first running the simulation with `tau=tau1` (line 20 of `BoguliobovExtended.m`) and then with `tau=tau2` (line 21).

Chapter 7

Spin wave measurements

7.1 Introduction

In this chapter we present and analyze inelastic neutron experiments on $LiNiPO_4$ performed at RITA-II, PSI and IN8, ILL. Additional data, from the thermal triple axis spectrometer HB1A at Oak Ridge National Laboratory, was kindly provided by David Vaknin from Ames Laboratory. Dispersions along the two main directions, $(0, K, 0)$ and $(0, 1, L)$, were extracted at low temperatures and in zero field on RITA. Including inelastic data along $(H, 1, 0)$, measured by David Vaknin and his group, this information was used to set up a spin Hamiltonian and evaluating the interaction parameters. The model Hamiltonian is described in section 6.5 and in 7.2.2. For many systems it would have been sufficient to analyze only the spin wave dispersions[1], but for $LiNiPO_4$ it is necessary also to analyze the intensities. We do this by the linear spin wave theory described in chapter 6. The MATLAB scripts calculating the dispersions and intensities are given in appendix C.

Using the powerful thermal triple axis spectrometer, IN8 at ILL, an inelastic map covering more than an entire Brillouin zone of the *bc* plane was measured in an impressive only 8 hours or so. Here, two non-degenerate inelastic dispersions were observed, providing further confirmation[2] of the model. We shall discuss the IN8 data in section 7.3.

7.2 The RITA experiments

We have performed several inelastic experiments on RITA, always with the instrument in the 7 blade imaging mode. During a measurement we would keep the energy of the scattered neutrons fixed at 5 meV while scanning the energy of the incoming neutrons at a given $\mathbf{Q}$ (this is called a constant $\mathbf{Q}$ monochromator scan). Fitting the observed peaks to Gaussians provide the spin wave dispersions as peak centers, and the spin wave intensities as integrated peak intensities, for the selected $\mathbf{Q}$. Depending on the direction of the desired dispersion we have used the imaging mode on RITA differently. When the direction of the dispersion was almost parallel to a line connecting the blade positions in reciprocal space (see figure 7.3) we would use the 7 blades as seven individual measurements. On the other hand, when the direction of the dispersion was mostly perpendicular to the line connecting the seven blades we chose to consider the collected intensity of the 3 center blades as a single data point, disregarding intensities from the outer blades.

[1] The spin wave dispersions for $LiNiPO_4$ are relatively easily calculated, for instance by a straightforward expansion of the Heisenberg equation of motion technique given in [8]. The intensity calculation is a different story, and here the full treatment of chapter 6 is needed.

[2] Strictly speaking, a simple symmetry argument show that at least two dispersion must be present in $LiNiPO_4$ regardless the model (section 6.4). However, not everyone was convinced until we found the experimental proof at IN8.

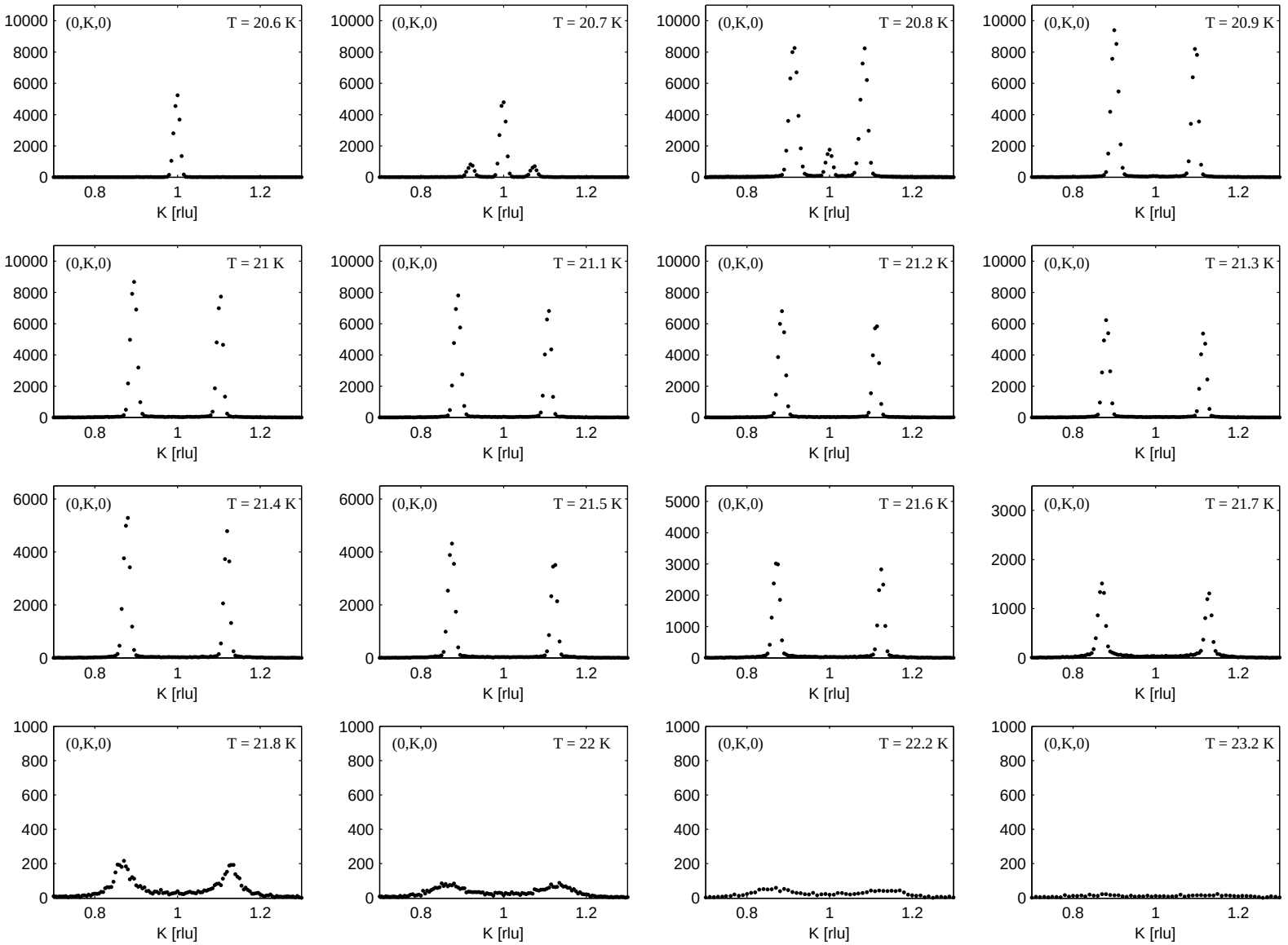

Figure 7.1: Examples of elastic (0,K,0) scans, measured at RITA, showing the C-IC phase transition around 20.7 K. We see that for temperatures above approximately 21.7 K there is no long range magnetic order, since here the reminiscent peaks are significantly broadened.

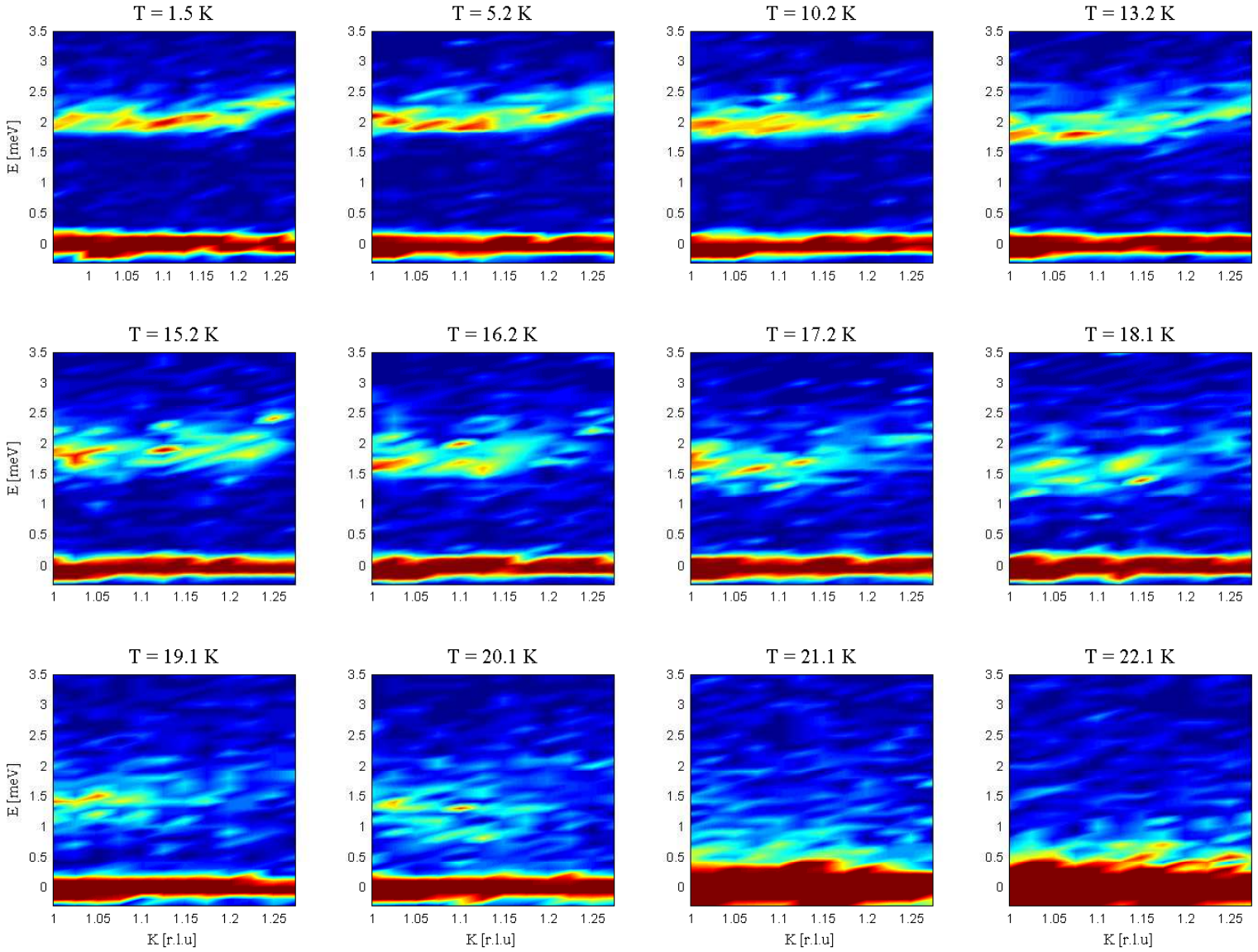

Figure 7.2: Inelastic colormaps of the (0,K,0) dispersion at various temperatures (`data-series 1`). The color scale is the same for all maps and depict the measured number of counts (interpolated for visual purposes) in arbitrary units (red for high counts, blue for low). Each of the maps consist of 2 scans, totalling 14 different K values at energies from -0.3 to 3.5 meV, and measuring one minute per point. The dispersion is visible and gapped in the commensurate phase, but above the C-IC transition temperature there is no visible dispersion. This is confirmed by more thorough measurements, shown in figure 7.6(c) and (d). The energy gap as function of temperature has been extracted from the data depicted here (the gap above $T_c = 20.8$ K being set to zero) and is shown in figure 7.4.

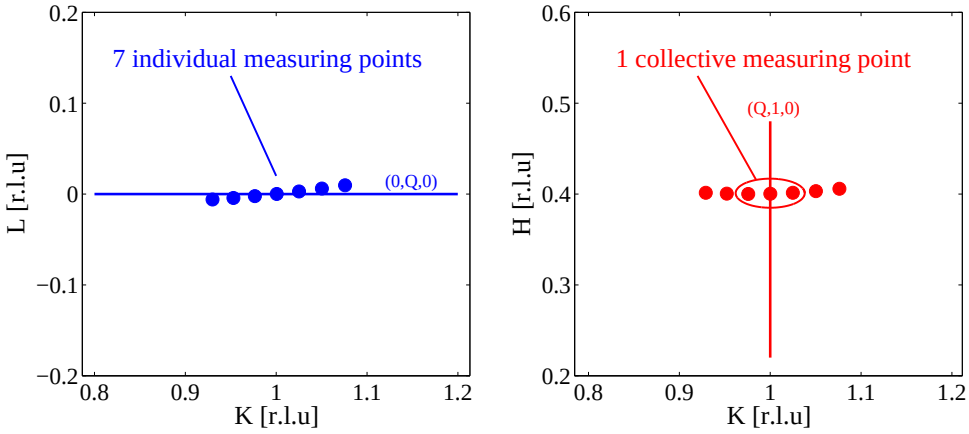

Figure 7.3: Example of the position of the 7 analyzer blades (filled dots) at RITA, during experiments measuring the dispersion along (0,Q,0) (blue line) and (Q,1,0) (red line). In general the blade positions are functions of **Q** and the energy [31], where **Q** is the scattering vector of the center blade. Therefore, in the imaging mode, only the position of the center blade is fully controlled by the user. Probing the (0,Q,0) spin waves all seven blades are essentially along the desired direction and can be used individually. Along (Q,1,0) the line connecting the blades is almost perpendicular to the desired direction. Here, collecting the total intensity of the 3 middle blades was chosen as the best compromise between having sufficient statistics and retaining a reasonable **Q** resolution.

7.2.1 (0,Q,0) measurements in zero field

A $5\times5\times9$ mm^3 irregular shaped $LiNiPO_4$ single crystal was glued to an aluminium holder and mounted in a standard Orange cryostat with the crystallographic *bc* plane as scattering plane (i.e. the *a*-axis in the vertical direction). Before beginning the inelastic measurements we performed elastic K and L scans around (0,1,0) as function of temperature in order to pinpoint the C-IC phase transition. The transition temperature, T_c, was found to be 20.7 K (within a margin of 0.1 K), and the long range ordered IC phase, beginning at T_c, continued to approximately 21.7 K (see figure 7.1).

Short scans: Temperature dependence of the energy gap

A series of relatively quick inelastic scans (`data-series 1`), measured at various temperatures from 1.5 to 23.1 K, is shown in figure 7.2. The depicted energy, E (in some later figures $\hbar\omega$), is the energy absorbed by the crystal, i.e. the difference between the energy of the detected neutrons and the incoming neutrons. The colormaps reveal a gapped dispersion in the commensurate phase, but show no clear dispersion at temperatures above $T_c = 20.8$ K. The counting time in `data-series 1` was approximately one minute per gridpoint.

In figure 7.4(a), we show some cuts from the data of figure 7.2. The depicted cuts correspond to constant **Q** scans at a scattering vector (0,1.02,0), and for T = 5.2, 13.2 and 17.2 K. Fitting the observed peaks to Gaussian functions, we have determined the energy gap of the spin waves. The energy gap as function of temperature is shown in figure 7.4(b). At base temperature the energy gap is $\sim$ 2.1 meV, and decrease approximately as $(1-T/T_c)^{0.13}$ for increasing temperatures. It must be emphasized that we are not discussing whether the fit to a power function has any physical merit; it is merely meant as a guide to the eye.

Long scans: The detailed dispersion at different temperatures

Next we performed extended measurements (`data-series 2`) at T = 1.5, 18.2, 19.2, 20.2 K in the commensurate phase, and T = 20.9 and 21.2 K in the incommensurate phase. The counting time in `data-series 2` was approximately seven minutes per grid-point (and even 14 minutes per gridpoint for the measurements at 20.9 K), and the dispersions were tracked further in K and E than for `data-series 1`.

Figure 7.5 compare constant **Q** cuts for T = 1.5, 18.2, 19.2 and 20.2 K at two different scattering vectors. Here the inelastic peaks, shown in the insets, are clearly broadened when the temperature is increased. The elastic peak at $(0, 1.005, 0)$ is more intense at 18.2 K than at 19.2 and 20.2 K, while it is the other way around for $\mathbf{Q} = (0, 1.055, 0)$. This indicates that the (0,1,0) Bragg peak is also broadened when the temperature is approaching T_c. The broadening is rather small and is hard to observe in the purely elastic measurements performed at the beginning of the experiment.

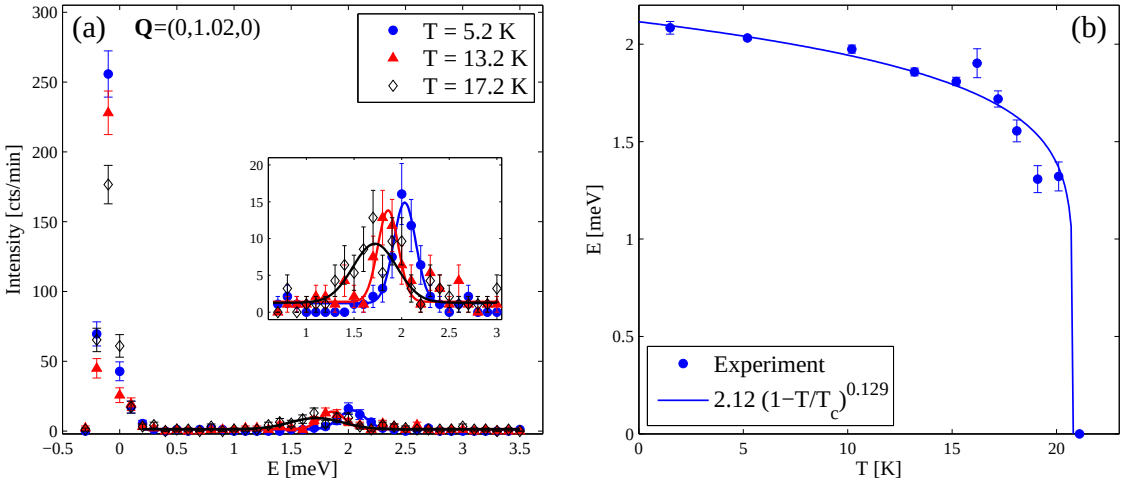

Figure 7.4: (a) Cuts from `data-series 1` corresponding to constant **Q** scans. The inset is a zoom in on the inelastic peaks. (b) The energy gap as function of temperature. The full line gives the best fit between the experimentally determined values and a power function $\propto (1 - T/T_c)^{\alpha}$ and can be used as a guide to the eye.

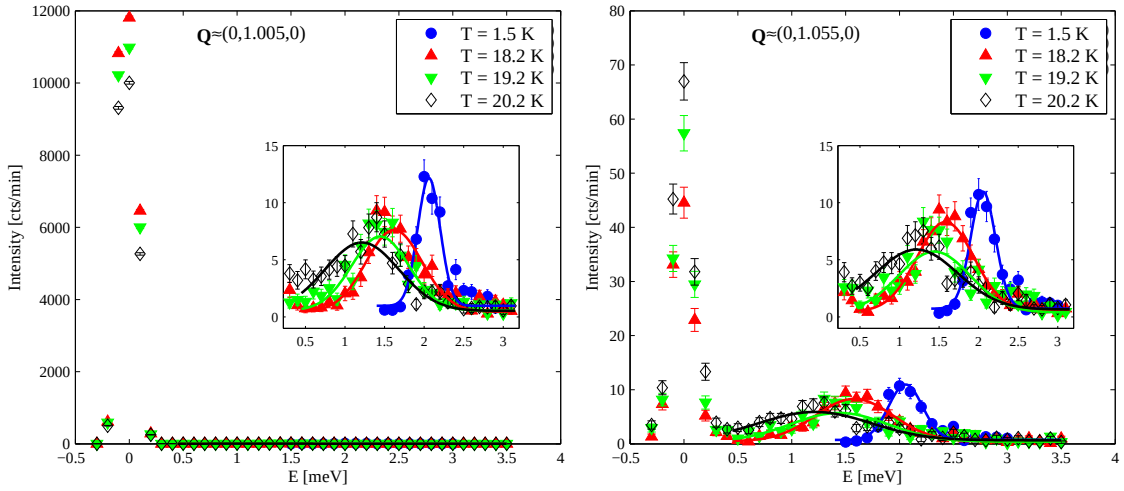

Figure 7.5: Constant **Q** cuts (`data-series 2`) at T = 1.5, 18.2, 19.2 and 20.2 K for (0,1.005,0) and (0,1.055,0). The insets zoom in on the inelastic peaks at the respective **Q**.

A series of (K, E) color-maps, measured along the $(0, K, 0)$ direction at temperatures 1.5, 20.9 and 21.2 K, are shown in figure 7.6. By manipulating the colors in (b) we are ably to track the 1.5 T dispersion longer by eye than in (a). We analyze the dispersion in the next section. Once entering the incommensurate phase, (c) and (d), we could not observe any inelastic peaks, not even with increased counting time. This is a contrast to the elastic measurements, where the elastic $(0, 1 \pm q, 0)$ peaks were intense and sharp in the incommensurate phase. In this thesis we will not try to explain the absence of detectable spin waves above 20.8 K.

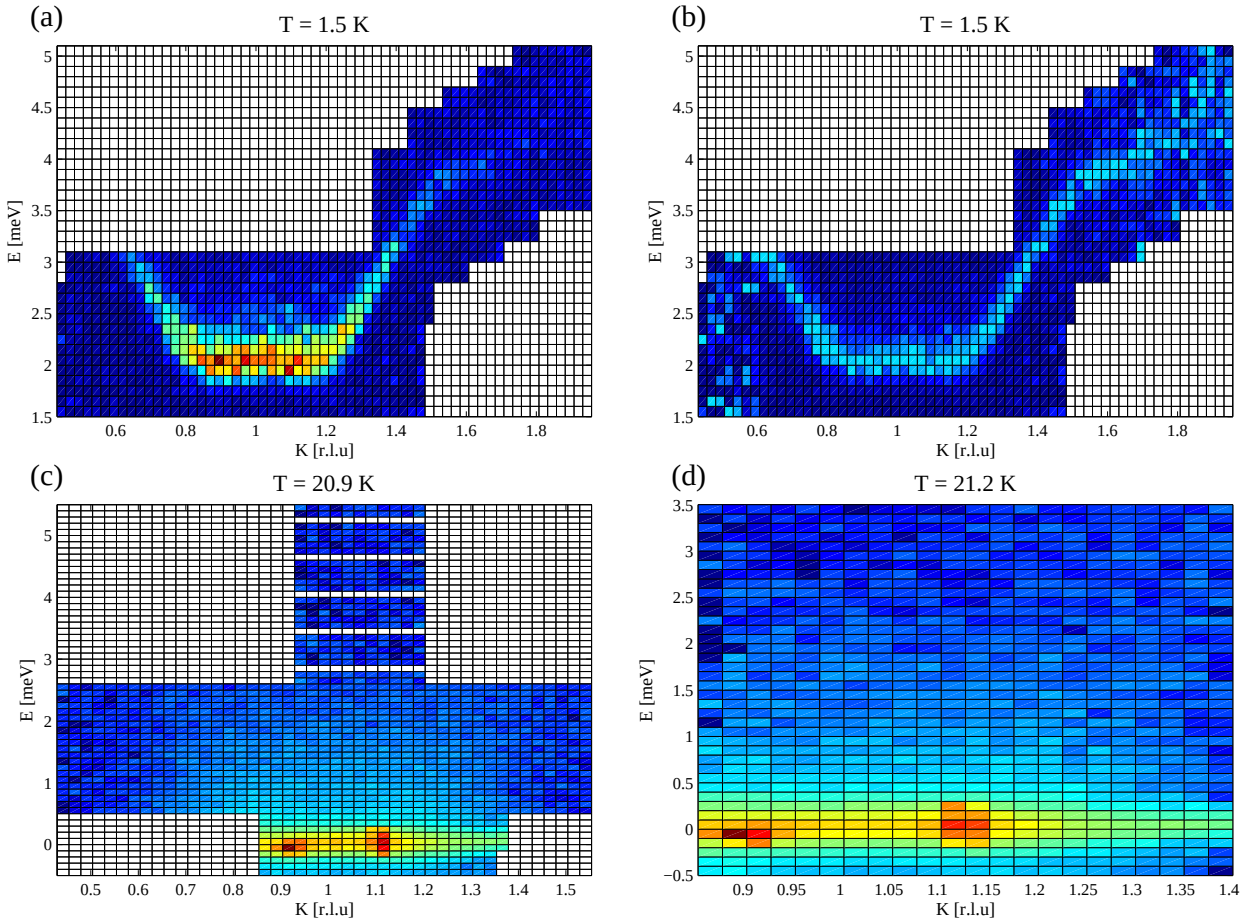

Figure 7.6: Inelastic color-maps of (K, E) grid scans (`data-series 2`), measured for $\mathbf{Q} = (0, K, 0)$ at RITA. (a) Base temperature with non-logarithmic color scale reflecting the measured intensity in arbitrary units. The measuring time for these scans were around 7 minutes per grid point. (b) Same as (a), but with manipulated colors allowing the eye to track the dispersion across the zone boundary at $K = 1.5$ r.l.u. It is noticeable that the dispersion is not symmetric around the zone boundary at K = 1.5 rlu. This is possible only if there are at least two non-degenerate branches in the dispersion, as discussed in section 6.4. (c) Measurements at 20.9 K. There is no sign of a dispersion for energies below 5.5 meV. Here the measuring time was 14 minutes per grid point. (d) The grid scans at 21.2 K also show no sign of a dispersion (7 minutes per grid point).

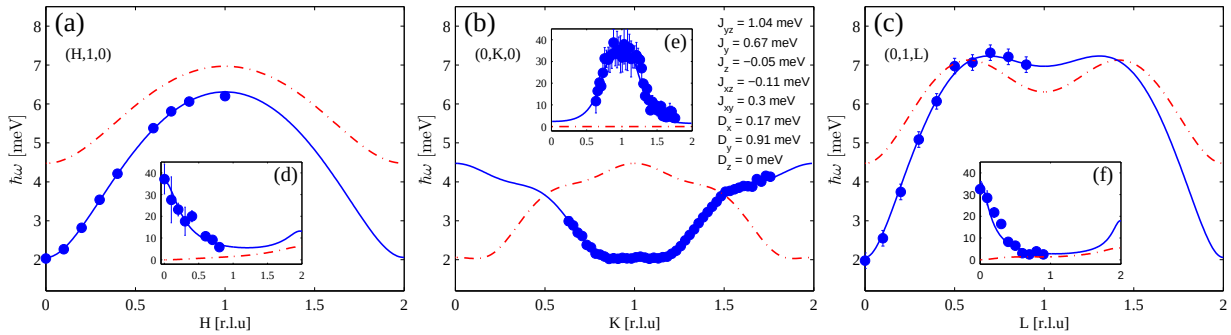

Figure 7.7: Measured (filled circles) spin wave dispersion along three reciprocal directions, compared with a Holstein-Primakoff spin-wave calculation (full and dashed lines) explained in the text. The insets show the measured and calculated intensities. The dispersions along (H,1,0) and (0,K,0) were measured at T = 2 K on RITA, while the dispersion along (0,1,L) was measured at T = 10 K on HB1A by the Ames group.

7.2.2 Analyzing low temperature dispersions along $(H,1,0)$, $(0,K,0)$ and $(0,1,L)$

The spin wave dispersions and integrated intensities measured along the a, b and c directions at zero field and low temperatures are shown in figure 7.7. The data were analyzed using linear spin wave theory, as described in chapter 6, with a spin Hamiltonian

$$H = H_{yz} + H_y + H_z + H_{xz} + H_{xy} + A_x + A_y + A_z. \tag{7.1}$$

Here $H_\alpha = J_\alpha \sum \mathbf{S}_i \cdot \mathbf{S}_j$ and $H_{\alpha\beta} = J_{\alpha\beta} \sum \mathbf{S}_i \cdot \mathbf{S}_j$ are Heisenberg type interactions between pairs of Ni-ions, as shown in figure 7.8, and $A_\alpha = D_\alpha \sum_i (S_i^\alpha)^2$ are single ion anisotropies. The subscripts, α and β, indicate the direction of the interactions, with x, y and z defined along a, b and c. In the calculations we have assumed an antiferromagnetic ground state with the spins pointing strictly along the c axis, as depicted in figure 7.8, and for computational convenience we have defined[3] $D_z = 0$.

All three dispersions of figure 7.7 were fitted simultaneously, using a fitting routine from the MATLAB package MFIT. The interaction parameters providing the best fit are given in table 7.1, and show strong nearest neighbor (J_{yz}) and next-nearest neighbor (J_y) Heisenberg interactions within the bc-planes, while the interactions between the planes (J_{xy} and J_{xz}) are somewhat smaller. The single ion anisotropy in the

[3]This amounts to redefining the zero point for the energy. Naturally this does not influence the spin wave spectrum.

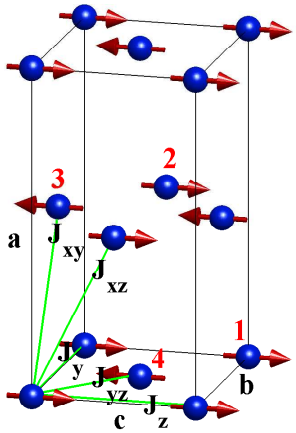

Figure 7.8: The spin structure and Heisenberg interactions used in the spin wave modelling (same as figure 6.4).

J_{yz}	J_y	J_z	J_{xz}	J_{xy}	D_x	D_y	D_z
1.036	0.6701	−0.0469	−0.1121	0.2977	0.1696	0.9097	0

Table 7.1: Interaction parameters used for the best model fit to the data in figure 7.7 as described in the text. All the parameters are given in units of meV.

b-direction is much larger than the anisotropies along a and c. As a result of the non-identical anisotropies along a and b, the calculated dispersions have two non-degenerate branches. At the RITA experiments we detected only one of the branches, but this is easily explained by comparing to the calculated spin wave intensities in the regions of Q-space we investigated. In the IN8 experiment (section 7.3) we have probed several other scattering vectors and observed both branches in good agreement with the model (7.1).

Simple considerations [51] on layered crystals with competing interactions show that incommensurate order is favorable if the exchange interactions, J_1 and $J_2 > 0$, between nearest and next-nearest neighboring layers fulfil that $|J_1| < 4J_2$. If this condition applies, the magnetic ordering vector Q is found from $\cos(Qd) = -J_1/4J_2$, where d is the distance between adjacent layers. Considering $LiNiPO_4$ as a layered crystal, where the layers are perpendicular to the b-direction, we can easily put the condition to the test. Using the exchange parameters found from table 7.1, we have that $J_1 = 2J_{yz} + 2J_{xy}$ and $J_2 = J_y$, while $d = b/2$. Therefore $J_1 = 2.67$ meV and $4J_2 = 2.68$ meV, showing that $LiNiPO_4$ is expected to have incommensurate order at 2 K with an ordering vector $Q = 0.97$ rlu. Since the two values, J_1 and $4J_2$, are almost identical, it is not surprising that the system is actually commensurate at low temperatures. However, the calculation does show that $LiNiPO_4$ in zero field is always on the verge to incommensurate order at low temperatures, and even small changes in the interactions may decide whether the system is commensurate or incommensurate.

The intensity calculation is important for determining the single ion anisotropies without ambiguity. We illustrate this by figure 7.9. Here the spin wave dispersions and intensities are calculated for a model using the parameters from table 7.1, except that D_x and D_y have been interchanged. Comparing to figure 7.7, we see that the dispersions, on their own, cannot determine whether D_x or D_y is the largest. Considering the calculated intensities, however, there is no doubt that $D_x = 0.17$ meV and $D_y = 0.91$ meV, and not the other way around.

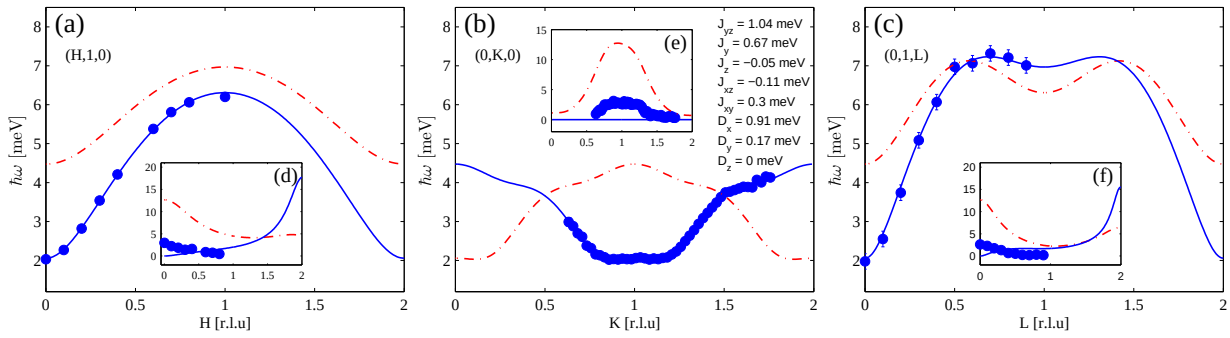

Figure 7.9: Measured (filled circles) spin wave dispersion along three reciprocal directions, compared with a Holstein-Primakoff spin-wave calculation (full and dashed lines) with interchanged D_x and D_y, as explained in the text. The insets show the measured and calculated intensities. We have scaled the measured intensities so best to track the corresponding calculated intensities (blue full line). The dispersions are not sensitive to interchanging D_x and D_y, but the intensities are. Here, for $D_x > D_y$, the measured and calculated intensities clearly do not match.

7.2.3 Temperature dependence of the $(0, K, 0)$ dispersion

In figure 7.10, the $(0, K, 0)$ spin wave dispersions and intensities at T = 1.5, 18.2, 19.2 and 20.2 K, extracted from `data-series 2`, are shown. Due to thermal broadening, the dispersions at 18.2, 19.2 and 20.2 K

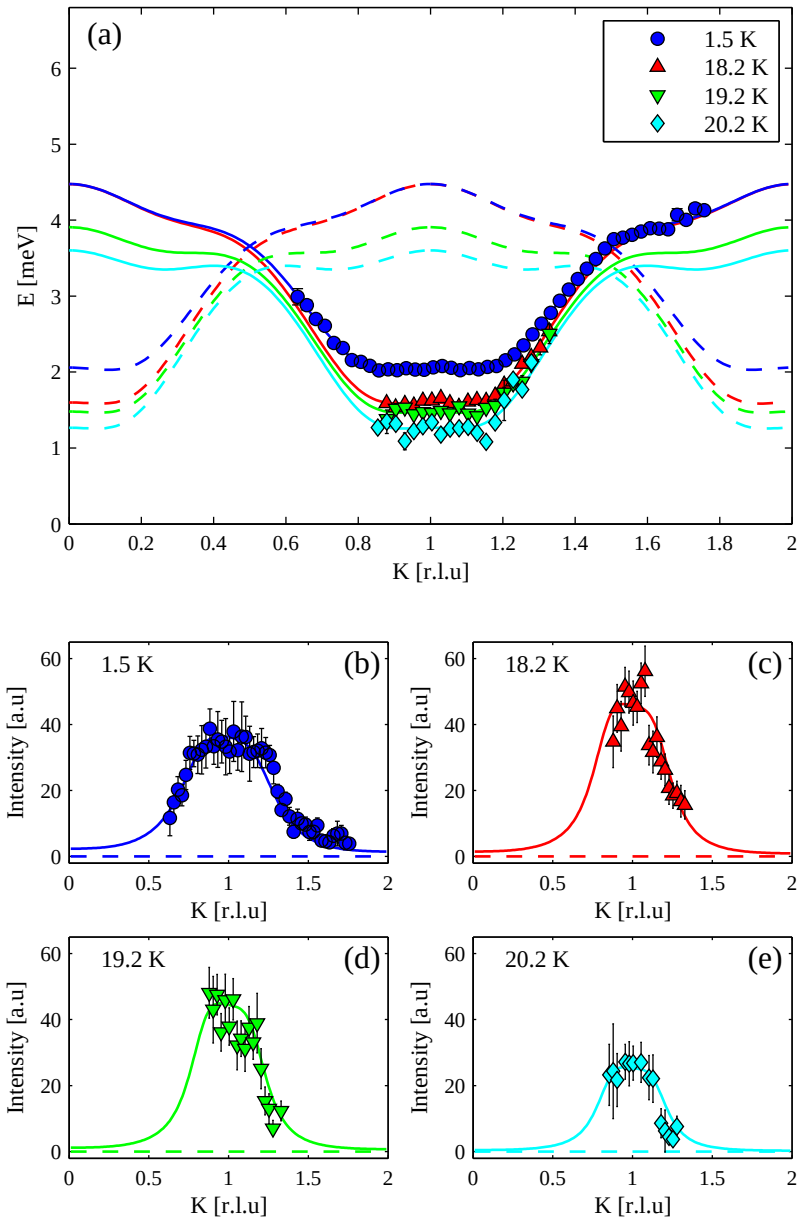

Figure 7.10: (a) The extracted dispersions as function of temperature. The markers are measured data, while the full and dashed lines are the calculated branches (see the text for details). The data at 1.5 K suffice to determine all the interaction parameters. At 18.2, 19.2 and 20.2 K this is not the case, since the measured K range does not include the region around the zone boundary. To determine the depicted curves we have assumed that the Heisenberg interactions found at 1.5 K do not change significantly when approaching T_c. The calculated curves at 18.2, 19.2 and 20.2 K are best model fits to the data while fixing the Heisenberg interactions and setting the anisotropy parameters free (at 20.2 K only one anisotropy parameter was set free). (b)-(e) The measured (markers) and calculated (full and dashed lines) spin wave intensities at the various temperatures.

T	J_{yz}	J_y	J_z	J_{xz}	J_{xy}	D_x	D_y	D_z
1.5 K	1.036	0.6701	−0.0469	−0.1121	0.2977	0.1696	0.9097	0
18.2 K	1.036	0.6701	−0.0469	−0.1121	0.2977	0.1023	0.9204	0
19.2 K	1.036	0.6701	−0.0469	−0.1121	0.2977	0.0906	0.7034	0
20.2 K	1.036	0.6701	−0.0469	−0.1121	0.2977	0.0675	0.6	0

Table 7.2: Interaction parameters used for the best model fit to the data in figure 7.10 as described in the text. All the interaction parameters are given in units of meV.

could not be tracked as far in reciprocal space as the 1.5 K dispersion. This presents a problem for the modelling, because the spin wave behavior around and above the zone boundary, at $K = 1.5$ r.l.u., is vital for determining reliable interaction parameters. Since this information is not available for the 18.2, 19.2 and 20.2 K data, we need to employ some additional assumptions concerning the fitting parameters.

We have previously seen (chapter 2), that single ion anisotropies are caused by the spin-orbit interaction mixing quantum states belonging to different energy levels. The energy levels considered here are the lowest lying levels of the Ni^{2+} ions, which are split by the crystal field. More specifically, for a nickel ion in the ground state, $|0\rangle$, the single ion anisotropy terms can be written as

$$A_{\mu\nu} = -\lambda^2 S_\mu \Lambda_{\mu\nu} S_\nu, \tag{7.2}$$

where

$$\Lambda_{\mu\nu} = \sum_{n\neq 0} \frac{\langle 0|L_\mu|n\rangle\langle n|L_\nu|0\rangle}{E_n - E_0}, \tag{7.3}$$

and λ is the spin-orbit coupling constant. At finite temperatures, the Ni ions do not remain exclusively in their ground state, but are constantly being exited between states due to thermal fluctuations. The probability, p_n, of finding the ion in a given quantum state, $|n\rangle$, is

$$p_n = Ze^{-E_n/k_BT}, \tag{7.4}$$

where E_n is the energy of the state, $|n\rangle$, and

$$Z = \sum_m e^{-E_m/k_BT}. \tag{7.5}$$

For the anisotropy terms, we must therefore write

$$\Lambda_{\mu\nu} = \sum_m \sum_{n\neq m} p_m \frac{\langle m|L_\mu|n\rangle\langle n|L_\nu|m\rangle}{E_n - E_m}. \tag{7.6}$$

When the temperature changes, so does the population of the energy levels. In the high-temperature limit, where all levels are equally populated, the single ion anisotropies vanish. We see this by considering a two level system as example. Here

$$\Lambda_{\mu\nu} = p_0 \frac{\langle 0|L_\mu|1\rangle\langle 1|L_\nu|0\rangle}{E_1 - E_0} + p_1 \frac{\langle 1|L_\mu|0\rangle\langle 0|L_\nu|1\rangle}{E_0 - E_1} = (p_0 - p_1)\frac{\langle 0|L_\mu|1\rangle\langle 1|L_\nu|0\rangle}{E_1 - E_0}. \tag{7.7}$$

We have used that the states $|n\rangle$ are determined by the crystal field and can be written as real functions. The angular momentum operators are purely imaginary. Therefore $\langle n|L_\mu|m\rangle$ is also purely imaginary and $\langle n|L_\mu|m\rangle = \langle m|L_\mu|n\rangle^* = -\langle m|L_\mu|n\rangle$, giving that $\langle 1|L_\mu|0\rangle\langle 0|L_\nu|1\rangle = \langle 0|L_\mu|1\rangle\langle 1|L_\nu|0\rangle$. At large temperatures $p_0 \simeq p_1$, and we see that $\Lambda_{\mu\nu} \simeq 0$. Extending (7.7) to more than two levels is trivial.

The Heisenberg interactions between the spins are super-exchange interactions, and determined by overlap integrals of the electronic clouds between the Ni ions. Although the position of the ions, and the electronic clouds surrounding them, may vary slightly with increasing temperature, we clearly expect the single ion

anisotropies to change more with temperature than the super-exchange interactions. We therefore make the modelling assumption that the anisotropy constants may change for T = 1.5, 18.2, 19.2 and 20.2 K, but the Heisenberg interactions will remain constant. In figure 7.10(a), we have fitted the 18.2, 19.2 and 20.2 K dispersions to a model, where J_α and $J_{\alpha\beta}$ are fixed at the 1.5 K values from table 7.1, and the anisotropies, D_α, are free fitting parameters. The dispersion at 1.5 K is shown for comparison. For the 20.2 K fit, the best result was achieved when manually fixing D_y to 0.6 meV, while using D_x as the only free fitting parameter. The spin wave intensities are shown in figure 7.10(b)-(e), and the interaction parameters are listed in table 7.2.

To further justify (at least to some degree) our approach, we compare, in figure 7.11, the following:

1. Blue full lines, for fits with fixed $J_\alpha, J_{\alpha\beta}$, and free D_α.
2. Red dashed lines, for fits with free $J_\alpha, J_{\alpha\beta}$, and fixed D_α.

From the figure, we see that approach no. 1. can explain the data, while approach no. 2 cannot. This is a good indication that, for the considered temperatures, the anisotropy constants change more with temperature than the Heisenberg interactions.

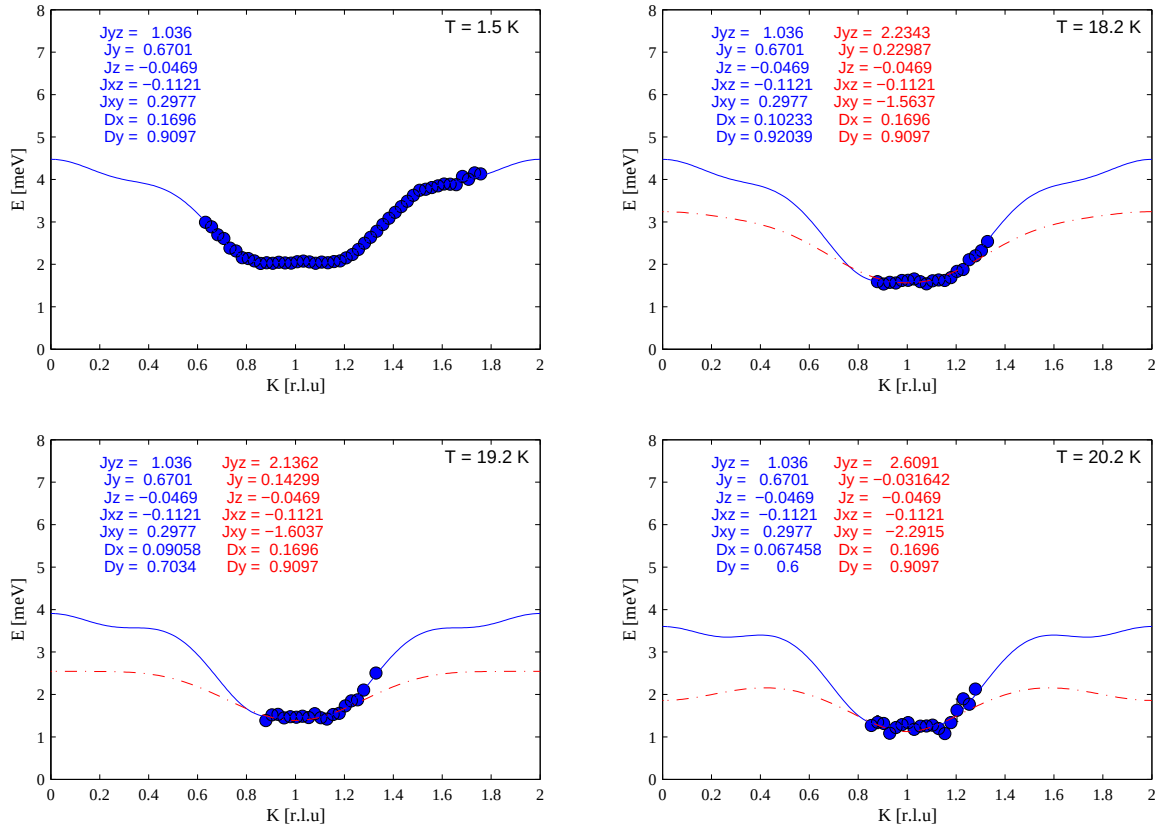

Figure 7.11: Spin wave dispersions at different temperatures comparing the best fit to the model with fixed exchange parameters (blue full lines) and fixed anisotropy parameters (red full lines), as explained in the text.

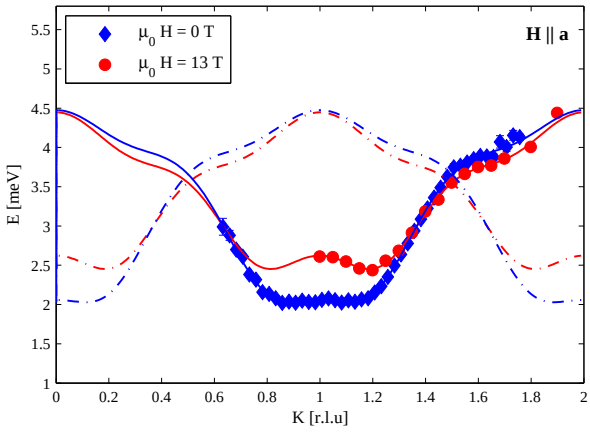

Figure 7.12: Spin wave dispersion at T = 1.5 K, μ_0H = 0 T (blue) and T = 2.3 K, μ_0H = 13 T (red), with the field parallel to the crystallographic a-axis and all fitting parameters set free (see text).

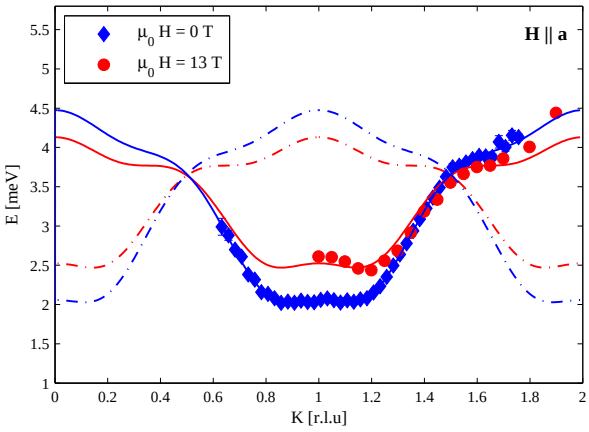

Figure 7.13: Spin wave dispersion at T = 1.5 K, μ_0H = 0 T (blue) and T = 2.3 K, μ_0H = 13 T (red), with the field parallel to the crystallographic a-axis and the exchange parameters fixed during the fit (see text).

7.2.4 Spin wave dispersion in 13 T, applied along the a-axis.

In figure 7.12 and 7.13, the $(0, K, 0)$ spin wave dispersion, measured at 2.3 K and in a magnetic field of 13 T applied along the crystallographic a-axis, is compared to the zero field dispersion. Applying a magnetic field, $\mathbf{H} = (H_x, 0, 0)$, along the a direction does not alter the entries in the Hamilton matrix (6.4) from chapter 6. This is because the Zeeman term

$$\begin{aligned} &- g\mu_B \sum_i \mathbf{H}\cdot\mathbf{S}_i - g\mu_B \sum_j \mathbf{H}\cdot\mathbf{S}_j = -g\mu_B \sum_i H_x S_i^x - g\mu_B \sum_j H_x S_j^x \\ &= -g\mu_B \sum_i H_x \sqrt{\frac{S}{2}}(a_i + a_i^+) - g\mu_B \sum_j H_x \sqrt{\frac{S}{2}}(b_j^+ + b_j), \end{aligned} \tag{7.8}$$

consist exclusively of terms linear in the Holstein-Primakoff operators. Such terms shift the overall spin direction, but does not influence the oscillation frequency, as discussed in section 6.5. We have therefore analyzed the 13 T dispersion with the same model as before. The interaction parameters for the best fit (figure 7.12) is given in the middle row (free) of table 7.3. Here both the exchange and anisotropy parameters are set free[4] in order to achieve the best possible fit. According to the discussion of section 7.2.3 we would expect the exchange parameters to stay relatively constant when applying the field. Fixing all the exchange parameters, J, to the zero field values gives the fit shown in figure 7.13. The corresponding parameters are given in the last row (fixed) of table 7.3. Clearly figure 7.12 gives a better fit than figure 7.13, but the more realistic parameters may well be given by the last row of table 7.3.

$\mu_0 H$	J_{yz}	J_y	J_z	J_{xz}	J_{xy}	D_x	D_y	D_z
0 T	1.036	0.6701	−0.0469	−0.1121	0.2977	0.1696	0.9097	0
13 T (free)	1.2365	0.7121	−0.0469	−0.1121	0.0843	0.2788	0.8891	0
13 T (fixed)	1.036	0.6701	−0.0469	−0.1121	0.2977	0.2614	0.7623	0

Table 7.3: Interaction parameters used to the best fit of the data in figure 7.12 (middle row - free) and figure 7.13 (last row - fixed), as described in the text. All the interaction parameters are given in units of meV.

[4] J_z and J_{xz} do not influence the $(0, K, 0)$ dispersion and are fixed at the zero field values.

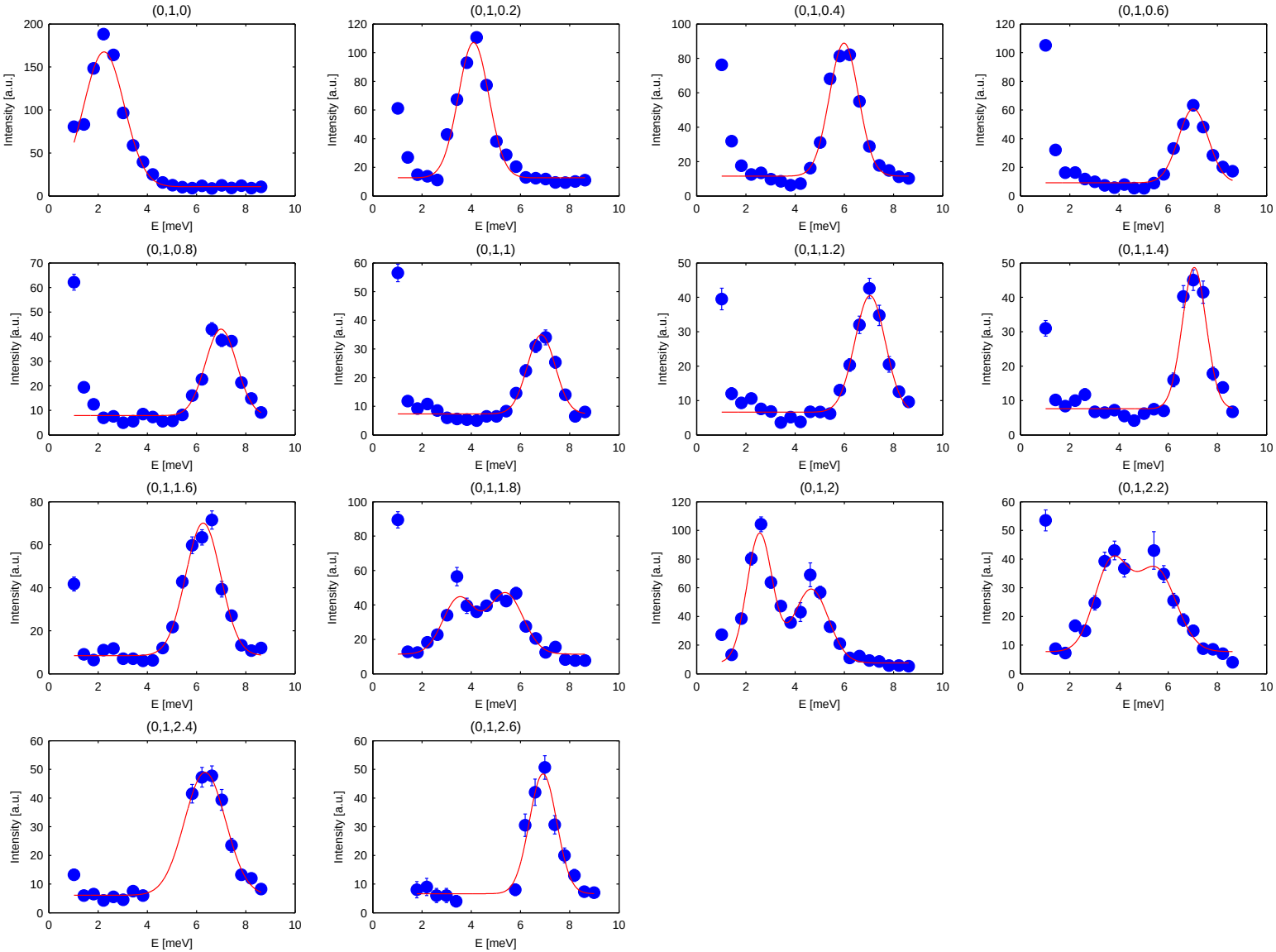

Figure 7.14: Cuts of data from IN8, corresponding to constant Q scans along $(0, 1, L)$, at $T = 2$ K, and using 30 meV neutrons. The measurements (full circles) have been fitted to one or two Gaussians functions (red lines). Clearly, both branches of the spin wave dispersion is observed at $L = 1.8, 2$ and 2.2 r.l.u.

7.3 The IN8 experiment

Besides the extensive studies at RITA, we also had an opportunity to measure spin waves at the thermal triple axis spectrometer IN8 at ILL, with the MAD detector box attached. The instrument and the detector box is briefly described in section 2.4.2. Since we only had the instrument for a short period of time, and since we used thermal neutrons with scattered energy 30 meV, the precision of the IN8 experiment could not match that of the RITA experiments. The amount of data, on the other hand, not only matched, but truly overpowered the amount of RITA data. With the large flux on IN8, and with aid from the MAD detector box, we were able to map more than an entire Brillouin zone in the $(0, K, L)$ reciprocal plane. This was very beneficiary, since we could now look for the second branch of the dispersion. At RITA we had only measured at $\mathbf{Q}$ where the intensity profile of the spin waves were such that only one branch of the dispersion could be detected.

Figure 7.14 show data corresponding to constant Q scans along the $(0, 1, L)$ direction measured on IN8. Due to the poor energy resolution, and to save time, we went in steps of $E = 0.5$ meV in these measurements. The depicted intensities are the collected number of counts in grid-points of size 1 r.l.u. $\times$ 1 r.l.u. around the given $\mathbf{Q}$ in the reciprocal $(0, K, L)$ plane, normalized to the number of measurements within the grid-point. Although the data do not have the quality of the RITA measurements, there are clearly two peaks at $\mathbf{Q} = (0, 1, 1.8), (0, 1, 2)$ and $(0, 1, 2.2)$. The spin wave dispersions have been extracted by fitting the peaks to one or two Gaussians, as illustrated by the full red lines. The measured (full circles) and calculated (full lines) $(0, 1, L)$ dispersions are shown in figure 7.15(a). Other dispersions in the (0,K,L) plane are ascertained in a similar fashion. In figure 7.15(b) and (c) we show the dispersions along $(0, K, 0)$ and $(0, K, 2)$ measured at IN8. Here, the $(0, K, 0)$ dispersion has only a single observed branch, while both branches are detected along $(0, K, 2)$. The insets in (a)-(c) show the corresponding calculated spin wave intensities. The agreement between the measured data and the spin wave model is illustrated by noting that both branches are detected experimentally, exactly when:

(1) The calculated intensity of both branches is non-negligible, and

(2) The difference in energy between the two branches is sufficiently large to be experimentally distinguishable.

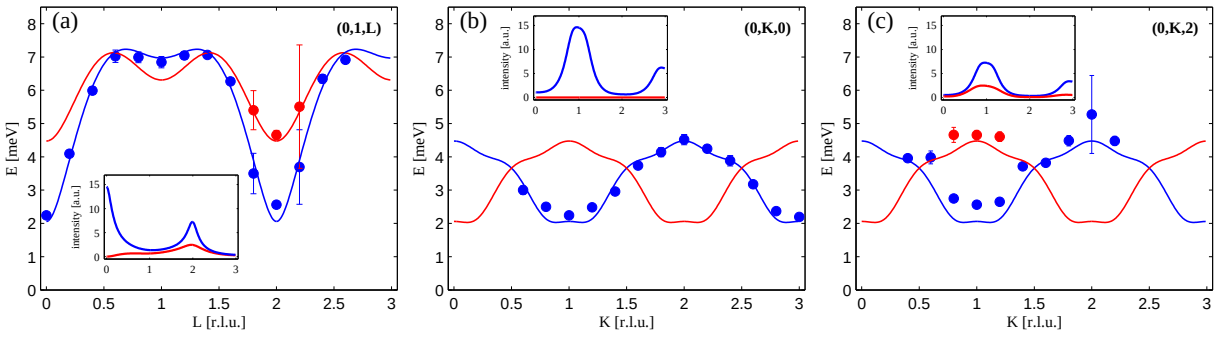

Figure 7.15: Measured (filled circles) spin wave dispersions along three directions from IN8, compared with a Holstein-Primakoff spin-wave calculation (full lines). The insets show the calculated intensities. Along both $(0, 1, L)$ and $(0, K, 2)$ both branches predicted by the model are observed. Along $(0, K, 0)$ only one branch is observed because the intensity of the other branch is zero.

We end this chapter by mapping the region of the $(0, K, L)$ plane investigated at IN8. The results of the IN8 measurements are given in figure 7.16, and can be compared to the model calculations of figure 7.17. The depicted dispersions correspond to the inelastic branch with the highest measured intensity, and we have interpolated and smoothed the data in figure 7.16 for clarity. The coloring in both figures is proportional to the measured (calculated) intensity of the depicted branch.

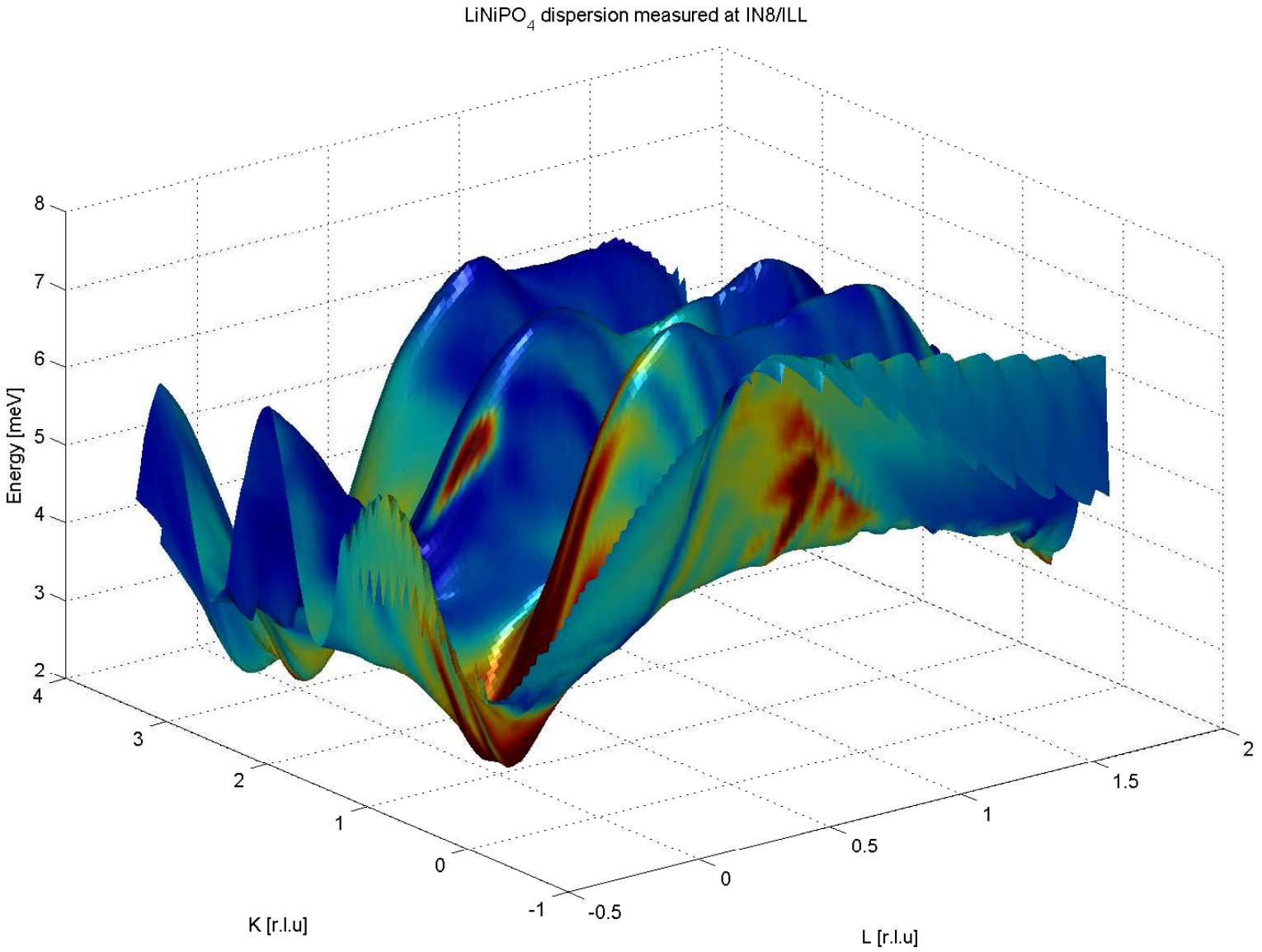

Figure 7.16: Spin wave dispersion in the $(0, K, L)$ plane, measured on IN8 at ILL. The depicted dispersion corresponds to the most intense branch, and the coloring is proportional to the observed spin wave intensity (red for high intensities, blue for low). The measurements took around 8 hours, using the MAD detector box.

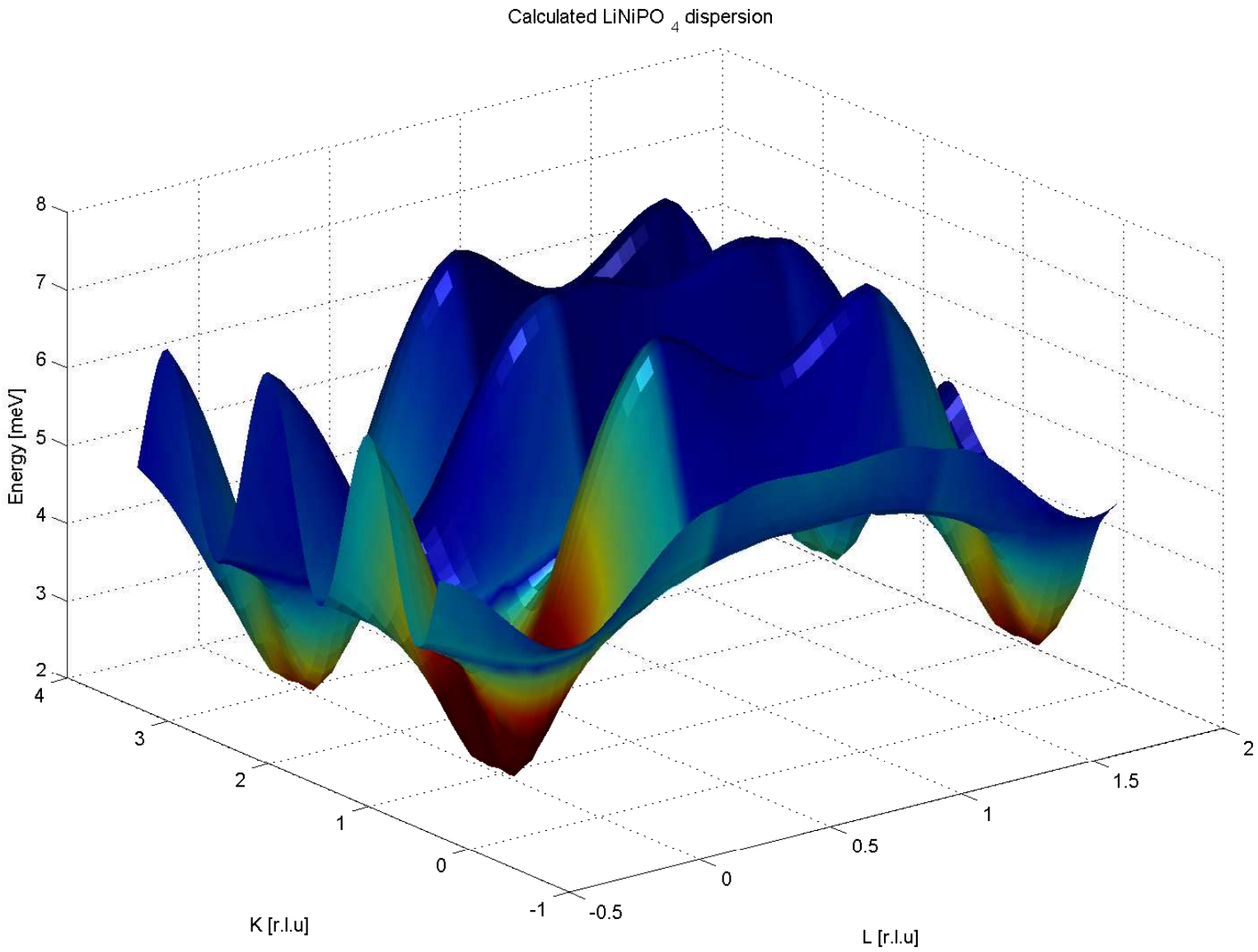

Figure 7.17: Calculated spin wave dispersion of the $(0, K, L)$ plane, using the spin wave model described in section 7.2.2, and the parameters from table 7.1. The depicted dispersion corresponds to that of figure 7.16, and the coloring is proportional to the calculated spin wave intensity (red for high intensities, blue for low).

Chapter 8

Concluding remarks

The main results of this study on $LiNiPO_4$ can be summarized as follows. We have determined the magnetic HT phase diagram for fields $\mathbf{H}||\mathbf{c}$ below 14.7 T, the magnetic structures of the corresponding phases, and have proposed a spin Hamiltonian based on performed inelastic measurements.

The picture of the phase diagram (figure 4.1) is that of two magnetically ordered phases; a commensurate phase surrounded by an incommensurate phase. At low fields the commensurate phase exist at temperatures below $T_C \sim 20$ K, and the incommensurate phase in a small temperature interval above T_C. At higher fields the incommensurate phase is extended as the commensurate phase transition temperature decreases. Above 13.5 T the system is never commensurate. Both the commensurate and incommensurate structures have spins pointing primarily along the c-axis, and the incommensurate structure is modulated in the b direction. Both phases also have small magnetic components along the a axis. The field independent part of these are consistent with the symmetry of the allowed Dzyaloshinsky-Moriya interactions, while the field dependent components, observed when a field is applied along c, are consequences of the crystal magnetization.

In the inelastic experiments we found well defined spin waves in the commensurate phase, but none in the incommensurate phase. Proposing a model Hamiltonian we have reproduced both dispersions and intensities of the spin waves measured in the commensurate phase. The evaluated interaction parameters (see table 7.1) show that $LiniPO_4$ has strong nearest- and next-nearest neighbor exchange interactions within the NiO planes, and that the spins experience a large anisotropy along b.

During my years as a phD student I have received invaluable help from a large number of people. It is impossible to mention all, but I would like to give special thanks to Michel Kenzelmann, Henrik Rønnow, and my supervisor Niels Hessel Andersen. Also special thanks to Asger Abrahamsen, Niels B. Christensen, Christof Niedermayer, Bente Lebeck, Kim Lefmann, Jürg Schefer, and to David Vaknin. At BW5 in Hamburg Martin Von Zimmermann has been great. I should of course mention the rest of my group at Risoe: Jean-Claude Grivel, Peter Willendrup, Christian Bahl, Linda Udby and Jari Hjøllum; and Jens Jensen from the university of Copenhagen. Finally I would like give a special thanks to my father, Mogens Stibius Jensen, for many fruitful discussions.

Appendix A

Proof of theorem 1

From [41] we have the following formal definition of an irreducible tensor operator.

Definition 3 *The $(2k+1)$ operators $T_q^{(k)}$, where $q = -k, -k+1, \ldots, k$, are the standard components of an irreducible k'th-order tensor operator, $\mathbf{T}^{(k)}$, if they transform in a rotation, R, according to*

$$RT_q^{(k)}R^{-1} = \sum_{q'} T_{q'}^{(k)} R(k)_{qq'}. \tag{A.1}$$

Here $R_{qq'}^{(k)}$ are the elements of the rotation matrix. Eq. (A.1) is equivalent to the following commutation rules between $T_q^{(k)}$ and the components of any angular momentum operator

$$\begin{aligned} [J_\pm, T_q^{(k)}] &= \sqrt{k(k+1) - q(q\pm 1)}\, T_{q\pm 1}^{(k)}, \\ [J_z, T_q^{(k)}] &= q T_q^{(k)}. \end{aligned} \tag{A.2}$$

Eq. (A.2) may also serve as the definition of an irreducible tensor operator.

We state without proof the Wigner-Eckart theorem [41].

Theorem 5 *In the standard representation of a given angular momentum, $\mathbf{J}^2$, J_z, the matrix elements of the q'th standard component, $T_q^{(k)}$, of an irreducible tensor operator, $\mathbf{T}^{(k)}$, are given as*

$$\langle \tau JM | T_q^{(k)} | \tau' J' M' \rangle = \frac{1}{\sqrt{2J+1}} \langle \tau J || \mathbf{T}^{(k)} || \tau' J' \rangle \langle J' k M' q | J M \rangle. \tag{A.3}$$

Here $\frac{1}{\sqrt{2J+1}} \langle \tau J || \mathbf{T}^{(k)} || \tau' J' \rangle$ is a quantity called the reduced matrix element, which is independent of M, M' and q. The quantities $\langle J' k M' q | J M \rangle$ are the Clebsch-Gordon coefficients.

We shall now prove theorem 1.

Theorem 1 *Within a LS multiplet the spin-orbit coupling term, $\mathcal{H}_{so}$, can be written as*

$$\mathcal{H}_{so} = \sum_{i=1}^{N} \xi(r_i) \mathbf{l}_i \cdot \mathbf{s}_i = \lambda (\mathbf{L} \cdot \mathbf{S}). \tag{A.4}$$

Proof *Defining the irreducible tensor operators*

$$
\begin{aligned}
L_1^{(1)} &= -\frac{1}{\sqrt{2}}(L^x + iL^y), \quad L_0^{(1)} = L^z, \quad L_{-1}^{(1)} = \frac{1}{\sqrt{2}}(L^x - iL^y), \\
S_1^{(1)} &= -\frac{1}{\sqrt{2}}(S^x + iS^y), \quad S_0^{(1)} = S^z, \quad S_{-1}^{(1)} = \frac{1}{\sqrt{2}}(S^x - iS^y), \\
l_1^{(1)} &= -\frac{1}{\sqrt{2}}(l^x + il^y), \quad l_0^{(1)} = l^z, \quad l_{-1}^{(1)} = \frac{1}{\sqrt{2}}(l^x - il^y), \\
s_1^{(1)} &= -\frac{1}{\sqrt{2}}(s^x + is^y), \quad s_0^{(1)} = s^z, \quad s_{-1}^{(1)} = \frac{1}{\sqrt{2}}(s^x - is^y),
\end{aligned}
\tag{A.5}
$$

we have that

$$
\mathbf{L}\cdot\mathbf{S} = L_0^{(1)}S_0^{(1)} - L_1^{(1)}S_{-1}^{(1)} - L_{-1}^{(1)}S_1^{(1)}, \tag{A.6}
$$

and

$$
\mathbf{l}\cdot\mathbf{s} = l_0^{(1)}s_0^{(1)} - l_1^{(1)}s_{-1}^{(1)} - l_{-1}^{(1)}s_1^{(1)}. \tag{A.7}
$$

Noting that $N\xi(r)l_q^{(1)}$, where $q = -1, 0, +1$, is also an irreducible tensor operator we use the Wigner-Eckart theorem (A.3), and find

$$
\langle \alpha L M_L | N\xi(r) l_q^{(1)} | \alpha' L M_L' \rangle = \frac{1}{\sqrt{2L+1}} \langle \alpha L || N\xi(r) l^{(1)} || \alpha' L \rangle \langle L 1 M_L' q | L M_L \rangle, \tag{A.8}
$$

$$
\langle \alpha L M_L | L_q^{(1)} | \alpha' L M_L' \rangle = \frac{1}{\sqrt{2L+1}} \langle \alpha L || L^{(1)} || \alpha' L \rangle \langle L 1 M_L' q | L M_L \rangle. \tag{A.9}
$$

The Clebsch-Gordan coefficient, $\langle L 1 M_L' q | L M_L \rangle$, can be found from (A.9) as

$$
\langle L 1 M_L' q | L M_L \rangle = \sqrt{2L+1} \langle \alpha L || L^{(1)} || \alpha' L \rangle \langle \alpha L M_L | L_q^{(1)} | \alpha' L M_L' \rangle, \tag{A.10}
$$

which, when inserted in (A.8), gives

$$
\begin{aligned}
\langle \alpha L M_L | N\xi(r) l_q^{(1)} | \alpha' L M_L' \rangle &= \langle \alpha L || \xi(r) l^{(1)} || \alpha' L \rangle \langle \alpha L || L^{(1)} || \alpha' L \rangle \langle \alpha L M_L | L_q^{(1)} | \alpha' L M_L' \rangle \\
&= B \langle \alpha L M_L | L_q^{(1)} | \alpha' L M_L' \rangle,
\end{aligned}
\tag{A.11}
$$

where B is independent of q. Similarly one finds that

$$
\langle \alpha S M_S | s_{q'}^{(1)} | \alpha' S M_S' \rangle = B' \langle \alpha S M_S | S_{q'}^{(1)} | \alpha' S M_S' \rangle, \tag{A.12}
$$

where B' is independent of q'. All in all

$$
\begin{aligned}
&\langle \alpha L S M_L M_S | \mathcal{H}_2 | \alpha' L S M_L' M_S' \rangle \\
&= \langle \alpha L S M_L M_S | N\xi(r)(l_0^{(1)}s_0^{(1)} - l_1^{(1)}s_{-1}^{(1)} - l_{-1}^{(1)}s_1^{(1)}) | \alpha' L S M_L' M_S' \rangle \\
&= \lambda \langle \alpha L S M_L M_S | (L_0^{(1)}S_0^{(1)} - L_1^{(1)}S_{-1}^{(1)} - L_{-1}^{(1)}S_1^{(1)}) | \alpha' L S M_L' M_S' \rangle \\
&= \langle \alpha L S M_L M_S | \lambda(\mathbf{L}\cdot\mathbf{S}) | \alpha' L S M_L' M_S' \rangle,
\end{aligned}
\tag{A.13}
$$

and the theorem is proved.

Appendix B

Rewriting the exchange interaction

Equation (2.42) is shown by rewriting

$$\begin{aligned}
&\sum_{s_1 s_2} a^\dagger_{\alpha_1 s_1} a_{\alpha_1 s_2} a^\dagger_{\alpha_2 s_1} a_{\alpha_2 s_2} = \\
&\quad a^\dagger_{\alpha_1\uparrow} a_{\alpha_1\uparrow} a^\dagger_{\alpha_2\uparrow} a_{\alpha_2\uparrow} + a^\dagger_{\alpha_1\uparrow} a_{\alpha_1\downarrow} a^\dagger_{\alpha_2\downarrow} a_{\alpha_2\uparrow} + a^\dagger_{\alpha_1\downarrow} a_{\alpha_1\uparrow} a^\dagger_{\alpha_2\uparrow} a_{\alpha_2\downarrow} + a^\dagger_{\alpha_1\downarrow} a_{\alpha_1\downarrow} a^\dagger_{\alpha_2\downarrow} a_{\alpha_2\downarrow} = \\
&\quad \frac{1}{2}(a^\dagger_{\alpha_1\uparrow} a_{\alpha_1\uparrow} + a^\dagger_{\alpha_1\downarrow} a_{\alpha_1\downarrow})(a^\dagger_{\alpha_2\uparrow} a_{\alpha_2\uparrow} + a^\dagger_{\alpha_2\downarrow} a_{\alpha_2\downarrow}) + \frac{1}{2}(a^\dagger_{\alpha_1\uparrow} a_{\alpha_1\uparrow} - a^\dagger_{\alpha_1\downarrow} a_{\alpha_1\downarrow})(a^\dagger_{\alpha_2\uparrow} a_{\alpha_2\uparrow} - a^\dagger_{\alpha_2\downarrow} a_{\alpha_2\downarrow}) \\
&\quad + a^\dagger_{\alpha_1\uparrow} a_{\alpha_1\downarrow} a^\dagger_{\alpha_2\downarrow} a_{\alpha_1\uparrow} + a^\dagger_{\alpha_1\downarrow} a_{\alpha_1\uparrow} a^\dagger_{\alpha_2\uparrow} a_{\alpha_1\downarrow},
\end{aligned} \tag{B.1}$$

where $\alpha = (n, m)$. Using

$$a^\dagger_{\alpha\uparrow} a_{\alpha\uparrow} + a^\dagger_{\alpha\downarrow} a_{\alpha\downarrow} = 1, \tag{B.2}$$

and introducing

$$s^z_\alpha = \frac{1}{2}(a^\dagger_{\alpha\uparrow} a_{\alpha\uparrow} - a^\dagger_{\alpha\downarrow} a_{\alpha\downarrow}), \quad s^+_\alpha = s^x_\alpha + i s^y_\alpha = a^\dagger_{\alpha\uparrow} a_{\alpha\downarrow}, \quad s^-_\alpha = s^x_\alpha - i s^y_\alpha = a^\dagger_{\alpha\downarrow} a_{\alpha\uparrow}, \tag{B.3}$$

we find that

$$\sum_{s_1 s_2} a^\dagger_{\alpha_1 s_1} a_{\alpha_1 s_2} a^\dagger_{\alpha_2 s_1} a_{\alpha_2 s_2} = \frac{1}{2} + 2 s^z_{\alpha_1} s^z_{\alpha_2} + 2 s^+_{\alpha_1} s^-_{\alpha_2} + 2 s^-_{\alpha_1} s^+_{\alpha_2} = \frac{1}{2} + 2 \mathbf{s}_{\alpha_1} \cdot \mathbf{s}_{\alpha_2}. \tag{B.4}$$

Inserting (B.4) into (2.41) we get

$$V_{DE} = -\frac{1}{2} \sum_{\substack{n_1 m_1 \\ n_2 m_2}} J^{m_1 m_2}_{n_1 n_2} \left(\frac{1}{2} + 2 \mathbf{s}^{m_1}_{n_1} \cdot \mathbf{s}^{m_2}_{n_2} \right) = K_0 - \sum_{\substack{n_1 m_1 \\ n_2 m_2}} J^{m_1 m_2}_{n_1 n_2} \mathbf{s}^{m_1}_{n_1} \cdot \mathbf{s}^{m_2}_{n_2}. \tag{B.5}$$

Appendix C

MATLAB scripts for spin wave calculations

BoguliobovExtended.m

```
function [Ecal,Ical_1,Ical_3]=BoguliobovExtended(Q,J1,J2,J3,J4,J5,Dx,Dy,S,Ef,temp);%

% function [E,Ical_1,Ical_3]=BoguliobovExtended(q,J1,J2,J3,J4,J5,Dx,S);
%
% Rutine finding the eigenvalues (E) and intensities (Ical) for LiNiPO4
% magnon problem including nearest and next-nearest neighbors interactions
% and isotropy Dx and Dy (Dz = 0 per definition)
%
% written by tbsj (2006)

if nargin<10,Ef=5;end if nargin<11,temp=1.5;end

Ecal=[]; Ical_1=[];Ical_2=[];Ical_3=[];Ical_4=[];

% Relevant neighboring vectors
r1=[0 0.5 0.5];r2=[0 0.5 -0.5];r3=[0.5 0.5 0];r4=[0.5 -0.5 0];% Up-Down neighbors
r5=[0 1 0];r6=[0 0 1];r7=[0.5 0 0.5];r8=[0.5 0 -0.5];% Up-Up neighbors
% Q, tau and q-values
Qx=Q(:,1);Qy=Q(:,2);Qz=Q(:,3); [tau1,tau2]=tau_LiNiPO4(Q);
tau=tau1; % (tau1,q1)
% tau=tau2; % check that (tau2,q2) gives same result as (tau1,q1)
qx=Qx-tau(:,1);qy=Qy-tau(:,2);qz=Qz-tau(:,3);
%qx=Q(:,1);qy=Q(:,2);qz=Q(:,3);

for n=1:length(qx)

    %[Q(n,:),tau(n,:),qx(n),qy(n),qz(n)]%,pause % delete after use

% Taking the scalar product between q and r
qr1=2*pi*[qx(n)*r1(1)+qy(n)*r1(2)+qz(n)*r1(3)];
qr2=2*pi*[qx(n)*r2(1)+qy(n)*r2(2)+qz(n)*r2(3)];
qr3=2*pi*[qx(n)*r3(1)+qy(n)*r3(2)+qz(n)*r3(3)];
qr4=2*pi*[qx(n)*r4(1)+qy(n)*r4(2)+qz(n)*r4(3)];
qr5=2*pi*[qx(n)*r5(1)+qy(n)*r5(2)+qz(n)*r5(3)];
qr6=2*pi*[qx(n)*r6(1)+qy(n)*r6(2)+qz(n)*r6(3)];
qr7=2*pi*[qx(n)*r7(1)+qy(n)*r7(2)+qz(n)*r7(3)];
qr8=2*pi*[qx(n)*r8(1)+qy(n)*r8(2)+qz(n)*r8(3)];
```

```
% At the moment all coupling and anisotropy constants must be real numbers
% a'a+b'b (' = dagger)
A1 = 4*(J1+J5)*S; % Up-Down interactions
A2 = -2*J2*S*(1-cos(qr5))-2*J3*S*(1-cos(qr6))-2*J4*S*(2-cos(qr7)-cos(qr8)); % Up-Up interactions
A3 = Dx*S+Dy*S; % Anisotropy
A = A1+A2+A3;
% ab+a'b'
D = 2*J1*S*(cos(qr1)+cos(qr2))+2*J5*S*(cos(qr3)+cos(qr4)); % Up-Down interactions
% aa+a'a'+bb+b'b'
B=S*(Dx-Dy)/2; % Anisotropy
C=0;

B=2*B; % Due to form of Hamiltonian matrix defined below

H=[ A   B   C   D; % True Hamiltonian matrix
    B   A   D   C;
    C   D   A   B;
    D   C   B   A];

I1=[1   0   0   0; % Inversionform 1
    0  -1   0   0;
    0   0   1   0;
    0   0   0  -1];

H1=I1*H;[T1 E1] = eig(H1);% First eigenvalue problem
m1=[];                    % (rutine does not at present handle eigenvalues that are zero)
m2=[];

if isreal(E1)
    for nn=1:4
        if E1(nn,nn)>0,m1=[m1 nn];end
        if E1(nn,nn)<0,m2=[m2 nn];end
    end

if length(m1)==2;
        if abs( E1(m1(1),m1(1)) + E1(m2(1),m2(1)) )<1e-8; % Securing column order
        T=[T1(:,m1(1)),T1(:,m2(1)),T1(:,m1(2)),T1(:,m2(2))];% Transformation matrix
                                                            % which may not respect
                                                            % Bose commutation rules
        elseif abs( E1(m1(1),m1(1)) + E1(m2(2),m2(2)) )<1e-8;
        T=[T1(:,m1(1)),T1(:,m2(2)),T1(:,m1(2)),T1(:,m2(1))];% Transformation matrix
                                                            % which may not respect
                                                            % Bose commutation rules
        end
    N=diag(I1*inv(T)*I1*inv(T'));% Finding transformation matrix respecting Bose commutators
    T=[sqrt(N(1))*T(:,1) sqrt(N(2))*T(:,2) sqrt(N(3))*T(:,3) sqrt(N(4))*T(:,4)];
    THT=T'*H*T;
    E=diag(THT); % Finding eigenvalues
    % E=[sqrt(A^2-(B+D)^2);
    %   -sqrt(A^2-(B+D)^2);
    %    sqrt(A^2-(B-D)^2);
    %   -sqrt(A^2-(B-D)^2)];% Analytical expression


Ical_1=[Ical_1;IntensityBE_alpha(T,E(1),Qx(n),Qy(n),Qz(n),tau(n,:),Ef,temp)];
Ical_3=[Ical_3;IntensityBE_beta(T,E(3),Qx(n),Qy(n),Qz(n),tau(n,:),Ef,temp)];
```

```
else % if lenght(m1)~=2
    E=NaN*ones(4,1);T=NaN*ones(4,4);Ical_1= [Ical_1;NaN];Ical_3=[Ical_3;NaN];
end % if length(m1)==2;

else % if ~isreal(E1)
    E=NaN*ones(4,1);
    T=NaN*ones(4,4);Ical_1= [Ical_1;NaN];Ical_3=[Ical_3;NaN];

end % isreal(E1)

Ecal=[Ecal;E']; end
```

tau_LiNiPO4.m

```
function [tau1,tau2]=tau_LiNiPO4(Q);

% written by tbsj (2006)

tau1=[];tau2=[];

Qx=Q(:,1)-1e-10*ones(length(Q(:,1)),1);
Qy=Q(:,2)+1e-10*ones(length(Q(:,1)),1);
Qz=Q(:,3)-1e-10*ones(length(Q(:,1)),1);

for n=1:length(Qx)

    if round((floor(Qx(n))+floor(Qz(n)))/2)==(floor(Qx(n))+floor(Qz(n)))/2;
        tau_1=[floor(Qx(n)) round(Qy(n)) floor(Qz(n))];
        tau_2=[ceil(Qx(n)) round(Qy(n)) ceil(Qz(n))];
    end

    if round((floor(Qx(n))+ceil(Qz(n)))/2)==(floor(Qx(n))+ceil(Qz(n)))/2;
        tau_1=[floor(Qx(n)) round(Qy(n)) ceil(Qz(n))];
        tau_2=[ceil(Qx(n)) round(Qy(n)) floor(Qz(n))];
    end

tau1=[tau1;tau_1]; tau2=[tau2;tau_2];

end
```

intensityBE_alpha.m

```
function [Ical]=IntensityBE_alpha(T,E,Qx,Qy,Qz,tau,Ef,temp);

if nargin<8,temp=1.5;end

% function [Ical]=IntensityBE_alpha(T,E,Qx,Qy,Qz,Ef);
% T - transformation matrix, E - energy transfer to crystal,
% [Qx,Qy,Qz] - scattering vector, Ef - experimental final energy (at analyser)
% Calculates intensities of LiNiPO4 alpha spin wave dispersions.
%
% written by tbsj (2006)


% Finding appropriate latticevector and spin-dependent structure factors
%tau=tau_LiNiPO4([Qx,Qy,Qz]);
d_up1=[1/4,1/4,0]';d_up2=[3/4,1/4,1/2]'; % Position of spin up ions in unit cell
d_down1=[1/4,3/4,1/2]';d_down2=[3/4,3/4,1]'; % Position of spin down ions in unit cell
F_up=exp(-2*pi*i*tau*d_up1)+exp(-2*pi*i*tau*d_up2); % Structure factors
F_down=exp(-2*pi*i*tau*d_down1)+exp(-2*pi*i*tau*d_down2);
%F_up=1;F_down=1;

% Defining M and N for alpha creation
M=F_up*T(1,1)+F_down*T(4,1); N=F_up*T(2,1)+F_down*T(3,1);

% T-dependent part of scattering cross-section
Kxx = (abs(M+N))^2; % abs(M)^2 + abs(N)^2 + 2*real(M*conj(N)); % xx alpha term
Kyy = (abs(M-N))^2; % abs(M)^2 + abs(N)^2 - 2*real(M*conj(N)); % yy alpha term
Kxy = 4*imag(M*conj(N));
%Kxx=0;
%Kyy=0;


% Lattice parameters for LiNiPO4
a=10.02;b=5.83;c=4.66; astar=2*pi/a;bstar=2*pi/b;cstar=2*pi/c;

% Reciprocal vectors in correct units [1/]
Qx=astar*Qx;Qy=bstar*Qy;Qz=cstar*Qz;

Q=sqrt(Qx^2+Qy^2+Qz^2); if Q~=0
    Qxnorm=Qx/Q;Qynorm=Qy/Q;

Ei=E+Ef; % Experimental intial energy (at monochromator)
t=temp/11; % t = temperature in meV, since 1 meV = 11 Kelvin
nB=1/(exp(E/t)-1); % Bose factor
f=formfactorNi(Q,2); % Ni^2+ formfactor with Lande's g-factor g = 2 (spin only)

Ixx=sqrt(Ef/Ei)*(1-Qxnorm*Qxnorm)*Kxx*(nB+1);
Iyy=sqrt(Ef/Ei)*(1-Qynorm*Qynorm)*Kyy*(nB+1);
Ixy=sqrt(Ef/Ei)*(-Qxnorm*Qynorm)*Kxy*(nB+1);

Ical=f^2*(Ixx+Iyy+Ixy);

else
    Ical=NaN;
end
```

intensityBE_beta.m

```
function [Ical]=IntensityBE_beta(T,E,Qx,Qy,Qz,tau,Ef,temp);

if nargin<8,temp=1.5;end

% function [Ical]=IntensityBE(T,E,Qx,Qy,Qz,Ef);
% T - transformation matrix, E - energy transfer to crystal,
% [Qx,Qy,Qz] - scattering vector, Ef - experimental final energy (at analyser)
% Calculates intensities of LiNiPO4 beta spin wave dispersions.
%
% written by tbsj (2006)

% Finding appropriate latticevector and spin-dependent structure factors
%tau=tau_LiNiPO4([Qx,Qy,Qz]);
d_up1=[1/4,1/4,0]';d_up2=[3/4,1/4,1/2]'; % Position of spin up ions in unit cell
d_down1=[1/4,3/4,1/2]';d_down2=[3/4,3/4,1]'; % Position of spin down ions in unit cell
F_up=exp(-2*pi*i*tau*d_up1)+exp(-2*pi*i*tau*d_up2); % Structure factors
F_down=exp(-2*pi*i*tau*d_down1)+exp(-2*pi*i*tau*d_down2);
%F_up=1;F_down=1;

% Defining M and N for beta creation
M=F_up*T(1,3)+F_down*T(4,3); N=F_up*T(2,3)+F_down*T(3,3);

% T-dependent part of scattering cross-section
Kxx = (abs(M+N))^2; % abs(M)^2 + abs(N)^2 + 2*real(M*conj(N)); % xx beta term
Kyy = (abs(M-N))^2; % abs(M)^2 + abs(N)^2 - 2*real(M*conj(N)); % yy beta term
Kxy = 4*imag(M*conj(N));
%Kxx=0;
%Kyy=0;


% Lattice parameters for LiNiPO4
a=10.02;b=5.83;c=4.66; astar=2*pi/a;bstar=2*pi/b;cstar=2*pi/c;

% Reciprocal vectors in correct units [1/]
Qx=astar*Qx;Qy=bstar*Qy;Qz=cstar*Qz;

Q=sqrt(Qx^2+Qy^2+Qz^2); if Q~=0
    Qxnorm=Qx/Q;Qynorm=Qy/Q;

Ei=E+Ef; % Experimental intial energy (at monochromator)
t=temp/11; % t = temperature in meV, since 1 meV = 11 Kelvin
nB=1/(exp(E/t)-1); % Bose factor
f=formfactorNi(Q,2); % Ni^2+ formfactor with Lande's g-factor g = 2 (spin only)

Ixx=sqrt(Ef/Ei)*(1-Qxnorm*Qxnorm)*Kxx*(nB+1);
Iyy=sqrt(Ef/Ei)*(1-Qynorm*Qynorm)*Kyy*(nB+1);
Ixy=sqrt(Ef/Ei)*(-Qxnorm*Qynorm)*Kxy*(nB+1);

Ical=f^2*(Ixx+Iyy+Ixy);

else
    Ical=NaN;
end
```

formfactorNi.m

```
function [f]=formfactorNi(Q,g);

% Form factor for Ni^2+. g is Lande's g-factor.
% For spin-only magnetism g = 2.
%
% written by tbsj (2006)

A0=0.0163;a0=35.883;B0=0.3916;b0=13.223;C0=0.6052;c0=4.339;D0=-0.0133;
A2=1.7080;a2=11.016;B2=1.2147;b2=4.103;C2=0.315;c2=1.533;D2=0.0018;

s=Q/(4*pi);

J0=A0*exp((-1)*a0*s.^2)+B0*exp((-1)*b0*s.^2)+C0*exp((-1)*c0*s.^2)+D0;
J2=(A2*exp((-1)*a2*s.^2)+B2*exp((-1)*b2*s.^2)+C2*exp((-1)*c2*s.^2)+D2).*(s.^2);

f=J0+(1-g/2)*J2;
```

Appendix D

Testing the MATLAB scripts

Wanting to check whether our MATLAB scripts for the spin wave modelling were in working order, they were tested on already published data. We have chosen data published by Coldea *et al.* [45] on the high temperature superconductor parent La_2CuO_4, since here both spin wave dispersions and intensities were measured and calculated. The model for La_2CuO_4 is simpler than for $LiNiPO_4$, so we could easily have re-done Coldea's simulations without the extended calculations of chapter 6. However, since this was a test, and since the simpler calculations are not sufficient for $LiNiPO_4$, we calculated the spin wave dispersions and intensities with MATLAB scripts similar to the ones given in appendix C. Of course the scripts were adapted to La_2CuO_4, and we used the values given by [45] as interaction parameters.

The result of our calculations are given in figure D.1 as full lines. The good match to the data (red circles) from [45], shows that the MATLAB scripts should be trustworthy.

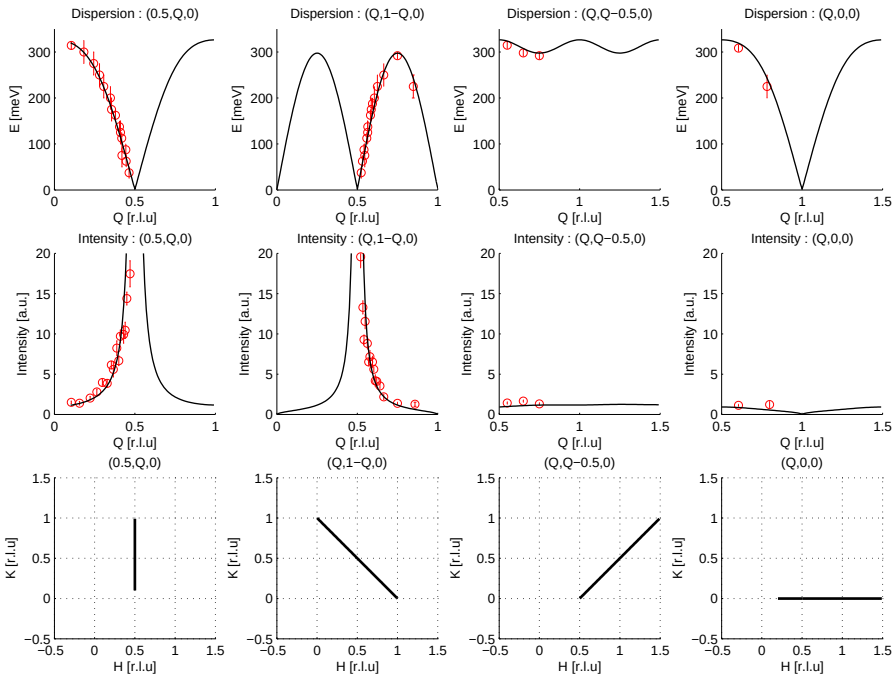

Figure D.1: Comparing spin wave data (red circled) from La_2CuO_4 taken from [45] with dispersions and intensities calculated by scripts similar to those of appendix C (full lines). The first row gives measured and calculated dispersion, the second row gives the spin wave intensities, and the third row shows the position of the considered scattering vectors in reciprocal space.

Appendix E

Travels abroad and list of publications

Travels abroad

During my phD study I have been abroad in a total of approximately 272 days (they may be small uncertainties in the dates given below). The travels and experiments have been distributed as follows:

- 12/8-24/8 2003: PSI, Villigen (Switzerland) - Flux lattice measurements on $La_{2-x}Sr_xCuO_4$ (SANS1)
- 17/9-24/9 2003: PSI, Villigen (Switzerland) - Instrument developments ect. (RITA-II)
- ca. 10 days jan/feb 2004: Hasylab, Hamburg (Germany) - Searching for structural stripes in $La_{2-x}Sr_xCuO_4$ (BW5)
- 21/2-3/4 2004 : ILL, ESRF a.o., Grenoble, Paris (France) - HERCULES course
- 31/5-11/6 2004: ILL, Grenoble (France) - Investigating detwinned $La_{2-x}Sr_xCuO_4$ (IN20)
- 4/7-14/7 2004: PSI, Villigen (Switzerland) - Spin wave measurements on $LiNiPO_4$ (RITA-II)
- 17/8-16/9 2004: PSI, Villigen (Switzerland) - Spin wave (RITA-II) and magnetic structure (TriCS) measurements on $LiNiPO_4$
- 7/11-13/11 2004: Hasylab, Hamburg (Germany) - Structural superstructure measurements in $TmNi_2B_2C$ as function of magnetic field and temperature (BW5)
- 7/12-21/12 2004: PSI, Villigen (Switzerland) - Investigating $La_{2-x}Sr_xCuO_4$ in magnetic field (RITA-II)
- 26/1-28/1 2005: PSI, Villigen (Switzerland) - PSI user meeting
- 28/2-11/3 2005: Hasylab, Hamburg (Germany) - Structural superstructure measurements in $TmNi_2B_2C$ as function of magnetic field and temperature (BW5)
- 10/04-22/04 2005: PSI, Villigen (Switzerland) og ILL, Grenoble (France) - Instrumentation (RITA-II) and spin wave measurements (IN8) on $LiNiPO_4$
- 16/8-24/8 2005: PSI, Villigen (Switzerland) - Spin wave measurements on $LiNiPO_4$ in magnetic field (RITA-II)
- 31/8-12/9 2005: PSI, Villigen (Switzerland) - Magnetic structure determination for $LiNiPO_4$ (TriCS)
- 12/10-25/10 2005: Hasylab, Hamburg (Germany) - $ErNi_2B_2C$ a.o. (BW5)
- 18/11-07/12 2005: PSI, Villigen (Switzerland) - Magnetic phase diagram determination of $LiNiPO_4$ (RITA-II)
- 3/5-17/5 2006: Hasylab, Hamburg (Germany) - $TbNi_2B_2C$, NH_4CuCl_3, $TlCuCl_3$ (BW5)

- 17/9-28/9 2006: Hasylab, Hamburg (Germany) - $TbNi_2B_2C$, $LiNiPO_4$ (BW5)
- 30/11-5/12 2006: Hasylab, Hamburg (Germany) - $LiNiPO_4$ (BW5)
- 22/03-28/03 2007: Hasylab, Hamburg (Germany) - $LiNiPO_4$ (BW5)

List of publications

- L. Sarholt, E. Johnson, A. Johansen, T. B. Stibius Jensen, A. B. Stibius Jensen and U. Dahmen, *'Nanosized Lead-Cadmium Inclusions in Aluminium'*, Mater. Sci. Forum **312-314**, 299 (1999).
- K. Flensberg, T. S. Jensen and N. A. Mortensen, *'Diffusion equation and spin drag in spin-polarized transport'*, PRB **64**, 245308 (2001).
- C. H. R. Bahl, K. Lefmann, A. B. Abrahamsen, H. M. Rønnow, F. Saxild, T. B. S. Jensen, L. Udby, N. H. Andersen, N. B. Christensen, H. S. Jakobsen, T. Larsen, P. S. Häfliger, S. Streule, Ch. Niedermayer, *'Inelastic neutron scattering experiments with the monochromatic imaging mode of the RITA-II spectrometer'*, NIMB **246**, 452 (2006).
- N. H. Andersen, J. Jensen, T. B. S. Jensen, M. v. Zimmermann, R. Pinholt, A. B. Abrahamsen, K. Nørgaard Toft, P. Hedegård and P. C. Canfield, *'Phonon-induced quadrupolar ordering of the magnetic superconductor $TmNi_2B_2C$'*, PRB **73**, 020504(R) (2006).
- N. H. Andersen, J. Jensen, T. B. S. Jensen, R. Pinholt, M. v. Zimmermann, K. Nørgaard Toft, A. B. Abrahamsen, P. Hedegård, P. Vorderwisch, P. C. Canfield, *'Magnetic and quadrupolar ordering in $TmNi_2B_2C$'*, Physica B **385**, 63 (2006).
- T. B. S. Jensen, N. B. Christensen, M. Kenzelmann, H. M. Rønnow, C. Niedermayer, N. H. Andersen, K. Lefmann, J. Schefer, M. v. Zimmermann, J. Li, J. L. Zarestky and D. Vaknin, *'Phase diagram and magnetic structures of the magneto-electric $LiNiPO_4$ (tentative)'*, pre-print.
- J. Li, L. Zarestky, D. Vaknin, T. B. S. Jensen, N. H. Andersen, J.-H. Chung, *'Tweaking the spin-wave dispersion and the incommensurate phase in $LiNiPO_4$ by iron substitution (tentative)'*, pre-print.
- T. B. S. Jensen *et al.*, *'Spin waves in the magneto-electric $LiNiPO_4$ (tentative)'*, in preparation.

Bibliography

[1] Andersen, N. H., Jensen, J., Jensen, T. B. S., v. Zimmermann, M., Pinholt, R., Abrahamsen, A. B., Toft, K. N., Hedegård, P., and Canfield, P. C. *Phys. Rev. B* **73**, 020504(R) (2006).

[2] Andersen, N. H., Jensen, J., Jensen, T. B. S., Pinholt, R., v. Zimmermann, M., Toft, K. N., Abrahamsen, A. B., Hedegård, P., Vorderwisch, P., and Canfield, P. C. *Physica B* **385**, 63 (2006).

[3] To be published.

[4] Chung, S.-Y., Bloking, J. T., and Chiang, Y.-M. *Nature Materials* **1**, 123 (2002).

[5] Abrahams, I. and Easson, K. S. *Acta Cryst.* **C49**, 925–926 (1993).

[6] Wilson, A. J. C., editor. *International Tables for Crystallography*, volume A. Kluver Academic Publishers.

[7] Santoro, R. P., Segal, D. J., and Newnham, R. E. *J. Phys. Chem. Solids* **27**, 1192–1193 (1966).

[8] Kittel, C. *Introduction to Solid State Physics.* John Wiley & Sons, (1996).

[9] Vaknin, D., Zarestky, J. L., Rivera, J.-P., and Schmid, H. *Phys. Rev. Lett.* **92**, 207201 (2004).

[10] Khrustalyov, V. M., Savitsky, V. N., and Kharchenco, N. F. *Czechoslovak Journal of Physics* **54**, D27 (2004).

[11] Eerenstein, W., Mathur, N. D., and Scott, J. F. *Nature* **442**, 759 (2006).

[12] Khomskii, D. *Journ. Magn. Magn. Mat.* **306**, 1 (2006).

[13] Spalding, N. A. and Fiebig, M. *Science* **309**, 391 (2005).

[14] Hur, N., Park, S., Sharma, P. A., Ahn, J. S., Guha, S., and Cheong, S.-W. *Nature* **429**, 392 (2004).

[15] Kimura, T., Goto, T., Shintani, H., Ishizaka, K., Arima, T., and Tokura, Y. *Nature* **426**, 55 (2003).

[16] Kenzelmann, M., Harris, A. B., Jonas, S., Broholm, C., Schefer, J., Kim, S. B., Zhang, C. L., Cheong, S.-W., Vajk, O. P., and Lynn, J. W. *Phys. Rev. Lett.* **95**, 087206 (2005).

[17] Lawes, G., Harris, A. B., Kimura, T., Rogado, N., Cava, R. J., Aharony, A., Entin-Wohlman, O., Yildirim, T., Kenzelmann, M., Broholm, C., and Ramirez, A. P. *Phys. Rev. Lett.* **95**, 087205 (2005).

[18] Kornev, I., Bichurin, M., Rivera, J.-P., Gentil, S., Schmid, H., Jansen, A. G. M., and Wyder, P. *Phys. Rev. B* **62**, 12247 (2000).

[19] Bransden, B. H. and Joachain, C. J. *Physics of atoms and molecules.* Longman Scientific & Technical, (1991).

[20] Ashcroft, N. W. and Mermin, N. D. *Solid State Physics.* W. B. Saunders Compagny, (1976).

[21] Tang, P. and Holzwarth, N. A. W. *Phys. Rew. B* **68**, 165107 (2003).

[22] Xu, Y.-N., Ching, W. Y., and Chiang, Y.-M. *J. Appl. Phys.* **95**, 6583 (2004).

[23] Kornev, I., Rivera, J.-P., Gentil, S., Jansen, A. G. M., Bichurin, M., Schmid, H., and Wyder, P. *Physica B* **270**, 82–87 (1999).

[24] Yoshida, K. *The Theory of Magnetism*. Springer, (1996).

[25] Bruus, H. and Flensberg, K. *Quantum field theory in condenced matter physics*. Niels Bohr Institute, (2001).

[26] Schweber, S. S. *An introduction to relativistic quantum field theory*. Harper & Row, (1964).

[27] Anderson, P. W. *Phys. Rev.* **115**, 2 (1959).

[28] Moriya, T. *Phys. Rev.* **120**, 91 (1960).

[29] Squires, G. L. *Introduction to the theory of thermal neutron scattering*. Cambridge University Press, (1978).

[30] Rossat-Mignod, J. *Methods of experimental physics, Vol. 23, part C, chapter 19*. Academic Press Inc, (1987).

[31] Bahl, C. R. H., Lefmann, K., Abrahamsen, A. B., Rønnow, H. M., Saxild, F., Jensen, T. B. S., Udby, L., Andersen, N. H., Christensen, N. B., Jakobsen, H. S., Larsen, T., Häfliger, P. S., Streule, S., and Niedermeyer, C. *NIMB* **246**, 452–462 (2006).

[32] Hiess, A., Jiménez-Ruiz, M., Courtois, P., Currat, R., Kulda, J., and Bermejo, F. J. *Physica B* **385-386**, 1077–1079 (2006).

[33] Demmel, F., Grach, N., and Rønnow, H. M. *NIMA* **530**, 404–409 (2004).

[34] Grach, N., Demmel, F., and Rønnow, H. M. A novel multiplexing three-axis spectrometer.

[35] Schefer, J., Könnecke, M., Murasik, A., Czopnik, A., Strässle, T., Keller, P., and Schlumpf, N. *Physica B* **276-278**, 168–169 (2000).

[36] Dianoux, A.-J. and Lander, G. ILL Neutron Data Booklet.

[37] Wilson, A. J. C., editor. *International Tables for Crystallography*, volume C. Kluver Academic Publishers.

[38] Hamermesh, M. *Group theory and its applications to physical problems*. Addison-Wesley, (1962).

[39] Heine, V. *Group Theory in Quantum Mechanics*. Pergamon press, (1964).

[40] Bertaut, E. F. *Acta Cryst.* **A24**, 217 (1968).

[41] Messiah, A. *Quantum Mechanics*. North-Holland Publishing Compagny, (1965).

[42] Kenzelmann, M. Private communication.

[43] Kharchenco, Y. N. and Kharchenco, N. F. *Low Temp. Phys.* **29**, 579 (2003).

[44] Lindgård, P. A., Kowalska, A., and Laut, P. *J. Phys. Chem. Solids* **28**, 1357 (1967).

[45] Coldea, R., Hayden, S. M., Aeppli, G., Perring, T. G., Frost, C. D., Mason, T. E., Cheong, S.-W., and Fisk, Z. *Phys. Rev. Lett.* **86**, 5377 (2001).

[46] Holstein, T. and Primakoff, H. *Phys. Rev.* **58**, 1098 (1940).

[47] Flügge, S. and Wijn, H. P. J., editors. *Handbuch der Physik*, volume XVIII/2. Springer Verlag, (1966).

[48] del Moral, A. *J. Phys.: Condens. Matter* **4**, 4687 (1992).

[49] del Moral, A. *J. Phys.: Condens. Matter* **4**, 4703 (1992).

[50] Zhi-dong, Z. and Tong, Z. *J. Phys.: Condens. Matter* **9**, 8101 (1997).

[51] Nagamiya, T. *Solid State Physics, edited by F. Seitz and D. Turnbull (Vol. 29, p. 346).* Academic, New York, (1967).